

Investigation of a Micro- and Nano-Particle In-Space Electrostatic Propulsion Concept

by

Louis D. Musinski

A dissertation submitted in partial fulfillment
of the requirements for the degree of
Doctor of Philosophy
(Electrical Engineering)
in The University of Michigan
2009

Doctoral Committee:

Professor Brian E. Gilchrist, Co-Chair
Professor Alec D. Gallimore, Co-Chair
Professor Yogesh B. Gianchandani
Associate Professor Michael J. Solomon

© Louis D. Musinski 2009
All Rights Reserved

Acknowledgements

First, I would like to thank everyone who helped and supported me throughout my entire education. This work was made possible by everyone who has touched my life and includes people too numerous to mention. To everyone who is not directly mentioned here, thank you!

I would like to express gratitude for my advisor and co-chairman, Dr. Brian Gilchrist. His support over the last several years has been invaluable towards my development as an engineer and a person. The enthusiasm he exudes motivates people around him and I consider myself privileged to have worked with him. I look forward to future collaborations. I also thank my other co-chairman, Dr. Alec Gallimore, who has also provided significant guidance throughout my graduate school career. Dr. Michael Solomon and Dr. Yogesh Gianchandani, thank you for your help and guidance as members of my dissertation committee.

I was fortunate to have been involved with a wonderful research group, nanoFET, which was composed of, not only excellent engineers, but also people that were a pleasure to work with. Thank you: Dr. Joanna Mirecki-Millunchick, Dr. Mark Burns, Dr. Michael Kiedar, Thomas Liu, Deshpremy Mukhija, Inkyu Eu, and David Liaw.

The members of the Space Electrodynamics and Tether Systems (SETS) research group provided support, guidance, friendship, and the needed distractions that were an

essential part my graduate school experience. Thank you: Chris Deline, Keith Fuhrhop, Rafael Ramos, Dave Morris, and Chris Davis.

The Horace H. Rackham School of Graduate Studies funded my graduate studies for one year, the NASA Institute for Advanced Concepts (NIAC) provided funding for almost two years, and the Air Force Office of Scientific Research (AFOSR) provided funding for another year.

The employees of the Space Physics Research Laboratory (SPRL) at the University of Michigan provided help on numerous on occasions. In particular, I would like to thank Robb Gillespie and Chuck Navarre for their help machining experimental equipment and prototypes.

Lastly, I would like to thank my family for all the love and support they have given me. Thank you Mom, Dad, and Alex.

Louis Musinski
December 12, 2008

Table of Contents

Acknowledgements	ii
List of Figures	vi
List of Tables.....	xiii
List of Appendices.....	xv
Glossary	xvi
Abstract.....	xxi

Chapter

1. Motivation, Background, and Introduction	1
1.1. Motivation of Research.....	1
1.2. Background of Space Electrostatic Propulsion.....	2
1.3. Introduction to the Micro- and Nano-Particle Thruster.....	10
1.4. Summary of Research Contributions.....	15
1.5. Dissertation Overview	17
2. Electrostatic Charging of Spherical and Cylindrical Particles	19
2.1. Introduction.....	19
2.2. Theory of Particle Charging.....	20
2.3. Experimental Setup	50
2.4. Experimental Results.....	58
2.5. Particle Charging Time.....	63
2.6. Effects of Particle Charging on Micro- and Nano-Particle Thrusters	69
2.7. Conclusion	70
3. Liquid Surface Instability Initiated by an Applied High Strength Electric Field..	72
3.1. Introduction.....	72
3.2. Liquid Instability Theory	73
3.3. Experimental Setup	89
3.4. Experimental Results.....	90
3.5. Conclusion	91
4. Extraction of Spherical and Cylindrical Particles From an Insulating Liquid	93
4.1. Introduction.....	93
4.2. Theory of Particle Extraction.....	94
4.3. Experimental Setup	129
4.4. Experimental Results.....	133
4.5. Discussion of Experimental Results.....	137

4.6. Effects of Particle Extraction on Micro- and Nano-Particle Thrusters ...	140
4.7. Conclusion	142
5. Adhesion and Cohesion of Dry Micro- and Nano-Particles.....	143
5.1. Introduction.....	143
5.2. Adhesion and Cohesion Forces	145
5.3. Overcoming the Adhesion Force Using High Strength Electric Fields ..	155
5.4. Experimental Setup	165
5.5. Experimental Results.....	173
5.6. Variables of the Experiment	177
5.7. Lifshitz-van der Waals Constant.....	189
5.8. Effects of the van der Waals Adhesion Force on Micro- and Nano-Particle Thrusters	191
5.9. Conclusion	193
6. Dry Particle Transport.....	195
6.1. Introduction.....	195
6.2. Particle Transport Using the Gradient in an Applied Electric Field	195
6.3. Particle Transport Through Micro- and Nano-Sieves	222
6.4. Conclusion	227
7. Conclusions and Recommendations for Future Research.....	229
7.1. Summary and Conclusions of Research	229
7.2. Recommendations for Future Work.....	235
Appendices.....	238
Bibliography.....	248

List of Figures

Figure 1.1: Dry mass fraction as a function of ΔV for specific impulses of 450 s and 3000 s.....	5
Figure 1.2: Diagram (left) and photograph (right) of the gridded ion thruster, NSTAR, used for NASA’s Deep Space 1.....	7
Figure 1.3: Diagram (left) and photograph (right) ¹³ of a Hall effect thruster.....	8
Figure 1.4: Diagram of a single FEEP emitter.....	9
Figure 1.5: Diagram of a single colloid emitter.	10
Figure 1.6: Transport of 20 μm particles from a large storage reservoir through microfluidic channels.....	12
Figure 1.7: Design of a single emitter from the insulating liquid configuration.....	12
Figure 1.8: Design of a single emitter from the conducting liquid configuration.....	14
Figure 2.1: Model for determining the charge acquired by a conducting spherical particle in contact with an infinite planar electrode and subjected to an electric field.....	20
Figure 2.2: Plot of $\alpha_{\text{sph}}(\theta, \zeta_{\text{sph}})$, the field-focusing term for a spherical particle between infinite plates, as a function of θ for several values of ζ_{sph}	24
Figure 2.3: Plot of $A_c(\zeta_{\text{sph}})$ as a function of ζ_{sph}	25
Figure 2.4: Plot of $q_{\text{sph}}(\zeta_{\text{sph}}):q_{\text{sph}}(\zeta_{\text{sph}}=0)$ as a function of ζ_{sph} when using a constant maximum electric field.	27
Figure 2.5: Model for the charge acquired by a conducting, vertically oriented, cylindrical particle in contact with a planar electrode and subjected to an electric field.	29
Figure 2.6: Plot of $\alpha_{\text{cyl}}(\beta)$ over the surface of the hemispherical cap.	32
Figure 2.7: Plot of $\alpha_{\text{cyl}}(\beta)$ over the surface of the cylindrical shaft.	32
Figure 2.8: Plot of $A_{\text{cyl}}(\beta)$ as a function of β , the aspect ratio of the cylindrical particle. Includes simulated results and a comparison with Felici’s calculations [29].	33

Figure 2.9: Plot of $\alpha_{cyl}(\beta, \theta=0)$ as a function of β and a linear fit over $5 < \beta < 80$	35
Figure 2.10: Plot of χ_{sph}/χ_{cyl} as a function of β using a constant background electric field.	37
Figure 2.11: Plot of χ_{sph}/χ_{cyl} as a function of β using a constant maximum electric field.	39
Figure 2.12: Specific impulse and exhaust velocity as a function of particle diameter for spherical and cylindrical particles per Equations (2.28) and (2.29), respectively.	41
Figure 2.13: Model for the charge acquired by a conducting spherical particle in contact with a planar electrode and subjected to a high strength electric field with additional particles in the vicinity of the particle of interest.	43
Figure 2.14: Plot of Γ_{group} as function of the ratio of the particle separation to the particle diameter.	45
Figure 2.15: Model for charging spherical particles on a high aspect ratio charging post	47
Figure 2.16: Plot of Γ_{post} as function of β , for the situation of a spherical particle on a post with a combined height to diameter ratio of β	48
Figure 2.17: Depiction of the experimental setup used for investigating the charging of spherical and cylindrical particles against a planar electrode with a high strength electric field.	50
Figure 2.18: Oscillation of a charged particle between parallel electrodes biased to electric potential, V	51
Figure 2.19: Expected system current as a function of time as the charged particle oscillates between the parallel electrodes.	53
Figure 2.20: Diagram of an inverting operational amplifier with a capacitor inserted in parallel with the feedback resistor used to measure current of the oscillating charged particle.	55
Figure 2.21: Experimental current trace when oscillating an 800 micron, spherical, aluminum particle with an electric field of approximately 570 kV/m.	59
Figure 2.22: Spherical particle charge measurements using titanium. Particle oscillation in 100 cSt silicone oil between 11.30 mm spaced electrodes. The solid line is the theoretical charge from Equation (2.12).	60
Figure 2.23: Spherical particle charge measurements using aluminum. Particle oscillation in 50 cSt silicone oil between 6.15 mm spaced electrodes. The solid line is the theoretical charge from Equation (2.12).	61

Figure 2.24: Cylindrical particle charge measurements using aluminum. Particle oscillation in 100 cSt silicone oil between 13.9 mm spaced electrodes. The solid line is the theoretical charge from Equation (2.20).	62
Figure 2.25: Spherical aluminum particle charging times. Particle oscillation in 50 cSt silicone oil between 6.15 mm spaced electrodes.....	64
Figure 2.26: Measured particle charging time constants for aluminum spheres.....	65
Figure 2.27: A spherical particle in contact with a planar electrode is modeled as an RC circuit.	66
Figure 3.1: Model for liquid surface instability induced by an applied electric field.	73
Figure 3.2: Model of the liquid perturbation.....	75
Figure 3.3: Model for liquid surface instability induced by an applied electric field.	77
Figure 3.4: Plot of $\alpha_{liq}(\theta,y)$ as a function of θ for several values of y	78
Figure 3.5: The predicted surface tension of silicone oil as a function of its temperature.	83
Figure 3.6: Model for suppressing the liquid surface instability with a knife-edge orifice. ^{61,62}	85
Figure 3.7: Plot of the threshold electric field required to initiate a liquid instability when using a knife-edge orifice in an earth-gravity environment.....	86
Figure 3.8: Plot of the threshold electric field required to initiate a liquid instability when using a knife-edge orifice in a zero-gravity environment.....	87
Figure 3.9: Series of frames showing the process of an instability forming on the surface of 100 cSt silicone oil using an applied electric field of approximately 1.7 MV/m.	90
Figure 4.1: Model for the extraction of a charged particle from an insulating liquid by an electric field.....	95
Figure 4.2: Forces acting on charged spherical and cylindrical particles during the extraction process through the liquid-vacuum interface.....	97
Figure 4.3: Plot of the predicted threshold extraction electric field to extract aluminum spherical particles from silicone oil using a maximum charging electric field strength of 15 MV/m.....	102
Figure 4.4: Plot of the threshold extraction electric field to extract aluminum cylindrical particles with an aspect ratio of 10 from silicone oil using a maximum electric field strength of 15 MV/m.	106

Figure 4.5: Plot of the threshold extraction electric field to extract aluminum cylindrical particles with an aspect ratio of 80 from silicone oil using a maximum electric field strength of 15 MV/m.	107
Figure 4.6: Plot of $E_{ex,sph,thresh}/E_{ex,cyl,thresh}$ in the surface tension dominant regime as a function of β using a constant maximum electric field	108
Figure 4.7: Forces acting on a charged spherical particle when traveling at terminal velocity.....	111
Figure 4.8: The terminal velocities and Reynolds numbers of aluminum spherical particles in 100 cSt Silicone oil using a maximum electric field strength of 15 MV/m.	114
Figure 4.9: The particle's maximum kinetic energy and the liquid surface potential energy using aluminum particles, 100 cSt silicone oil, and a maximum electric field strength of 15 MV/m.	116
Figure 4.10: Viscous flow from the surface of a spherical particle.	117
Figure 4.11: Velocity profile of liquid draining from the surface of a spherical particle at $\theta=90^\circ$	122
Figure 4.12: Plot of the lower and upper bounds of the threshold extraction electric field to extract aluminum spherical particles from silicone oil using a maximum electric field strength of 15 MV/m	124
Figure 4.13: Plot of the required extraction electric field to extract aluminum spherical and cylindrical particles from silicone oil using a maximum electric field of 15 MV/m in a 1-g environment. Also included in the plot is the predicted threshold electric field required to initiate an instability on the liquid surface.	126
Figure 4.14: Plot of the required extraction electric field to extract aluminum spherical and cylindrical particles from silicone oil using a maximum electric field of 15 MV/m. Also included in the plot is the predicted threshold electric field required to initiate an instability on the liquid surface for several various liquid surface radii, r_k . The thickness of the liquid film coating the particles is assumed to be zero.	128
Figure 4.15: Illustration of a single emitter from the particle extraction prototype.....	130
Figure 4.16: Photograph of micro-particle emitter.....	131
Figure 4.17: Series of frames showing the successful extraction of a spherical particle from 100 cSt silicone oil. See Table 4.6 for particle details.	133
Figure 4.18: Series of frames showing the successful extraction of a cylindrical particle from 100 cSt silicone oil. See Table 4.6 for particle details.	134

Figure 4.19: Measured electric fields required for spherical particle extraction as a function of the charging electric field for various particle sizes.	135
Figure 4.20: Photograph of a cylindrical particle at approximately 42° off vertical just before removal from the source electrode.	139
Figure 5.1: Illustration of the no liquid design configuration showing only the charging and accelerating processes. Not included is the particle delivery system.	144
Figure 5.2: Illustration of a spherical particle in contact with a planar surface (Adhesion).	149
Figure 5.3: Illustration of two spherical particles in contact (cohesion).	150
Figure 5.4: Plot of the adhesion and cohesion forces using a Lifshitz-van der Waals constant of 9 eV and the weight of an aluminum particle.	151
Figure 5.5: Plot of the energies in the adhesion and cohesion bonds using a Lifshitz-van der Waals constant of 9 eV.	153
Figure 5.6: Plot of the required accelerations to overcome the adhesion and cohesion forces using a Lifshitz-van der Waals constant of 9 eV and a particle density of 2,700 kg/m ³	154
Figure 5.7: Model for the removal of a conducting spherical particle from a planar electrode using a high strength electric field.	156
Figure 5.8: Plot of $A_f(\zeta_{sph})$ as a function of ζ_{sph}	159
Figure 5.9: Plot of $F_{el,z}(\zeta_{sph}):F_{el,z}(\zeta_{sph}=0)$ as a function of ζ_{sph}	161
Figure 5.10: Plot of the threshold electric field to overcome the adhesion and gravitational forces holding a spherical particle in contact with the source electrode. The particle has a density of 1,000 kg/m ³	164
Figure 5.11: Depiction of the experimental setup used for investigating the adhesion force and using an electric force to overcome this adhesion force.	165
Figure 5.12: photograph of the 100 micron particles in contact with the bottom electrode before the electric fields were applied.	167
Figure 5.13: SEM photos of the silver 53 μm (a and b), tin 102 μm (c and d), silver 196 μm (e and f), and tin 305 μm (g and h) micron particles.	169
Figure 5.14: Picture of a gold electrode deposited on a glass wafer.	171
Figure 5.15: AFM surface profile of the gold (a) and platinum (b) electrodes.	172

Figure 5.16: Picture the UHV chamber at the Space Electrodynamics and Tether Systems Laboratory at the University of Michigan.	173
Figure 5.17: Measured threshold electric fields for removal of spherical particles from a gold planar electrode when in the adhesion dominant regime.....	174
Figure 5.18: Measured threshold electric fields for removal of spherical particles from a platinum planar electrode when in the adhesion dominant regime.....	175
Figure 5.19: Plots of the particle removal efficiency as a function of applied electric field for all eight test cases.....	176
Figure 5.20: Illustration showing deformation of electrode (left) and particle (right)...	179
Figure 5.21: The estimated percent error of the evaluated Lifshitz-van der Waals constants due to deformation of the particle.	182
Figure 5.22: The estimated spread in the threshold electric field due to deformation of the particle.	183
Figure 5.23: Possible electrode and particle surface orientations.	186
Figure 5.24: Van der Waals adhesion force as a function of the separation. The four curves are for the four particles tested.....	188
Figure 6.1: An uncharged spherical particle subjected to a gradient in the electric field experiences a force pulling it to the region of maximum intensity.....	197
Figure 6.2: Electric dipole with charges $\pm q'$ separated by a distance d' and subjected to a non-uniform electric field.	198
Figure 6.3: Conducting sphere subjected to a uniform external electric field.	200
Figure 6.4: Field-focusing factor on a conducting spherical particle in a uniform background electric field.....	203
Figure 6.5: Two conducting spherical particles modeled as electric dipoles induced by an applied electric field.	205
Figure 6.6: Normalized radial and tangential components of the force between two conducting spherical particles.	207
Figure 6.7: Particles are maintained in contact with a planar surface, which is normal to the applied electric field, during transport.	209
Figure 6.8: 1D standing wave and the gradient force.....	212
Figure 6.9: Threshold amplitude of a standing wave required to move a particle across a planar surface.	214

Figure 6.10: Possible setup using high aspect ratio posts to generate strong gradients in the electric field. An infinitely thin dielectric planar surface coincides with the x-y plane	215
Figure 6.11: Normalized electric field strength and gradient force on conducting spheres in the x-y plane.....	217
Figure 6.12: Experimental setup to prove the feasibility of transporting spherical particle by way of the gradient force generated by a high aspect ratio post.	219
Figure 6.13: Series of frames showing the transport of an aluminum spherical particle by the gradient force, which is generated by a high aspect ratio post.....	221
Figure 6.14: Simplified model of sieving delivery system for dry particles.	223
Figure 6.15: (a) Schematic and (b) photograph of the sieving delivery system prototype.	225
Figure 6.16: Photograph showing individual micron particles as they transit the gap between the charging grid and the collection anode.	226
Figure 6.17: Images showing individual aluminum particles collected on a glass slide after bombardment.....	226
Figure B.1: Meshed COMSOL structure used to determine the electric field at the surface of a spherical particle when charged in contact with a planar electrode and subjected to an applied electric field.	244
Figure B.2: Close-up image of the particle when charging against a planar electrode. ...	246
Figure B.3: Relative magnitude of the electrical field everywhere in the system.	246

List of Tables

Table 2.1: Properties of the particles used in the particle charge experiment and the electrode gap and liquid viscosity used for each test case.	54
Table 2.2: Predicted electrical contact area between spherical aluminum particles and the electrode.....	68
Table 3.1: Theoretical threshold electric field strengths required to initiate an instability on various liquid surfaces and the corresponding perturbation radii.	82
Table 3.2: Theoretical charging time constants for a few liquids.	88
Table 3.3: Measured and predicted threshold electric field strengths required to initiate an instability on various liquid surfaces.	91
Table 4.1: Dependence of the drag coefficient on the Reynolds number in the three flow regimes.....	113
Table 4.2: Particle terminal velocity in the three flow regimes.	113
Table 4.3: The lower and upper bounds of the liquid film thickness.	123
Table 4.4: Predicted particle diameter ranges for extracting spherical and cylindrical aluminum particles from 100 cSt silicone oil without initiating a liquid instability.....	127
Table 4.5: Predicted particle diameter ranges for extracting spherical and cylindrical aluminum particles from 100 cSt silicone oil.	129
Table 4.6: Properties of the particles used in the particle extraction experiment.	132
Table 4.7: Measured minimum required extraction electric fields for various spherical and cylindrical particles.....	136
Table 4.8: Maximum obtainable specific impulses using the particles from Table 4.5.	141
Table 5.1: Properties of the four particles used in the particle adhesion experiment.....	167
Table 5.2: Lifshitz-van der Waals constants evaluated to match experimental data for all material combinations tested.....	176

Table 5.3: Threshold electric fields required to remove 15%, 33%, 50%, 67%, and 85% of the particles.	177
Table 5.4: The estimated spread in the threshold electric field due to the spread in particle size and the measured threshold electric field spread.....	178
Table 5.5: Reported values of the Young’s Modulus and Poisson’s ratio of the materials used in the experimental section. ⁶⁶	184
Table 5.6: First order predicted contact radii between particles and electrodes.	185
Table 5.7: List of ranges of published values of the Lifshitz-van der Waals constant for many materials.	190
Table 5.8: List of ranges of the expected values of the Lifshitz-van der Waals constant for select test cases compared with the evaluated values.	191
Table 5.9: The predicted specific impulse when using the smallest removable particles from the source electrode by electric force only.....	192
Table 6.1: Required force to overcome the frictional force and the maximum gradient force on various sized conducting spherical particles.	218

List of Appendices

Appendix A: Matlab Code.....	239
Appendix B: COMSOL Multiphysics®	243

Glossary

A_c	=	Integrated charging field-focusing factor
A_f	=	Integrated force field-focusing factor
A_l	=	Liquid perturbation cross-sectional area [m ²]
A_p	=	Particle contact area [m ²]
a_r	=	Resisting acceleration [m/s ²]
α	=	field-focusing factor
α_{cyl}	=	Cylindrical particle field-focusing factor
α_{liq}	=	Liquid perturbation field-focusing factor
α_p	=	Particle field-focusing factor
α_{sph}	=	Spherical particle field-focusing factor
β	=	Aspect ratio
C_D	=	Coefficient of drag
C_f	=	Feedback capacitance [F]
C_p	=	Particle Capacitance [F]
χ_{cyl}	=	Charge-to-mass ratio of cylinder [C/kg]
χ_{sph}	=	Charge-to-mass ratio of sphere [C/kg]
D	=	Electrode gap separation [m]
d	=	Particle diameter [m]
d_{ch}	=	Charging gap separation [m]
d_{ex}	=	Extraction gap separation [m]
d_k	=	Kapton tape thickness [m]
d_{liq}	=	Liquid height [m]
d_{ox}	=	Oxide thickness [m]
Δs	=	Distance traveled [m]
ΔV	=	Spacecraft change in velocity [m/s]

δ_l	=	Liquid thickness [m]
E_{BG}	=	Background electric field [V/m]
E_{ch}	=	Charging electric field [V/m]
E_{dipole}	=	Electric field from a dipole moment [V/m]
E_{ex}	=	Extraction electric field [V/m]
$E_{ex,cyl,thresh}$	=	Threshold electric field for extracting cylinders [V/m]
$E_{ex,sph,thresh}$	=	Threshold electric field for extracting spheres [V/m]
E_{liq}	=	Electric field applied to liquid [V/m]
$E_{liq,p}$	=	Electric field applied to liquid perturbation [V/m]
$E_{liq,thresh}$	=	Threshold electric field for instability [V/m]
E_{max}	=	Maximum electric field [V/m]
E_s	=	Surface electric field [V/m]
E_{spread}	=	Electric field spread [V/m]
E_{sw}	=	Standing wave electric field [V/m]
E_{thresh}	=	Threshold electric field [V/m]
ϵ	=	Permittivity [F/m]
ϵ_k	=	Kapton tape Permittivity [F/m]
ϵ_l	=	Liquid permittivity [F/m]
ϵ_o	=	Vacuum permittivity [F/m]
η	=	Liquid viscosity [Pa-s]
F_b	=	Buoyant force [N]
f_c	=	Cutoff frequency [Hz]
F_d	=	Drag force [N]
F_{edl}	=	Electric double layer force [N]
F_{el}	=	Electric force [N]
F_{ep}	=	Electric force on liquid perturbation [N]
F_{ex}	=	Extraction force [N]
F_f	=	Frictional force [N]
F_g	=	Gravitational force [N]
F_{grad}	=	Gradient electric force [N]
F_N	=	Normal force [N]

F_r	=	Resisting force [N]
F_s	=	Surface tension force [N]
F_{sw}	=	Standing wave gradient force [N]
F_{up}	=	Electric force on unperturbed liquid surface [N]
F_{vdw}	=	Van der Waals force [N]
g	=	Gravitational Acceleration [m/s^2]
Γ_{group}	=	Charging ratio for particles in a group
Γ_{post}	=	Charging ratio for particles on a post
γ	=	Liquid surface tension [N/m]
I_{sp}	=	Specific impulse [s]
$I_{sp_{cyl}}$	=	Specific impulse from cylindrical particle [s]
$I_{sp_{sph}}$	=	Specific impulse from spherical particle [s]
$i(t)$	=	Current [A]
$i_s(t)$	=	System current [A]
h	=	Lifshitz-van der Waals constant [J]
K	=	Particle kinetic energy [J]
ℓ	=	Particle length [m]
m	=	Propellant mass [kg]
m_{cyl}	=	Mass of cylindrical particle [kg]
m_p	=	Payload mass [kg]
m_{sph}	=	Mass of spherical particle [kg]
m_t	=	Total spacecraft mass [kg]
\dot{m}	=	Mass flow rate [kg/s]
P	=	Power [W]
p	=	Electric dipole moment [C-m]
P_ℓ	=	Polarization vector within liquid medium [C/m^2]
q	=	Propellant charge [C]
q_{cyl}	=	Charge of cylindrical particle [C]
q_m	=	Measured charge [C]
q_o	=	Initial charge [C]
q_{sph}	=	Charge of spherical particle [C]

R	=	Particle separation [m]
Re	=	Reynolds number
R_f	=	Feedback resistance [Ω]
R_l	=	Perturbation radius [m]
R_p	=	Particle resistance [Ω]
r	=	Particle radius [m]
r_c	=	Contact radius [m]
r_k	=	Radius of knife edge orifice [m]
r_s	=	Liquid perturbation radius within plane containing liquid surface [m]
ρ	=	Particle density [kg/m^3]
ρ_l	=	Liquid density [kg/m^3]
ρ_s	=	Surface charge density [C/m^2]
ρ_{ps}	=	Liquid surface polarization charge density [C/m^2]
σ_l	=	Liquid conductivity [S/m]
σ_{ox}	=	Oxide conductivity [S/m]
T	=	Thrust [N]
T_{osc}	=	Oscillation time [s]
t	=	Time [s]
τ_c	=	RC circuit time constant [s]
τ_l	=	Liquid charging time constant [s]
τ_p	=	Particle charging time constant [s]
$\tau_{r\theta}$	=	Shear stress [Pa]
θ	=	Angle with respect to z-axis [rad]
U_{dipole}	=	Potential energy of dipole moment [V/m]
$u(t)$	=	Velocity [m/s]
u_{ex}	=	Propellant exhaust velocity [m/s]
u_t	=	Terminal velocity [m/s]
V	=	Voltage [V]
V_{ch}	=	Charging voltage [V]
V_{ch}	=	Electric double layer voltage [V]
V_{ex}	=	Extraction voltage [V]

V_{offset}	=	Offset voltage [V]
V_{out}	=	Output voltage [V]
W_s	=	Liquid surface potential energy [J]
W_{vdw}	=	Van der Waals adhesion/cohesion energy [J]
y	=	Height of liquid perturbation above liquid surface [m]
z	=	Adhesion/cohesion separation [m]
z_{ad}	=	Adhesion separation [m]
z_c	=	Separation between charge centers [m]
z_{co}	=	Cohesion separation [m]
ζ_{sph}	=	Ratio of spherical particle diameter to electrode gap
ζ_{cyl}	=	Ratio of cylindrical particle length to electrode gap

Abstract

Investigation of a Micro- and Nano-Particle In-Space Electrostatic Propulsion Concept

by

Louis D. Musinski

Co-Chairs: Brian E. Gilchrist and Alec D. Gallimore

A new electrostatic propulsion system that utilizes micro- and nano-particles is under development. At its core, multi-layer grids establish electric fields that charge and accelerate the particles. Before charging, the particles are transported to charging/accelerating zones from storage reservoirs. One method of transport delivers the particles suspended in liquid through microfluidic channels. Another method transports the particles through micro-sieves as a dry powder.

Advantages over current technologies include the ability to tune its operational parameters over a large range, elimination of life-limiting characteristics, and increased design flexibility. Note that other applications such as materials processing and nano-printing may also benefit from emitted high-energy particles.

This thesis investigates several limiting obstacles, which are associated with charging particles, extracting particles from liquids, and overcoming adhesion/cohesion of

particles. The results provide new direction towards the final thruster design concept. Here, the obstacles under discussion include:

- The ability to accurately charge the particles and to maximize their charge-to-mass ratios is investigated. Theoretical analyses and simulations suggest that restricting the maximum electric field at the particles' surfaces is a necessary condition to avoid breakdown or field emission. With this constraint, spheres obtain greater charge-to-mass ratios than cylinders because they more uniformly distribute charge over their surfaces. Experimental results suggest that the charging models are reasonable under appropriate conditions.
- When transporting particles in a liquid suspension, the ability to extract them with an electric force while preventing the liquid from becoming unstable is critical. Theoretical modeling and experimentation prove that both spherical and cylindrical particles can be extracted successfully. But, it may not be possible to extract particles smaller than the micron range without inducing an instability, which leads to the formation of Taylor cones and limits thruster performance.
- When transporting and emitting dry particles, preventing particle adhesion/cohesion is important. Theoretical models developed here, which are supported by experimental results, suggest that an electric force can be used to overcome the adhesion of particles in the nanometer range. A functional micro-sieve thruster prototype capable of operating continuously has demonstrated the ability to overcome adhesion/cohesion in the micron range.

Chapter 1

Motivation, Background, and Introduction

1.1. Motivation of Research

The research presented in this thesis investigates the development of a new space electrostatic propulsion concept that is motivated by the use of micro- and nano-electromechanical systems (MEMS/NEMS) to transport, charge, and accelerate micro- and nano-particle propellant.^{1,2,3,4} This propulsion concept may have the potential to be a revolutionary system, which is likely to be critical for the success of future in-space missions.

Unlike traditional electrostatic propulsion systems, which ionize atoms, the micro- and nano-particle thruster concept electrostatically charges the particles with a high strength electric field, which allows the charge-to-mass ratio of the propellant to be efficiently and precisely adjusted over a large range. Adjusting the charge-to-mass ratio enables the capability of tuning operational parameters such as the specific impulse. In addition, this concept appears to offer a way to reduce life-limiting physical characteristics of present state-of-the-art ion propulsion systems by eliminating the need for a discharge chamber and reducing or eliminating charge-exchange (CEX) collision effects in the ion optics region. Further, MEMS technologies may provide an approach to achieve scalability and system simplification by creating scalable “flat panel” thrusters.

This “plug-and-play” technology also decouples the thruster design from the spacecraft design. The system scalability provides may be ideal for micro-satellites and formation flying. By providing a wider range of operating parameters, eliminating life-limiting characteristics, and offering greater design and operational flexibility, micro- and nano-particle thrusters are both a mission enhancing and mission enabling technology.

1.2. Background of Space Electrostatic Propulsion

State-of-the-art electrostatic propulsion systems operate by accelerating charged ions with an applied static electric field to produce thrust. However, regardless of whether the propellant is ions, macroscopic liquid droplets, or solid particles, they are all subject to the same governing physics. This section presents the governing physics of electrostatic propulsion systems, compares electrostatic propulsion with chemical propulsion, and briefly discusses the operation of four electrostatic propulsion technologies.

1.2.1. Electrostatic Propulsion Physics

The rocket equation that governs all propulsion systems was developed by Tsiolkovsky and provides a relation between the dry mass, m_o , the total mass, m_t , the specific impulse, I_{sp} , and the net velocity change of the vehicle, ΔV .^{5,6,7}

$$\frac{m_o}{m_t} = \exp\left(-\frac{\Delta V}{gI_{sp}}\right) \quad (1.1)$$

As seen in the rocket equation, the specific impulse, I_{sp} , describes the fuel efficiency. It is defined as a function of the thrust, T , and the propellant mass flow rate, \dot{m} .

$$Isp = \frac{T}{\dot{m}g} \quad (1.2)$$

The thrust is defined as a function of the mass flow rate and the propellant exhaust velocity, u_{ex} .

$$T = \dot{m}u_{ex} \quad (1.3)$$

A more common expression for the specific impulse is determined by combining Equations (1.2) and (1.3), which reveals that the specific impulse scales with the propellant exhaust velocity.

$$Isp = \frac{u_{ex}}{g} \quad (1.4)$$

Using conservation of energy, the exhaust velocity of an electrostatic propulsion system is easily shown to be a function of the propellant's charge-to-mass ratio, q/m , and the total accelerating voltage, V .⁸

$$u_{ex} = \sqrt{\frac{2qV}{m}} \quad (1.5)$$

Substituting Equation (1.5) into Equation (1.4), the specific impulse of an electrostatic propulsion system is expressed as a function of its operating parameters.

$$I_{sp} = \frac{1}{g} \sqrt{\frac{2qV}{m}} \quad (1.6)$$

The thruster power is a function of the propellant's charge-to-mass ratio, the mass flow rate, and the accelerating voltage.

$$P = q \frac{\dot{m}}{m} V \quad (1.7)$$

The thrust-to-power ratio is determined from Equations (1.3), (1.5), and (1.7).

$$\frac{T}{P} = \sqrt{\frac{2m}{qV}} \quad (1.8)$$

It is important to note the importance the propellant's charge-to-mass ratio on the thruster performance, particularly the specific impulse and the thrust-to-power ratio. The specific impulse is directly proportional to the square root of the charge-to-mass ratio, and the thrust-to-power ratio is inversely proportional to the same square root quantity.

1.2.2. Comparison of Electrostatic and Chemical Propulsion

Current state-of-the-art electrostatic propulsion systems, such as ion and Hall thrusters, operate with much higher specific impulses than standard chemical rockets. Typical electrostatic thrusters have a specific impulse on the order of a few thousand seconds. For example, the NSTAR ion thruster used by NASA's Deep Space 1 has a specific impulse of 3,200 seconds.⁹ Conversely, chemical rockets generally operate with a specific impulse on the order of several hundred seconds. The chemically driven space

shuttle main engine (SSME) has a specific impulse on the order of 450 seconds.^{10,11} As discussed in the previous sub-section, a thrusters' specific impulse describes its fuel efficiency, where a higher specific impulse indicates a more efficient use of propellant. Therefore, electrostatic propulsion systems are typically more propellant efficient, which provides advantages over standard chemical propulsion. To illustrate how the specific impulse affects the propellant efficiency, Figure 1.1 is a plot of the dry mass fraction from Equation (1.1) as a function of the mission ΔV for two specific impulses. The dry mass fraction is defined as the ratio of the dry mass to the total mass (dry mass + propellant mass).

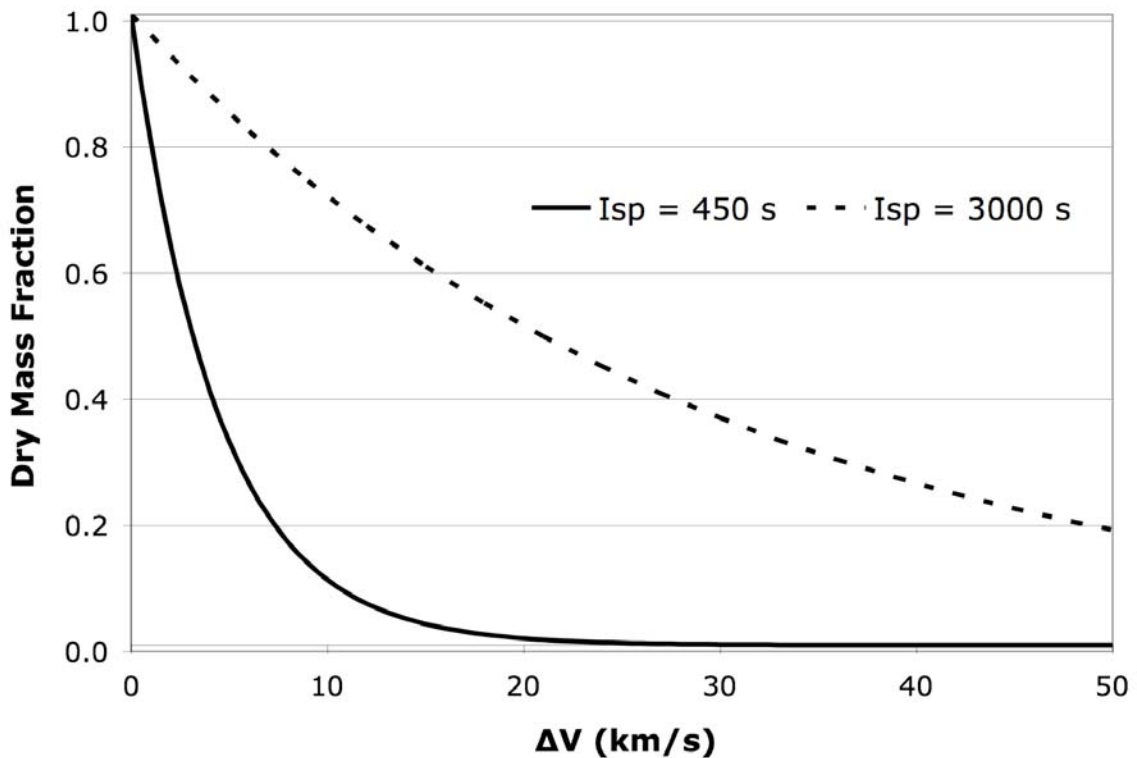


Figure 1.1: Dry mass fraction as a function of ΔV for specific impulses of 450 s and 3000 s.

Figure 1.1 illustrates that an electric propulsion system operating with a specific impulse of 3,000 seconds has a much higher dry mass fraction than a chemical rocket operating with a specific impulse of 450 seconds, when achieving the same ΔV . Therefore, an electrostatic propulsion system operating with a high specific impulse can afford a larger payload mass and/or a larger ΔV .

While an electrostatic propulsion system is typically more fuel-efficient than a chemical rocket, it does have its disadvantages. The mass flow rate of an electrostatic propulsion system is generally much less than for a chemical rocket. Therefore, chemical rockets typically have the ability to produce much higher thrust levels, which is important for launch vehicles and fast maneuvers.

1.2.3. Current Electrostatic Propulsion Technologies

This subsection presents a brief overview of the operation of four current electrostatic propulsion technologies.

1.2.3.1. Gridded Ion Thruster

Figure 1.2 is a diagram and photograph of the gridded electrostatic ion thruster, NSTAR.

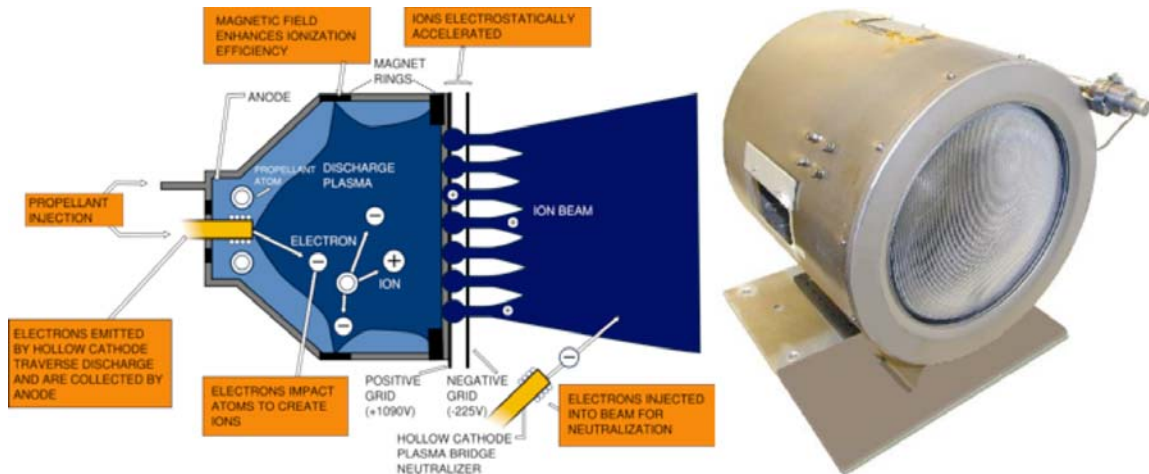


Figure 1.2: Diagram (left)¹² and photograph (right)¹³ of the gridded ion thruster, NSTAR, used for NASA's Deep Space 1.

The gridded electrostatic ion thruster uses an ionized gas as propellant and is composed of a large plasma discharge chamber mounted behind a dual electrode grid structure.^{14,15} Neutral propellant, usually xenon, is injected into the plasma discharge chamber through the anode, and is ionized by bombardment with high-energy electrons. The resulting ions are accelerated by the electric potential applied across the dual grids and ejected to generate thrust. To maintain spacecraft neutrality, an electron source is required.

1.2.3.2. Hall Effect Thruster

Figure 1.3 is a diagram and a photograph of a Hall effect thruster. The photograph is of the NASA-173M Hall thruster.

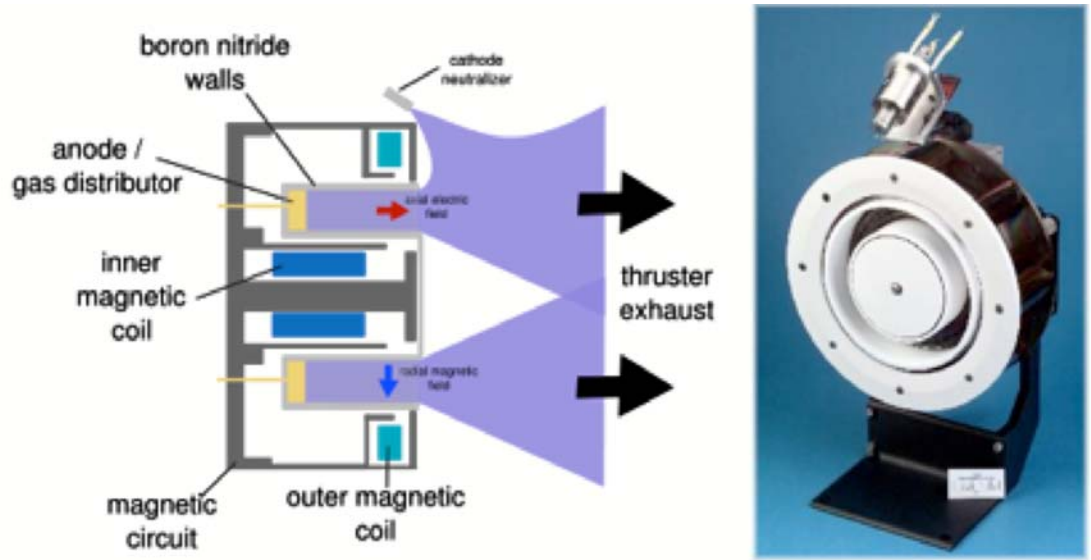


Figure 1.3: Diagram (left)¹⁶ and photograph (right)¹³ of a Hall effect thruster.

The Hall effect thruster is an axially symmetric system that generates a radial magnetic field and an axial electric field in a circular channel as shown in Figure 1.3.^{17,18} Electrons emitted from the cathode are trapped in the exit plane of the thruster by the $E \times B$ force and circulate in the trench generating a Hall current. The propellant, generally xenon, is injected into the trench through the anode and ionized by collisions with the high-energy electrons. The axial electric field, which is generated by the potential difference between the anode and the hollow cathode plasma in the exit plane, accelerates and ejects the ionized propellant to produce thrust. As the ions are ejected, they pull along electrons to neutralize the thruster.

1.2.3.3. Field Emission Electric Propulsion

Figure 1.4 is a diagram of a single emitter from a field emission electric propulsion (FEEP) system.

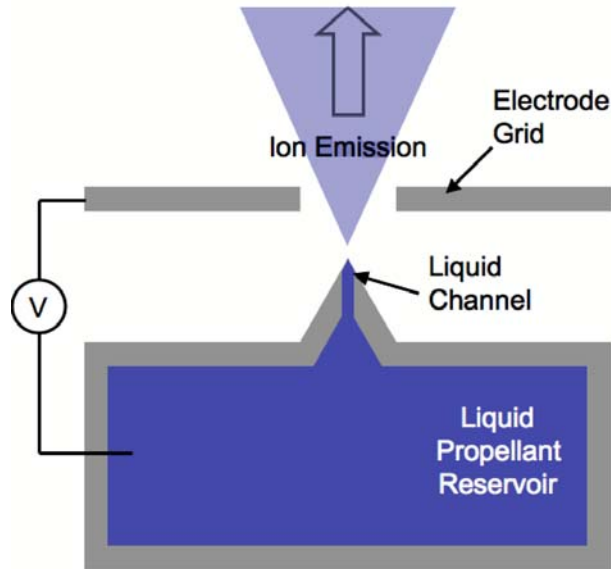


Figure 1.4: Diagram of a single FEEP emitter.

The field emission electric propulsion system operates by flowing a liquid metal, typically cesium or indium, through a small channel or over the surface of a high aspect ratio tip.^{19,20,21,22} A high strength electric field is generated at the surface of the liquid metal by applying a large electric potential difference between the liquid and a downstream electrode grid. Note that the field strength at the emitter tip is intensified due to the field-focusing that occurs at sharp points. As a result, the liquid becomes unstable forming a Taylor cone. Under the appropriate conditions, ions are stripped from the tip of the cone structure. These ions are accelerated and ejected to produce thrust.

1.2.3.4. Colloidal Thruster

Figure 1.5 is a diagram of a single emitter from a colloidal thruster.

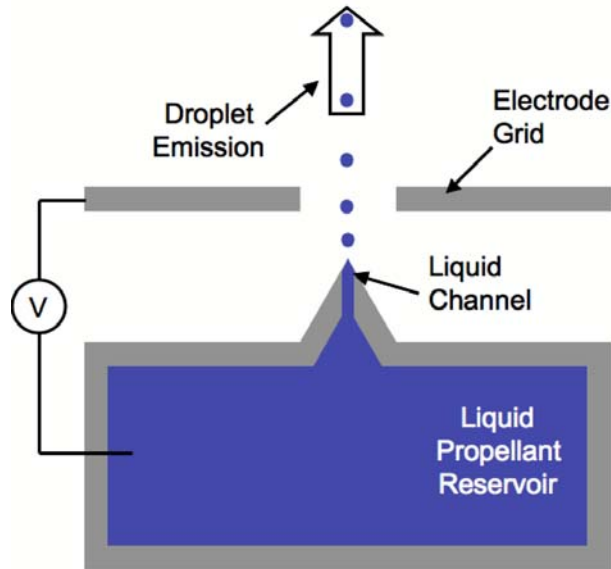


Figure 1.5: Diagram of a single colloid emitter.

The design of a colloidal thruster is very similar to that of a FEEP thruster as shown by a comparison of Figure 1.4 and Figure 1.5.^{23,24,25} The main difference between the operations of these two systems is that a colloidal thruster accelerates small liquid droplets from the tip of the Taylor cone instead of ions. Using larger liquid droplets as opposed to ions decreases the propellant charge-to-mass ratio, which offers a different operational regime with a decreased Isp and increased thrust-to-power.

1.3. Introduction to the Micro- and Nano-Particle Thruster

At the core of the MEMS/NEMS based micro- and nano- particle thruster concept, we propose to use millions of MEMS based micron-size vias that have a multi-layer electrode grid to establish the critical electric fields to charge, accelerate, and eject the conducting particles to generate thrust. The concept operates by transporting the conducting particle propellant from a storage reservoir to the charging zones. Note that multiple transport systems are under development and are discussed later in this section.

Once delivered to the charging zones, the particles are charged by an applied high strength electric field against a source electrode. The electric force acting on the charged particles then accelerates the particles through the acceleration zones, made up of a series of stacked grids that are electrically biased to generate the accelerating electric fields. Finally the particles are ejected to generate thrust.

Three design configurations of the micro- and nano-particle propulsion system are under consideration, all of which charge, accelerate, and eject the particle propellant in a similar manner. The difference between the configurations is the method of particle transport from the storage reservoir to the charging zones. The three configurations are termed insulating liquid, conducting liquid, and no liquid. This section presents an overview of each configuration.

1.3.1. Insulating Liquid Configuration

The insulating liquid configuration stores the particles in an insulating, low vapor pressure liquid. The particle solution is circulated and transported between the storage and the charging zones through pressure driven microfluidic channels as is shown by a proof-of-concept experiment in Figure 1.6.²⁶ This proof-of-concept experiment demonstrated the transport of 20 μm polystyrene particles in both water and 50 cSt silicone oil.

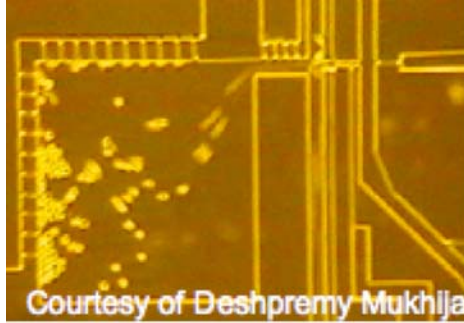


Figure 1.6: Transport of 20 μm particles from a large storage reservoir through microfluidic channels.

Particles delivered to the charging zones through the microfluidic transport system become electrically charged when they contact the source electrode that is submersed in the liquid, shown in the diagram of a single emitter in Figure 1.7. After acquiring sufficient charge, the particles are transported by the applied electric field to the liquid surface, extracted through the surface, accelerated in the channels, and finally ejected to produce thrust. Note that the liquid surface is pinned between the charging grid and extraction grid in Figure 1.7 using a knife-edge orifice (not shown), which is discussed at a top level in Chapter 3.

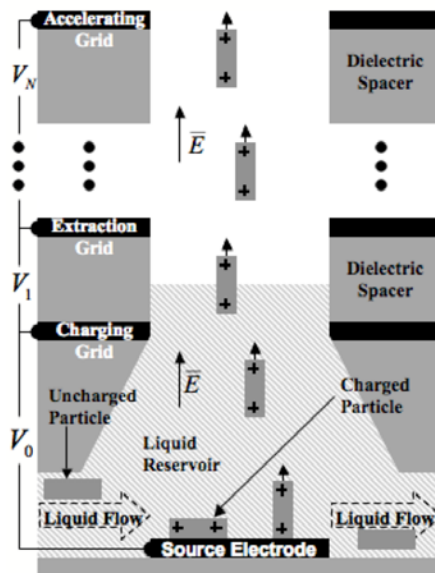


Figure 1.7: Design of a single emitter from the insulating liquid configuration

The insulating liquid configuration was the first design considered in the development of the micro- and nano-particle thruster, which is discussed in further detail throughout this thesis.

1.3.2. Conducting Liquid Configuration

The conducting liquid configuration (Figure 1.8) is very similar to the insulating liquid configuration in that the particles are transported in a liquid solution through microfluidic channels from the storage reservoir to the charging zones. But, since the liquid is conducting, the application of the electric potential across the stacked grids does not generate an electric field within the liquid, and the particles cannot be charged while submerged. Therefore, the particles must break through the liquid surface without the aid of the electric force. This may be possible through the use of thermal motion or convective mixing. Particles that break through the liquid surface are charged by the electric field in the vacuum region and use the liquid surface as the source electrode. Once charged, the particles are fully extracted from the liquid, accelerated, and ejected just as in the insulating liquid configuration. Similar to the insulating liquid case, the liquid surface is pinned below the extraction grid using a knife-edge orifice (not shown) to assure that the liquid does not climb up the channel and short out the applied electric fields.

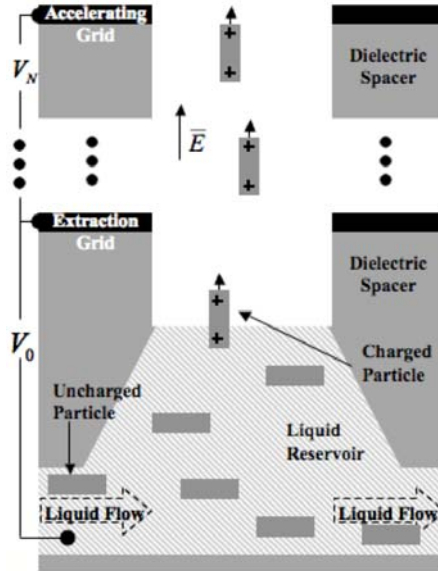


Figure 1.8: Design of a single emitter from the conducting liquid configuration

The conducting liquid configuration is the least developed design considered in the development of the micro- and nano-particle thruster and is not discussed any further in this thesis.

1.3.3. No Liquid Configuration

Concerns of the liquid surface becoming unstable when subjected to high strength electric fields led to the development and design of the no liquid configuration, which eliminates the liquid and microfluidic channels, and instead transports dry particles in powder form. Two methods of transporting the dry particles are discussed in Chapter 6. First, the dry propellant is transported through an ultra-fine sieve with the aid of mechanical vibrations to separate the clumped powder into individually isolated particles prior to charging. The conducting particle sieve is mounted beneath the stacked accelerating gates and serves as the source electrode for particle charging. The second

method uses the electric force that arises from a gradient in an applied electric field to separate and transport the propellant to the source electrodes.

1.4. Summary of Research Contributions

The purpose of the research presented in this thesis is the development of the new concept regarding the micro- and nano-particle propulsion system and is focused on developing an understanding of the fundamental physics governing and limiting the thruster operation, fabricating functional prototypes to demonstrate operation, and providing insight and direction for the overall system design. Research topics and contributions of this work include the following:

- The charge acquired by individual conducting spherical particles when subjected to a high strength electric field is derived with the aid of simulation software. An extension of this derivation studies the effects of charging groups of particles. An investigation of a method to increase the particles' total charge by charging them on high aspect ratio charging posts is presented. In addition, this thesis discusses an overview of the cylindrical particle charging model and compares spherical and cylindrical particle charging as potential particle shapes for use with micro- and nano-particle thrusters. Experimental results of charging spherical and cylindrical conducting particles are presented and reveal limitations affecting the time required to charge the particles.
- The initiation of a liquid surface instability when applying high strength electric fields is investigated, and the threshold electric fields required to induce the instability in both earth-gravity and zero-gravity environments are derived. A method to suppress

- and control the liquid instability is discussed as well as the time required to induce the instability. Experimental results of inducing a liquid surface instability on both insulating and conducting liquids in an earth-gravity environment are presented.
- The process of extracting charged spherical and cylindrical particles through the surface of an insulating liquid by way of an applied high strength electric field is investigated, and the strength of the electric fields required to extract both particle shapes are derived. An extension of this derivation studies the effects of particle kinetic energy on the extraction process and the dynamics of liquid draining from the particle surface. In addition, this thesis discusses the effects and limitations of the liquid instability on particle extraction and compares the extraction of spherical and cylindrical particles as potential particle shapes for use with micro- and nano-particle thrusters. Experimental results of extracting spherical and cylindrical particles are presented.
 - The adhesion force between a single conducting spherical particle and the planar source electrode and the cohesion force between two conducting spherical particles are investigated. In addition, the electric force arising from the charging electric field acting on the charged particle is investigated, both theoretically and experimentally, as a method to overcome the adhesion force and achieve particle removal, specifically for the application of micro- and nano-particle thrusters.
 - Two potential methods of transporting dry micro- and nano-particles from the storage reservoir to the charging zones are investigated. The first method utilizes the electric force on uncharged particles that arises from the gradient in the electric field, and the second method uses a simple method of expelling the particles through micro- and

nano-sieves. In addition to theoretical discussions, this thesis presents simple proof-of-concept experiments of each method.

1.5. Dissertation Overview

This thesis is composed of seven chapters, five of which address the five research topics discussed in the previous section.

Chapter 1 introduces the topic and provides motivation and background information. It also lists the contributions of this thesis.

Chapter 2 presents a theoretical and experimental investigation of spherical and cylindrical particle charging.

Chapter 3 discusses the tendency of a liquid surface to become unstable when subjected to a high strength electric field.

Chapter 4 provides theoretical and experimental results for extracting both spherical and cylindrical particles through the surface of an insulating liquid.

Chapter 5 investigates the adhesion and cohesion forces that affect the behavior of micro-particles.

Chapter 6 details two potential methods of transporting dry micro- and nano-particles from the storage reservoir to the charging zones.

Chapter 7 concludes the research presented in this thesis, summarizes the results, and suggests a path for future development.

Chapter 2

Electrostatic Charging of Spherical and Cylindrical Particles

2.1. Introduction

Regardless of the operational design configuration (insulating liquid, conducting liquid, or no liquid), micro- and nano-particle thrusters charge particle propellant electrostatically by inducing a charge transfer from an electrode surface onto the particles with an applied high strength electric field. The ability to accurately and reliably charge conducting particles is important to the foundation of micro- and nano-particle thrusters. This chapter first presents an analytical derivation of the charge acquired by individual conducting spherical and cylindrical particles. An extension of this derivation studies the effects of charging groups of particles and investigates a method of increasing the particles' total charge by charging them on high aspect ratio charging posts. In addition, this chapter discusses an overview of the cylindrical particle charging model and compares spherical and cylindrical particles as potential particle shapes for use with micro- and nano-particle thrusters. Here, experimental results of charging scaled up spherical titanium and aluminum micro-particles with diameters ranging from approximately 800 μm to 4,000 μm and cylindrical aluminum particles with diameters of 300 μm and lengths of 1.3 mm and 1.7 mm are presented.

2.2. Theory of Particle Charging

This section presents the theory of the charge acquired by spherical and cylindrical particles when in contact with a planar source electrode in the presence of an electric field. The resulting charge-to-mass ratio of the spherical and cylindrical particles are presented and compared as possible particle shapes for use with micro- and nano-particle thrusters. Finally, the effects of charging spherical particles in groups and on high aspect ratio charging posts are investigated.

2.2.1. Spherical Particle Charging

The model for the charge acquired by a spherical particle in contact with an infinite planar electrode and subjected to an applied electric field is shown in Figure 2.1, and consists of two infinite parallel planar electrodes with a conducting spherical particle in contact with the upper surface of the bottom electrode. An electric potential bias, V , is applied across the electrodes to generate an electric field within the gap.

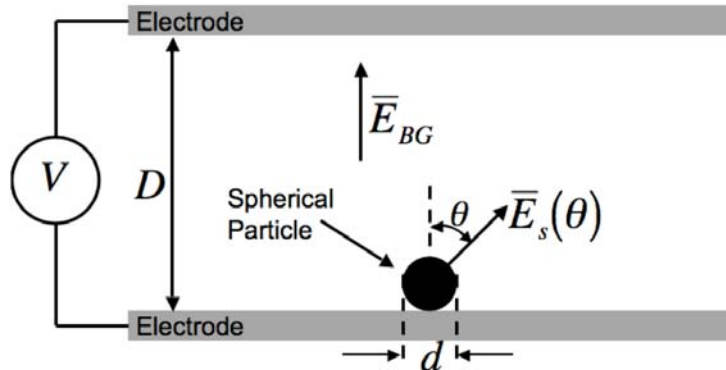


Figure 2.1: Model for determining the charge acquired by a conducting spherical particle in contact with an infinite planar electrode and subjected to an electric field.

Here, the background electric field, E_{BG} , is assumed to be the electric field in the electrode gap of two infinite plates without the presence of the particle and is only dependent on the applied voltage and the electrode separation.

$$E_{BG} = \frac{V}{D} \quad (2.1)$$

The presence of the particle in the electrode gap modifies the electric field, with the largest field modification occurring in the vicinity of the particle as presented later in this section. The electric field at the surface of the conducting particle, E_s , is normal to the particle surface and is the key to understanding the charge acquired by the particle.

The charge acquired by the particle is computed by integrating the particle's surface charge density over the particle's surface as described by Gauss's Law.²⁷ Due to the symmetry about ϕ , the surface charge density is a function of θ , where $\theta=0^\circ$ corresponds to the top of the particle and $\theta=180^\circ$ corresponds to the bottom of the particle.

$$q_{sph} = \iint \rho_s(\theta) dA \quad (2.2)$$

The surface charge density is dependent on the electric field normal to the particle surface and the permittivity of the surrounding medium. \hat{r}' is the radial unit vector.

$$\rho_s(\theta) = \hat{r}' \cdot \epsilon \bar{E}_s(\theta) = \epsilon E_s(\theta) \quad (2.3)$$

The electric field at the surface of the particle is calculated in the same way as for a single tip of a field emission device. This field is a function of the background electric field, θ , and the ratio of the particle diameter to the electrode gap, ζ_{sph} .²⁸

$$E_s(\theta) = E_{BG} \alpha_{sph}(\theta, \zeta_{sph}) \quad (2.4)$$

$\alpha_{sph}(\theta, \zeta_{sph})$ can be thought of as the spherical particle field-focusing factor. Equations (2.3) and (2.4) are substituted into Equation (2.2), and the only unknown in the particle charge expression is $\alpha_{sph}(\theta, \zeta_{sph})$.

$$q_{sph} = \int_0^{2\pi} \int_0^{\pi} \epsilon E_{BG} \alpha_{sph}(\theta, \zeta_{sph}) r^2 \sin(\theta) d\theta d\phi = 2\pi r^2 \epsilon E_{BG} \int_0^{\pi} \alpha_{sph}(\theta, \zeta_{sph}) \sin(\theta) d\theta \quad (2.5)$$

The solution to the integral, $A_c(\zeta_{sph})$, is only a function of the ratio of the particle diameter to the electrode gap, ζ_{sph} , and can be thought of as the integrated field focusing factor for spherical particle charging.

$$A_c(\zeta_{sph}) = \int_0^{\pi} \alpha_{sph}(\theta, \zeta_{sph}) \sin(\theta) d\theta \quad (2.6)$$

Thus, the particle charge is directly proportional to the square of the particle radius, the background electric field, the permittivity of the surrounding medium, and $A_c(\zeta_{sph})$.

$$q_{sph} = 2\pi r^2 \epsilon E_{BG} A_c(\zeta_{sph}) \quad (2.7)$$

Before finding values for $A_c(\zeta_{\text{sph}})$, $\alpha_{\text{sph}}(\theta, \zeta_{\text{sph}})$ needs to be examined. $\alpha_{\text{sph}}(\theta, \zeta_{\text{sph}})$ was investigated for conducting spherical particles as shown in Figure 2.1 by employing COMSOLTM Version 3.3a, a multi-physics simulation environment. COMSOLTM provides a method of modeling the electric field in the presence of complex structures. Note that the simulation presented here is an extension to the simulation performed by Smith et al, which determined the field-focusing factor of 2-dimensional posts.²⁸ The simulation reported here was created in a 2-dimensional environment with axial symmetry. The potential difference between the electrodes was chosen so that the bottom electrode and particle were charged positively, although it was verified that reversing the polarity does not change the problem. The width of the simulation environment was set to 10 times the electrode gap to eliminate field screening due to edge effects,²⁸ which was verified to be a sufficient margin by experimentation and is discussed in Appendix B. The simulation cell size was chosen to ensure that the simulation solution was not a function of cell size. A cell size on the order of a hundred times smaller than the particle was determined to be adequate in the vicinity of the particle surface. Here, the medium separating the electrodes was vacuum, although other insulating medium can be used between the electrodes as long as its dielectric properties are accounted for.

It is expected that $\alpha_{\text{sph}}(\theta, \zeta_{\text{sph}})$ is maximum at the top of the particle ($\theta=0^\circ$) where field focusing occurs and minimum at the bottom of the particle ($\theta=180^\circ$) where the particle contacts the electrode. To understand how $\alpha_{\text{sph}}(\theta, \zeta_{\text{sph}})$ depends on the ratio of the particle diameter to the electrode gap and θ , ζ_{sph} was varied from 0.005 to 0.95 and $\alpha_{\text{sph}}(\theta, \zeta_{\text{sph}})$ was measured for θ ranging from 0° to 180° . Figure 2.2 is a plot of $\alpha_{\text{sph}}(\theta, \zeta_{\text{sph}})$ as a function of θ for several values of ζ_{sph} .

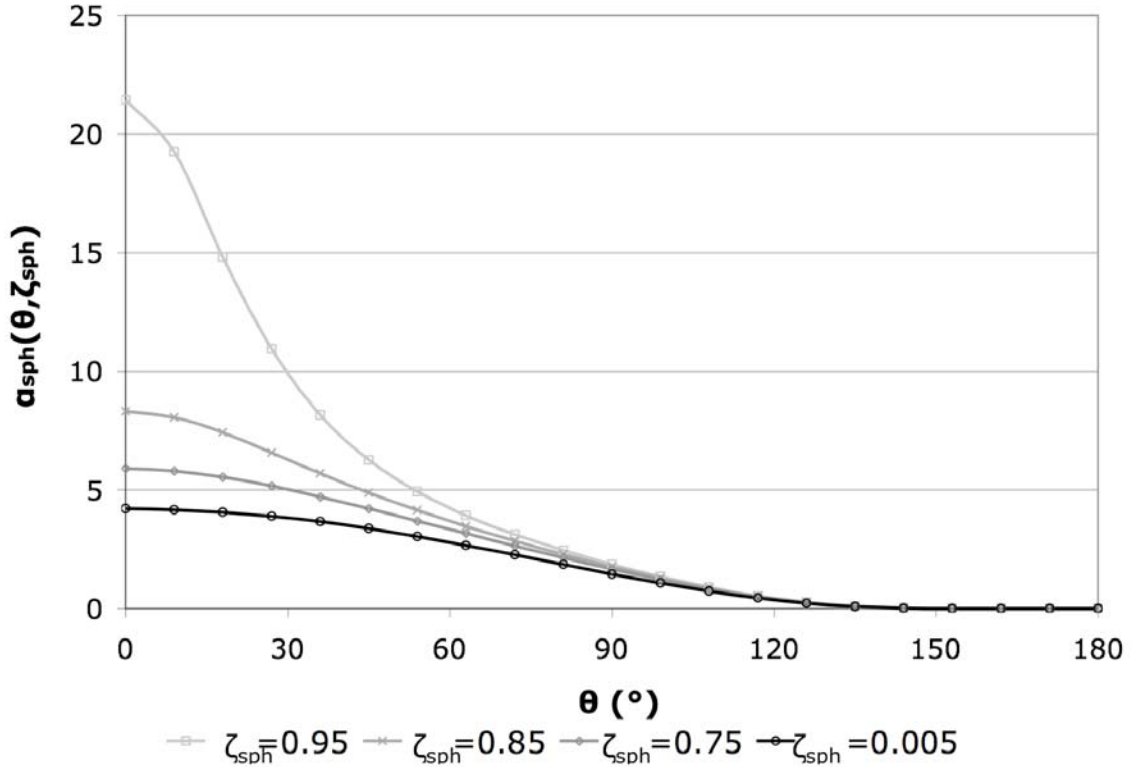


Figure 2.2: Plot of $\alpha_{\text{sph}}(\theta, \zeta_{\text{sph}})$, the field-focusing term for a spherical particle between infinite plates, as a function of θ for several values of ζ_{sph} .

The plot in Figure 2.2 shows that regardless of the ratio of the particle diameter to the electrode gap, ζ_{sph} , the electric field at the surface of the spherical particle is maximum at the top of the particle ($\theta=0^\circ$) and goes to zero at the bottom of the particle ($\theta=180^\circ$) where it contacts the electrode, as expected. When holding the background electric field constant and changing ζ_{sph} , the electric field at the particle surface is larger for larger ζ_{sph} . In addition, as the ratio of the particle diameter to the electrode gap goes to zero, $\alpha_{\text{sph}}(\theta=0, \zeta_{\text{sph}} \rightarrow 0)$ approaches a constant value of approximately 4.2, which is the field-focusing factor for a spherical particle on an infinite planar electrode when the top electrode is at an infinite distance. Felici confirmed this value using image theory for the same geometry.²⁹

Using the plot of $\alpha_{\text{sph}}(\theta, \zeta_{\text{sph}})$ in Figure 2.2 and Equation (2.6), $A_c(\zeta_{\text{sph}})$ can be numerically calculated. Figure 2.3 is a plot of $A_c(\zeta_{\text{sph}})$ as ζ_{sph} ranges from 0.005 to 0.95.

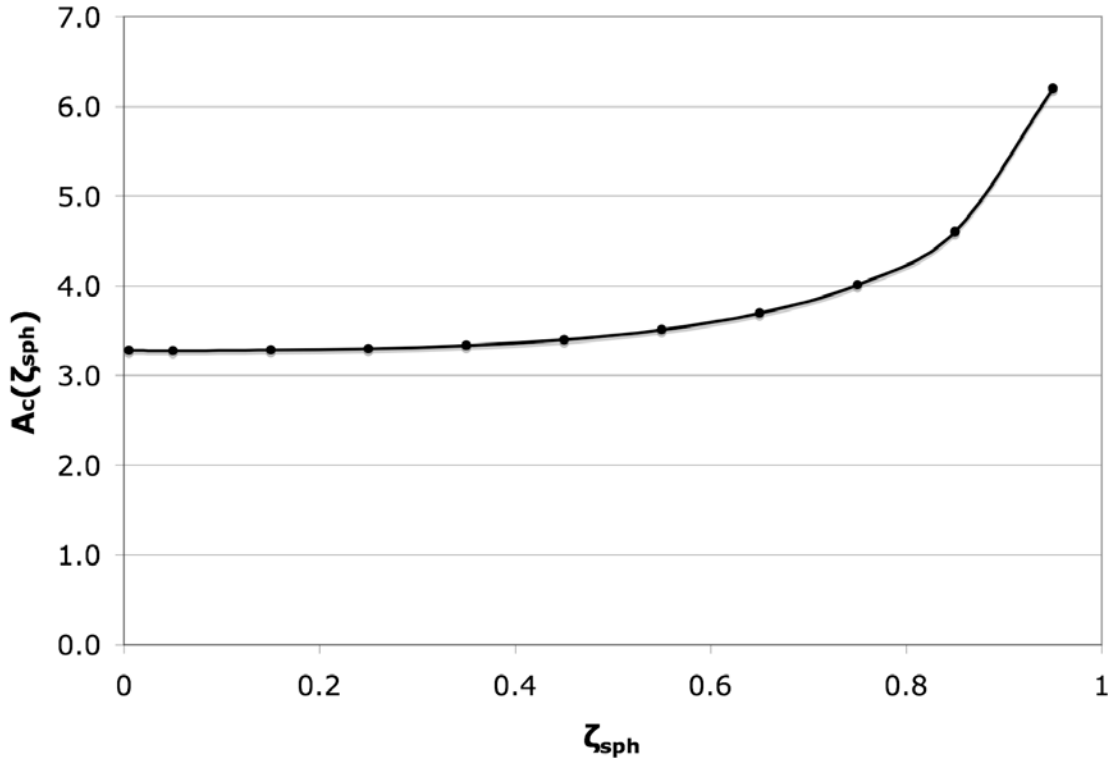


Figure 2.3: Plot of $A_c(\zeta_{\text{sph}})$ as a function of ζ_{sph} .

According to Figure 2.3, $A_c(\zeta_{\text{sph}})$ approaches approximately 3.28 as the ratio of the particle diameter to the electrode gap approaches 0 ($\zeta_{\text{sph}} \rightarrow 0$). This approximation appears to be valid to within less than 2% error when the particle diameter is less than one-third of the electrode gap ($\zeta_{\text{sph}} < 0.33$). As the particle size increases relative to the electrode gap, $A_c(\zeta_{\text{sph}})$ increases. Figure 2.3 along with Equation (2.7) completes the derivation of the charge acquired by a spherical particle when in contact with the source electrode and subjected to an electric field. As ζ_{sph} increases, the particle charge increases when holding everything else constant. This result can be somewhat

misleading. When charging spherical particles on a source electrode as shown in Figure 2.1, it may be important to maintain the maximum electric field in the system, which is located at the top of the particle, below the electrical breakdown of the background medium or below the electron field emission threshold. If this maximum electric field is held constant as ζ_{sph} varies, the background electric field does not remain constant as suggested by Figure 2.2.

The following analysis investigates the effects on the particle charge as ζ_{sph} varies while holding the maximum electric field in the system constant. The maximum electric field at the top of the particle, E_{max} , is determined from Equation (2.4).

$$E_{max} = E_{BG}(\zeta_{sph})\alpha_{sph}(\theta = 0, \zeta_{sph}) \quad (2.8)$$

The expression in Equation (2.8) is substituted into Equation (2.7) to find the particle charge when the maximum electric field is held constant. Note that it is assumed that $\theta=0^\circ$ for the remainder of this analysis.

$$q_{sph}(\zeta_{sph}) = 2\pi r^2 \epsilon \left(\frac{E_{max}}{\alpha(\zeta_{sph})} \right) A_c(\zeta_{sph}) \quad (2.9)$$

The ratio of the particle charge when $\zeta_{sph} = \zeta_1$ to the charge when $\zeta_{sph} = \zeta_2$ is only dependent on $\alpha_{sph}(\zeta_{sph})$ and $A_c(\zeta_{sph})$.

$$\frac{q_{sph}(\xi_1)}{q_{sph}(\xi_2)} = \frac{A_c(\xi_1) \alpha_{sph}(\xi_2)}{A_c(\xi_2) \alpha_{sph}(\xi_1)} \quad (2.10)$$

Figure 2.4 is a plot of $q_{sph}(\zeta_{sph}):q_{sph}(\zeta=0)$, and illustrates how the particle charge changes when the maximum electric field is held constant as the ratio of the particle diameter to the electrode gap varies. In other words, it is a plot of the particle charge normalized to the case when the particle is much smaller than the electrode gap.

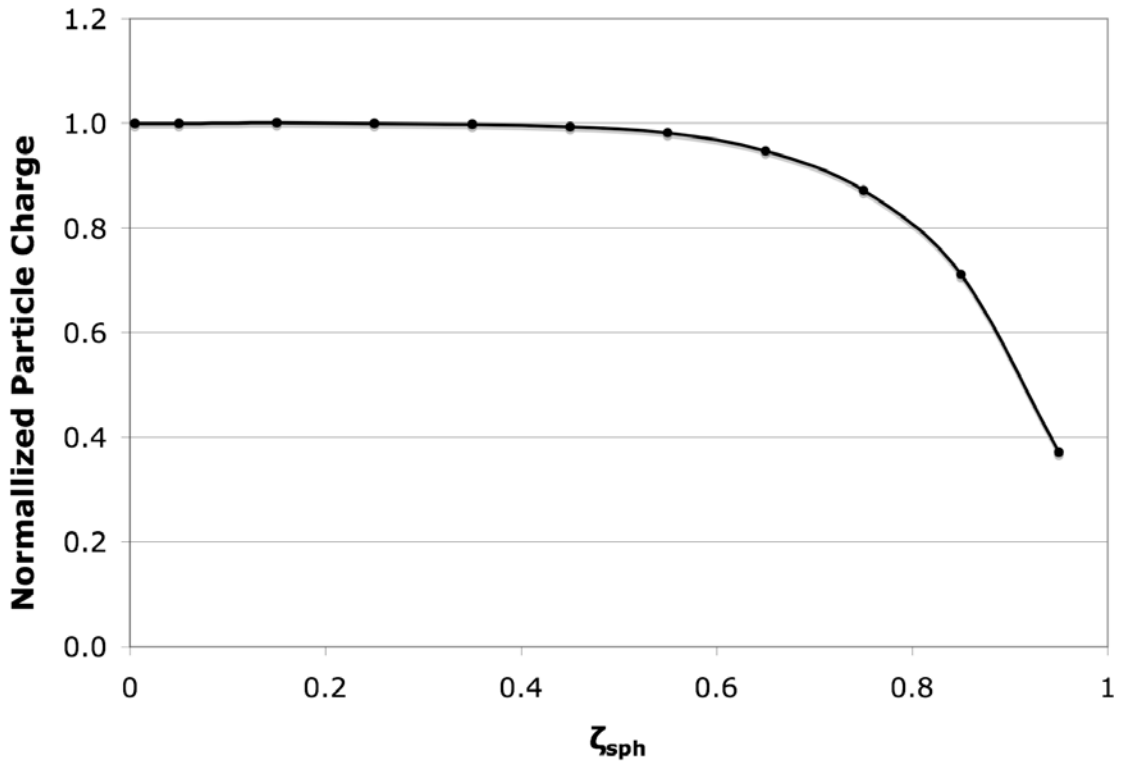


Figure 2.4: Plot of $q_{sph}(\zeta_{sph}):q_{sph}(\zeta_{sph}=0)$ as a function of ζ_{sph} when using a constant maximum electric field.

Figure 2.4 indicates that when the maximum electric field is held constant, the particle charge is greatest when the ratio of the particle diameter to the electrode gap is small, but the acquired charge decreases slowly as ζ_{sph} increases up to approximately 0.6. This occurs because minimizing the ratio of the particle diameter to the electrode gap ensures

that the charge density is distributed as evenly over the entire particle surface as allowed by this model as shown by Figure 2.2.

The remainder of this chapter focuses on the case where the particle is small relative to the electrode gap, which is valid to within less than 1% error when the particle diameter is less than one-third of the electrode gap ($\xi_{sph} < 0.33$).

$$q_{sph}(\xi_{sph} < 0.33) \approx 2\pi r^2 \epsilon E_{BG} 3.28 \quad (2.11)$$

It should be noted this result agrees with Felici's calculation to within three significant figures.²⁹

$$q_{sph,Felici} \approx 2\pi r^2 \epsilon E_{BG} \frac{\pi^2}{3} \quad (2.12)$$

2.2.2. Cylindrical Particle Charging

The model for the charge acquired by a vertically oriented cylindrical particle in contact with an infinite planar electrode and subjected to an applied electric field is very similar to the model used for the charge acquired by a spherical particle. It is shown in Figure 2.5, and again consists of two parallel infinite planar electrodes with a conducting vertically oriented cylindrical particle in contact with the upper surface of the bottom electrode. The cylindrical particle is modeled as a cylinder capped with a hemisphere. It has been determined that the exact shape of the bottom of the particle (flat or rounded) does not significantly affect the total particle charge when its length is more than five times its diameter. Note that the derivation of the charge acquired by a cylindrical

particle assumes that the particle length is much smaller than the electrode gap as a result of the conclusions made from charging spherical particles in the previous section. According to Smith et al, this assumption is valid when the particle length is less than one-third of the total electrode gap, which is the same result obtained for spherical particles.²⁸

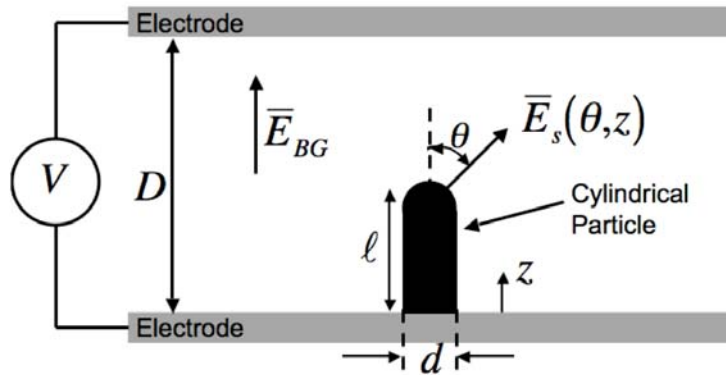


Figure 2.5: Model for the charge acquired by a conducting, vertically oriented, cylindrical particle in contact with a planar electrode and subjected to an electric field.

The charge acquired by a vertically oriented cylindrical particle can be calculated using Gauss's Law just as the case of a spherical particle.

$$q_{cyl} = \iint \rho_s dA \quad (2.13)$$

The surface charge density is dependent on the electric field normal to the particle surface and the permittivity of the surrounding medium as given by Equation (2.4). The electric field at the surface of the particle is calculated in a similar way as for a spherical particle, but uses a modified field-focusing factor, $\alpha_{cyl}(\beta, \theta, z)$, specific to the cylindrical geometry, where β is the particle aspect ratio $\beta = l/d$.

$$E_s(\theta, z) = E_{BG} \alpha_{cyl}(\beta, \theta, z) \quad (2.14)$$

Note that this derivation assumes the length of the cylinder to be much less than the electrode gap ($\ell \ll D$). Equations (2.3) and (2.14) are substituted into Equation (2.13), and the only unknown in the particle charge expression is $\alpha_{cyl}(\beta, \theta, z)$.

$$q_{cyl} = \iint \epsilon E_{BG} \alpha_{cyl}(\beta, \theta, z) dA = \epsilon E_{BG} \iint \alpha_{cyl}(\beta, \theta, z) dA \quad (2.15)$$

Due to the particle geometry, the integral must be broken down into two terms. The first term integrates the field-focusing factor over the surface of the hemispherical cap, and the second term integrates over the shaft of the cylinder.

$$q_{cyl} = \epsilon E_{BG} \left[\int_0^{2\pi} \int_0^{\pi/2} \alpha_{cyl}(\beta, \theta, z) r^2 \sin \theta d\theta d\phi + \int_0^{2\pi} \int_0^{\ell-r} \alpha_{cyl}(\beta, \theta, z) r dz d\phi \right] \quad (2.16)$$

$$q_{cyl} = 2\pi r^2 \epsilon E_{BG} \left[\int_0^{\pi/2} \alpha_{cyl}(\beta, \theta, z) \sin \theta d\theta + \frac{1}{r} \int_0^{\ell-r} \alpha_{cyl}(\beta, \theta, z) dz \right]$$

The solution to the sum of the integrals, $A_{cyl}(\beta)$, is only a function of the particle geometry, and can be thought of as the integrated field focusing factor for cylindrical particle charging.

$$A_{cyl}(\beta) = \int_0^{\pi/2} \alpha_{cyl}(\beta, \theta, z) \sin \theta d\theta + \frac{1}{r} \int_0^{\ell-r} \alpha_{cyl}(\beta, \theta, z) dz \quad (2.17)$$

Thus, the particle charge is directly proportional to the square of the particle radius, the background electric field, the permittivity of the surrounding medium, and $A_{cyl}(\beta)$.

$$q_{cyl} = 2\pi r^2 \epsilon E_{BG} A_{cyl}(\beta) \quad (2.18)$$

Note the similarity between the expressions for the charge acquired by spherical and cylindrical particles from Equations (2.7) and (2.18), respectively. Before finding values for $A_{cyl}(\beta)$, $\alpha_{cyl}(\beta, \theta, z)$ needs to be examined. Values for $\alpha_{cyl}(\beta, \theta, z)$ were simulated using the same simulation environment described in the previous section with the only change being the shape of the particle.

To understand how $\alpha_{cyl}(\beta, \theta, z)$ depends on the particle dimensions, the length and diameter were varied and $\alpha_{cyl}(\beta, \theta, z)$ was measured over the surface of the entire particle. The results indicate that the field-focusing factor depends on the particle aspect ratio, β , and not the length or diameter independently. Figure 2.6 is a plot of $\alpha_{cyl}(\beta, \theta, z)$ for several values of β over the surface of the hemispherical cap, and Figure 2.7 is a plot of $\alpha_{cyl}(\beta, \theta, z)$ for several values of β over the surface of the cylindrical shaft.

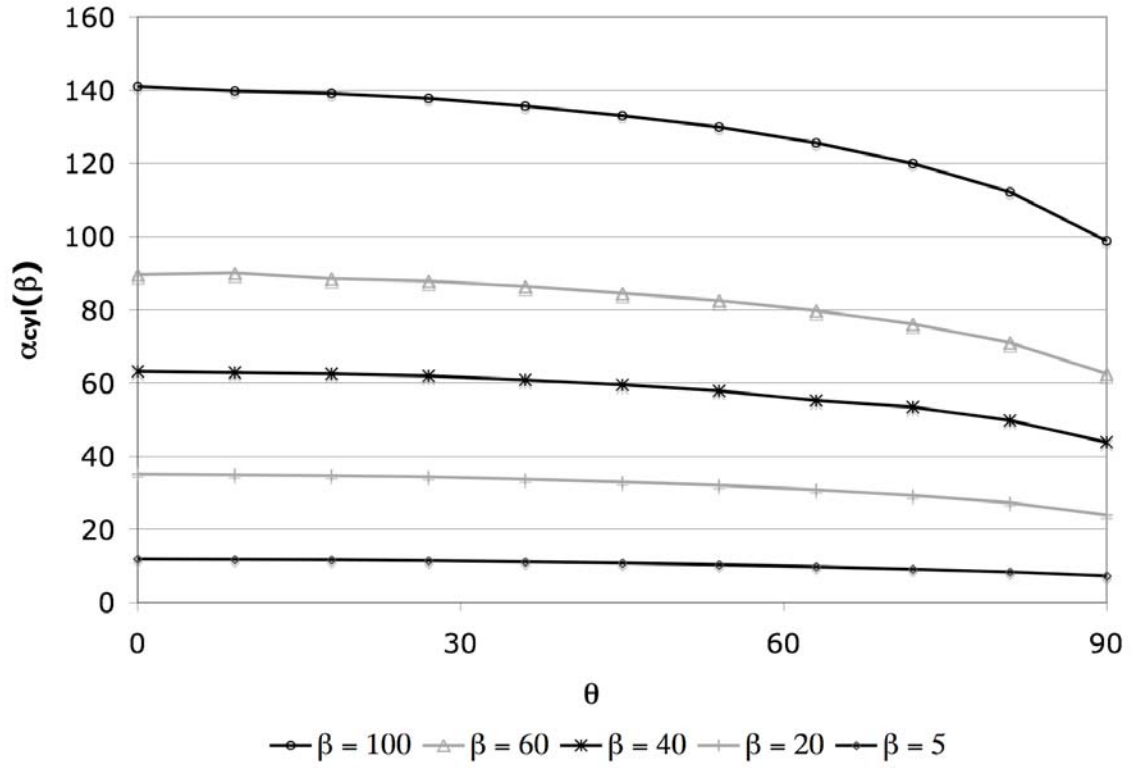


Figure 2.6: Plot of $\alpha_{cyl}(\beta)$ over the surface of the hemispherical cap.

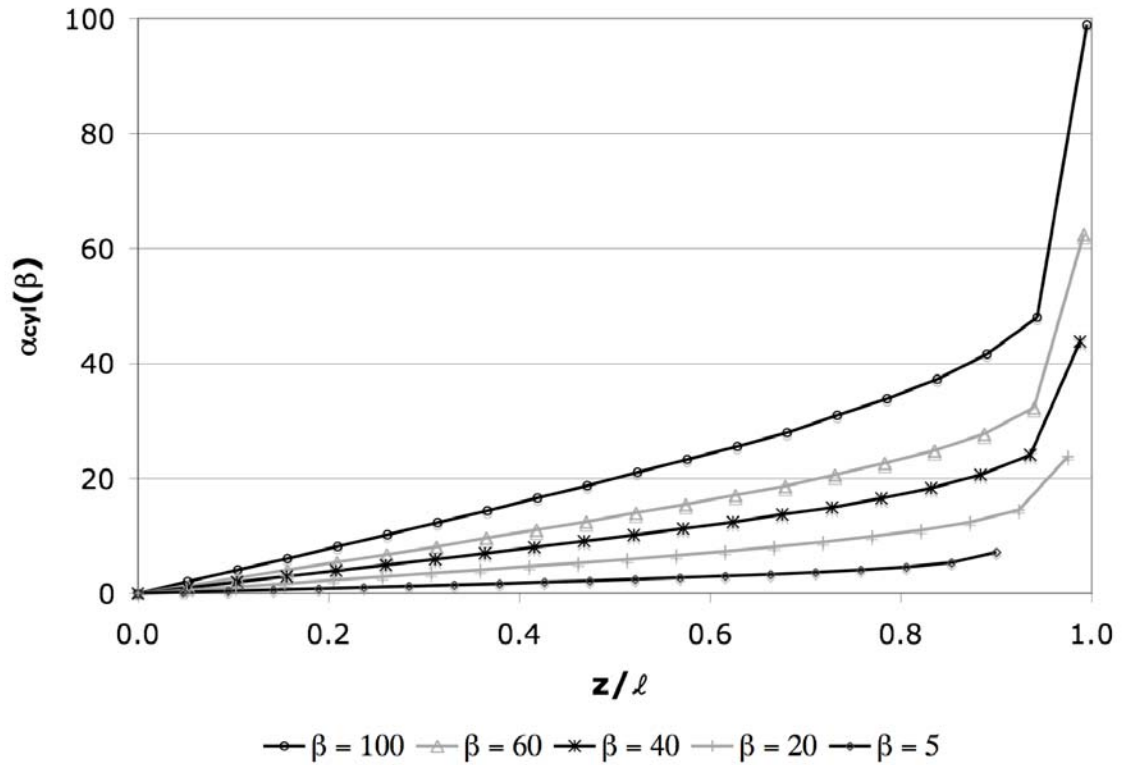


Figure 2.7: Plot of $\alpha_{cyl}(\beta)$ over the surface of the cylindrical shaft.

The plots show that regardless of the particle aspect ratio the electric field at the surface of the cylindrical particle is maximum at the top of the particle ($\theta=0^\circ$) and goes to zero at the base of the particle ($z/\ell=0$) where it contacts the electrode. When holding the background electric field constant and changing β , the electric field at the particle surface is larger for larger β as expected.

Using the plots of $\alpha_{cyl}(\beta, \theta, z)$ and Equation (2.18), $A_{cyl}(\beta)$ can be numerically calculated. Figure 2.8 is a plot of $A_{cyl}(\beta)$ as β ranges from 5 to 100.

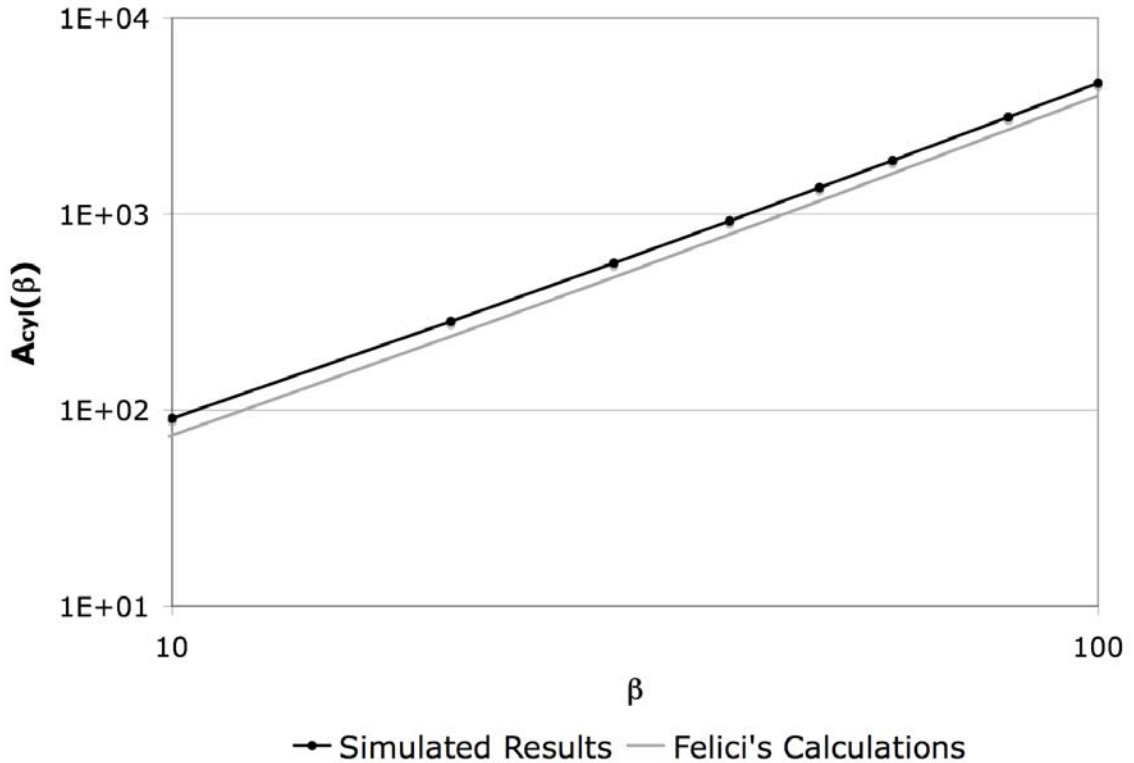


Figure 2.8: Plot of $A_{cyl}(\beta)$ as a function of β , the aspect ratio of the cylindrical particle. Includes simulated results and a comparison with Felici's calculations [29].

According to the simulation results in Figure 2.8, $A_{cyl}(\beta)$ increases with β . Also included in Figure 2.8 are Felici's calculations for the charge acquired by a cylindrical particle.²⁹

Note that the difference between Felici's results and the simulation presented here is due

to a difference in the shape of the particle. Felici modeled the particle as an elongated ellipse, but obtained very similar results that deviate by no more than 20%. The actual shape of the particle will depend on the method of fabrication. Note that largest discrepancy between the models occurs for small values of β (19% at $\beta=5$), and the models approach each other as β increases (14% at $\beta=100$). Due to this similarity, the remainder of this thesis will use Felici's expression to approximate the charge obtained by a cylindrical particle regardless of the exact geometry as given by Equation (2.19).

$$q_{\text{cyl}} \approx \frac{\pi \epsilon E_{BG} \ell^2}{\ln\left(\frac{2\ell}{r}\right) - 1} \quad (2.19)$$

The cylindrical particle charge is rewritten in terms of the particle's aspect ratio.

$$q_{\text{cyl}} \approx \frac{4\pi r^2 \beta^2 \epsilon E_{BG}}{\ln(4\beta) - 1} \quad (2.20)$$

Before comparing the charge acquired by spherical and cylindrical particles in the next subsection, it is important to understand the electric field intensification that occurs at the top of the cylindrical particle, $\alpha_{\text{cyl}}(\beta, \theta=0)$, which is plotted in Figure 2.9 and also discussed for the spherical particle above.

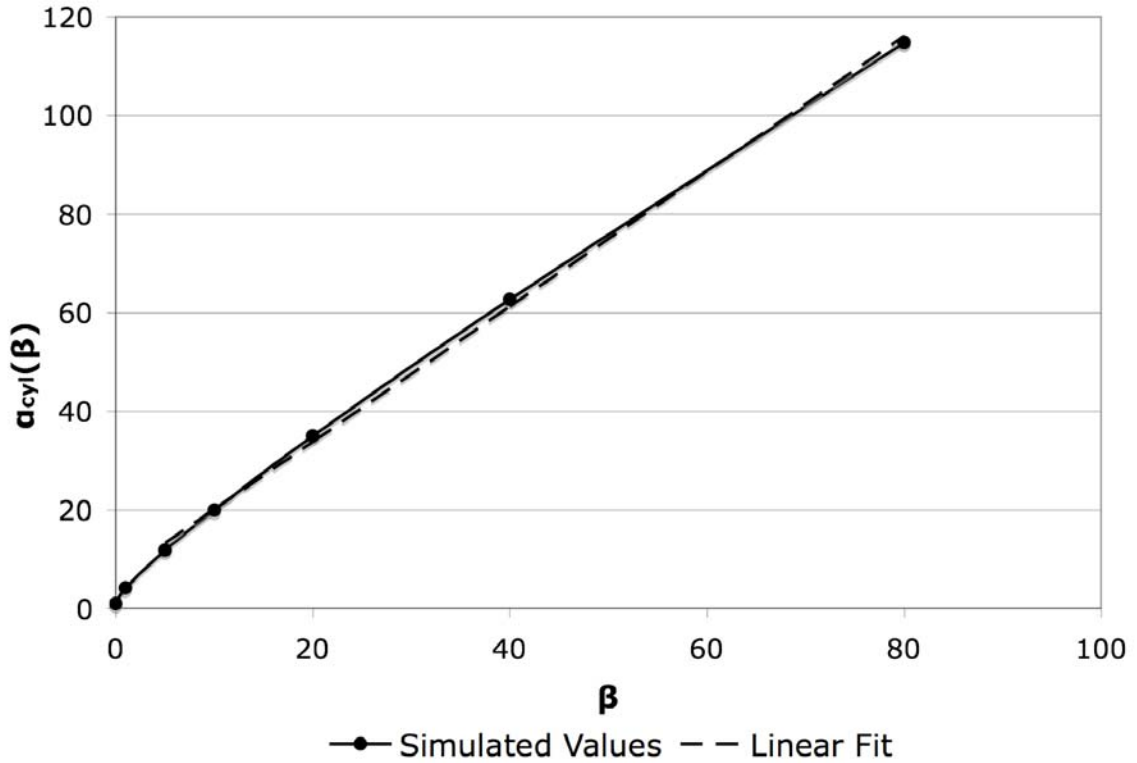


Figure 2.9: Plot of $\alpha_{cyl}(\beta, \theta=0)$ as a function of β and a linear fit over $5 < \beta < 80$.

Figure 2.9 suggests that the cylindrical field-focusing factor is approximately linear as the aspect ratio ranges from 5 to 80.

$$\alpha_{cyl}(\beta) \approx 1.4\beta + 6.5 \quad (2.21)$$

This cylindrical particle field-focusing factor is used in the next section, which compares the charging of spherical and cylindrical particles.

2.2.3. Comparison of Spherical and Cylindrical Particle Charging

The charge-to-mass ratio of propellant used with electric propulsion systems is an important parameter that directly influences the efficiency of propellant usage (specific

impulse) of the thruster. This section compares the maximum attainable charge-to-mass ratios of both spherical and cylindrical particles. The charge-to-mass ratio of a spherical particle, χ_{sph} , is approximated using Felici's model from Equation (2.12) and the mass of a spherical particle with mass density ρ . Note that this section assumes the particle size to be much smaller than the electrode gap.

$$\chi_{sph} \approx \frac{\pi^2 \varepsilon E_{BG}}{2r\rho} \quad (2.22)$$

Similarly, the charge-to-mass ratio of a cylindrical particle, χ_{cyl} , is approximated using Felici's model from Equation (2.20) and the mass of a cylindrical particle with mass density ρ .

$$\chi_{cyl} \approx \frac{2\beta\varepsilon E_{BG}}{r\rho[\ln(4\beta) - 1]} \quad (2.23)$$

Using the same radius for the spherical and cylindrical particles and keeping all other parameters constant, specifically the background electric field, the ratio of the charge-to-mass ratios of a spherical particle to that of a cylindrical particle is only a function of β over the range $5 < \beta < 80$.

$$\frac{\chi_{sph}}{\chi_{cyl}} \approx \frac{\pi^2 [\ln(4\beta) - 1]}{4\beta} \quad (2.24)$$

Figure 2.10 is a plot of the ratio of the charge-to-mass ratios of a spherical particle to that of a cylindrical particle as a function of β when keeping the background electric field constant.

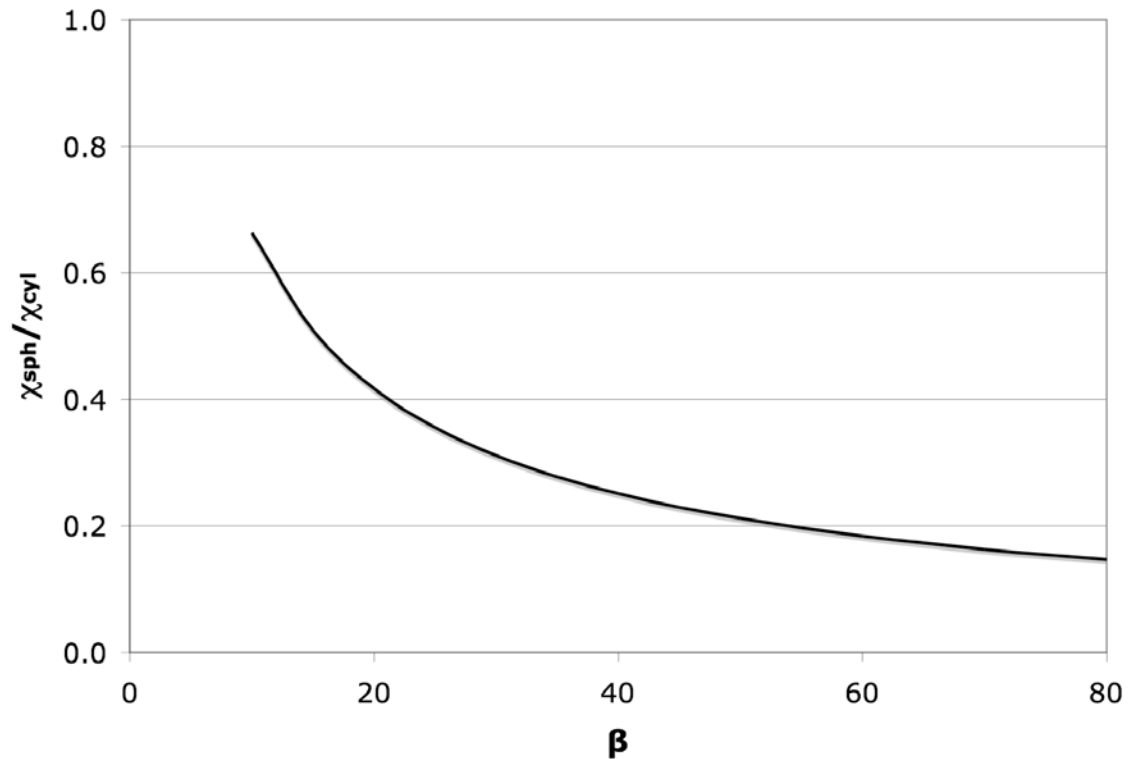


Figure 2.10: Plot of χ_{sph}/χ_{cyl} as a function of β using a constant background electric field.

As shown in Figure 2.10, a cylindrical particle has a greater charge-to-mass ratio, which is a result of the highly intensified electric fields and charge densities that occur at the sharp tip of a high aspect ratio cylinder. However, this result can be misleading. When charging spherical and cylindrical particles, it may be important to maintain the maximum electric field strength in the system, which is located at the top of the particles, below the electrical breakdown of the background medium and the electron field emission limit.

The following analysis investigates the effects of charging spherical and cylindrical particles while holding the maximum electric field in the system constant. The maximum electric field at the top of the particle, E_{\max} , is determined from the background electric field and the field focusing-factor, regardless of the particle shape.²⁸

$$E_{\max} = E_{BG} \alpha \quad (2.25)$$

The ratio of the charge-to-mass ratios of a spherical particle to that of a cylindrical particle is calculated by substituting Equation (2.25) into Equations (2.22) and (2.23) and using the appropriate field-focusing factor for each particle shape.

$$\frac{\chi_{sph}}{\chi_{cyl}} \approx \frac{\pi^2 [\ln(4\beta) - 1]}{4 \beta} \frac{\alpha_{cyl}}{\alpha_{sph}} \quad (2.26)$$

Recall from Section 2.2.1 that the spherical particle field-focusing factor approaches approximately 4.2 when the particle is much smaller than the electrode gap and the cylindrical particle field-focusing factor is approximated as Equation (2.21).

$$\frac{\chi_{sph}}{\chi_{cyl}} \approx \frac{\pi^2 (1.4\beta + 6.5) [\ln(4\beta) - 1]}{16.8 \beta} \quad (2.27)$$

Figure 2.11 is a plot of the ratio of the charge-to-mass ratios of a spherical particle to that of a cylindrical particle as a function of β when holding the maximum electric field at the top of the particle constant.

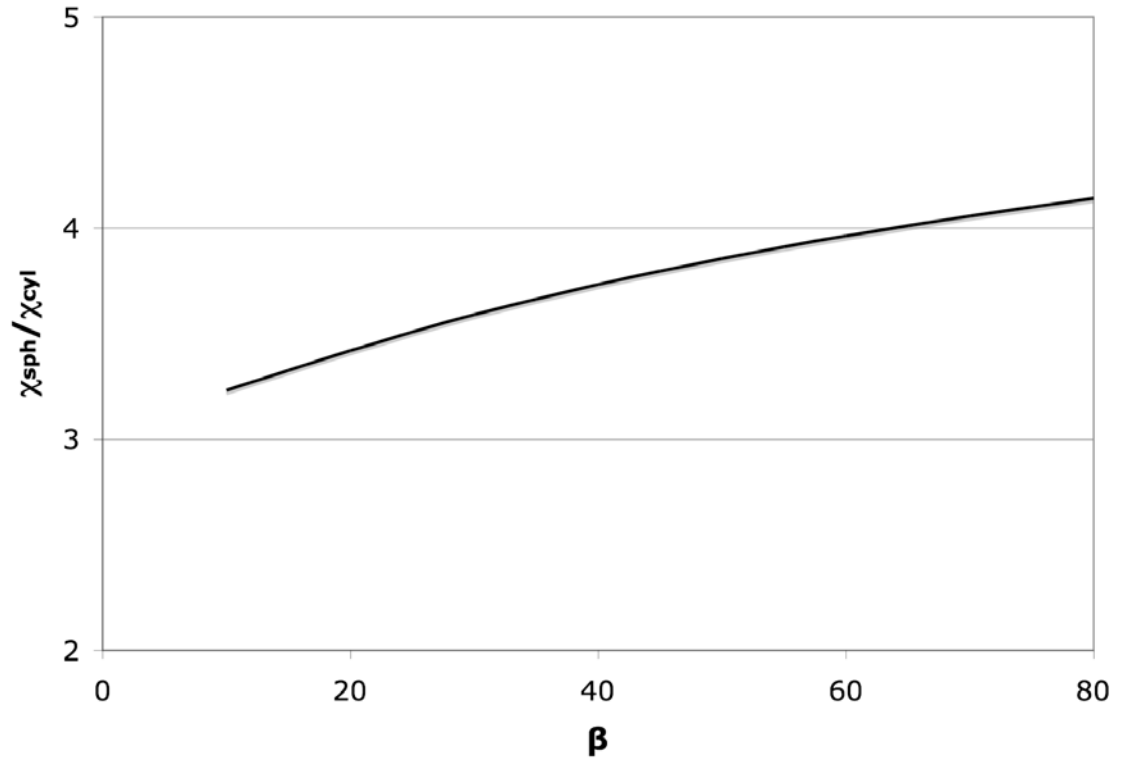


Figure 2.11: Plot of χ_{sph}/χ_{cyl} as a function of β using a constant maximum electric field.

The plot in Figure 2.11 suggests that when using a constant maximum electric field, a spherical particle will always have a greater charge-to-mass ratio. In addition, a larger cylindrical particle aspect ratio leads to a smaller charge-to-mass ratio, which is opposite of the case when the background electric field is constant.

This analysis suggests that when using solid particles that cylindrical particles may be the better choice when limiting the strength of the background electric field, but spherical particles may be the better choice when limiting the strength of the maximum electric field at the top of the particle.

2.2.4. Specific Impulse using Spherical and Cylindrical Particles

This section discusses the particle size requirements and the obtainable specific impulses when using spherical and cylindrical particles and maintaining the maximum focused electric field strengths at the top of the particles constant. Using Equations (1.6), (2.22), (2.23), and (2.25) the specific impulses of a micro- and nano-particle thruster are predicted when using both spherical and cylindrical particles.

$$ISP_{sph} \approx \frac{1}{g} \sqrt{\frac{0.24\pi^2 \epsilon E_{\max} V}{r\rho}} \quad (2.28)$$

$$ISP_{cyl} \approx \frac{1}{g} \sqrt{\frac{4\beta \epsilon E_{\max} V}{[\ln(4\beta) - 1][1.4\beta + 6.5]r\rho}} \quad (2.29)$$

Figure 2.12 plots the specific impulse and the exhaust velocity as a function of particle diameter for a spherical particle and a cylindrical particle with an aspect ratio of 80. The maximum focused electric field strength at the top of both particles is 500 MV/m, the particles' densities are as 1,000 kg/m³, and an accelerating voltage of 40 kV is applied. A 1,000 kg/m³ density can be either a hollow particle or a glass particle with a thin metallic coating. The strength of the electric field is limited to 500 MV/m to assure that the electron emission threshold is not exceeded. An accelerating voltage of 40 kV is used as approximate upper limit for space applications.

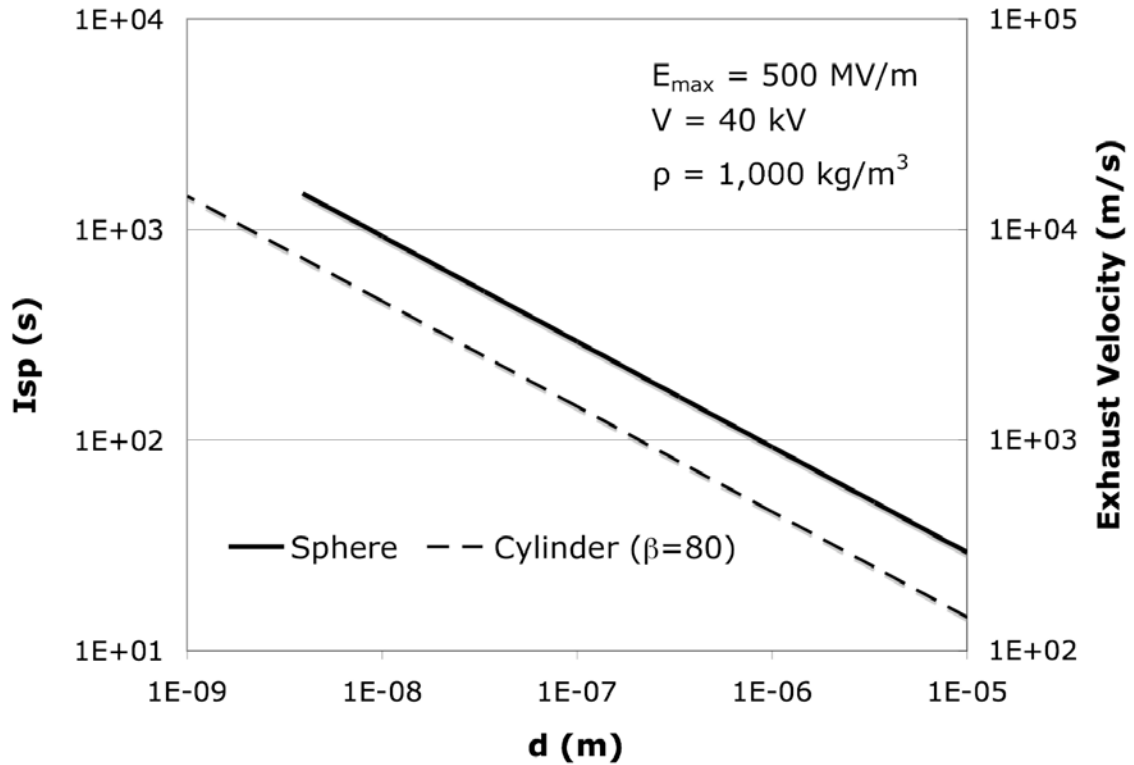


Figure 2.12: Specific impulse and exhaust velocity as a function of particle diameter for spherical and cylindrical particles per Equations (2.28) and (2.29), respectively.

Figure 2.12 suggests that a micro- and nano-particle thruster may be capable of producing a specific impulse greater than 1,000 seconds when using spherical particles on the order of 10 nm and smaller (future work must address quantum effects). Increasing the particle size or decreasing the applied electric field and voltage can reduce the specific impulse, if required. Note that the specific impulse of the cylindrical particle is less than the specific impulse of the spherical particle, which is a result of the intense field-focusing that occurs at the sharp tip of a high aspect ratio cylinder.

2.2.5. Required Particle Separation During the Charging Process

The spherical particle charging model presented in section 2.2.1 assumes that a single particle is charged on an infinite planar electrode. This subsection investigates the effects

of the charge acquired by a particle of interest when it is charged in a group. It is possible that a group of particles charging in close proximity may modify the electric fields, and, as a result, each particle may not be able to reach the highest possible charge that an isolated particle can achieve. To investigate the effects that a group of particles has on the charge acquired by the particle of interest, the model used for a single particle, shown in Figure 2.1, is extended. The new model is a modification of the single particle model and introduces additional particles in the vicinity of the particle of interest. Figure 2.13 is an illustration of the model showing a horizontal cross-sectional view and a top down view of the source electrode. The particle of interest is located in the center and surrounded by densely packed particles at a separation distance of R . Note that this is a worse case scenario, and it is expected that the spacing of the nearby particles would be much lower than shown in Figure 2.13.

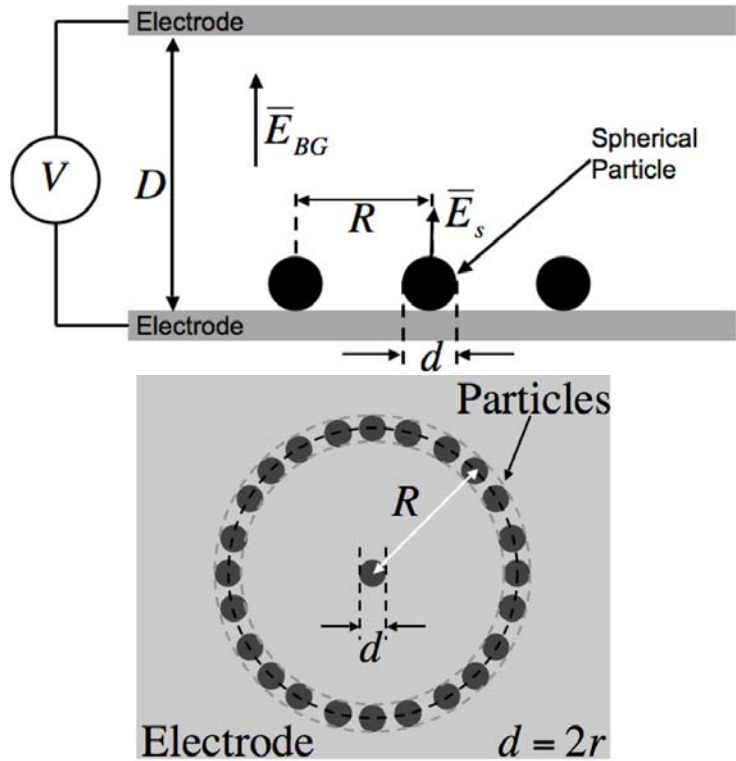


Figure 2.13: Model for the charge acquired by a conducting spherical particle in contact with a planar electrode and subjected to a high strength electric field with additional particles in the vicinity of the particle of interest.

The charge acquired by the particle of interest is calculated using the method from section 2.2.1 and utilizes Equations (2.6) and (2.7), but requires a modified spherical particle field-focusing factor, $\alpha_{\text{sph}}(\theta, R)$, and integrated field-focusing factor, $A_c(R)$. These two variables are independent of ζ_{sph} because of the assumption that $\zeta_{\text{sph}} \ll 1$, but are now functions of the particle separation distance, R . Again, COMSOLTM was used to establish the field focusing factor variation as a function of θ . The group of particles surrounding the particle of interest was approximated with a solid metal ring. This is the worst case scenario when the surrounding particles are tightly packed. Again, the width of the simulation environment was set to 10 times the electrode gap to eliminate field screening due to edge effects,²⁸ and the simulation cell size was chosen through trial and

error to ensure that the simulation solution was not a function of cell size, but truly represents the expected results.

To understand the effects that the group of particles has on the charge acquired by the particle of interest, the ratio of the charge acquired by the particle of interest to the charge acquired by a single isolated particle charged on a planar electrode, Γ_{group} , is evaluated as a function of the ratio of the particle separation to the particle diameter, R/d , when keeping everything else constant.

$$\Gamma_{\text{group}} = \frac{q_{\text{sph}}(R/d)}{q_{\text{sph}}(R/d \rightarrow \infty)} \quad (2.30)$$

Figure 2.14 is a plot of Γ_{group} as function of the ratio of the particle separation to the particle diameter.

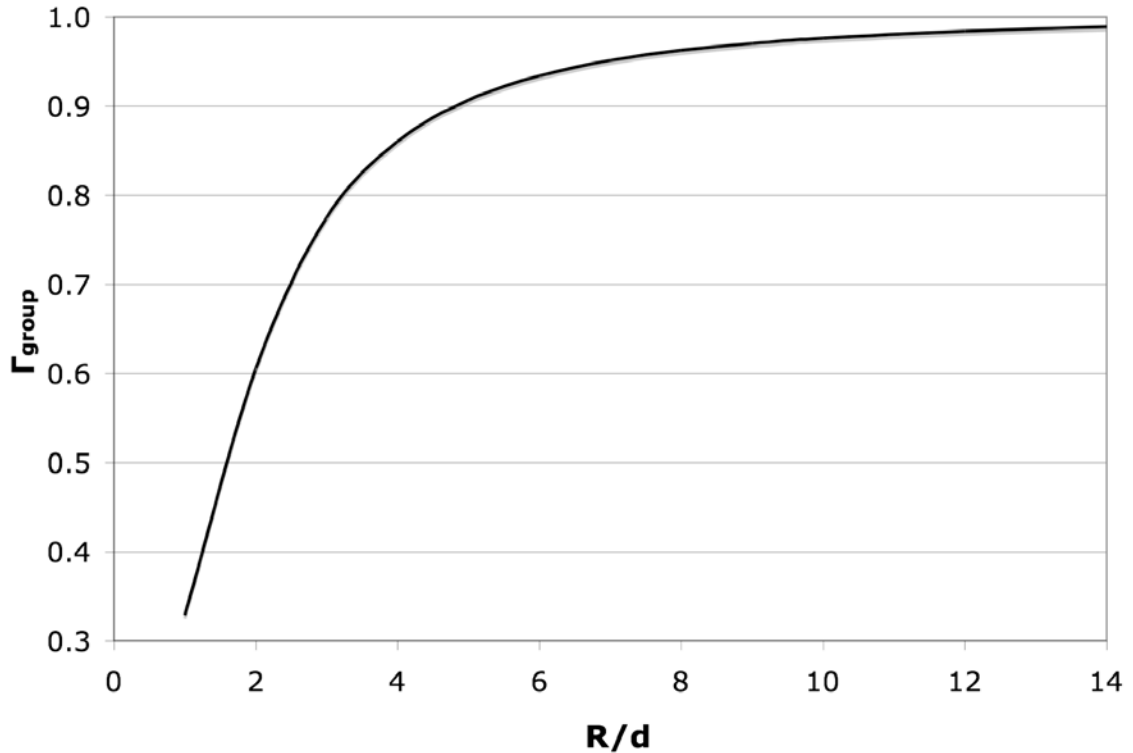


Figure 2.14: Plot of Γ_{group} as function of the ratio of the particle separation to the particle diameter.

Figure 2.14 indicates that the total charge acquired by the particle of interest is highly dependent on the particle spacing. A small particle spacing results in the particle acquiring much less charge than a single isolated particle, but a particle spacing of at least one order of magnitude larger than the particle ($R/d \geq 10$) results in the particle acquiring at least 98% that of a single isolated particle. This analysis suggests that it is best to separate the particles while charging them, and it is recommended that the particles have a separation distance of at least one order of magnitude of the particle size. The solid ring used to represent the particles is expected to produce the worst-case scenario. In reality, the particles surrounding the particle of interest would be spaced further apart, and the spacing with respect to the particle of interest could be decreased slightly.

2.2.6. Charging Spherical Particles on High Aspect Ratio Posts

The spherical particle charging model presented in section 2.2.1 investigated charging spherical particles in contact with an infinite planar source electrode. According to Equation (2.5), the total charge on the particle is directly related to the strength of the electric field at the particle surface. Figure 2.2 indicates that the strength of the electric field is greatest at the top of the particle and zero at the bottom of the particle. When charging particles against a source electrode, the maximum electric field at the top of the particle may be limited by the electrical breakdown of the surrounding medium [$E_s(\theta=0^\circ) \leq E_{BD}$], and the electric field is always zero at the contact point between the particle and the electrode [$E_s(\theta=180^\circ) = 0$]. But, it may be possible to increase the strength of the electric field over the remaining particle surface ($0^\circ < \theta < 180^\circ$) by manipulating the geometry of the source electrode. This subsection investigates the possibility of increasing the total particle charge by charging the spherical particle on a high aspect ratio post as opposed to an infinite planar surface.

Figure 2.15 is the model for charging spherical particles on a high aspect ratio post, which is an extension to the model used for charging particles on a planar electrode. The charging post is a conducting cylinder capped with a hemisphere and mounted on an infinite planar electrode. The charging post and the spherical particle have the same diameter and a combined height of ℓ , which is much less than the electrode gap so that the strength of the electric field at the surface of the particle is approximately a function of the aspect ratio and not the electrode gap as shown in Figure 2.15.

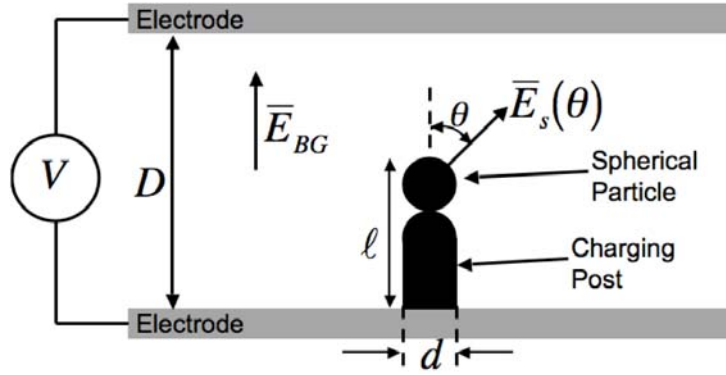


Figure 2.15: Model for charging spherical particles on a high aspect ratio charging post

The charge acquired by the particle is calculated using the method from section 2.2.1 and section 2.2.5 and utilizes Equations (2.6) and (2.7), but requires a modified spherical particle field-focusing factor, $\alpha_{\text{sph}}(\theta, \beta)$, and integrated field-focusing factor, $A_c(\beta)$. These two variables are independent of ζ_{sph} because of the assumption that the post length is much less than the electrode gap, but are now functions of the combined aspect ratio of the post and particle, $\beta = \ell/d$. The modified spherical particle field-focusing factor and integrated field-focusing factor were evaluated using an extension to the simulation presented in section 2.2.1, which utilizes COMSOLTM. Again, the width of the simulation environment was set to 10 times the electrode gap to eliminate field screening due to edge effects,²⁸ and the simulation cell size was chosen through trial and error to ensure that the simulation solution was not a function of cell size, but truly represents the expected results. A cell size of two orders of magnitude smaller than the particle diameter was used.

To understand the effects that the high aspect ratio charging post has on the charge acquired by the particle, the ratio of the charge acquired by the particle when charged on a post to the charge acquired by a particle when charged on a planar electrode, Γ_{post} , is

evaluated as a function of β , when keeping the maximum electric field strength at the top of the particle constant. The case when the particle is charged on a planar electrode corresponds to $\beta=1$.

$$\Gamma_{post} = \frac{q_{sph}(\beta)}{q_{sph}(\beta \rightarrow 1)} \quad (2.31)$$

Figure 2.16 is a plot of Γ_{post} as function of β .

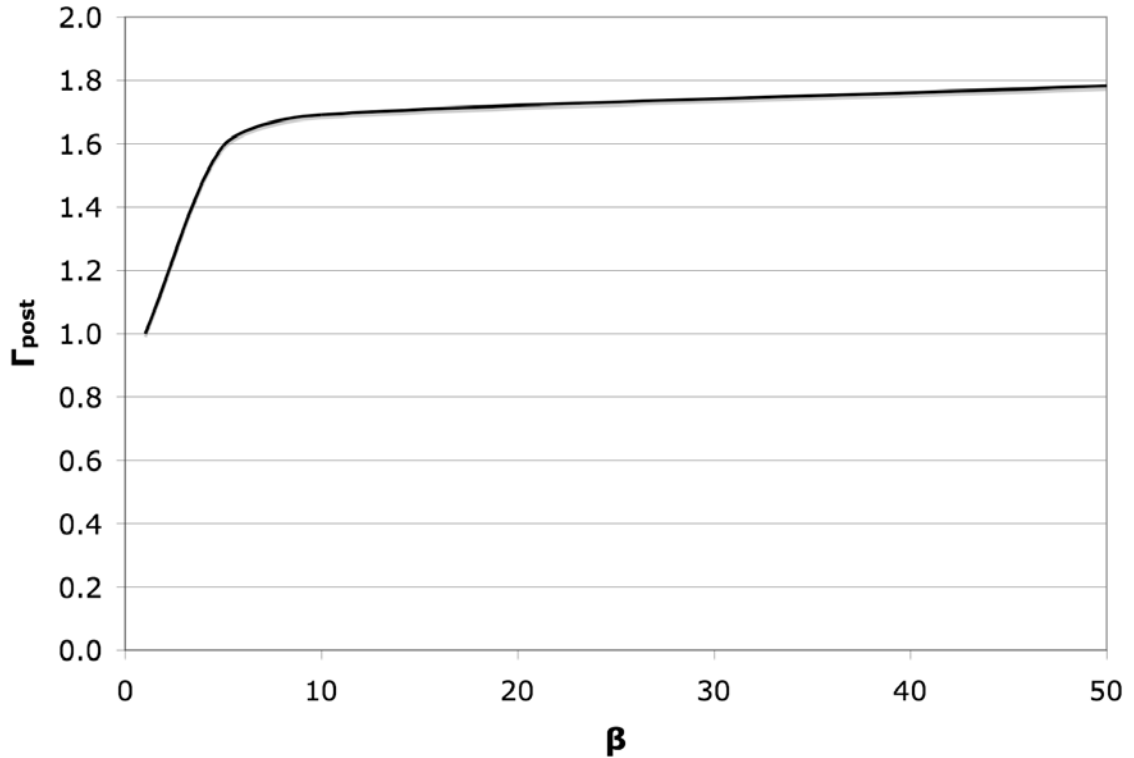


Figure 2.16: Plot of Γ_{post} as function of β , for the situation of a spherical particle on a post with a combined height to diameter ratio of β .

Figure 2.16 indicates that the total charge acquired by the particle when charged on a high aspect ratio charging post is dependent on the post aspect ratio. An aspect ratio of

80 may be capable of increasing the particle charge approximately by a factor of 1.8 when compared to the charge acquired on an infinite planar electrode.

The absolute theoretical charging limit when constraining the strength of the electric field on the surface of the particle is obtained by allowing the electric field over the entire surface of the particle to be equal to the maximum electric field allowed by the background medium. This is not possible when charging against a source electrode since the surface electric field must go to zero at the contact point, but does provide insight to the limit. The resulting particle charge is approximately 2.5 times greater than when charged on a planar electrode. This analysis suggests that charging spherical particles on a high aspect ratio charging post as opposed to a planar electrode can increase the particle charge slightly, but not by orders of magnitude.

It should be noted that the high aspect ratio posts would need to have larger separations than the spherical particles discussed in Section 2.2.5 to assure that adjacent posts do not affect particle charging. The exact spacing required is beyond the scope of this thesis, but it is expected that high aspect ratio posts will affect the shape of the electric field at much larger distances than spherical particles with the same diameter. Increasing the separation distances would decrease the thrust density, but can be used as a method of increasing the propellant charge-to-mass ratio and therefore the thruster specific impulse. An initial assessment indicates that the required post spacing is dependent on the length of the posts. But, it is recommended that future work further investigate the required post spacing and its effects on the thruster performance.

2.3. Experimental Setup

To experimentally investigate the charge acquired by spherical and cylindrical conducting particles when in contact with an infinite planar electrode and exposed to a high strength electric field, the system depicted in Figure 2.17 was constructed with 10 cm square stainless steel electrodes, which is very similar to the models in Figure 2.1 and Figure 2.5, with the addition of an insulating liquid medium filling the electrode gap.

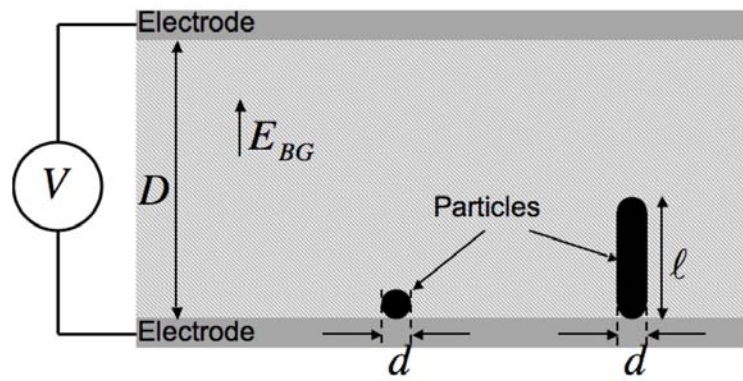


Figure 2.17: Depiction of the experimental setup used for investigating the charging of spherical and cylindrical particles against a planar electrode with a high strength electric field.

The main goal of the experiment is to measure the charge acquired by both spherical and vertically oriented cylindrical particles against an infinite planar electrode when exposed to a high strength electric field. An additional goal is to measure the time required to fully charge the particles.

The experiment is performed by depositing a single test particle on the surface of the bottom electrode. Once the particle is in place, the upper electrode is carefully secured to provide the correct uniform electrode gap, which is regulated by an insulating spacer that ranges from approximately 6.0 mm to 14.0 mm thick. Next, a large electrical potential difference is applied between the parallel electrodes to generate the strong electric field

within the gap, which charges the particle in contact with the bottom electrode. Note that the fringing fields at the edges of the electrodes can be neglected since the electrode width is much greater than the electrode gap. At sufficiently high electric fields, the particle is lifted from the bottom electrode and transported through the liquid to the top electrode. Once contacting the top electrode, the particle becomes charged with the opposite polarity and is transported back down to the bottom electrode by the electrostatic and gravitational forces. This process continues and the particle oscillates between the electrodes as depicted in Figure 2.18. Tobazeon^{30,31,32} presents an in-depth explanation of the dynamics of particle oscillation between parallel electrodes in an insulating liquid along with some charge measurements for spherical and cylindrical particles.

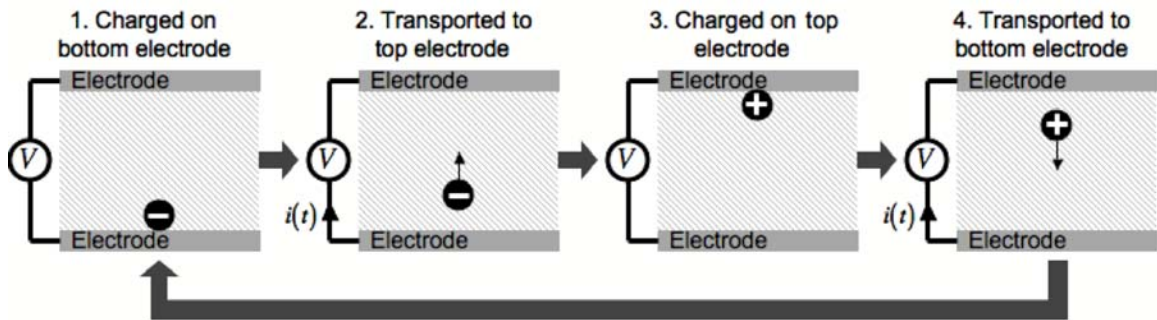


Figure 2.18: Oscillation of a charged particle between parallel electrodes biased to electric potential, V .

The oscillation of the charged particle produces a current, $i(t)$, in the system directly related to the particle current, which is dependent on the charge, q , and velocity, $u(t)$, of the particle, and the electrode separation, s .³²

$$\Delta i(t) = \frac{qu(t)}{s} \quad (2.32)$$

The total charge and location of the particle modifies the electric fields within the electrode gap, which causes movement of charge on the constant voltage electrode surfaces and gives rise to the system current. The measurement of the current using a low-pass current measuring circuit, which is presented in Section 2.3.1, has five distinct stages dependent on the particle location and motion, which are depicted in Figure 2.19.³⁰

The stages are interpreted as follows.

1. The particle is at rest on either the top or bottom electrode, and the stationary particle does not produce any system current. All measured current is leakage current through the liquid.
2. The particle is lifted from the electrode and accelerated. As the particle's velocity increases, the system current increases as described by Equation (2.32).
3. The particle reaches terminal velocity. Once the drag force balances the opposing electric force, the particle no longer accelerates. Since the particle is moving at a constant velocity, the current resulting from the motion of the particle is constant.
4. The particle reaches the opposite electrode, deposits its charge, and then charges with the opposite polarity. The large spike in current occurs as a result of the transfer of charge between the particle and the electrode.
5. The current measuring system dissipates the charge built up on an internal capacitor.

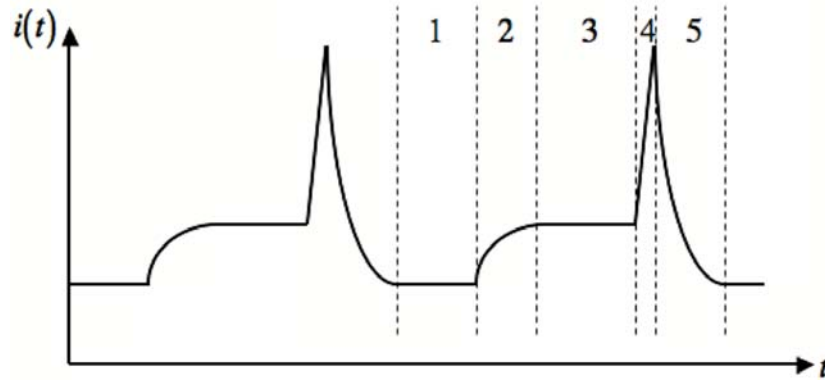


Figure 2.19: Expected system current as a function of time as the charged particle oscillates between the parallel electrodes.

According to Ampere’s law, the total charge of the particle, q_m , can be calculated by measuring the current resulting from the oscillating particle and integrating over the time that the particle is in transport, which are stages 2 and 3 from Figure 2.19.

$$q_m = \int i(t)dt \quad (2.33)$$

The insulating liquid filling the electrode gap serves to increase the viscous drag on the particle and reduces the velocity of the particle during oscillation, which simplifies the current measurement procedure. The insulating liquid used in this experiment is silicone oil purchased from Clearco, which has a relative dielectric constant of approximately 1.97³³ and conductivity on the order of 10^{-13} S/m.³⁴ Silicone oil was chosen because of its very low conductivity, low vapor pressure, and because of its availability in various viscosities. The viscosity was chosen to control the velocity of the oscillating particle and was varied depending on the particle size and applied voltage from 50 cSt to 100 cSt. Note that the small conductivity of the liquid leads to a loss of

charge from the particle during transport, which is dependent on the liquid's charging time constant, τ_ℓ .³⁰

$$q(t) = q_0 e^{-t/\tau_\ell} \quad (2.34)$$

The liquid's time constant is dependent on its conductivity and dielectric constant.³⁰

$$\tau_\ell = \frac{\epsilon_\ell}{\sigma_\ell} \quad (2.35)$$

According to Equation (2.35), the liquid's time constant is on the order of 200 s, which is much greater than the time of a single particle oscillation, which is on the order of a tenth of a second. Therefore, the particle charge lost to the liquid during transport is neglected.

The experiment was performed using spherical particles made of aluminum and titanium with diameters ranging from approximately 800 μm to 4,000 μm and cylindrical aluminum particles with diameters of 300 μm and lengths of 1.7 mm and 1.3 mm. Table 2.1 lists the dimensions and tolerances of all the particles used in the experiment along with the electrode gap and liquid viscosity used for each test case.

Particle Shape	Particle Material	Particle Diameter (mm)	Particle Length (mm)	Electrode Gap (mm)	Liquid Viscosity (cSt)
Sphere	Titanium	3.97 \pm 0.025	NA	11.3 \pm 0.25	100
Sphere	Aluminum	2.37 \pm 0.025	NA	6.15 \pm 0.25	50
Sphere	Aluminum	1.98 \pm 0.025	NA	6.15 \pm 0.25	50
Sphere	Aluminum	1.59 \pm 0.025	NA	6.15 \pm 0.25	50
Sphere	Aluminum	0.79 \pm 0.025	NA	6.15 \pm 0.25	50
Cylinder	Aluminum	0.33 \pm 0.025	1.3 \pm 0.2	13.9 \pm 0.25	100
Cylinder	Aluminum	0.33 \pm 0.025	1.7 \pm 0.2	13.9 \pm 0.25	100

Table 2.1: Properties of the particles used in the particle charge experiment and the electrode gap and liquid viscosity used for each test case.

The following subsections present the design of the current measuring system and the method used to calculate the particle charge from the measured current.

2.3.1. Design of the Current Measuring System

Measuring the system current resulting from the oscillating particle requires a system capable of detecting currents on the order of tens to hundreds of pico-amperes with a very high sampling rate. This experiment used an inverting operational amplifier with a capacitor inserted in parallel with the feedback resistor, which is shown in Figure 2.20. The operational amplifier was a low-bias-current, high-stability, JFET operational amplifier from Analog Devices (OP41EJ).³⁵

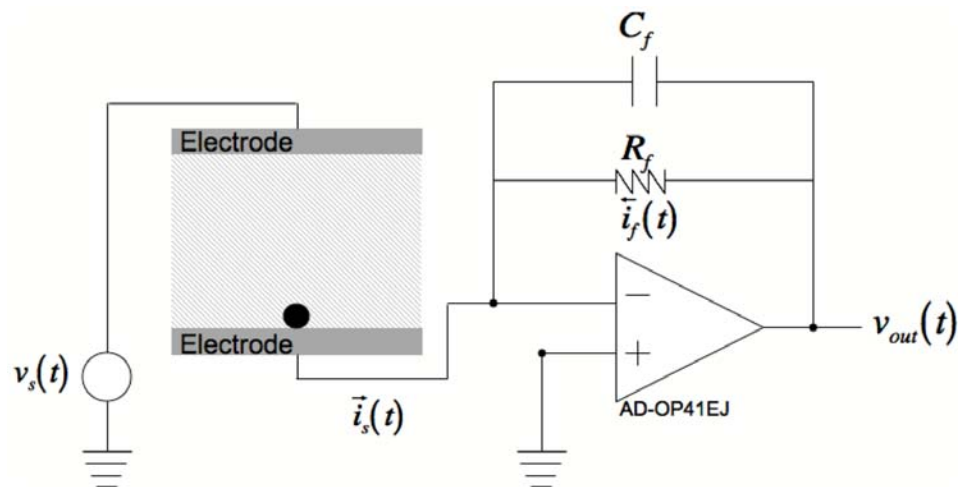


Figure 2.20: Diagram of an inverting operational amplifier with a capacitor inserted in parallel with the feedback resistor used to measure current of the oscillating charged particle.

The system current, $i_s(t)$, resulting from the oscillating particle and leakage current through the liquid is calculated as a function of the output voltage, $v_{out}(t)$, the feedback resistor, R_f , the feedback capacitor, C_f , and an offset voltage, v_{offset} , which is a

characteristic of the operational amplifier. The output voltage is monitored with an oscilloscope.

$$i_s(t) = -C_f \frac{dv_{out}(t)}{dt} - \frac{(v_{out}(t) + v_{offset})}{R_f} \quad (2.36)$$

The values of the feedback resistor and capacitor are critical parameters that depend on the expected current through the test cell and the noise in the system. The signal-to-noise ratio was typically greater than 30. Determining the value of the feedback resistor is straightforward and depends on the expected range of the system current and the allowable range of the output voltage, which is a characteristic of the operational amplifier. The resolution of the measured current is maximized when its range fills the entire range of the output voltage. Typical resolutions were on the order of tens of pico-amps.

$$R_f \approx \frac{v_{out,max}}{i_{s,max}} \quad (2.37)$$

The feedback capacitor serves as a low-pass filter to attenuate the high frequency noise above the cutoff frequency, f_c .³⁶

$$f_c \approx \frac{1}{2\pi R_f C_f} \quad (2.38)$$

Measuring currents below the nano-ampere range proved to be very difficult due to noise in the testing environment from the laboratory lights, noises, computers, and even the

experiment personnel. Therefore, it is desirable to choose the value of the feedback capacitor that minimizes the cutoff frequency and attenuates as much high frequency noise as practical without severely decreasing the response time of the output voltage, which is dependent on the circuit's RC time constant, τ_c .³⁶

$$\tau_c \approx R_f C_f \quad (2.39)$$

To ensure that the system can differentiate the upward and downward movement of the particle within a single oscillation, the response time of the circuit must be less than half of the oscillation time of the particle, T_{osc} . This section defines the response time to be five times the RC time constant, which ensures that the circuit relaxes to over 99%. Finally, the maximum allowable value for the feedback capacitor is dependent on the particle oscillation time and the value of the feedback resistor.

$$C_f \leq \frac{T_{osc}}{10R_f} \quad (2.40)$$

The expressions for the feedback components given in Equations (2.37) and (2.40) provide reasonable values for the feedback resistor and capacitor, but need to be optimized through experimental trial and error to account for additional unknown inductances, capacitances, and resistances in the entire system. The experimental results presented in Section 2.4 used a feedback capacitance of 100 pF and feedback resistances ranging from approximately 400 M Ω to 2 G Ω .

In addition to choosing a proper feedback resistor and capacitor, other precautions are taken to minimize the noise. The two main precautions are grounding and shielding of the experimental setup.³⁷ All ground wires are as short as possible and the entire experimental setup is inside a grounded shielding box. Using these methods, the total noise in the system was typically below a few tens of pico-amps.

2.3.2. Calculation of Particle Charge

The charge of the particles is calculated numerically by integrating the measured current as shown in Equation (2.33) over the time that the particle is in transit from the bottom electrode to the upper electrode, which corresponds to stages 2 and 3 in Figure 2.19. The numerical integration is performed using a MATLABTM script, which takes the output voltage from the operational amplifier and calculates the current from Equation (2.36) before integrating.

2.4. Experimental Results

Figure 2.21 is an experimental trace of the current arising from an oscillating particle that is 800 microns in diameter and subjected to an approximate electric field of 570 kV/m. The numbered current stages correspond to the stages listed in Section 2.3.

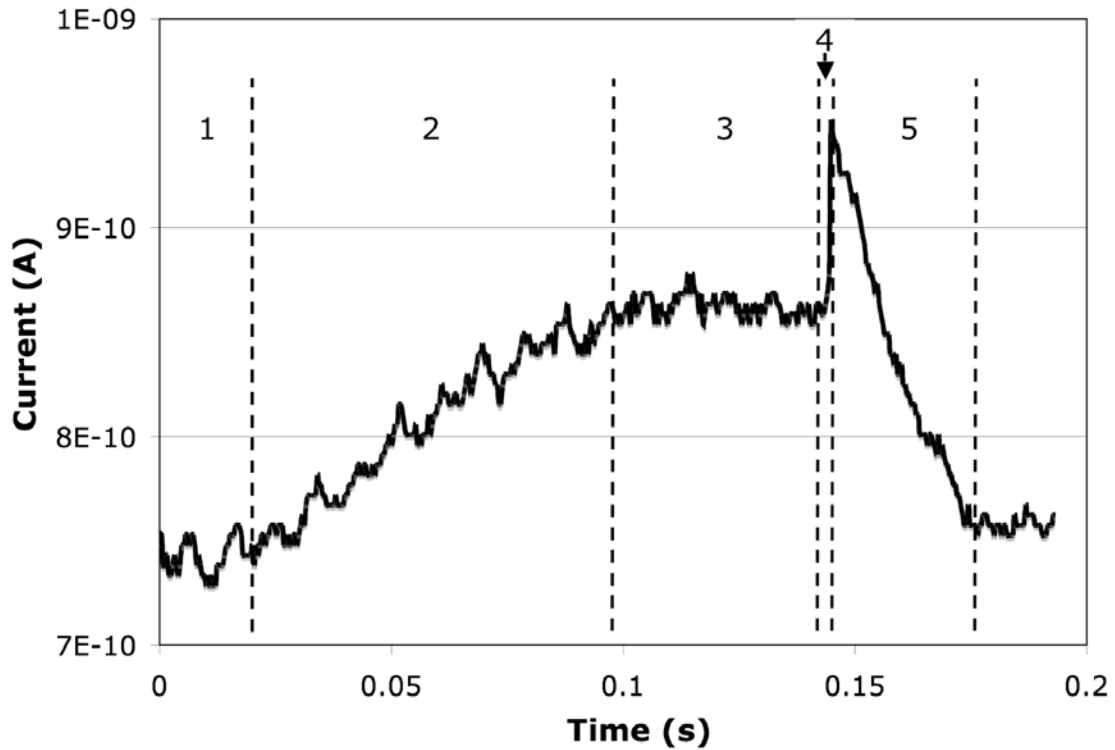


Figure 2.21: Experimental current trace when oscillating an 800 micron, spherical, aluminum particle with an electric field of approximately 570 kV/m.

Figure 2.22, Figure 2.23, and Figure 2.24 are plots of the average charge acquired by various size and shape titanium and aluminum particles when charged between planar parallel electrodes and submersed in silicone oil as shown in Figure 2.17. The particle charge is plotted as a function of the applied electric field. The ranges of electric fields used were determined by the required field strengths to induce particle oscillation and the response of the ammeter. Note that these conditions change with particle size and shape. The test conditions are listed in Table 2.1. There is a maximum estimated total error of approximately 10% in the measurements, which was determined with the sum of squares method. The error in the measured particle charge is due mostly to three error terms in the experimental setup. These error terms are as follows: the numerical integration (9%), the electrode gap separation (4%), and the applied voltage (0.1%).

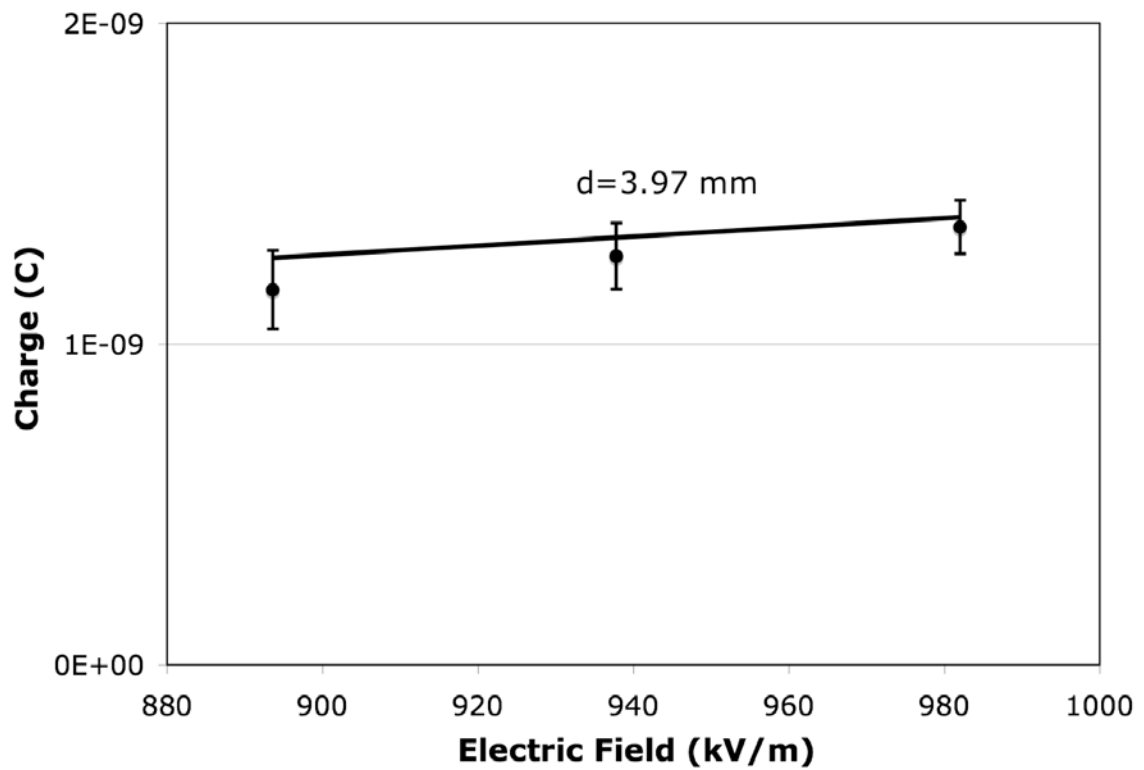


Figure 2.22: Spherical particle charge measurements using titanium. Particle oscillation in 100 cSt silicone oil between 11.30 mm spaced electrodes. The solid line is the theoretical charge from Equation (2.12).

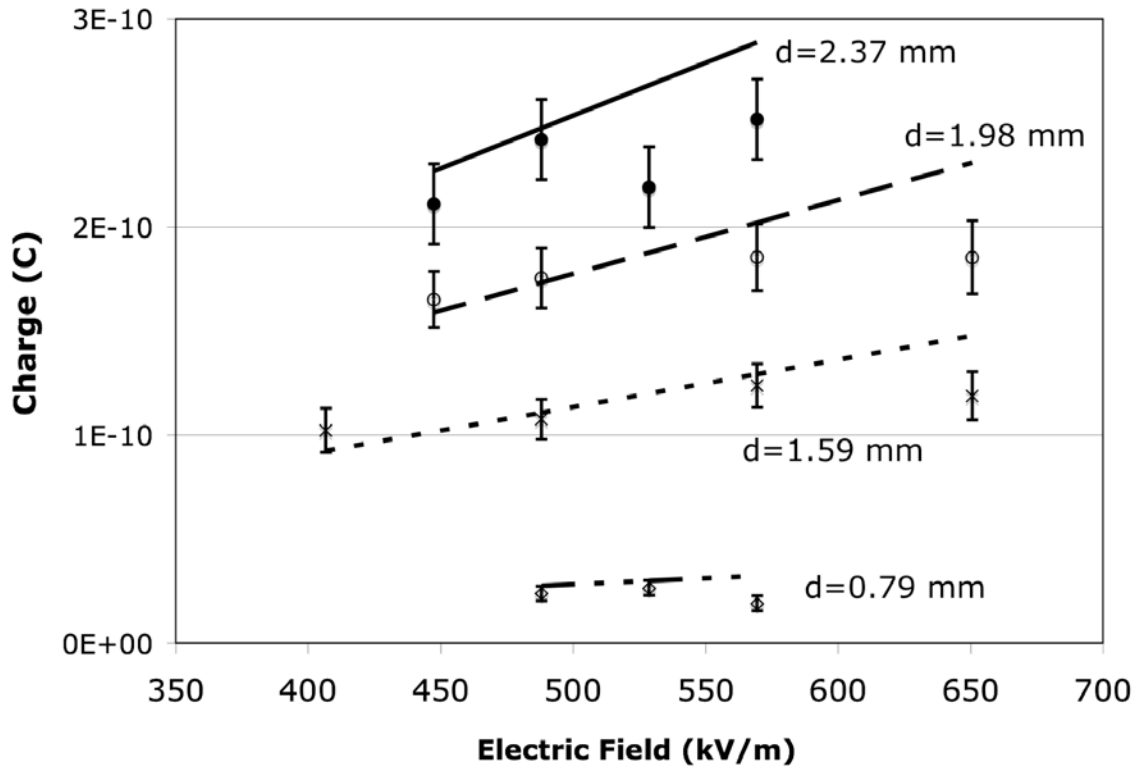


Figure 2.23: Spherical particle charge measurements using aluminum. Particle oscillation in 50 cSt silicone oil between 6.15 mm spaced electrodes. The solid line is the theoretical charge from Equation (2.12).

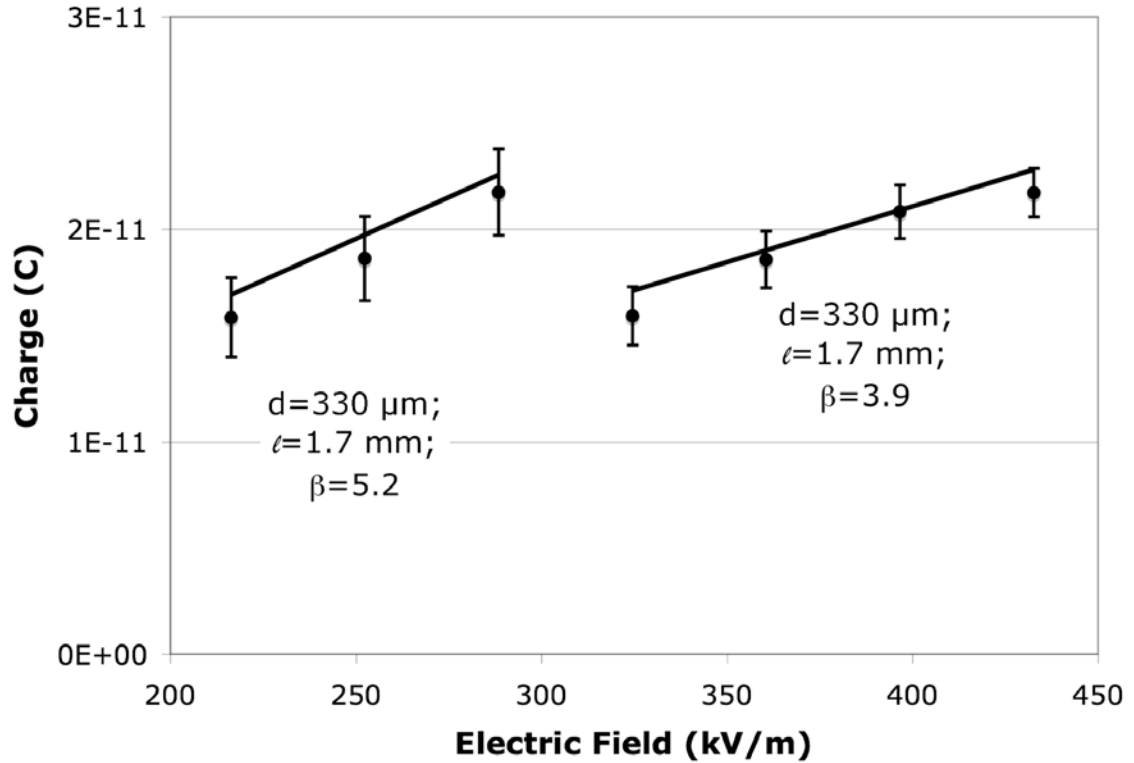


Figure 2.24: Cylindrical particle charge measurements using aluminum. Particle oscillation in 100 cSt silicone oil between 13.9 mm spaced electrodes. The solid line is the theoretical charge from Equation (2.20).

The experimental data are plotted against the theoretical particle charge according to Equations (2.11) and (2.19). The measured charge of the titanium spherical particle (Figure 2.22) and the measured charge of the aluminum cylindrical particles (Figure 2.24) all follow the theoretical models closely for all tested electric fields. But, according to the plot in Figure 2.23, the aluminum spherical particles only acquired the predicted charge when lower strength electric fields were applied and acquired less charge than predicted when higher strength electric fields were applied. One possible explanation is presented in the following section.

2.5. Particle Charging Time

It is possible that the aluminum spherical particles did not acquire the charge predicted by the model when higher strength electric fields were applied because they were lifted from the electrode surface before the charging process was completed due to a poor electrical contact between the particle and the electrode. This section investigates the total time that the particles were allowed to charge and develops a model to predict the charging time constant of spherical particles against a source electrode.

2.5.1. Measured Particle Charging Times

The total time that the aluminum particles were allowed to charge is determined from the experiment by investigating the total time that the particles were in contact with the electrode before being lifted, which is represented as stages 4 and 5 from the previous oscillation and stage 1 from the present oscillation in Figure 2.19. Figure 2.25 shows the average charging time for the aluminum spherical particles as a function of applied electric field for three of the particles. Note that the charging times for the smallest aluminum particle in Figure 2.23 could not be measured.

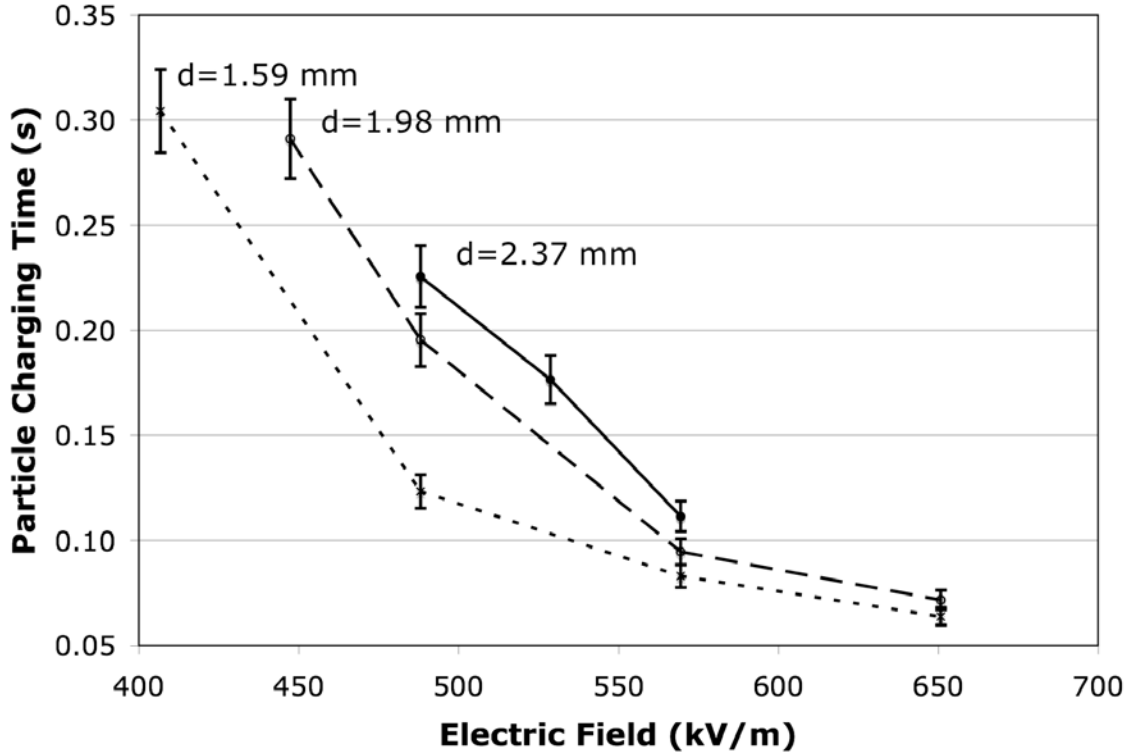


Figure 2.25: Spherical aluminum particle charging times. Particle oscillation in 50 cSt silicone oil between 6.15 mm spaced electrodes.

According to Figure 2.25, the particle charging times for the aluminum spheres decreases as the applied electric field increases and increases as the particle size increases. If the aluminum particles are lifted from the charging electrode before becoming fully charged, the particle charging time constant, τ_p , can be approximated from the measured charge, q_m , the expected charge, q_o , and the charging time, t .

$$q_m(t) = q_o \left(1 - e^{-t/\tau_p} \right) \quad (2.41)$$

The calculated particle charging time constants for the three diameters of aluminum particles are plotted in Figure 2.26. Also included in the plot is a linear fit of the data points.

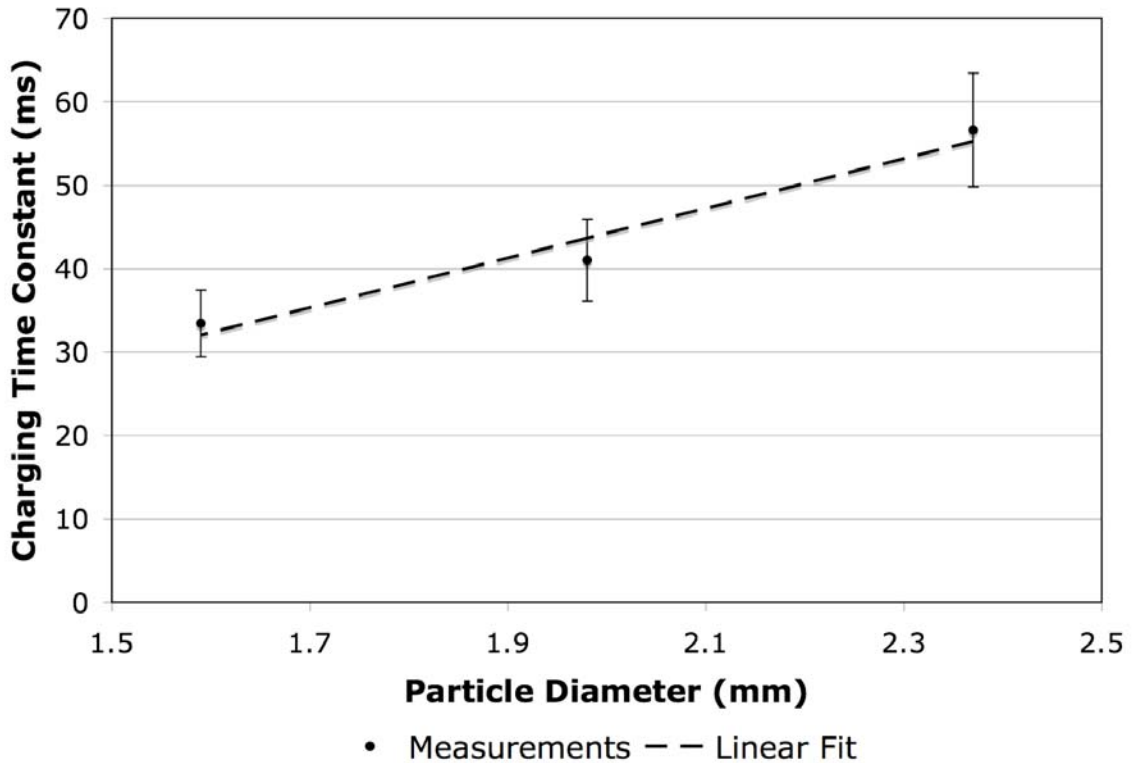


Figure 2.26: Measured particle charging time constants for aluminum spheres.

Figure 2.26 suggests that the charging time constants for aluminum spherical particles increase with the particle diameter for the particle sizes presented. In addition, it may take tenths of a second to charge spherical aluminum particles to their maximum capacity. The relatively large charging time constant is most likely a result of a poor electrical contact between the particle and the electrode surface. The following section develops a model for the particle charging time constant.

2.5.2. Theoretical Particle Charging Time Constant

This section develops a model for the particle charging time constant. It assumes that the insulating oxide layer that forms on the surface of most metals and the small contact

area between the spherical particle and the electrode are the sources of the poor electrical contact, which results in the large charging time constants. Figure 2.27 illustrates a possible simple RC circuit model of a spherical particle with an insulating oxide layer and in contact with an electrode.

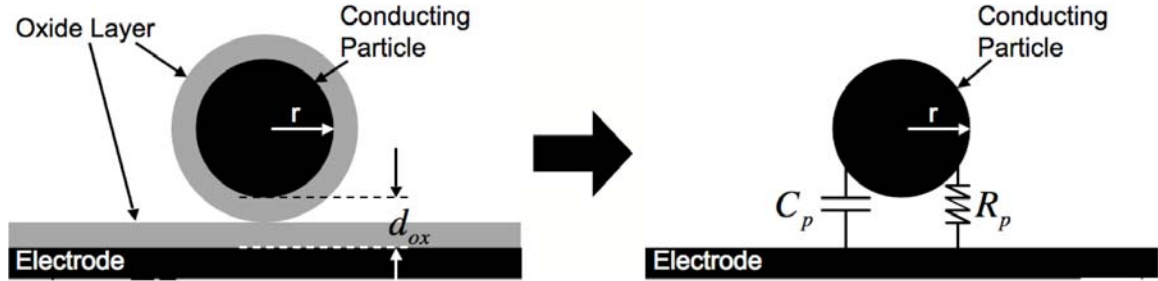


Figure 2.27: A spherical particle in contact with a planar electrode is modeled as an RC circuit.

The value of the capacitance, C_p , is approximated as the capacitance between the spherical particle and infinite planar electrode when assuming that the oxide layer thickness is much smaller than the particle.³⁸

$$C_p \approx 4\pi\epsilon r \left(1 + \alpha_p + \frac{\alpha_p^2}{1 - \alpha_p^2} \right) \quad (2.42)$$

The constant α_p is dependent on the particle size and the separation between the electrode and the particle, which is regulated by the thickness of the oxide layers, which is dependent on the oxide conductivity, σ_{ox} , and the contact area, A_p .

$$\alpha_p = \frac{r}{2(r + d_{ox})} \quad (2.43)$$

The particle charging resistance, R_p , is approximated as the resistance through the physical contact between the electrode and particle.

$$R_p \approx \frac{d_{ox}}{\sigma_{ox} A_p} \quad (2.44)$$

Combining Equations (2.42) and (2.44) gives the theoretical particle charging time constant.

$$\tau_p \approx R_p C_p \approx \left(\frac{4\pi\epsilon r d_{ox}}{\sigma_{ox} A_p} \right) \left(1 + \alpha_p + \frac{\alpha_p^2}{1 - \alpha_p^2} \right) \quad (2.45)$$

Using the approximation that the oxide layers are much smaller than the particle diameter, the particle charging time constant is simplified and approximated.

$$\tau_p \approx \frac{8\pi\epsilon r d_{ox}}{\sigma_{ox} A_p} \quad (2.46)$$

Equation (2.46) suggests that the particle charging time constant is directly proportional to the particle size, which agrees with the measured particle charging time constants plotted in Figure 2.26 as shown by the linear fit. The variables in Equation (2.46) are known for many materials except the contact area, which is difficult to determine and depends on factors such as the particle and electrode surface roughness and the deformation of the particle and electrode. The theoretical investigation of the contact area is beyond the scope of this chapter, but is briefly discussed in Chapter 5. The oxide layer that forms on the surface of aluminum when exposed to the atmosphere, Al_2O_3 , is a

very good insulator with a conductivity of approximately 10^{-12} S/m,³⁹ and a typical thickness of approximately 4 nm.⁴⁰ Note that most metals form thin oxides layers with thickness typically on the order of a few nanometers, thus justifying the thin approximation for the particle sizes greater than tens of nanometers.

Even though theoretically evaluating the contact area is beyond the scope of this chapter, it can be predicted using Equation (2.46) and the data from Figure 2.26. The predicted contact areas of the three particle diameters are listed in Table 2.2 and are approximately equal. The predicted contact area ranges from about 0.4% to 1.0% of the maximum cross-sectional areas of the particles ($A_{\max} = \pi r^2$).

Particle Dia. (mm)	Approximate Contact Area (mm ²)	Percent of Maximum Cross Sectional Area (%)
1.59	0.02	1.0
1.98	0.02	0.7
2.37	0.02	0.4

Table 2.2: Predicted electrical contact area between spherical aluminum particles and the electrode

The expression for the particle charging time constant in Equation (2.46) may provide an explanation why only the aluminum spherical particles were not charged completely, yet the titanium spherical particles and aluminum cylindrical particles appear to have charged completely. For comparison, titanium does form a layer of titanium dioxide, TiO₂, on its surface when exposed to the atmosphere.⁴¹ But, titanium dioxide has a conductivity of approximately two orders of magnitude greater than aluminum oxide (10^{-10} S/m),⁴² which indicates that the particle charging time constant of a titanium particle may be two orders of magnitude less than the charging time constant of an aluminum particle when keeping all other variables constant. The higher conductivity of titanium dioxide may be the reason that the titanium particle in Figure 2.22 is fully charged

according to Equation (2.11) for all applied electric fields. Additionally, the contact area between the aluminum cylindrical particles and the electrode is expected to be equal to the cross sectional area of the particle, 0.07 mm^2 , which is almost four times greater than the evaluated contact area between the aluminum spherical particles and the electrode. The greater contact area between the aluminum cylindrical particles and the electrode may be the reason that the cylinders in Figure 2.24 are fully charged according to Equation (2.19) for all applied electric fields.

The evaluation of the electrical contact between the particles and the electrode presented in this section suggests that the oxide layer on metallic surfaces and the small contact area between a particle and the planar electrode may lead to an increase in particle charging time constants, which increases the time required to fully charge particles.

2.6. Effects of Particle Charging on Micro- and Nano-Particle Thrusters

The results from the experimental section indicate that spherical and cylindrical conducting particles are charged as predicted when using high strength electric fields as long as they remain in contact with the electrode much longer than the charging time constant. This result does impact the ability to use micro- and nano-particles as propellant for an electrostatic thruster because it is important that all of the particles are charged to the same state. Therefore, a good electrical contact between the particles and the electrode needs to be established, which means that the particles and electrode may need to be made from highly oxidation resistant materials, such as gold or platinum.^{43,44} Future experiments need to confirm the validity of the particle charging models and the

particle charging time constants as the particle size decreases down to the micron and nanometer ranges.

2.7. Conclusion

A method of charging spherical and cylindrical conducting particles against a source electrode with an applied electric field was investigated for use with micro- and nano-particle thrusters. The models suggest that the attainable charge-to-mass ratios of both spherical and cylindrical particles are increased when the particle diameters are decreased. Further, the charge-to-mass ratio of a spherical particle is greater than the charge-to-mass ratio of a cylindrical particle when keeping the maximum focused electric field constant. In addition, it may be possible to increase the charge on a spherical particle by charging it on a high aspect ratio charging post.

To investigate the particle charging models, various particle shapes, sizes, and materials were studied. The tests agreed reasonably well with the models when the particles remained in contact with the source electrode much longer than the particle charging time constants. But, the charge acquired by the spherical aluminum particles was less than predicted when the particles were removed from the source electrode faster than required by the particle charging time model. It is possible that the aluminum particles were not charged as predicted due to a limited electrical contact, which may result from the oxide layer coating the surfaces and the small contact area between the particle and the electrode.

Using micro- and nano-particles charged electrostatically by high strength electric fields still appears feasible from the charging standpoint, but charging time issues were made apparent.

Chapter 3

Liquid Surface Instability Initiated by an Applied High Strength Electric Field

3.1. Introduction

A potential limiting factor of the conducting and insulating liquid design configurations for use with micro- and nano-particle thrusters is the tendency of a liquid surface to become unstable when subjected to high strength electric fields. It is possible that a liquid instability may affect the extraction of the charged particle propellant, coat various components of the thruster with the liquid, or emit charged liquid droplets, all of which may degrade the thruster performance and possibly the lifetime. Therefore, it is desirable to operate micro- and nano-particle thrusters in a regime that does not induce any instabilities. This chapter investigates the initiation of the liquid instability caused solely due to an electric field and presents a derivation of the threshold electric field required to induce the instability in both earth-gravity and zero-gravity environments. A method to suppress and control the liquid instability is discussed as well as the time required to induce the instability. Experimental results of inducing a liquid surface instability on both insulating and conducting liquids in an earth-gravity environment is presented and compared to the theoretical predictions.

3.2. Liquid Instability Theory

This section presents the theory of the liquid surface instability initiated by an applied high strength electric field and derives the minimum electric field required to induce the instability for the earth-gravity and zero-gravity cases. Further, a method to suppress the liquid instability is presented along with the time required to induce the instability.

The model for the liquid surface instability induced by an applied electric field is shown in Figure 3.1, and consists of two infinite parallel electrodes. The electrode gap is partially filled with a liquid medium and the remaining volume is vacuum. An electric potential bias, V , is applied across the electrodes to generate an electric field within the gap, E_{liq} .

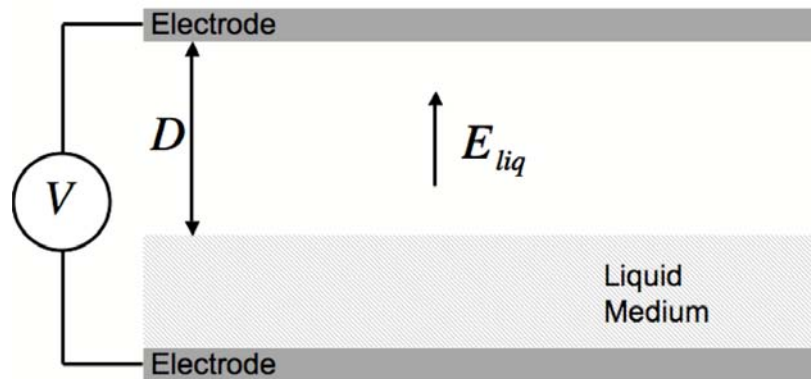


Figure 3.1: Model for liquid surface instability induced by an applied electric field.

Assuming that the liquid has a finite conductivity greater than the vacuum region, free charge within the liquid medium ultimately migrates to the liquid surface until the electric field strength within the liquid is equal to zero. The time required for this to happen will depend on the conductivity of the liquid. The electric field strength in the vacuum gap is then only dependent on the applied voltage and the separation between the upper electrode and the liquid surface.²⁷

$$E_{liq} = \frac{V}{D} \quad (3.1)$$

The instability of the liquid is a result of the electric field acting non-uniformly on the charged surface, which may occur due to small perturbations on the surface. A perturbation on the surface may lead to a locally intensified electric field and sufficiently strong electric force capable of deforming the surface into the shape of a cone, termed a Taylor cone.^{45,46,47} With the appropriate conditions, either charged liquid droplets or ions are ripped from the tip of the Taylor cone and accelerated to the upper electrode.^{48,49}

The following subsections investigate the minimum electric field required to initiate the liquid instability.

3.2.1. Instability Threshold Electric Field in an Earth-Gravity Environment on an Infinite Liquid Surface

The perturbation on a liquid surface that may lead to an instability can be the result of mechanical, thermal, or any other source capable of perturbing the liquid. Tonks⁵⁰ used the simplified model of the liquid perturbation phenomenon shown in Figure 3.2. The perturbation is represented as a spherical hump protruding slightly above the plane containing the unperturbed surface. This analysis assumes an incompressible liquid.

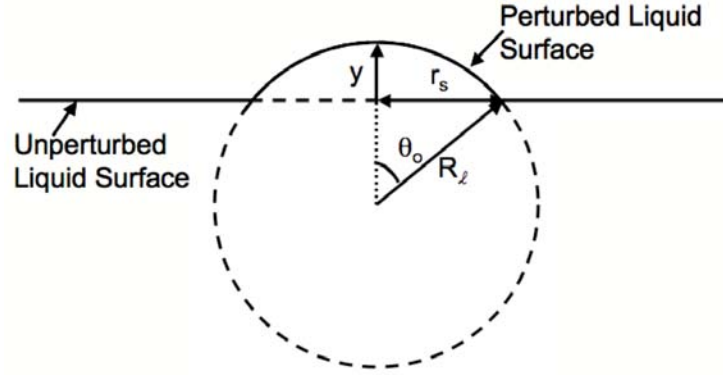


Figure 3.2: Model of the liquid perturbation.

The radius of the sphere, R_ℓ , is related to the perturbation radius in the plane containing the unperturbed surface, r_s , and the height of the hump above the same plane, y .

$$R_\ell = \frac{r_s^2 + y^2}{2y} \quad (3.2)$$

$$\sin \theta_o = \frac{r_s}{R_\ell} \quad (3.3)$$

Four forces act on the charged liquid surface: the electric force acting on the perturbation, F_{ep} , the electric force acting on the unperturbed liquid surface, F_{eu} , the gravitational force, F_g , and the surface tension force, F_s .⁵⁰

The most complex and difficult force to approximate is the electric force acting on the liquid perturbation, which directly pulls on the liquid hump to initiate the instability, and is the product of the liquid's surface charge density with the electric field at the liquid surface and integrated over the perturbation.

$$\bar{F}_{ep} = \frac{1}{2} \iint \rho_{s,p} \bar{E}_{liq,p} dA \quad (3.4)$$

Due to the symmetry about ϕ , the surface charge density and the electric field at the surface of the perturbation are functions of θ . In addition, the net force on the perturbation is only in the vertical direction, $F_{ep,z}$.

$$F_{ep,z} = F_{ep} = \frac{1}{2} \iint \rho_{s,p}(\theta, y) E_{liq,p,z}(\theta, y) dA \quad (3.5)$$

The surface charge density is dependent on the electric field normal to the perturbation surface and the permittivity of the vacuum region.

$$\rho_{s,p}(\theta, y) = \epsilon_o E_{liq,p}(\theta, y) \quad (3.6)$$

The vertical component of the electric field at the surface of the perturbation is easily calculated for the given geometry.

$$E_{liq,p,z}(\theta, y) = E_{liq,p}(\theta, y) \cos(\theta) \quad (3.7)$$

The electric field at the surface of the perturbation is a function of the electric field in the vacuum region, E_{liq} , and a field-focusing factor that is dependent on the geometry of the perturbation, $\alpha_{liq}(\theta, y)$.

$$E_{liq,p}(\theta, y) = E_{liq} \alpha_{liq}(\theta, y) \quad (3.8)$$

Equations (3.6), (3.7), and (3.8), are substituted into Equation (3.5).

$$F_{ep} = \frac{1}{2} \int_0^{2\pi} \int_0^{\theta_o} \epsilon_o E_{liq}^2 \alpha_{liq}(\theta, y)^2 \cos(\theta) R_\ell^2 \sin(\theta) d\theta d\phi \quad (3.9)$$

Equation (3.9) is simplified by leaving only the θ dependent functions inside the integral.

$$F_{ep} = \pi R_\ell^2 \epsilon_o E_{liq}^2 \int_0^{\theta_o} \alpha_{liq}(\theta, y)^2 \cos(\theta) \sin(\theta) d\theta \quad (3.10)$$

Before solving the integral, $\alpha_{liq}(\theta, y)$ is examined using COMSOLTM, a multi-physics simulation environment, to simulate the electric field at the surface of a perturbation when subjected to a uniform background electric field, shown by the model in Figure 3.3. Note this is an extension to the simulations presented in Chapter 2.

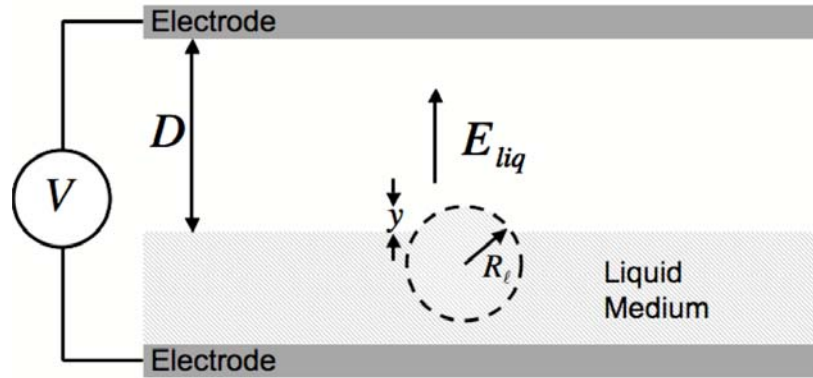


Figure 3.3: Model for liquid surface instability induced by an applied electric field.

The simulation was created in 2-dimensions with axial symmetry. The width of the simulation environment was set to 10 times the electrode gap to eliminate field screening due to edge effects.²⁸ The field focusing term, $\alpha_{liq}(\theta, y)$, was evaluated for θ ranging from

0° to θ_0 for several perturbation heights and is plotted in Figure 3.4. θ_0 is the angle where the perturbation intersects with the unperturbed surface.

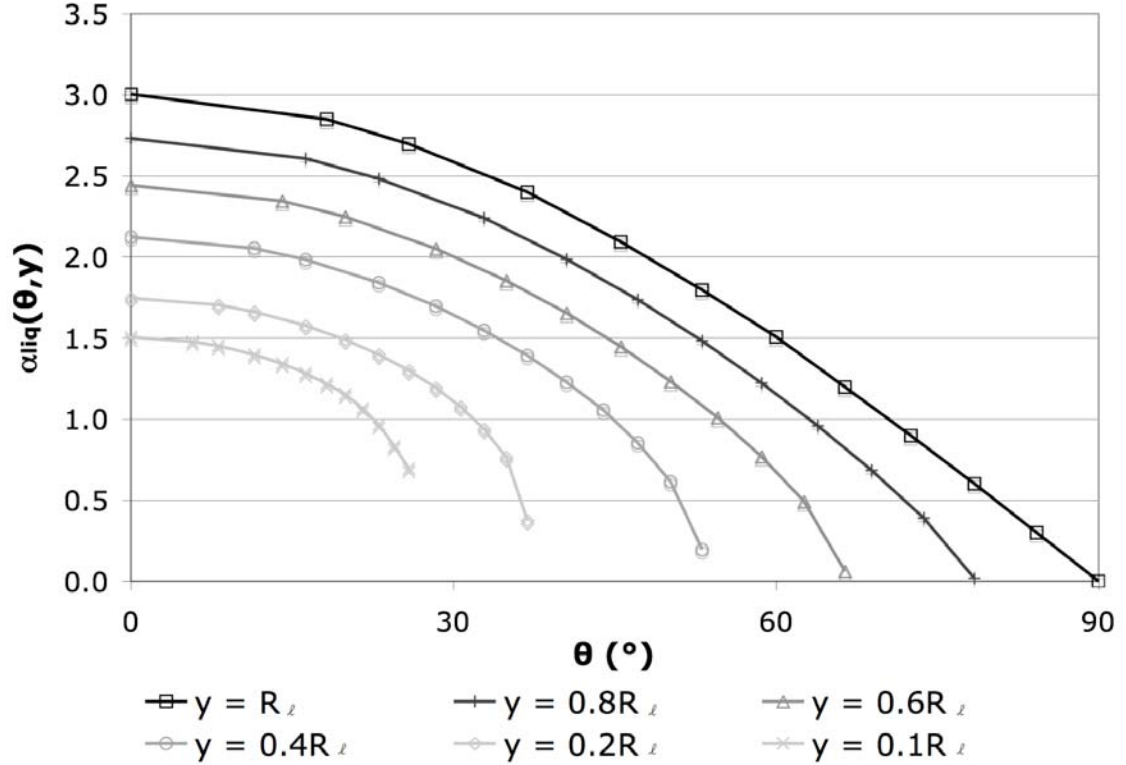


Figure 3.4: Plot of $\alpha_{liq}(\theta, y)$ as a function of θ for several values of y .

Figure 3.4 shows that regardless of the perturbation height, the electric field at the surface of the perturbation is maximum at the top of the perturbation ($\theta=0^\circ$) and is minimum at $\theta = \theta_0$. Due to complexity of the field-focusing factor and its dependence on both the perturbation height and θ , Equation (3.10) is approximated by replacing $\alpha_{liq}(\theta, y)$ with its average value over the entire perturbation surface, which is only a function of the perturbation height.

$$\alpha_{liq,avg}(y) = \frac{\int_0^{2\pi} \int_0^{\theta_o} \alpha_{liq}(\theta, y) R_\ell^2 \sin\theta d\theta d\phi}{\int_0^{2\pi} \int_0^{\theta_o} R_\ell^2 \sin\theta d\theta d\phi} \quad (3.11)$$

Using the simulated data from Figure 3.4, the average field-focusing factor on the liquid perturbation is independent of θ and can be approximated as a linear function of the ratio of the perturbation height to the radius for $0 < y < R_\ell$.⁵⁰

$$\alpha_{liq,avg}(y) \approx 1 + \frac{2y}{r_s} \quad (3.12)$$

The electric force on the liquid perturbation is simplified by substituting in Equation (3.12).

$$F_{ep} \approx \pi R_\ell^2 \epsilon_o E_{liq}^2 \alpha_{liq,avg}(y)^2 \int_0^{\theta_o} \cos(\theta) \sin(\theta) d\theta \quad (3.13)$$

The integral is now easily solved, and the electric force on the liquid perturbation is simplified.

$$F_{ep} \approx \frac{1}{2} \pi \epsilon_o E_{liq}^2 (r_s + 2y)^2 \quad (3.14)$$

The electric force on the unperturbed surface transfers a force to the perturbation, which resists the initiation of the instability. According to Tonks, the electric force transferred to the perturbation from the electric force on the unperturbed liquid surface,

F_{eu} , is a function of the electric field in the vacuum region, the charge density of the unperturbed surface, and the cross-sectional area of the perturbation.⁵⁰

$$F_{eu} \approx \frac{1}{2} \rho_s E_{liq} A \approx \frac{1}{2} \epsilon_o E_{liq}^2 \pi r_s^2 \quad (3.15)$$

The surface tension force depends on the surface tension of the liquid, γ , the radius of curvature of the liquid perturbation and the exposed cross-sectional area of the liquid perturbation.⁵¹

$$F_s = \frac{2\gamma A}{R_\ell} = \frac{4\gamma\pi r_s^2 y}{r_s^2 + y^2} \quad (3.16)$$

The gravitational force acting on the perturbation is simply the weight of the liquid above the plane that contains the liquid surface and is calculated using simple geometry.

$$F_g = \left(\frac{\pi \rho_\ell g}{6} \right) (3r_s^2 y + y^3) \quad (3.17)$$

The threshold electric field required to initiate an instability on an infinite liquid surface in an earth-gravity environment is determined by combining Equations (3.14), (3.15), (3.16), and (3.17).

$$E_{liq,thresh} \approx \sqrt{\frac{\frac{2\gamma r_s^2}{r_s^2 + y^2} + \frac{\rho_\ell g}{12} (3r_s^2 + y^2)}{\epsilon_o (r_s + y)}} \quad (3.18)$$

Assuming that the perturbation height is small compared to its radius, Equation (3.18) simplifies with the assumption that $y \ll r_s$.⁵⁰

$$E_{liq,thresh} \approx \sqrt{\frac{2\gamma}{\epsilon_o r_s} + \frac{\rho_l g r_s}{4\epsilon_o}} \quad (3.19)$$

It is important to note that the threshold electric field required to initiate an instability is a function of the perturbation radius and has two terms: the surface tension term and the gravitational term. The surface tension term scales inversely with the square root of the perturbation radius, while the gravitational term scales directly with the square root of the perturbation radius. This implies that the threshold electric field increases as r_s increases in the gravitational regime and increases as r_s decreases in the surface tension regime. Therefore, there exists a value for r_s between the two regimes that gives rise to the minimum threshold electric field required to initiate the instability on an infinite liquid surface. The threshold value of r_s is calculated from Equation (3.19).

$$r_s \approx \sqrt{\frac{8\gamma}{\rho_l g}} \quad (3.20)$$

The minimum threshold electric field required to initiate an instability on an infinite liquid surface is determined by substituting Equation (3.20) into Equation (3.19).

$$E_{liq,thresh} \approx \left(\frac{2\gamma\rho_l g}{\epsilon_o^2} \right)^{1/4} \quad (3.21)$$

The threshold electric field required to initiate the instability on the liquid surface is directly proportional the fourth root of the liquid surface tension and density, which indicates that the threshold electric field is larger for liquids with a higher surface tension and density. It should be noted that the expression derived here scales the same as Tonks’s model, but differs slightly in value. The difference is a result of using a different assumption when calculating the gravitational force acting on the perturbed surface. Tonks determined the gravitational force acting on the liquid perturbation by approximating the perturbation as a cylinder with height y and radius r . The derivation presented here determined the gravitational force by calculating the volume and mass of the perturbation with its shape given by Figure 3.2.

Table 3.1 lists the room temperature densities and surface tensions of many liquids. In addition, the table lists the predicted threshold electric fields required to initiate the instability on an infinite liquid surface for many liquids along with the corresponding perturbation radii.

Liquid Name	Density (kg/m ³)	Surface Tension (N/m)	Predicted Threshold Electric Field (MV/m)	Tonks Predictions (MV/m)	r_s (mm)	References Density / Surface Tension
Acetone	785	0.023	1.5	1.8	4.9	[52] / [53]
Corn Oil	923	0.033	1.7	2.0	5.4	[57] / [58]
Distilled Water	1,000	0.073	2.1	2.5	7.7	[54] / [54]
Ethanol	789	0.022	1.4	1.7	4.8	[52] / [55]
Formamide	1,130	0.057	2.0	2.4	6.4	[52] / [56]
Hydrazine	795	0.066	1.9	2.3	8.3	[52] / [53]
Mercury	13,550	0.485	6.4	7.6	5.4	[52] / [54]
Methanol	791	0.022	1.4	1.7	4.8	[52] / [53]
Peanut Oil	916	0.036	1.7	2.0	5.6	[57] / [58]
Propanol	804	0.023	1.5	1.8	4.9	[52] / [53]
Silicone Oil	965	0.021	1.5	1.8	4.2	[33] / [33]

Table 3.1: Theoretical threshold electric field strengths required to initiate an instability on various liquid surfaces and the corresponding perturbation radii.

According to Table 3.1, most liquid surfaces in an earth-gravity environment become unstable when subjected to an electric field strength on the order of a couple megavolts per meter, and the corresponding perturbation radii are on the order of several millimeters.

Note that a liquid's surface tension is typically inversely related to the surface temperature. For example, the temperature coefficient of surface tension, γ_T , for silicone oil has been reported to be -0.069 mN/m-K and -0.036 mN/m-K by Basu⁵⁹ and -0.072 mN/m-K by Ohta.⁶⁰ Using these values of temperature coefficients, Figure 3.5 plots the predicted surface tension of silicone oil as a function of temperature.

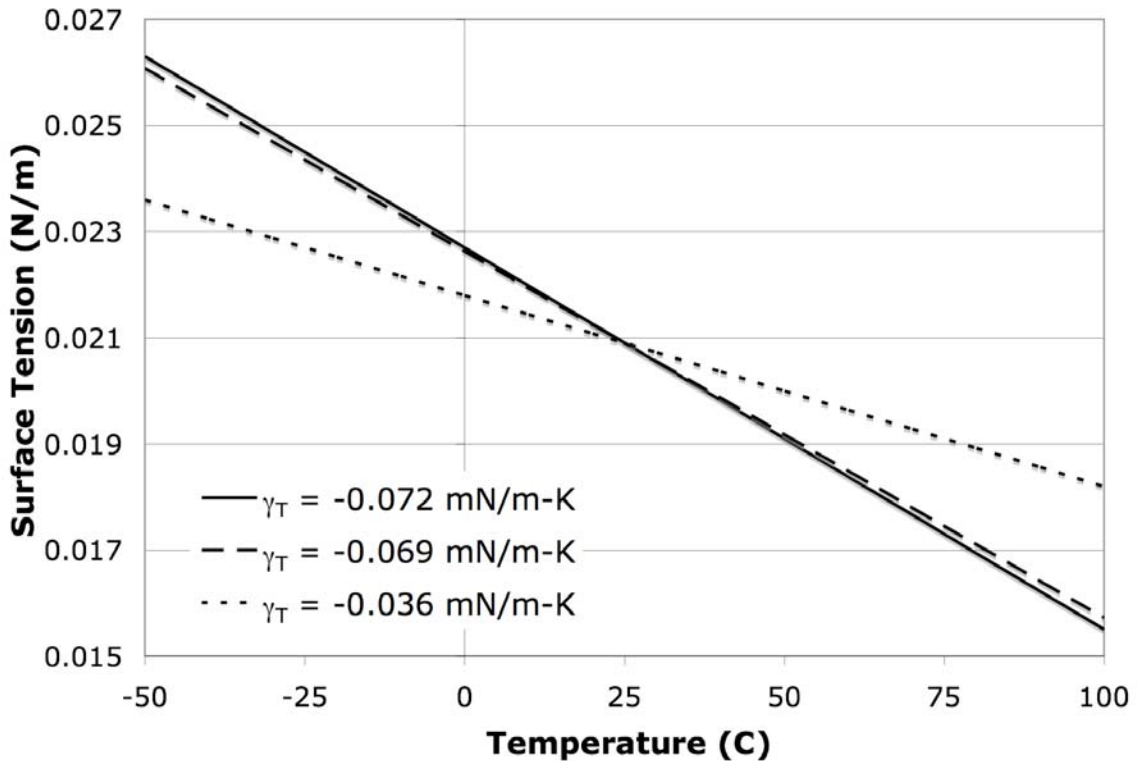


Figure 3.5: The predicted surface tension of silicone oil as a function of its temperature.

Figure 3.5 suggests that temperature has a large effect on the surface tension of silicone oil. This suggests that the threshold electric field required to induce a liquid instability will also be a function of temperature and will need to be addressed for a flight ready system. The remainder of this thesis will assume that all operations are at room temperature.

3.2.2. Instability Threshold Electric Field in a Zero-Gravity Environment

An instability can form on the surface of a liquid in a zero-gravity environment just as it does in an earth-gravity environment when subjected to an electric field. The derivation for the threshold electric field in the zero-gravity case follows the derivation presented in Section 3.2.1 closely with the exclusion of the gravitational force, and is easily determined from Equation (3.19) by setting g equal to zero.

$$E_{liq,thresh} \approx \sqrt{\frac{2\gamma}{\epsilon_o r_s}} \quad (3.22)$$

Note that the threshold electric field strength scales inversely with the square root of r_s , and there does not exist a minimum threshold value that corresponds to a finite perturbation radius, as in the earth-gravity case. This suggests that the liquid will become unstable when subjected to very small electric field strengths and the perturbation will be very large, unless it is controlled.

3.2.3. Suppressing the Liquid Instability

It has been shown by many researchers that liquids can be contained in open-ended reservoirs by way of a method that utilizes a knife-edge orifice to trap the liquids.^{61,62}

Figure 3.6 depicts a model of a knife-edge that may be capable of suppressing the liquid instability. It consists of a thin cover over the liquid surface with a small orifice. The orifice is machined so that the surface against the liquid is recessed, which creates a pressure barrier. The physics of the knife-edge orifice is beyond the scope of this thesis, and it is only presented as a method of controlling the liquid instability.

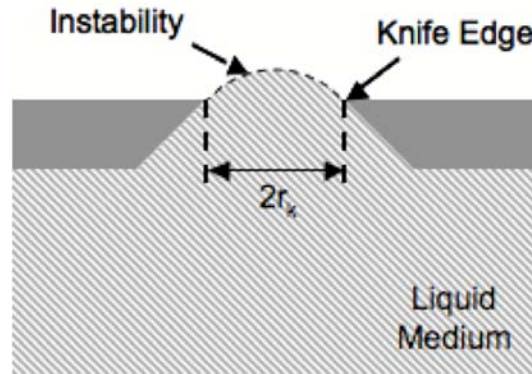


Figure 3.6: Model for suppressing the liquid surface instability with a knife-edge orifice.^{61,62}

To understand the effects of the knife-edge orifice on the threshold electric field required to initiate the instability, recall from Equation (3.19) that the threshold field is a function of the perturbation radius, r_s . When in an earth-gravity environment, Section 3.2.1 demonstrated that the minimum threshold electric field occurs at an optimum value of r_s , which is generally on the order of several millimeters. But, it is possible to control the value of r_s with the knife-edge orifice when the radius of the orifice, r_k , is less than the optimum perturbation radius. This analysis assumes that the perturbation radius is equal to the orifice radius when r_k is less than or equal to the optimum radius. Note that it is

possible that the perturbation radius may be less than the orifice radius depending on the mode of the perturbation.^{62,63}

$$\begin{aligned}
 E_{liq,thresh} &\approx \sqrt{\frac{2\gamma}{\epsilon_o r_k} + \frac{\rho_\ell g r_k}{4\epsilon_o}} & \text{when } r_k < \sqrt{\frac{8\gamma}{g\rho_\ell}} \\
 E_{liq,thresh} &= \left(\frac{2\gamma\rho_\ell g}{\epsilon_o^2}\right)^{1/4} & \text{when } r_k > \sqrt{\frac{8\gamma}{g\rho_\ell}}
 \end{aligned}
 \tag{3.23}$$

Figure 3.7 plots the expected threshold electric fields required to initiate the instability as a function of the knife-edge radius for several liquids listed in Table 3.1 in an earth-gravity environment.

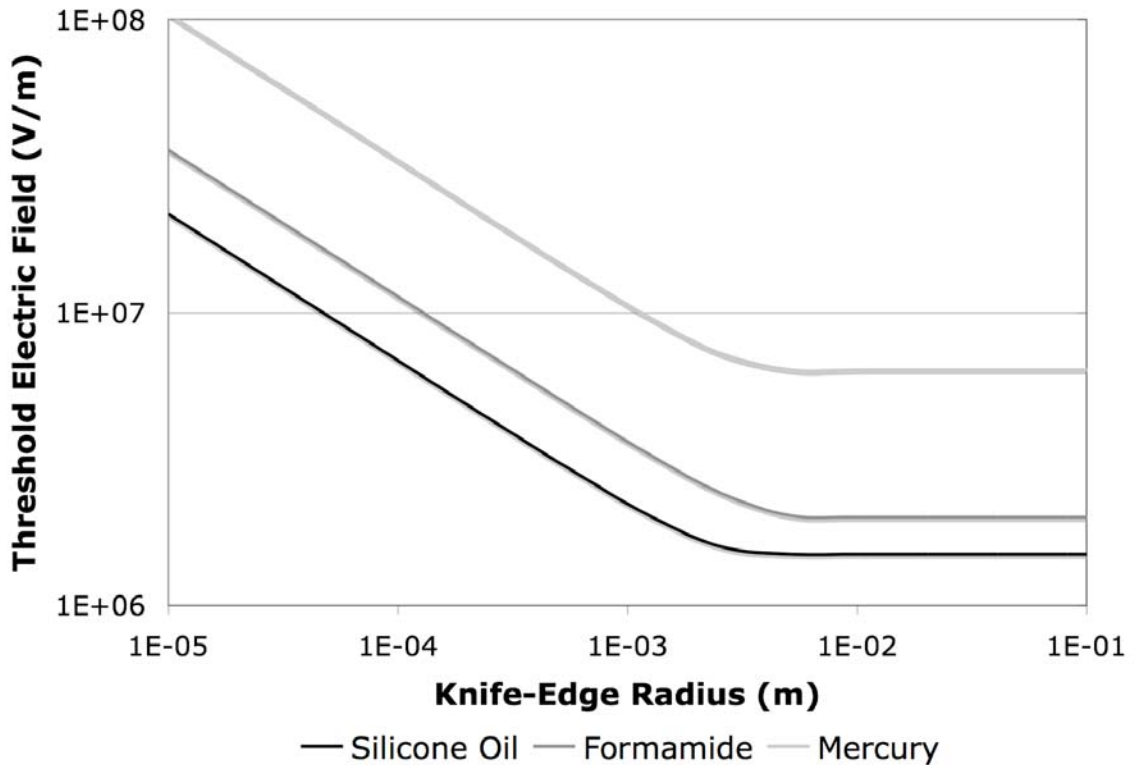


Figure 3.7: Plot of the threshold electric field required to initiate a liquid instability when using a knife-edge orifice in an earth-gravity environment.

It is also possible to utilize the knife-edge orifice in a zero-gravity environment to control the liquid instability. Recall from Section 3.2.2 that even a very small applied electric field may be able to induce an instability, which corresponds to a very large perturbation radius as described by Equation (3.22). When using a knife-edge orifice in zero-gravity, the perturbation radius is set equal to the knife-edge radius for all values. Figure 3.8 plots the expected threshold electric fields required to initiate the instability as a function of the knife-edge radius for several liquids listed in Table 3.1 in a zero-gravity environment.

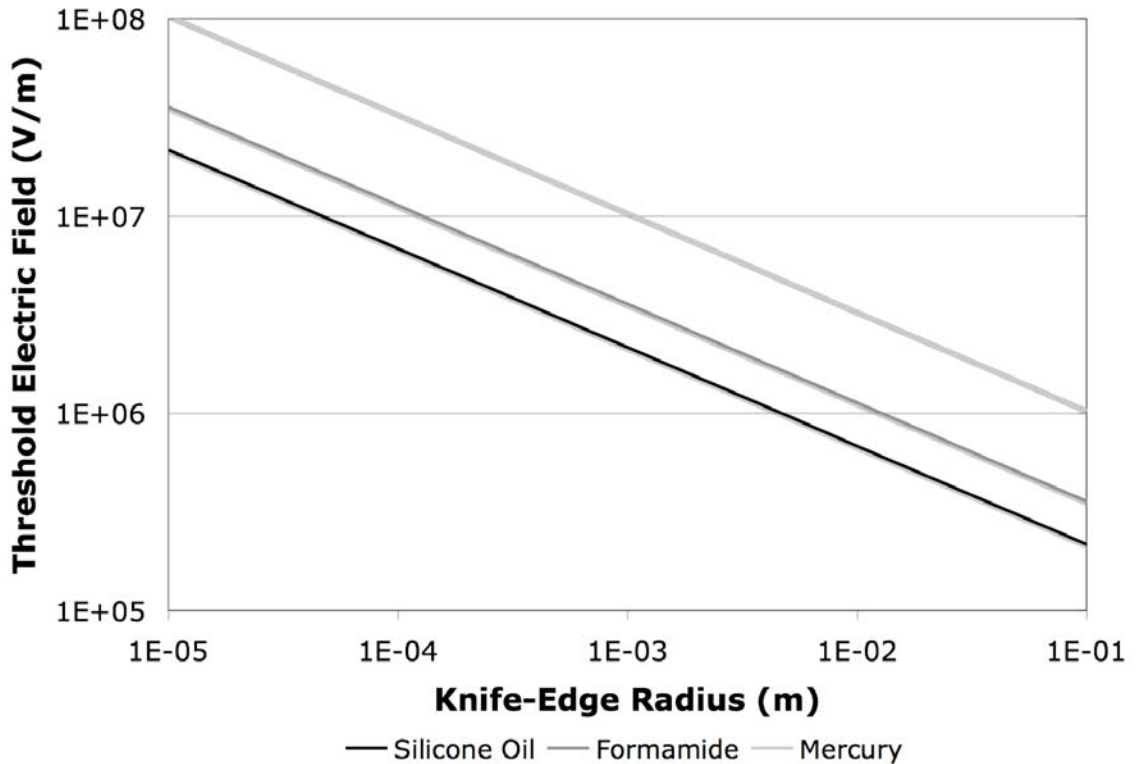


Figure 3.8: Plot of the threshold electric field required to initiate a liquid instability when using a knife-edge orifice in a zero-gravity environment.

3.2.4. Time Required to Induce the Liquid Instability

It is important to note that the threshold electric fields presented in the previous sections are not functions of the liquid conductivity. But, the time required for the liquid instability to occur after generating the electric fields is a function of the conductivity. The derivations of the threshold electric field assume that the liquid surface is sufficiently charged so that the electric field within the liquid is zero. The surface charge density of the liquid is a function of the elapsed time after generating the electric fields and the liquid's charging time constant.

$$\rho_s(t) = \rho_s(t \rightarrow \infty) \left[1 - \exp\left(-t/\tau_\ell\right) \right] \quad (3.24)$$

The liquid's charging time constant is a function of the conductivity and permittivity.

$$\tau_\ell = \epsilon_\ell / \sigma_\ell \quad (3.25)$$

Equation (3.24) illustrates that after a time of approximately five charging time constants, the liquid surface is charged to approximately 99% of its final value, which provides insight to the time required to initiate the instability. Table 3.2 lists the charging time constants of various liquids.

Liquid Name	Conductivity (S/m)	Relative Dielectric Constant	Charging Time Constant (s)	References Conductivity / Permittivity
Distilled Water	10^{-3}	80	$7*10^{-5}$	[64] / [65]
Mercury	10^6	NA	$< 10^{-17}$	[66]
Silicone Oil	10^{-13}	1.97	170	[33] / [34]

Table 3.2: Theoretical charging time constants for a few liquids.

Table 3.2 suggests that the time required to initiate the liquid instability may vary significantly from almost instantly to minutes depending on the liquid conductivity.

3.3. Experimental Setup

To experimentally investigate the threshold electric field required to initiate the instability on an infinite liquid surface in an earth-gravity environment, the system depicted in Figure 3.1 was constructed with 10 cm stainless steel electrodes in a liquid tight acrylic container. Note that the experiment is performed in atmosphere, not vacuum.

The main goal of the experiment is to measure the minimum electric field required to induce the instability on an infinite surface using various liquids, and is performed by partially filling the electrode gap with the desired liquid. Next, the upper electrode is secured in place to provide the correct uniform electrode gap, which is regulated by an insulating spacer to range from approximately 6 mm to 18 mm. Note that the exposed liquid surface is approximately two orders of magnitude larger than the expected perturbation radius, which allows the surface to be approximated as infinite. The electric potential between the electrodes is applied to generate the electric field and is increased slowly while visually monitoring the liquid surface for the instability. Note that the electric field is increased at a slow enough rate $\left(< \frac{1}{3\tau_\ell} \right)$ to ensure the liquid surface reaches its equilibrium charge density, which occurs when the electric field strength in the liquid is zero. Finally, the procedure is repeated for various liquid heights and electrode gaps to ensure that the experiment is repeatable.

The experiment was performed using silicone oil, corn oil, and peanut oil. The properties of each liquid are listed in Table 3.1 and Table 3.2.

3.4. Experimental Results

Figure 3.9 is a series of frames from the high speed camera showing the process of an instability forming on the surface of 100 cSt silicone oil when subjected to an electric field strength of approximately 1.7 MV/m. Frame (a) shows the unperturbed liquid surface just before the liquid becomes unstable. The liquid surface begins to deform under the force from the applied electric field as shown in frame (b). Due to field-focusing, the perturbation grows in frame (c). Frame (d) shows the evolution of the instability as the small perturbation evolves into a Taylor cone. Finally, the surface tension is broken and liquid droplets are accelerated away from the liquid surface in frame (e).

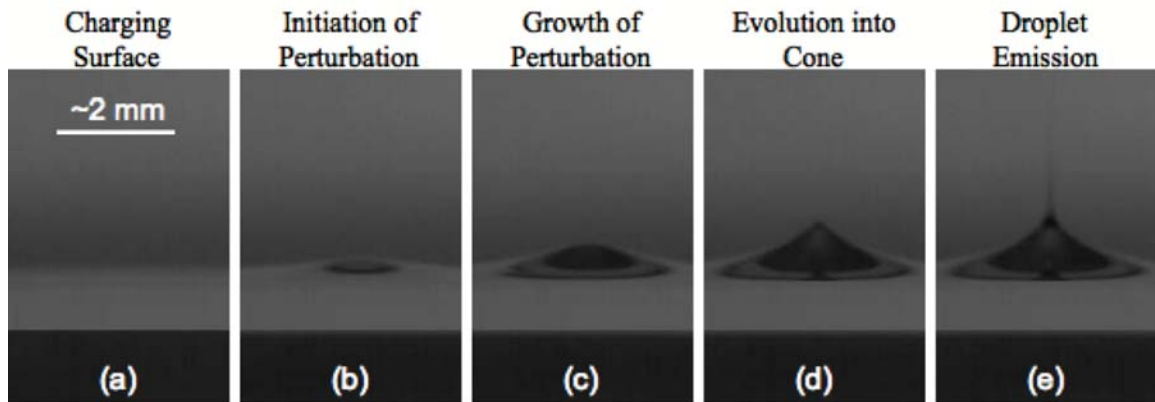


Figure 3.9: Series of frames showing the process of an instability forming on the surface of 100 cSt silicone oil using an applied electric field of approximately 1.7 MV/m.

Table 3.3 lists the measured minimum electric fields required to initiate the instability on the surface of various liquids. Also included in the table are the theoretical predicted field strengths. There is an estimated total error of approximately 10% in the

measurements, which was determined with the sum of squares method. The error in the electric field is due mostly to three error terms in the experimental setup. These error terms are as follows: the liquid height (8.5%), the electrode gap separation (4%), and the applied voltage (0.3%).

Liquid Name	Measured Threshold Electric Field (MV/m)	Predicted Threshold Electric Field (MV/m)	Tonks's Threshold Electric Field (MV/m)
Corn Oil	1.61 ± 0.18	1.7	2.0
Peanut Oil	1.58 ± 0.17	1.7	2.0
Silicone Oil	1.66 ± 0.18	1.5	1.8

Table 3.3: Measured and predicted threshold electric field strengths required to initiate an instability on various liquid surfaces.

The experimental results listed in Table 3.3 suggest that the liquid instabilities occurred in the appropriate range predicted by the model.

3.5. Conclusion

The effects of a liquid instability on the performance of micro- and nano-particle thrusters when using either the insulating or conducting liquid design configuration is beyond the scope of this chapter, but is presented in Chapter 4.

The initiation of an instability on a liquid surface by way of an applied high strength electric field was investigated in both earth-gravity and zero-gravity environments. In addition, a method to suppress and control the liquid instability and the time required for the instability to form were presented. Experimental results of inducing a liquid surface instability on various liquid surfaces in an earth-gravity environment agreed with the

theoretical predictions. It was also noted that the temperature may effect the surface tension of liquids, which can change the required threshold electric fields.

Chapter 4

Extraction of Spherical and Cylindrical Particles From an Insulating Liquid

4.1. Introduction

A critical issue associated with the insulating liquid design configuration for use with micro- and nano-particle thrusters is the ability to extract the charged micro- and nano-particle propellant through the liquid surface. This chapter investigates the process of charged particle extraction by way of an applied high strength electric field and derives the electric field strengths required to extract both spherical and cylindrical particles.^{67,68} An extension of this derivation studies the effects of particle kinetic energy on the extraction process and the dynamics of liquid draining from the particle surface. In addition, this chapter discusses the effects and limitations of the liquid instability, presented in Chapter 3, on particle extraction and compares the extraction of spherical and cylindrical particles as potential particle shapes for use with micro- and nano-particle thrusters. Experimental results of extracting spherical aluminum and tin particles with diameters ranging from approximately 300 μm to 800 μm and cylindrical aluminum and tungsten particles with diameters ranging from approximately 25 μm to 300 μm and lengths ranging from approximately 700 μm to 2,200 μm are presented to prove the feasibility of extracting particles through a liquid surface and for comparison with theoretical predictions.

4.2. Theory of Particle Extraction

This section presents the theory of charged particle extraction from an insulating liquid by way of an applied high strength electric field for spherical and cylindrical particles. The effects of the particle kinetic energy and the liquid draining from the particle surface are discussed. In addition, the limitation of the liquid instability imparted on particle extraction is addressed. Finally, the extraction of spherical versus cylindrical particles is compared as potential particle shapes for use with micro- and nano-particle thrusters.

4.2.1. Overview of Particle Extraction and Theoretical Assumptions

The model for charged particle extraction from an insulating liquid by way of an applied electric field is shown in Figure 4.1 and consists of three infinite parallel planar electrodes. The bottom electrode is the source electrode, the middle electrode is the charging grid, and the top electrode is the extraction electrode. Here, an insulating liquid completely fills the gap between the source electrode and the charging grid, and partially fills the gap between the charging grid and the extraction electrode. An electric potential difference, V_{ch} , is applied between the source electrode and the charging grid to generate the charging electric field, E_{ch} , and an electric potential difference, V_{ex} , is applied between the charging grid and the extraction electrode to generate the extraction electric field, E_{ex} . A conducting particle much smaller than the electrode gaps, either spherical or cylindrical, is placed in contact with the source electrode directly beneath a hole in the charging grid, which has a diameter d_h .

The charging electric field is responsible for inducing the charge transfer from the source electrode onto the particles and transporting the particles from the source electrode through the liquid towards the liquid surface. The extraction electric field is responsible for extracting the particles through the liquid surface and then accelerating the particles to the extraction electrode. Note that model would need to be modified for an actual thruster, where a hole in the extraction electrode would be included to allow the particles to be ejected. Additional grid structures could also be mounted above the extraction electrode to provide additional electric potential to further accelerate the particles.

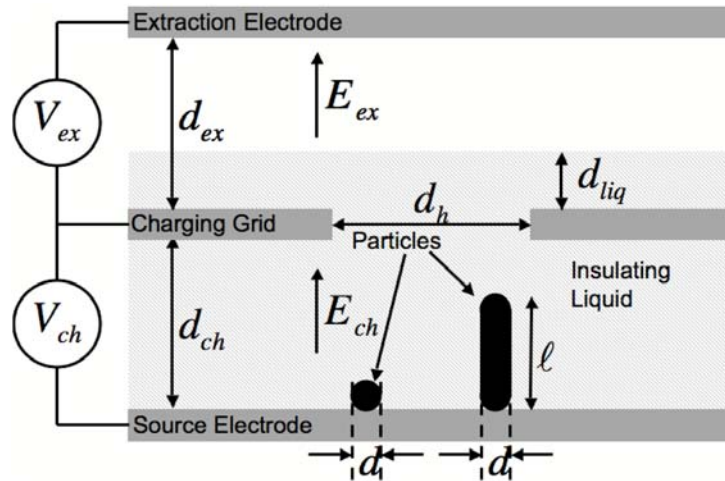


Figure 4.1: Model for the extraction of a charged particle from an insulating liquid by an electric field.

Assuming that the diameter of the hole in the charging grid is less than the separation of both electrode gaps ($d_h < d_{ch}$; $d_h < d_{ex}$), the charging and extraction electric fields are approximately uniform except near the edges of the hole in the grid.⁶⁹ The strength of the charging electric field is approximated without the presence of the particle or the hole.

$$E_{ch} \approx \frac{V_{ch}}{d_{ch}} \quad (4.1)$$

The strength of the extraction electric field is approximated as the electric field strength in the non-liquid region of the upper electrode gap without the presence of the hole in the grid and is dependent on the liquid height and permittivity. The electric field strength is calculated using $V = -\int \bar{E} \cdot d\hat{z}$.

$$E_{ex} \approx \frac{V_{ex}}{d_{ex} - d_{liq} \left(1 - \frac{\epsilon_o}{\epsilon_l}\right)} \quad (4.2)$$

The particle in contact with the source electrode is charged electrostatically in the presence of the charging electric field as described in Chapter 2. Assuming that the particle diameter and length are much smaller than the gap between the source electrode and the charging grid, the charge acquired by the spherical and cylindrical particles is dependent on the particle size, the strength of the charging electric field, and the dielectric constant of the liquid medium as described by Equations (2.12) and (2.20), respectively. As a result of the electric force arising from the charging electric field acting on the charged particle, the particle is removed and lifted from the source electrode and transported through the hole in the charging grid and to the liquid surface. It is assumed that the time required to transport the particle from the source electrode to the liquid surface is much less than the discharge time of the particle in contact with the insulating liquid, and the particle does not lose significant charge. The liquid's charging time constant and its effect on the particle charge are discussed in Chapter 2.3.

Upon arriving at the liquid surface, the electric force arising from the extraction electric field acting on the charged particle, F_{ex} , works to pull the particle through the

liquid surface. Three additional forces must be considered at the liquid surface: the surface tension force, F_s , the gravitational force, F_g , and the buoyant force, F_b . These are illustrated in the free body diagram in Figure 4.2. Note that in a zero gravity environment, the gravitational and buoyant forces are neglected.

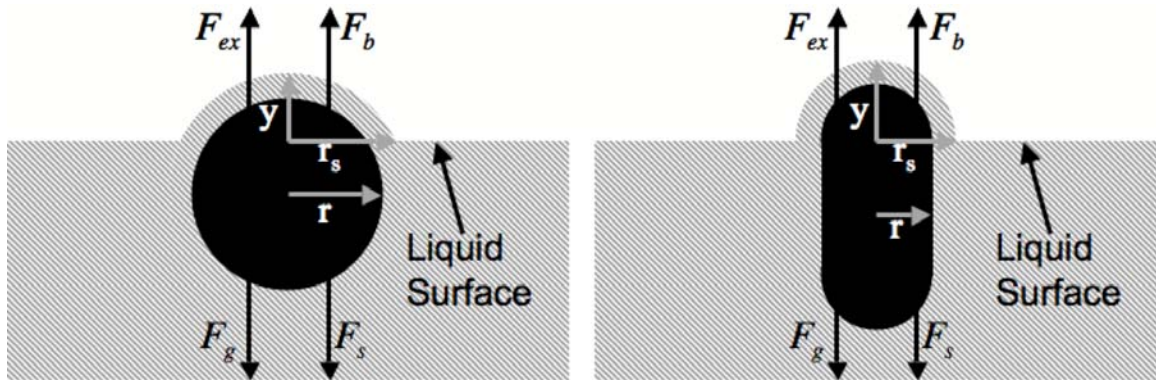


Figure 4.2: Forces acting on charged spherical and cylindrical particles during the extraction process through the liquid-vacuum interface.

The following two subsections use the forces on the particles shown in Figure 4.2 to derive the minimum strength of the extraction electric field required to achieve particle extraction for both spherical and cylindrical particles. But, before continuing with the derivations, several assumptions are considered to simplify the models and to provide insight into the process of particle extraction. Note that these assumptions may slightly sacrifice the accuracy of the resulting solution but are necessary to allow for a time-independent solution. Therefore, the derivations in the following subsections are intended to provide approximate estimates of the required extraction electric fields and, more importantly, to illustrate the trends of the required extraction electric field as a function of particle size. The following is a list and brief explanation of the assumptions used to simplify the particle extraction models.

- The particle arrives at the liquid surface with negligible kinetic energy compared to the liquid surface energy:

This assumption allows the models to neglect the energy absorbed by the liquid surface when decelerating the particle during the extraction process. A later section discusses the expected particle kinetic energy and suggests that for most particles with diameters of a couple hundred microns and smaller, it is generally much less than the potential energy of the liquid surface used in the experimental section. In addition, the kinetic energy of larger particles is also shown to be negligible under certain restrictions.

- The liquid surface is charge free and the polarization charge is negligible:

The liquid is assumed to be a perfect insulator and allows the models to approximate the extraction electric field without accounting for free charge on the liquid. In addition, it is assumed that the polarization surface charge density on the liquid surface is much less than the charge density on the particle.

- The particle is extracted with a uniform liquid film coating:

This assumption allows the models to approximate the liquid film coating the particle during the extraction process to have a uniform thickness, δ_c . The thickness of liquid film and the dynamics of liquid draining are discussed in Section 4.2.7.

- The particle is approximated as a point charge when at the liquid surface:

This assumption simplifies the electric force arising from the extraction electric field acting on the charged particle when at the liquid surface.

- The liquid is at room temperature:

This assumption allows the surface tension of the liquid to be treated as a constant. Note that when in space applications, the temperature of the liquid may change, which could change the thruster performance.

4.2.2. Spherical Particle Extraction

This subsection presents an evaluation of the forces on a spherical particle during the extraction process using the assumptions presented in Section 4.2.1 and derives an expression for the threshold extraction electric field required for the case of a spherical particle. The force responsible for extracting the spherical particle through the liquid surface is the electric force created by the extraction electric field acting on the charged particle. The particle is approximated as a point charge with the value given by Equation (2.12). Section 5.3.1 investigates the force applied to the particle by the electric field and suggests that the particle can be approximated as a point charge as long as the particle is not within several diameter of the electrode surface.

$$F_{ex} \approx q_{sph} E_{ex} \approx 2\pi r^2 \epsilon_{\ell} E_{ch} E_{ex} \frac{\pi^2}{3} \quad (4.3)$$

A force resisting the extraction of a spherical particle is the surface tension force, which is identical to the surface tension force (Equation (3.16)) discussed in Chapter 3 regarding the liquid surface instability. Note that the surface tension force is dependent on the location of the particle relative to the plane containing the liquid surface. The derivation of the threshold extraction electric field required for particle extraction requires the maximum value of the surface tension force. An analysis of the surface

tension force indicates that it is maximized when the center of the particle coincides with the plane containing the liquid surface ($r_s = y = r + \delta_\ell$), where it reduces to a function of the liquid's surface tension, the particle radius, and the thickness of the liquid film.

$$F_s = 2\pi\gamma(r + \delta_\ell) \quad (4.4)$$

The gravitational force is equal to the sum of the weight of the particle and the weight of the liquid film for the case when the particle center coincides with the plane containing the liquid surface.

$$F_g = \frac{2g\pi}{3} \left\{ 2r^3\rho + \left[(r + \delta_\ell)^3 - r^3 \right] \rho_\ell \right\} \quad (4.5)$$

Similarly, the buoyant force is equal to the weight of the liquid displaced by the particle when the particle center coincides with the plane containing the liquid surface.

$$F_b = \frac{2}{3} \pi r^3 \rho_\ell g \quad (4.6)$$

The threshold extraction electric field required for spherical particle extraction is determined by combining Equations (4.3), (4.4), (4.5), and (4.6).

$$E_{ex,sph,thresh} = \frac{3\gamma(r + \delta_\ell) + g \left[(r + \delta_\ell)^3 \rho_\ell + 2r^3(\rho - \rho_\ell) \right]}{\pi^2 r^2 \varepsilon_\ell E_{ch}} \quad (4.7)$$

It is important to note that the threshold extraction electric field required for spherical particle extraction has two terms: the surface tension dominant term and the gravitational dominant term. The surface tension dominant term scales inversely with the particle size while the gravitational term scales directly with the particle size. Also note that the presence of the liquid film coating the particle surface increases the threshold extraction electric field.

It is possible to minimize the threshold extraction electric field by increasing the charging electric field, which increases the particle charge. Recall from Chapter 2 that the strength of the charging electric field is limited by the strength of the maximum intensified electric field at the top of the particle, which is dependent on the particle field-focusing factor, and must remain less than the breakdown strength of the liquid. A spherical particle has a field-focusing factor of approximately 4.2 when it is charged against an infinite planar source electrode and is much smaller than the electrode gap.²⁹

$$E_{\max} = E_{ch} \alpha_{sph} \approx 4.2 E_{ch} \quad (4.8)$$

Equation (4.8) is substituted into Equation (4.7) to give an expression for the threshold extraction electric field when holding the maximum field strength at the top of the particle constant.

$$E_{ex,sph,thresh} = \frac{3\gamma(r + \delta_\ell) + g[(r + \delta_\ell)^3 \rho_\ell + 2r^3(\rho - \rho_\ell)]}{\pi^2 r^2 \epsilon_\ell E_{\max}} \quad (4.9)$$

Figure 4.3 is a plot of the predicted threshold extraction electric field required for extracting aluminum spherical particles from silicone oil using a maximum electric field strength of 15 MV/m, which is the approximate breakdown strength of the liquid, and varying the thickness of the liquid film from 0 to 100 μm . Note that silicone oil is chosen for this analysis due to its low conductivity and low vapor pressure and is used throughout this chapter for all analyses and experiments. The properties of the particle and liquid materials are presented in Section 4.3.

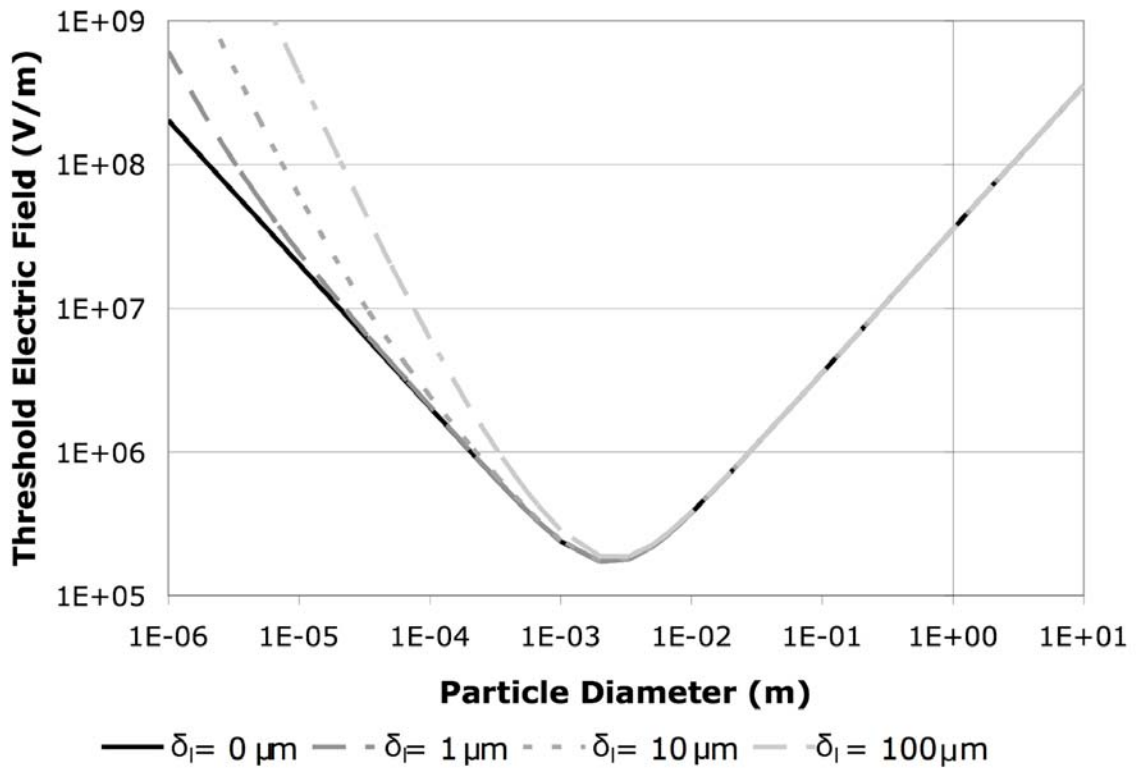


Figure 4.3: Plot of the predicted threshold extraction electric field to extract aluminum spherical particles from silicone oil using a maximum charging electric field strength of 15 MV/m.

The plot of the threshold extraction electric field clearly illustrates the two regimes. Particles larger than the centimeter range lie within the gravitational regime and particles smaller than the millimeter range lie within the surface tension regime. Both forces

affect particles between these two ranges significantly. The liquid film coating the particle appears to significantly increase the threshold extraction electric field when the particle diameter is less than ten times the film thickness ($d < 10\delta$). The expected thickness of the liquid film is presented in a later section.

4.2.3. Cylindrical Particle Extraction

This subsection evaluates the forces on a cylindrical particle during the extraction process using the assumptions presented in Section 4.2.1 and derives an expression for the threshold extraction electric field required for the case of a cylindrical particle. The derivation presented in this subsection for a cylindrical particle mirrors the derivation for a spherical particle from Section 4.2.2, and, consequently, many ideas are repeated. When considering the forces at the liquid surface, the cylindrical particle is modeled as a cylinder with the top end capped with a hemisphere as shown in Figure 4.2.

The force responsible for extracting cylindrical particles through the liquid surface is the electric force created by the extraction electric field acting on the charged particle. The particle is approximated as a point charge with the value given by Equation (2.20).

$$F_{ex} \approx q_{cyl} E_{ex} \approx \frac{4\pi r^2 \beta^2 \epsilon E_{ch} E_{ex}}{\ln(4\beta) - 1} \quad (4.10)$$

A force resisting the extraction of small cylindrical particles is the surface tension force. Using the assumption that the ends of the cylindrical particle are hemispheres, the surface tension force on a vertically oriented cylindrical particle is identical to the surface tension force on a spherical particle, which is given by Equation (4.4).

The gravitational force is equal to the sum of the weight of the particle and the weight of the liquid film, and is simplified using the assumption that the aspect ratio of the particle is much greater than one.

$$F_g \approx 2\pi g \left\{ \beta r^3 \rho + \frac{1}{3} \rho_\ell \left[(r + \delta)^3 - r^3 \right] \right\} \quad (4.11)$$

Similarly, the buoyant force is approximated as the weight of the liquid displaced by the particle assuming the aspect ratio to be much greater than one.

$$F_b \approx \pi r^2 \ell \rho_\ell g \approx 2\beta \pi r^3 \rho_\ell g \quad (4.12)$$

The threshold extraction electric field required for cylindrical particle extraction is approximated by combining Equations (4.4), (4.10), (4.11), and (4.12).

$$E_{ex,cyl,thresh} \approx \frac{3\gamma(r + \delta_\ell) + g \left[(r + \delta_\ell)^3 \rho_\ell + 3\beta r^3 (\rho - \rho_\ell) \right]}{6r^2 \beta^2 \varepsilon_\ell E_{ch}} \left[\ln(4\beta) - 1 \right] \quad (4.13)$$

Similar to the case of the spherical particle, note that the threshold extraction electric field required for particle extraction has two terms: the surface tension dominant term and the gravitational dominant term. Again, the surface tension dominant term scales inversely with the particle size while the gravitational term scales directly with the particle size. Also note that the presence of the liquid film coating the particle surface increases the threshold extraction electric field.

Just as was done with spherical particles, it is possible to minimize the threshold extraction electric field for cylindrical particles by increasing the charging electric field. Recall from Chapter 2 that the strength of the charging electric field is limited by the strength of the maximum intensified electric field at the top of the particle, which is dependent on the particle field-focusing factor, to ensure that the breakdown strength of the liquid is not exceeded. The field-focusing factor of a cylindrical particle is a function of the particle aspect ratio when it is charged in a vertical orientation against an infinite planar source electrode and is much smaller than the electrode gap. It is shown to be approximately linear as a function of the aspect ratio for values ranging from 5 to 80 in Chapter 2 (Equation (2.21)). The maximum electric field at the top of the particle, E_{\max} , is determined from the charging electric field and the field focusing-factor.

$$E_{\max} = E_{ch} \alpha_{cyl}(\beta) \quad (4.14)$$

Equations (2.21) and (4.14) are substituted into Equation (4.13) to give an expression for the threshold extraction electric field when holding the maximum field strength at the top of the particle constant.

$$E_{ex,cyl,thresh} \approx \frac{3\gamma(r + \delta_\ell) + g \left[(r + \delta_\ell)^3 \rho_\ell + 3\beta r^3 (\rho - \rho_\ell) \right]}{6r^2 \beta^2 \epsilon_\ell E_{\max}} \left[\ln(4\beta) - 1 \right] (1.4\beta + 6.5) \quad (4.15)$$

Figure 4.4 and Figure 4.5 are plots of the predicted threshold extraction electric field required for extracting aluminum cylindrical particles from silicone oil using particle

aspect ratios of 10 and 80, respectively. The plots use a maximum electric field strength of 15 MV/m and vary the thickness of the liquid film from 0 to 100 μm .

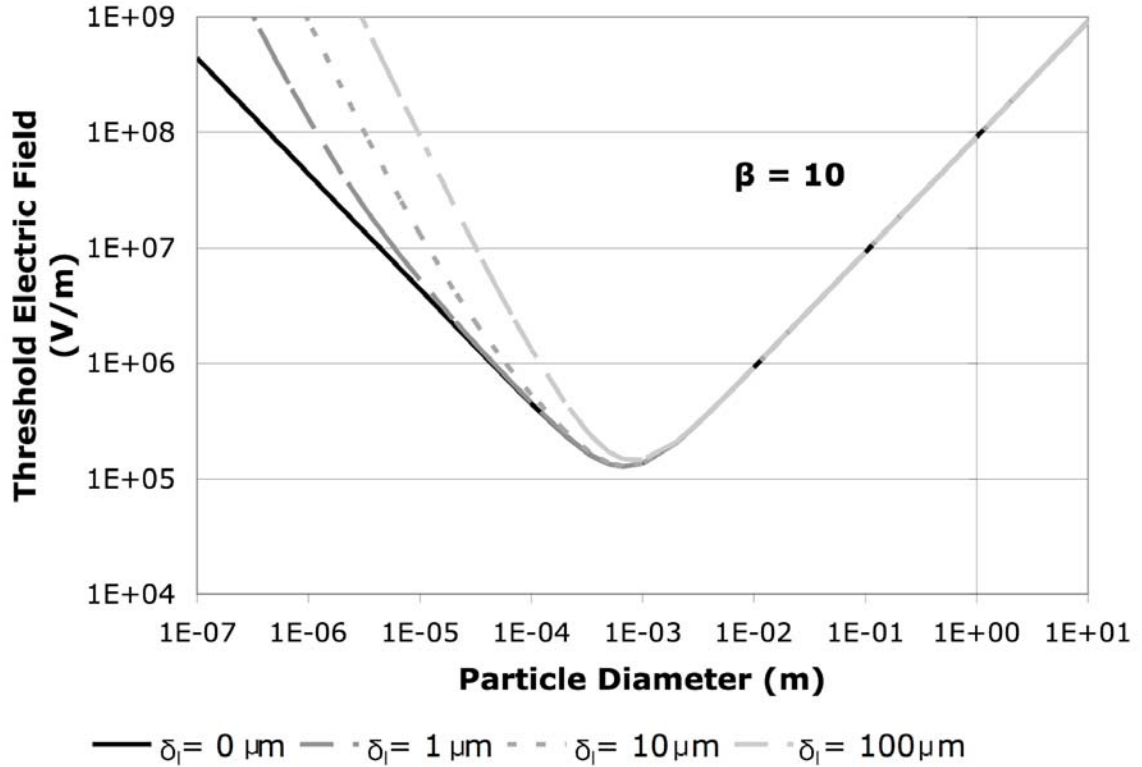


Figure 4.4: Plot of the threshold extraction electric field to extract aluminum cylindrical particles with an aspect ratio of 10 from silicone oil using a maximum electric field strength of 15 MV/m.

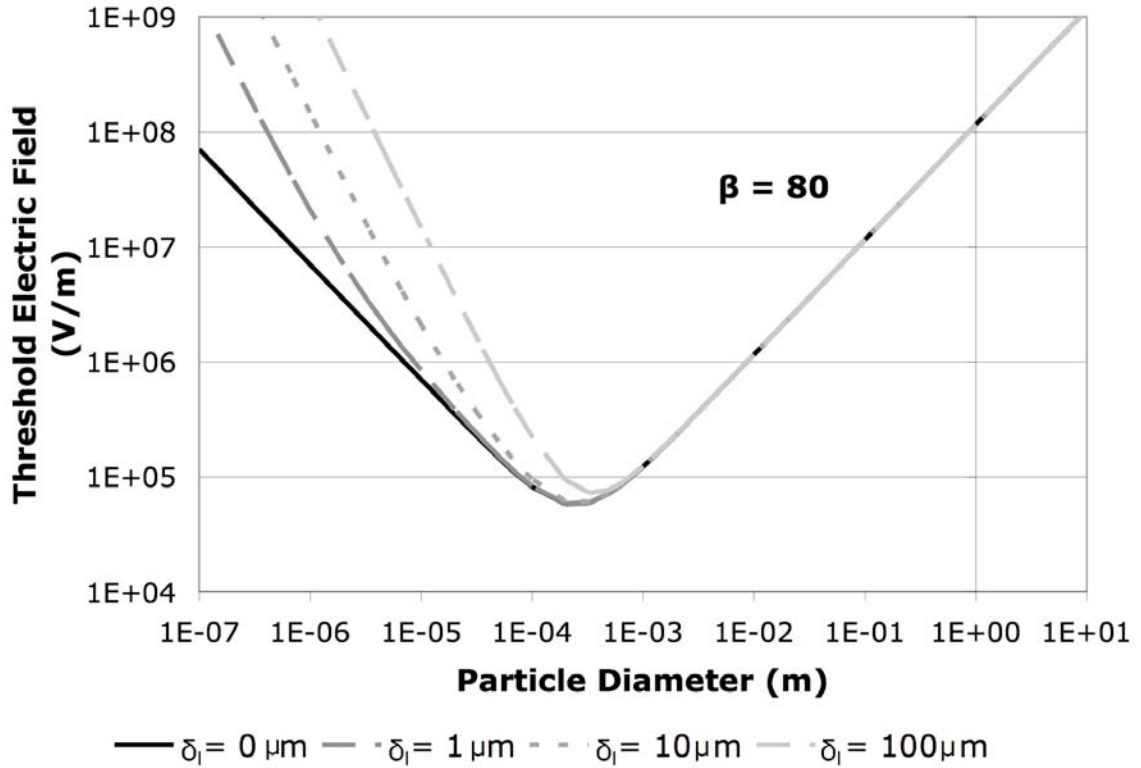


Figure 4.5: Plot of the threshold extraction electric field to extract aluminum cylindrical particles with an aspect ratio of 80 from silicone oil using a maximum electric field strength of 15 MV/m.

The plots of the threshold extraction electric field clearly illustrate the two regimes. The liquid film coating the particles appears to significantly increase the threshold extraction electric field when the particle diameter is less than ten times the film thickness ($d < 10\delta$), just as it does for spherical particles.

4.2.4. Comparison of Spherical and Cylindrical Particle Extraction

This section contains a comparison of the threshold extraction electric fields of spherical and cylindrical particles when in the surface tension dominant regime to determine which particle shape is more desirable when considering particle extraction. Due to the intense field-focusing that occurs at the sharp tips of particles, this section

assumes a maximum focused electric field strength below the electric breakdown of the liquid. The ratio of the threshold extraction electric field of a spherical particle to that of a cylindrical particle in the surface tension dominant regime is determined from Equations (4.9) and (4.15).

$$\frac{E_{ex,sph,thresh}}{E_{ex,cyl,thresh}} \approx \frac{25.2\beta^2}{\pi^2(1.4\beta + 6.5)[\ln(4\beta) - 1]} \quad (4.16)$$

Figure 4.6 is a plot of the ratio of the threshold extraction electric field of a spherical particle to that of a cylindrical particle as a function of β when holding the maximum electric field at the top of the particles constant.

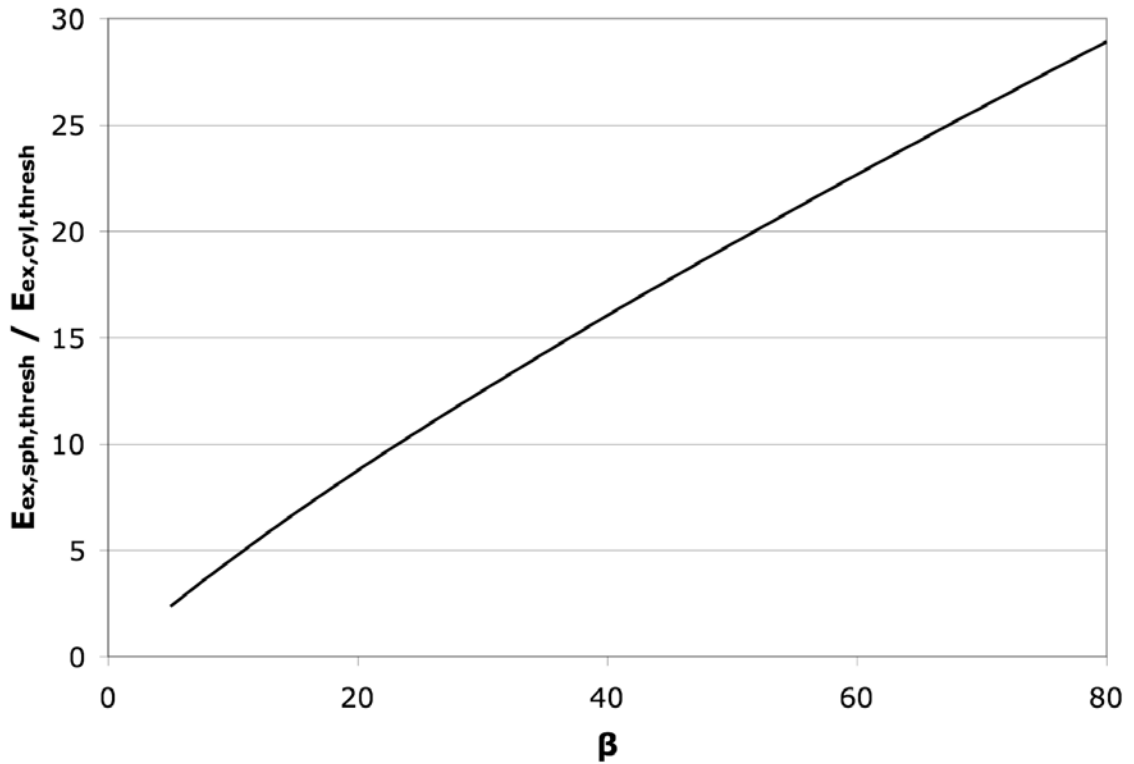


Figure 4.6: Plot of $E_{ex,sph,thresh}/E_{ex,cyl,thresh}$ in the surface tension dominant regime as a function of β using a constant maximum electric field .

The plot in Figure 4.6 suggests that when using a constant maximum electric field and particle diameter, a cylindrical particle always has a lower threshold extraction electric field. In addition, increasing the cylindrical particle aspect ratio reduces the threshold extraction electric field. The analysis presented in this section suggests that cylindrical particles are a better choice for propellant with the insulating liquid design configuration when considering the threshold extraction electric field.

4.2.5. Liquid Polarization Surface Charge Density

Section 4.2.1 states that the particle extraction models assume that the liquid polarization surface charge density is much less than the particle surface charge density. This assumption allows the model to neglect the electrostatic force of the extraction electric field acting on the polarized liquid surface during particle extraction. This subsection investigates the expected liquid polarization charge density and compares it with the expected particle surface charge density to validate the assumption.

The polarization charge density, ρ_{ps} , on the surface of the liquid at the vacuum/air interface shown in Figure 4.1 is defined as a function of the polarization vector, \mathbf{P}_l , within the liquid. The polarization vector is defined as a function of the extraction electric field and the relative dielectric constants of the liquid and air/vacuum regions.³⁸

$$\rho_{ps} = \bar{P}_l \cdot \hat{n} = \epsilon_o E_{ex} \left(1 - \frac{\epsilon_o}{\epsilon_l} \right) \quad (4.17)$$

Recall from Section 2.2 that the surface charge density of the particle scales as a function of the charging electric field, the relative dielectric constant of the liquid, and the field-focusing factor.

$$\rho_s(\theta) = \varepsilon_\ell E_{ch} \alpha(\theta) \quad (4.18)$$

A comparison of the expressions given by Equations (4.17) and (4.18) reveals that the charge density on the particle surface is more than one order of magnitude greater than the polarization charge density on the liquid surface for most practical situations, which assumes the following.

- $\varepsilon_\ell \geq \varepsilon_o$: The liquid dielectric constant is greater than or equal to the air/vacuum dielectric constant.
- $E_{ch} > E_{ex}$: The charging electric field is greater than the extraction electric field. This is a reasonable assumption when using silicone oil because the upper limit for the charging electric field, which is limited by electrical breakdown, is approximately an order of magnitude greater than the upper limit for the extraction electric field, which is limited by surface instability.
- $\alpha \geq 4.2$: When using spherical or cylindrical particles, the field-focusing factor is greater than or equal to 4.2 as discussed in Sections 2.2.1 and 2.2.2.

4.2.6. Particle Kinetic Energy

Section 4.2.1 states that the particle extraction models presented in Sections 4.2.2 and 4.2.3 both assume that the particle kinetic energy within the liquid is negligible compared to the potential energy of the liquid surface and therefore can be neglected in the particle

extraction derivations. This subsection investigates the expected particle kinetic energy and compares it to the liquid surface potential energy to confirm the assumption.

The maximum particle kinetic energy is dependent on the maximum velocity of the particle within the liquid, which is equal to the maximum terminal velocity. The maximum terminal velocity occurs when the charging electric field is set to its greatest allowable value, which is limited by Equations (4.8) and (4.14) for spherical and cylindrical particles, respectively, to ensure that the maximum electric fields at the top of the particles do not exceed the breakdown strength of the liquid. This section only investigates the terminal velocity of spherical particles and not cylindrical particles because when using the same maximum electric field strength, spherical particles have a higher terminal velocity due to their higher charge-to-mass ratio, as presented in Chapter 2, and lower drag coefficient.³²

When traveling at terminal velocity during transport within the liquid, four balanced forces act on the particle as shown in Figure 4.7: the electric force, the gravitational force, the buoyant force, and the drag force.

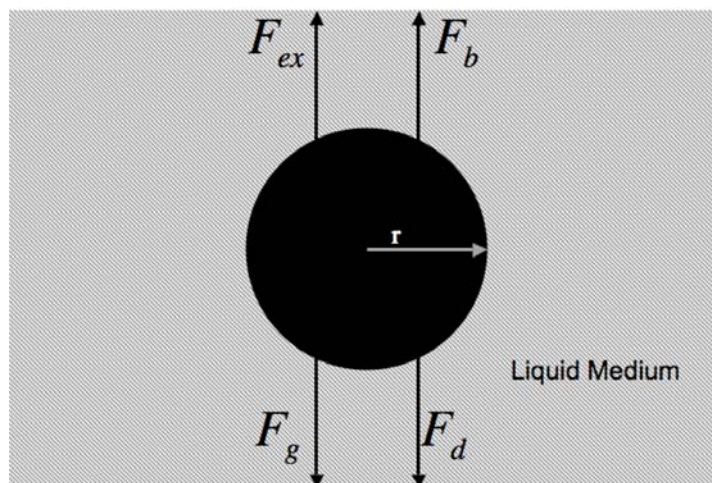


Figure 4.7: Forces acting on a charged spherical particle when traveling at terminal velocity.

The electric and gravitational forces are slight modifications of Equations (4.3) and (4.5), respectively, and the buoyant force is given by Equation (4.6).

$$F_{ex} \approx 2\pi r^2 \epsilon_\ell E_{ch}^2 \frac{\pi^2}{3} \quad (4.19)$$

$$F_g = \frac{4}{3} \pi r^3 \rho g \quad (4.20)$$

The drag force acts on a particle in the direction opposing the relative motion between the particle and the surrounding medium and is comprised of two parts, which are the viscous drag and form drag. Viscous drag results from velocity gradients in the liquid near the surface of the particle, and form drag results from unstable turbulent vortices that are shed from the particle and induce a pressure gradient in the liquid around the particle. The drag force is dependent on the coefficient of drag, C_D , the particle cross-sectional area, A_p , the liquid density, ρ_ℓ , and the terminal velocity, u_t .⁵¹

$$F_d = \frac{1}{2} C_D \pi r^2 \rho_\ell u_t^2 \quad (4.21)$$

The drag coefficient is a dimensionless term that behaves as a function of the Reynolds number, Re , another dimensionless term dependent on the liquid viscosity, η .⁵⁰

$$Re = \frac{2\rho_\ell r u_t}{\eta} \quad (4.22)$$

The behavior of the drag coefficient is a function of the Reynolds number and is dependent on the type of flow, which is approximated in Table 4.1.⁷⁰

Stokes Flow	$Re < 1$	$C_D \approx \frac{24}{Re}$
Transitional Regime	$1 < Re < 10^3$	$C_D \approx 18Re^{-0.6}$
Turbulent Flow	$Re > 10^3$	$C_D \approx 0.44$

Table 4.1: Dependence of the drag coefficient on the Reynolds number in the three flow regimes.

The terminal velocity of the spherical particle is calculated from Equations (4.6), (4.19), (4.20), and (4.21), and listed in Table 4.2.

Stokes Flow	$u_t = \frac{r[\pi^2 \varepsilon_\ell E_{ch}^2 + 2gr(\rho_\ell - \rho)]}{9\eta}$
Transitional Regime	$u_t = \frac{2}{9} \left\{ \frac{2r^3[\pi^2 \varepsilon_\ell E_{ch}^2 + 2gr(\rho_\ell - \rho)]^5}{3\eta^3 \rho_\ell^2} \right\}^{1/7}$
Turbulent Flow	$u_t = 10 \sqrt{\frac{\pi^2 \varepsilon_\ell E_{ch}^2 + 2gr(\rho_\ell - \rho)}{33\rho_\ell}}$

Table 4.2: Particle terminal velocity in the three flow regimes.

Figure 4.8 plots the predicted terminal velocities and Reynolds numbers of charged spherical aluminum particles in 100 cSt silicone oil using the maximum electric field strength of 15 MV/m. The strength of the maximum electric field is chosen so that it is approximately equal to the breakdown strength of the liquid.

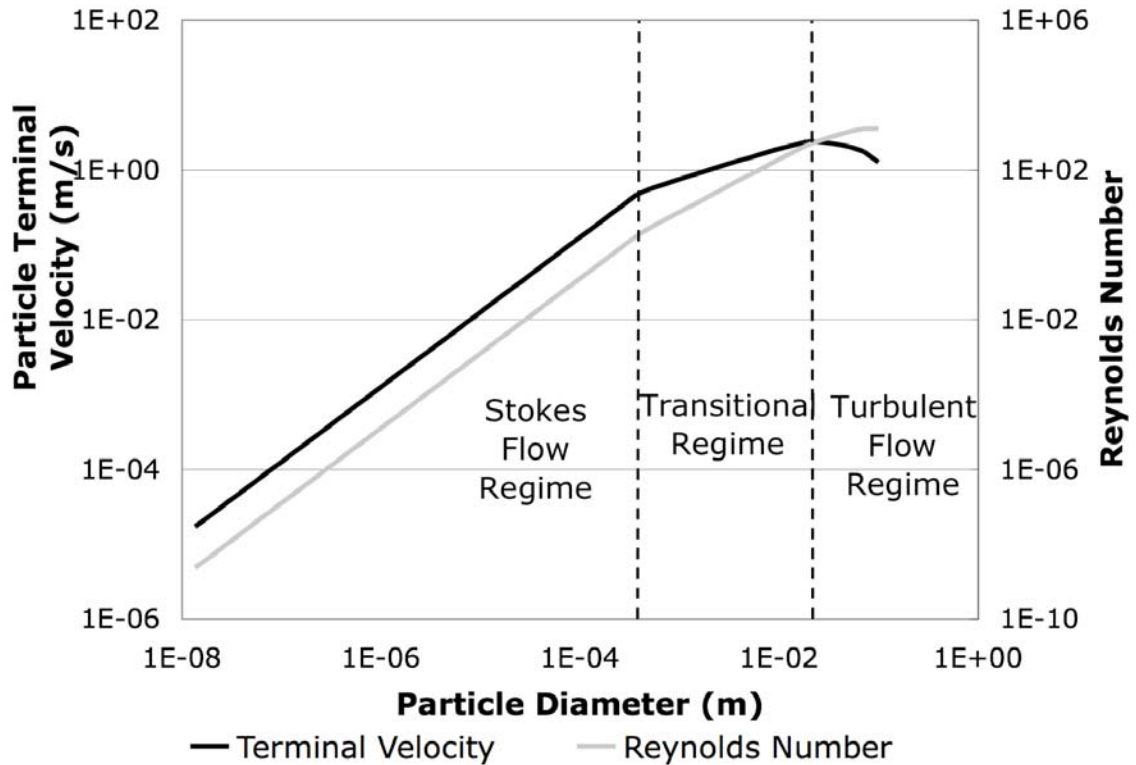


Figure 4.8: The terminal velocities and Reynolds numbers of aluminum spherical particles in 100 cSt Silicone oil using a maximum electric field strength of 15 MV/m.

According to Figure 4.8, the terminal velocity and Reynolds number increase with the particle diameter when in the stokes flow and transitional regimes. The Reynolds number continues to increase with the particle diameter in the turbulent regime, but the terminal velocity decreases with the particle diameter in this regime. Using a maximum electric field strength of approximately 15 MV/m, which is the breakdown strength of silicone oil, a particle with a diameter less than approximately 500 μm is in stokes flow, a particle with a diameter greater than approximately 2 cm is in turbulent flow, and all particles with diameters ranging from approximately 400 μm to 2 cm are in the transitional regime.

The maximum particle kinetic energy is dependent on the particle's terminal velocity and mass.

$$K = \frac{1}{2} m u_i^2 \quad (4.23)$$

The work required to break the liquid surface tension is approximated by integrating the surface tension force from Equation (3.16). The limits of integration can be approximated from the point when the particle is beneath the liquid surface ($y=0$) to the point when the particle is just above the liquid surface ($y= 2R_\ell$).

$$W_s \approx \int_0^{2R_\ell} \frac{2\gamma A_\ell}{R_\ell} dy \quad (4.24)$$

The cross-sectional area of the liquid perturbation is a function of the liquid perturbation within the plane of the liquid surface.

$$A_\ell = \pi r_s^2 = \pi(2yR_\ell - y^2) \quad (4.25)$$

The radius of the liquid perturbation is approximated as the sum of the radius of the particle and the thickness of the liquid film coating the particle.

$$W_s \approx \int_0^{2(r+\delta_\ell)} \frac{2\gamma\pi[2y(r+\delta_\ell) - y^2]}{r+\delta_\ell} dy \approx \frac{8}{3} \gamma\pi(r+\delta_\ell)^2 \quad (4.26)$$

Figure 4.9 is a plot of the particle's maximum kinetic energy and the work required to break the surface tension of the liquid. This analysis uses various values for the liquid

film thickness, aluminum particles, 100 cSt silicone oil, and a maximum electric field strength of 15 MV/m.

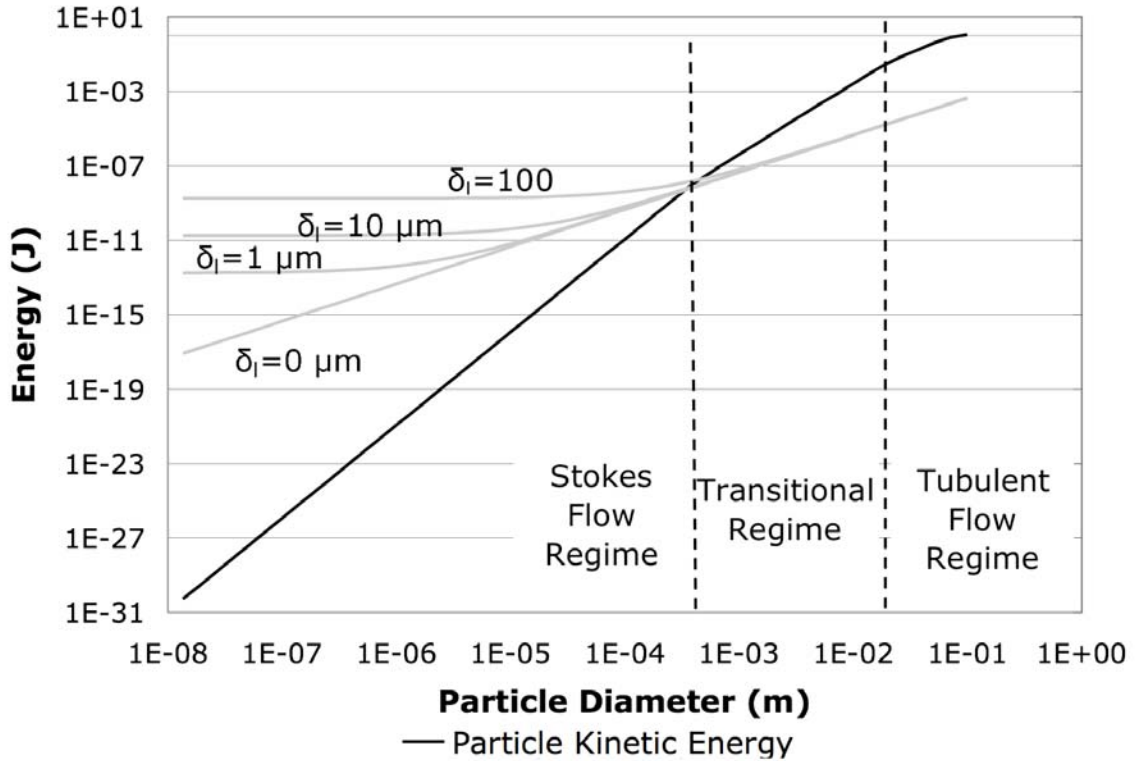


Figure 4.9: The particle’s maximum kinetic energy and the liquid surface potential energy using aluminum particles, 100 cSt silicone oil, and a maximum electric field strength of 15 MV/m.

According to Figure 4.9, for the particle and liquid materials presented here, the particle’s kinetic energy is less than the work required to break the liquid surface potential energy when the particle has a diameter less than approximately 300 μm for the conditions presented here. Further, it is reasonable to assume that the particle’s kinetic energy is negligible compared to the liquid surface tension potential energy when the particle’s kinetic energy is more than an order of magnitude less than the liquid surface potential energy, which occurs when the particle has a diameter less than approximately 150 μm . Therefore, the assumption that the particle kinetic energy is negligible is valid

for particles smaller than 150 μm when using a maximum electric field strength of 15 MV/m with aluminum particles and 100 cSt silicone oil. Note that reducing the maximum electric field strength and increasing the liquid viscosity reduces the particle energy, which implies that the assumption is still valid for larger particles under certain situations. The experimental section is careful to ensure that this assumption is valid for all test cases.

4.2.7. Liquid Draining from the Particle Surface

This section investigates the thickness of the thin liquid film coating a spherical particle, which is assumed to be uniform for simplicity. The thickness is assumed to be a result of the rate at which liquid drains from the particle surface and is approximated by solving a viscous flow problem. The goal of the derivation presented in this section is to provide lower and upper bounds of the film thickness and to understand its potential impact on particle extraction. Since the derivation is only intended to provide bounds on the film thickness, the wetting properties of the liquid and particle are neglected. Figure 4.10 shows the model for the viscous flow problem of liquid draining from the surface of a spherical particle.

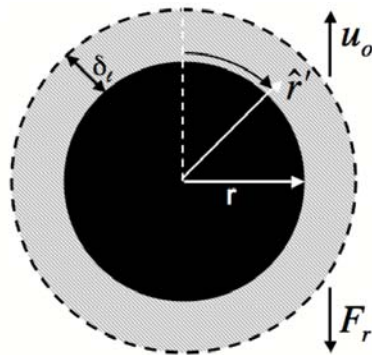


Figure 4.10: Viscous flow from the surface of a spherical particle.

The model shown in Figure 4.10 depicts the spherical particle traveling in the vertical direction with a constant velocity, u_o , with respect to the laboratory frame of reference. A resisting force, F_R , provides an acceleration, a_R , in the downward direction. This acceleration accounts for gravity (when appropriate), viscous drag, surface tension effects, and all other possible resisting forces.

Due to the geometry of the problem, a spherical coordinate system with the origin at the center of the particle and in the particle frame of reference is implemented. The resisting acceleration is expressed in terms of its components.

$$\bar{a}_R = -\hat{r}'a_R \cos\theta + \hat{\theta}a_R \sin\theta \quad (4.27)$$

Previous work has shown that the viscous flow around a spherical surface is unsolvable, and requires many simplifying assumptions, which are listed below.⁵⁰

- The flow is steady and Newtonian, with constant density and viscosity.
- The ϕ direction is disregarded due to symmetry. Therefore, all ϕ components and derivatives with respect to ϕ are set to zero.
- The only non-zero component of the velocity in the particle's frame of reference is in the θ -direction, u_θ .
- The pressure, p , is not a function of θ .

The continuity equation in spherical coordinates reduces from the assumptions.⁵⁰

$$\frac{1}{r' \sin\theta} \frac{\partial(\rho u_\theta \sin\theta)}{\partial\theta} = 0 \quad (4.28)$$

Equation (4.28) is rewritten in terms of the derivative of u_θ with respect to θ .

$$\frac{\partial u_\theta}{\partial \theta} = -u_\theta \cot \theta \quad (4.29)$$

The second derivative of u_θ with respect to θ is determined from Equation (4.29).

$$\frac{\partial^2 u_\theta}{\partial \theta^2} = u_\theta (\cot^2 \theta + \csc^2 \theta) \quad (4.30)$$

The momentum equation in spherical coordinates reduces from the assumptions.⁵⁰

$$\rho_\ell \frac{u_\theta}{r'} \frac{\partial u_\theta}{\partial \theta} = \eta \left[\frac{1}{r'^2} \frac{\partial}{\partial r'} \left(r'^2 \frac{\partial u_\theta}{\partial r'} \right) + \frac{1}{r'^2 \sin \theta} \frac{\partial}{\partial \theta} \left(\sin \theta \frac{\partial u_\theta}{\partial \theta} \right) - \frac{u_\theta}{r'^2 \sin \theta} \right] + \rho_\ell a_{R,\theta} \quad (4.31)$$

Equation (4.31) simplifies from substituting in Equations (4.27), (4.29), and (4.30).

$$\frac{\partial^2 u_\theta}{dr'^2} + \frac{2}{r'} \frac{\partial u_\theta}{dr'} + \frac{\rho \cot \theta}{\eta r'} u_\theta^2 + \frac{\csc^2 \theta - \csc \theta}{r'^2} + \frac{\rho_\ell a_R \sin \theta}{\eta} = 0 \quad (4.32)$$

Equation (4.32) is an unsolvable second order differential equation, but is simplified further by investigating the case when $\theta = \pi/2$. This case provides a reasonable estimate of the average rate at which liquid drains from the particle surface when assuming a uniform liquid film.

$$\frac{\partial^2 u_\theta}{\partial r'^2} + \frac{2}{r'} \frac{\partial u_\theta}{\partial r'} + \frac{\rho_\ell a_R}{\eta} = 0 \quad (4.33)$$

Equation (4.33) is solved for u_θ .

$$u_\theta\left(r', \pi/2\right) = -\frac{\rho_\ell a_R}{6\eta} r'^2 - \frac{C_1}{r'} + C_2 \quad (4.34)$$

The first derivative of u_θ with respect to r' is determined from Equation (4.34).

$$\frac{\partial u_\theta}{\partial r'} = -\frac{\rho_\ell a_R}{3\eta} r' + \frac{C_1}{r'^2} \quad (4.35)$$

The second derivative of u_θ with respect to r' is determined from Equation (4.35).

$$\frac{\partial^2 u_\theta}{\partial r'^2} = -\frac{\rho_\ell a_R}{3\eta} - \frac{2C_1}{r'^3} \quad (4.36)$$

Two boundary conditions are needed to find the values of the constants, C_1 and C_2 . First, the liquid velocity at the particle/liquid interface ($r' = r$) is zero in the particle's frame of reference.⁵⁰

$$u_\theta\left(r' = r, \theta = \pi/2\right) = -\frac{\rho_\ell a_R}{6\eta} r^2 - \frac{C_1}{r} + C_2 = 0 \quad (4.37)$$

Second, the boundary condition of zero shear stress at the liquid/vacuum interface ($r' = r + \delta_\ell$) is invoked.⁵⁰

$$\tau_{r\theta}(r' = r + \delta_\ell, \theta = \pi/2) \approx \eta \left(r' \frac{\partial}{\partial r'} \left(\frac{u_\theta}{r'} \right) \right) \approx \frac{-a_R \rho_\ell (r + \delta_\ell)}{6} + \frac{2\eta C_1}{(r + \delta_\ell)^2} - \frac{\eta C_2}{(r + \delta_\ell)} = 0 \quad (4.38)$$

The constants, C_1 and C_2 , are solved from Equations (4.37) and (4.38).

$$C_1 = \frac{a_R \rho_\ell r (r + \delta_\ell)}{6\eta} \left[\frac{r^2 + (r + \delta_\ell)^2}{r - \delta_\ell} \right] \quad (4.39)$$

$$C_2 = \frac{a_R \rho_\ell}{6\eta} \left[\frac{2r^3 + (r + \delta_\ell)^3}{r - \delta_\ell} \right] \quad (4.40)$$

The velocity of the liquid draining from the surface of the particle at $\theta = \pi/2$ in the particle's reference frame is obtained by substituting Equations (4.39) and (4.40) into Equation (4.34).

$$u_\theta(r', \frac{\pi}{2}) = -\frac{\rho_\ell a_R}{6\eta} \left\{ r'^2 + \frac{r(r + \delta_\ell)}{r'} \left[\frac{r^2 + (r + \delta_\ell)^2}{r - \delta_\ell} \right] - \left[\frac{2r^3 + (r + \delta_\ell)^3}{2r - (r + \delta_\ell)} \right] \right\} \quad (4.41)$$

The velocity of the liquid draining from the surface of the particle at $\theta = \pi/2$ is rewritten in the laboratory frame of reference.

$$u_{\theta,lab}(r', \frac{\pi}{2}) = u_o + \frac{\rho_\ell a_R}{6\eta} \left\{ r'^2 + \frac{r(r + \delta_\ell)}{r'} \left[\frac{r^2 + (r + \delta_\ell)^2}{r - \delta_\ell} \right] - \left[\frac{2r^3 + (r + \delta_\ell)^3}{2r - (r + \delta_\ell)} \right] \right\} \quad (4.42)$$

Figure 4.11 is an example of the velocity profile of liquid draining from a spherical particle normalized to the velocity of the particle.

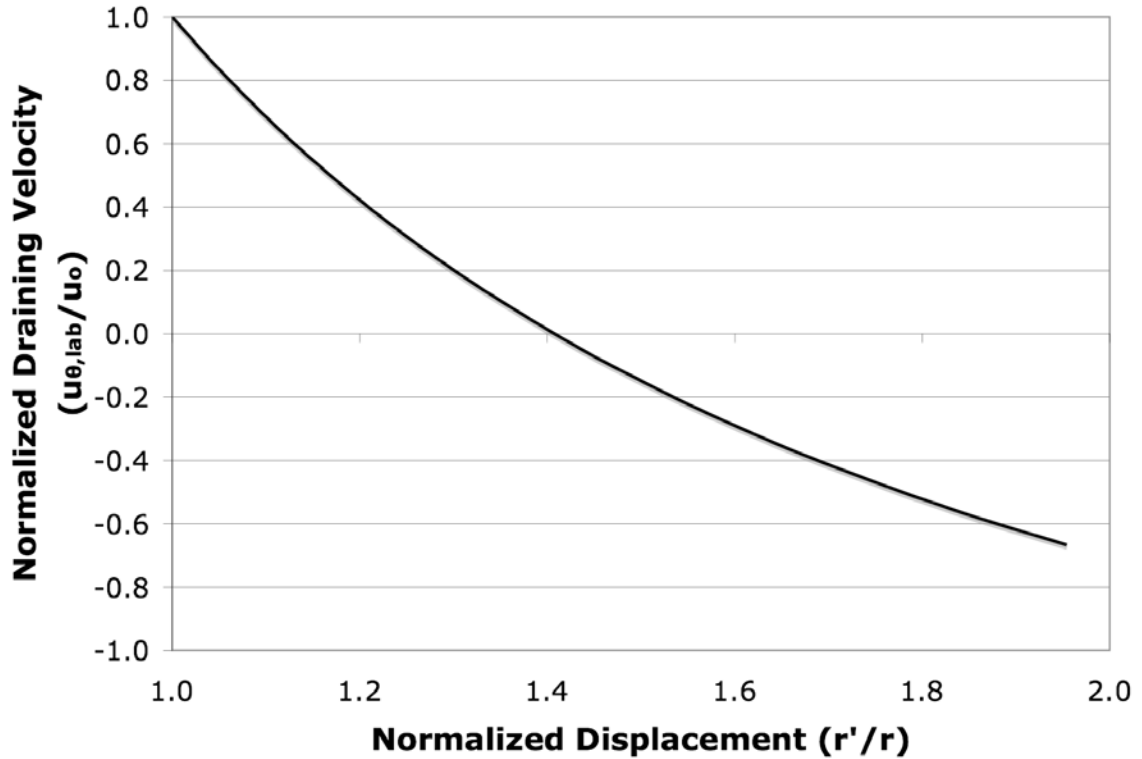


Figure 4.11: Velocity profile of liquid draining from the surface of a spherical particle at $\theta=90^\circ$.

The velocity profile indicates that the liquid near the surface of the particle moves at the same velocity as the particle and decreases as the distance from the particle surface increases. The thickness of the liquid film is approximated by calculating the equilibrium thickness, which occurs when the net flow of the liquid is zero. The net flow of the liquid, Q , is approximated by integrating the liquid velocity over two dimensions.⁵⁰

$$Q = \int_0^{2\pi} \int_r^{r+\delta_f} u_{\theta,lab} dr' r' \sin\theta d\phi = 0 \quad (4.43)$$

$$Q = 2\pi \left\{ \frac{u_o - C_2}{2} \left[(r + \delta_\ell)^2 - r^2 \right] + \frac{\rho_\ell a_r}{24\eta} \left[(r + \delta)^4 - r^4 \right] + C_1 \delta_\ell \right\} = 0 \quad (4.44)$$

The solution to Equation (4.44) provides the expected equilibrium thickness of the liquid film coating the particle, which is used to calculate the lower and upper bounds. The bounds, which are listed in Table 4.3 along with a physical explanation, are evaluated from the expression by taking the limits as each parameter approaches zero and infinity.

Limit	Boundary	Explanation
$u_o \rightarrow 0$	$\delta_\ell \rightarrow 0$	Increasing the particle velocity decreases the time allowed for draining, which increases the film thickness
$u_o \rightarrow \infty$	$\delta_\ell \rightarrow r$	
$a_R \rightarrow 0$	$\delta_\ell \rightarrow r$	Increasing the acceleration increases the draining rate, which decreases the film thickness
$a_R \rightarrow \infty$	$\delta_\ell \rightarrow 0$	
$\rho_\ell \rightarrow 0$	$\delta_\ell \rightarrow r$	Increasing the liquid density increases the liquid's resistance to acceleration, which increases the film thickness
$\rho_\ell \rightarrow \infty$	$\delta_\ell \rightarrow 0$	
$\eta \rightarrow 0$	$\delta_\ell \rightarrow 0$	Increasing the liquid viscosity decreases the liquid flow rate, which increases the film thickness
$\eta \rightarrow \infty$	$\delta_\ell \rightarrow r$	

Table 4.3: The lower and upper bounds of the liquid film thickness.

According to Table 4.3, the thickness of the liquid film coating a spherical particle is bounded and ranges from zero to the radius of the particle.

Recall from Figure 4.3 that the threshold extraction electric field for a spherical particle is affected significantly by the thickness of the liquid film if the film thickness is greater than one-tenth of the particle diameter ($d < 10\delta_\ell$). Using the results from this subsection, Figure 4.12 plots the upper and lower bounds of the predicted threshold extraction electric field required for extracting aluminum spherical particles from silicone oil using a maximum electric field strength of 15 MV/m.

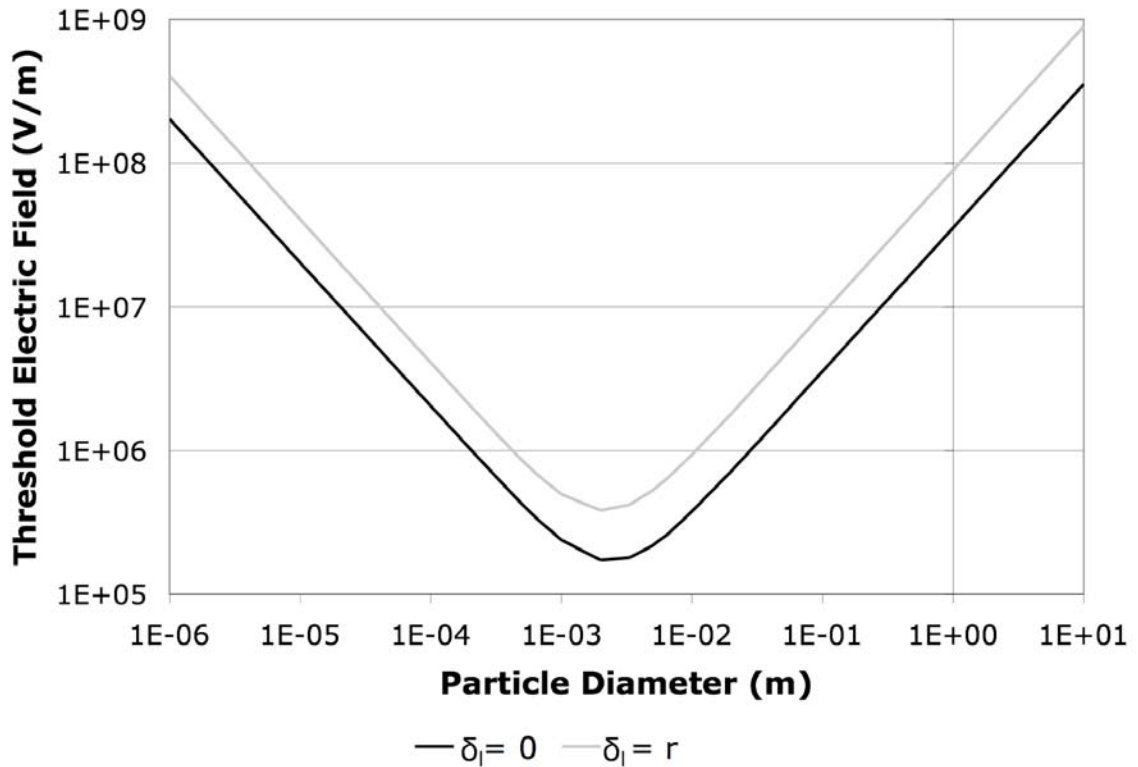


Figure 4.12: Plot of the lower and upper bounds of the threshold extraction electric field to extract aluminum spherical particles from silicone oil using a maximum electric field strength of 15 MV/m

4.2.8. Limitations of Liquid Instability

Chapter 3 investigated the instability of a liquid surface when subjected to a high strength electric field. This subsection investigates the limitations of the liquid instability on the threshold extraction electric field while maintaining the strength of the extraction electric field less than the strength required to initiate a liquid instability. Two cases of liquid instability and their effects on particle extraction are discussed. First, the particle is extracted through an infinite planar liquid surface, using no method to suppress the liquid instability. Second, the particle is extracted through a finite liquid surface, using a method such as a “knife edge” to suppress the liquid instability.

4.2.8.1. Particle Extraction Through an Infinite Liquid Surface

Recall from Chapter 3 that the minimum electric field required to initiate an instability on an infinite planar liquid surface in an Earth-gravity environment is dependent on the liquid's surface tension and density as given by Equation (3.21).

The ranges of extractable spherical and cylindrical diameter sizes are determined by comparing Equations (4.9) and (4.15) with Equation (3.21) and assuring that the extraction electric fields are less than the instability electric field. Figure 4.13 is a plot of the predicted threshold extraction electric field required for extracting aluminum spherical and cylindrical particles with various aspect ratios, β , from silicone oil using a maximum electric field strength of 15 MV/m. Also included in the plot is the predicted threshold electric field required to initiate an instability on the liquid surface. Note that the thickness of the liquid film coating the particle is assumed to be zero for this comparison.

Threshold Extraction and Instability Electric Fields

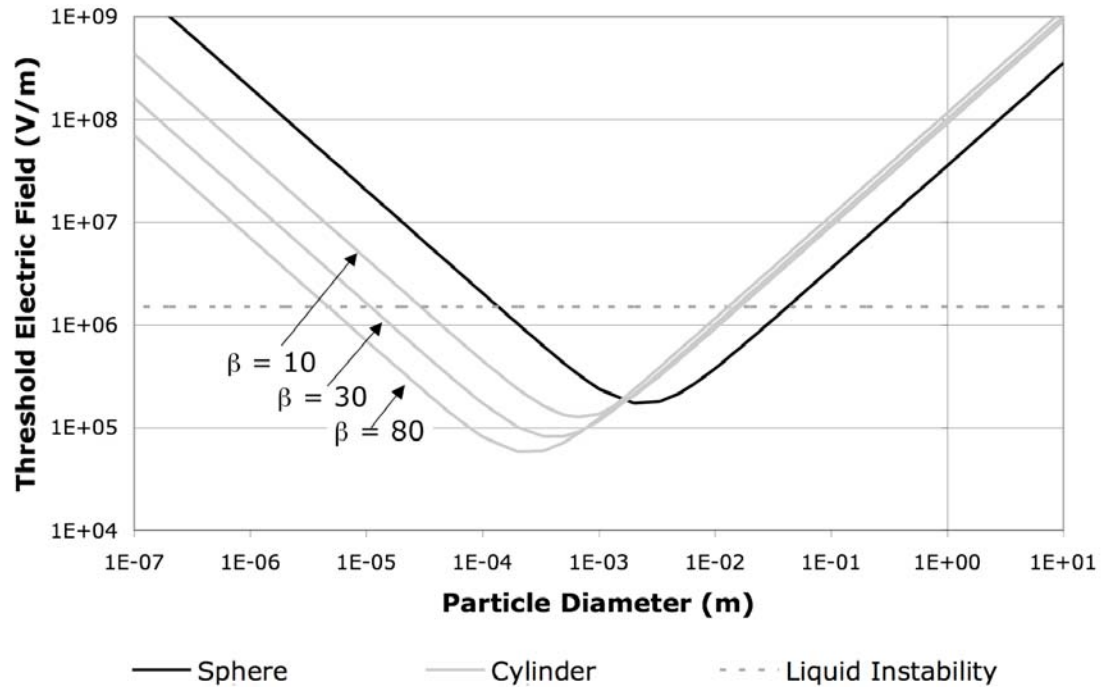


Figure 4.13: Plot of the required extraction electric field to extract aluminum spherical and cylindrical particles from silicone oil using a maximum electric field of 15 MV/m in a 1-g environment. Also included in the plot is the predicted threshold electric field required to initiate an instability on the liquid surface.

It is only desirable to extract particles using an extraction electric field that is less than the liquid instability threshold to ensure that the liquid remains stable. Table 4.4 lists the expected extractable particle diameter ranges for aluminum spheres and cylinders with various aspect ratios from 100 cSt silicone oil. The charging electric fields were chosen so that the maximum electric fields focused at the particle tips were 15 MV/m.

Particle Shape	Aspect Ratio	Charging Electric Field (kV/m)	Expected Extractable Particle Diameter Range
Sphere	N/A	3,600	140 μm – 4.2 cm
Cylinder	10	770	28 μm – 1.7 cm
Cylinder	30	300	11 μm – 1.5 cm
Cylinder	80	120	5 μm – 1.2 cm

Table 4.4: Predicted particle diameter ranges for extracting spherical and cylindrical aluminum particles from 100 cSt silicone oil without initiating a liquid instability.

Table 4.4 indicates that when holding the maximum electric field constant, it is expected that cylindrical particles with high aspect ratios can be extracted with the smallest particle diameter, which agrees with Equation (4.16). But, note that the minimum extractable diameters are on the order of microns to a hundred microns, which may be too large for many applications.

4.2.8.2. Particle Extraction Through a Finite Liquid Surface

Recall from Chapter 3 that the minimum electric field required to initiate an instability on a finite liquid surface, which can be controlled with a knife-edge orifice with radius r_k , in an Earth-gravity environment is dependent on the liquid's surface tension and density as well as the radius of the knife-edge orifice as given by Equation (3.23). Recall that the analysis presented here assumes that that perturbation radius is equal to the knife-edge radius as is the case when operating in mode 1. It may be possible that higher order modes would be excited that would require higher electric fields to induce the liquid instability. The ranges of spherical and cylindrical particle sizes capable of extraction when suppressing the liquid instability are determined by comparing Equations (4.9) and (4.15) with Equation (3.23) and assuring that the

extraction electric fields are less than the instability electric field. Figure 4.14 is a plot of the predicted threshold extraction electric field required for extracting aluminum spherical and cylindrical particles from silicone oil using a maximum electric field strength of 15 MV/m. Also included in the plot is the predicted threshold electric field required to initiate an instability on the liquid surface for various knife-edge radii.

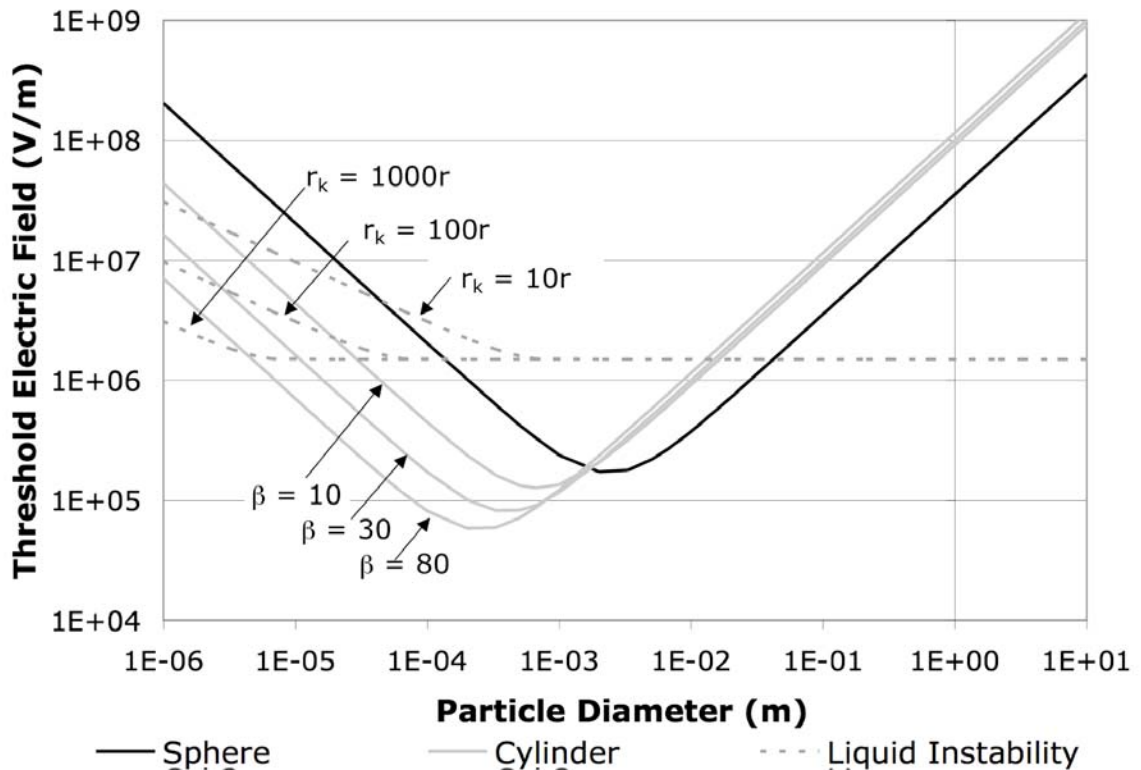


Figure 4.14: Plot of the required extraction electric field to extract aluminum spherical and cylindrical particles from silicone oil using a maximum electric field of 15 MV/m. Also included in the plot is the predicted threshold electric field required to initiate an instability on the liquid surface for several various liquid surface radii, r_k . The thickness of the liquid film coating the particles is assumed to be zero.

It is only desirable to extract particles using an extraction electric field that is less than the liquid instability threshold to ensure that the liquid remains stable. Table 4.5 lists the expected extractable particle diameter ranges for aluminum spheres and cylinders

with various aspect ratios from 100 cSt silicone oil. The charging electric fields were chosen so that the intensified electric fields focused at the particle tips were 15 MV/m.

Particle Shape	Aspect Ratio	Charging Electric Field (kV/m)	Expected Extractable Particle Diameter Range ($r_k=10r$)	Expected Extractable Particle Diameter Range ($r_k=100r$)	Expected Extractable Particle Diameter Range ($r_k=1,000r$)
Sphere	N/A	3,600	44 μm – 4.2 cm	140 μm – 4.2 cm	140 μm – 4.2 cm
Cylinder	10	770	2 μm – 1.7 cm	18 μm – 1.7 cm	23 μm – 1.7 cm
Cylinder	30	300	0.3 μm – 1.5 cm	3 μm – 1.5 cm	11 μm – 1.5 cm
Cylinder	80	120	0.06 μm – 1.2 cm	0.6 μm – 1.2 cm	5 μm – 1.2 cm

Table 4.5: Predicted particle diameter ranges for extracting spherical and cylindrical aluminum particles from 100 cSt silicone oil.

Table 4.5 indicates that the when holding the maximum electric field constant, it is expected that cylindrical particles with high aspect ratios can be extracted with the smallest particle diameter, and reducing the size of the knife-edge orifice allows the extraction of smaller particles. Note that the minimum extractable particle diameters, when suppressing the liquid instability, may be as low as many tens of nanometers.

4.3. Experimental Setup

To experimentally prove the feasibility of extracting charged particles from an insulating liquid and to measure the threshold extraction electric fields required to extract various sized particles, a prototype with approximately 100 emitters was constructed. Figure 4.15 is a cross-sectional illustration of a single emitter from the prototype.

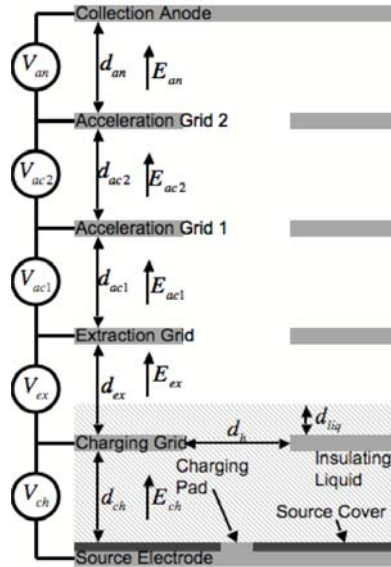


Figure 4.15: Illustration of a single emitter from the particle extraction prototype.

The prototype is very similar to the model from Figure 4.1 with additional accelerating grids stacked above the extraction grid, which allows the use of larger accelerating electric potentials. Note that the accelerating grids can be added or removed to provide the option of increasing or decreasing the total accelerating voltages. Above the top accelerating grid, the collection anode is used to catch ejected particles for examination and/or verification. The electrodes/grids are made from thin aluminum sheets, and the gaps separating the grids are maintained by insulating spacers fabricated from Teflon[®]. The source electrode is a slight modification from the original model, and is covered with an insulating source cover made from Teflon[®]. Directly beneath the holes in the stacked grids, charging pads, which are electrically connected to the source electrode, protrude through the source cover to ensure that particles are only charged directly beneath the accelerating channels. Figure 4.16 is a photograph of the prototype without the collection anode attached. Note that the stacked grids are aligned with pins made from Ultem[®].

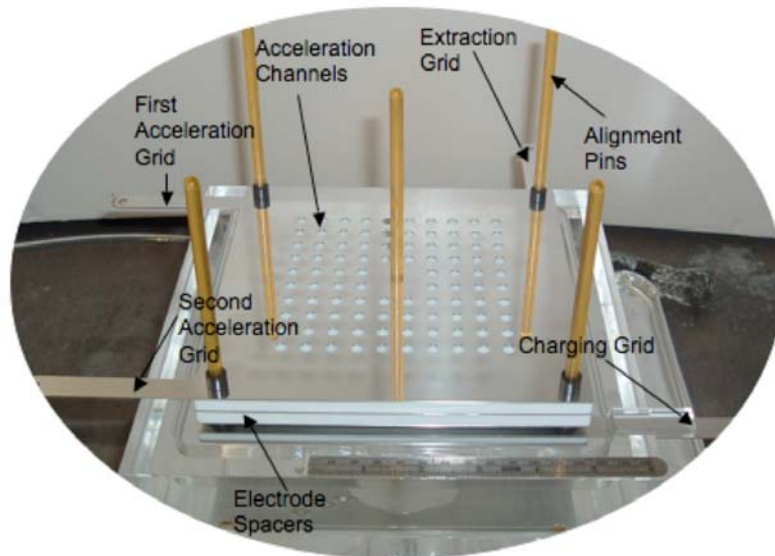


Figure 4.16: Photograph of micro-particle emitter.

The main goal of the experiment is to prove the feasibility of extracting conducting spherical and cylindrical particles from an insulating liquid by way of an applied high strength electric field without inducing a liquid instability. An additional goal is to measure the required extraction electric fields of various size and shape particles and compare with theory.

The experiment is performed by depositing individual particles onto the charging pads. Next, the voltages are applied between all of the electrodes and grids with the exception of the charging voltage. The charging voltage is applied after all other voltages are at their desired values and is applied through a high voltage relay so that it reaches its desired value almost instantly. Once the charging voltage is applied, the particles are charged and transported through the liquid to the liquid interface, where they are extracted and then accelerated to the collection anode. The success of particle extraction is verified by the presence of particles on the collection anode and through the use of a high-speed camera system that records the particle extraction.

All of the electrode gaps, with the exception of the gap between the charging and extraction grids are set at 6.35 mm. The gap between the charging and extraction grids is set at 12.7 mm. The holes in the grids have a diameter of 6.35 mm, and the charging pads have a diameter of 2 mm and a height of 0.8 mm. The insulating liquid is at a height of 3.18 mm above the charging grid.

The insulating liquid filling the bottom two electrode gaps is silicone oil purchased from Clearco, which has a relative dielectric constant of approximately 1.97, a density of 965 kg/m^3 , a surface tension of 0.0209 N/m ,³³ a conductivity on the order of 10^{-13} S/m ,³⁴ and an electrical breakdown strength of approximately 15 MV/m .⁷¹

The experiment was performed using spherical particles made of aluminum and a tin/antimony alloy with diameters ranging from approximately $300 \text{ }\mu\text{m}$ to $1,600 \text{ }\mu\text{m}$ and cylindrical aluminum and tungsten particles with diameters ranging from approximately $25 \text{ }\mu\text{m}$ to $300 \text{ }\mu\text{m}$ and lengths ranging from approximately 0.7 mm to 2.2 mm . Table 4.6 lists the dimensions of all the particles used in the experiment along with the densities.

Particle Shape	Particle Material	Particle Diameter (mm)	Particle Length (mm)	Particle Density (kg/m^3)
Sphere	Al	0.79 ± 0.025	NA	2,700
Sphere	95Sn/5Sb	0.51 ± 0.025	NA	7,300
Sphere	95Sn/5Sb	0.30 ± 0.025	NA	7,300
Cylinder	Al	0.33 ± 0.025	2.2 ± 0.2	2,700
Cylinder	W	0.152	2.0 ± 0.2	19,250
Cylinder	W	0.102	1.3 ± 0.2	19,250
Cylinder	W	0.50	0.7 ± 0.1	19,250
Cylinder	W	0.025	1.5 ± 0.2	19,250

Table 4.6: Properties of the particles used in the particle extraction experiment.

4.4. Experimental Results

Figure 4.17 and Figure 4.18 are a series of frames from the high speed camera showing the successful extraction of an aluminum spherical and cylindrical particle, respectively, from 100 cSt silicone oil. The spherical particle has a diameter of 790 μm , and the cylindrical particle has a diameter of 330 μm and a length of 1.25 mm. Frames (a) show the particles in contact with the charging pads just before the charging electric field is applied. After generating the charging electric field, the particles are charged and transported through the liquid towards the liquid surface as shown in frames (b). Frames (c) show the particles during the extraction process. Finally, the surface tension is broken and the particles are accelerated away from the liquid surface in frames (d).

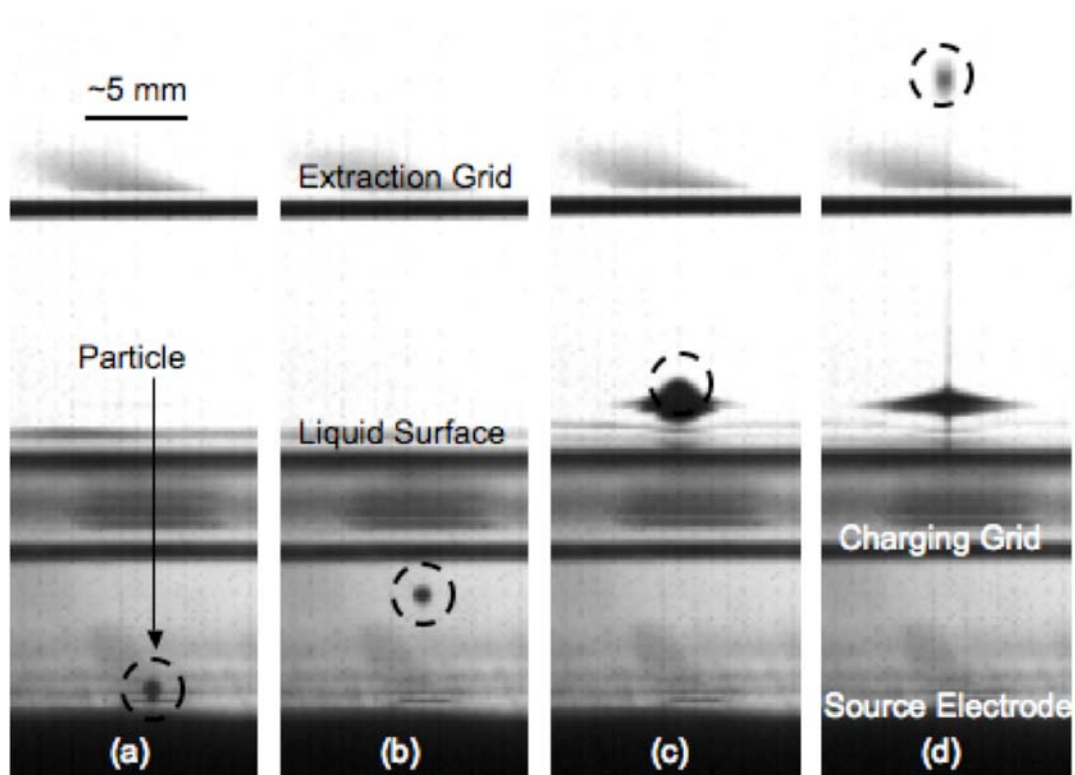


Figure 4.17: Series of frames showing the successful extraction of a spherical particle from 100 cSt silicone oil. See Table 4.6 for particle details.

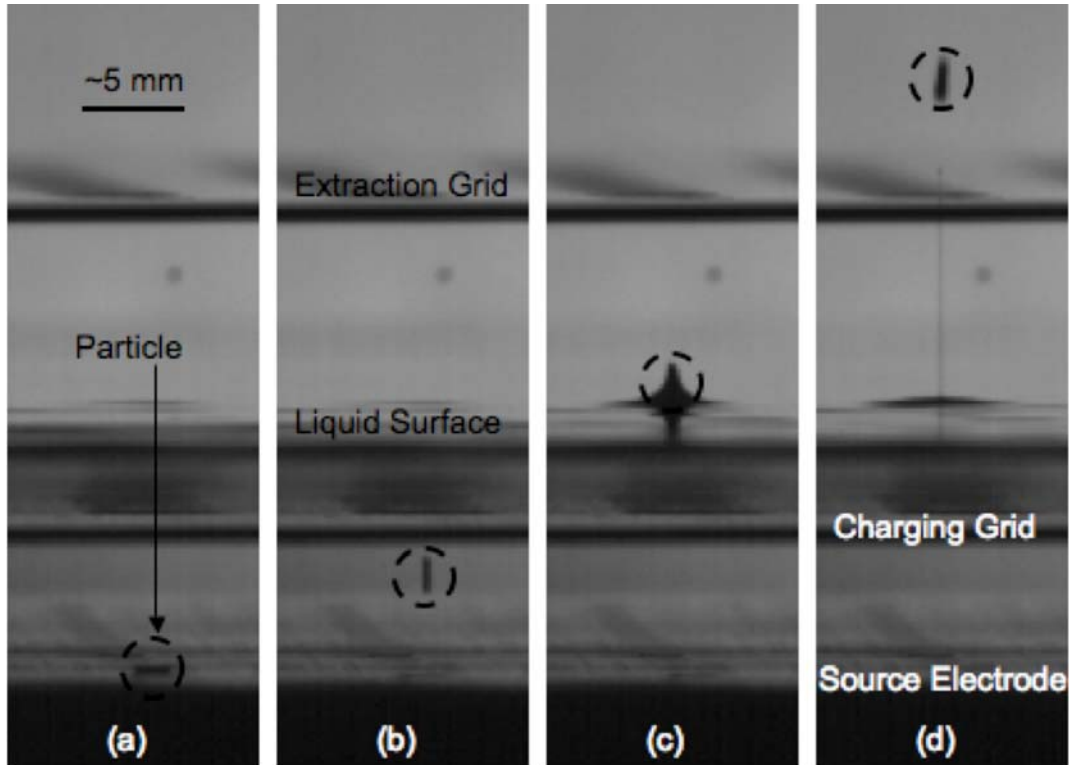


Figure 4.18: Series of frames showing the successful extraction of a cylindrical particle from 100 cSt silicone oil. See Table 4.6 for particle details.

The series of frames from Figure 4.17 and Figure 4.18 demonstrate the feasibility of extracting charged spherical and cylindrical particles from an insulating liquid with an applied high strength electric field. Note that the extraction of all the particles listed in Table 4.6 was verified.

Figure 4.19 plots the measured threshold extraction electric fields required to extract the spherical particles listed in Table 4.6 as a function of the charging electric field. Also included in the plot is the lower ($\delta_e = 0$) bound of the theoretical predictions from Equation (4.7). There is a maximum estimated total error of approximately 10% in the measurements, which was determined with the sum of squares method. The error in the measured extraction electric fields is due mostly to three error terms in the experimental

setup. These error terms are as follows: the liquid height (8.5%), the electrode gap separation (4%), and the applied voltage (0.3%).

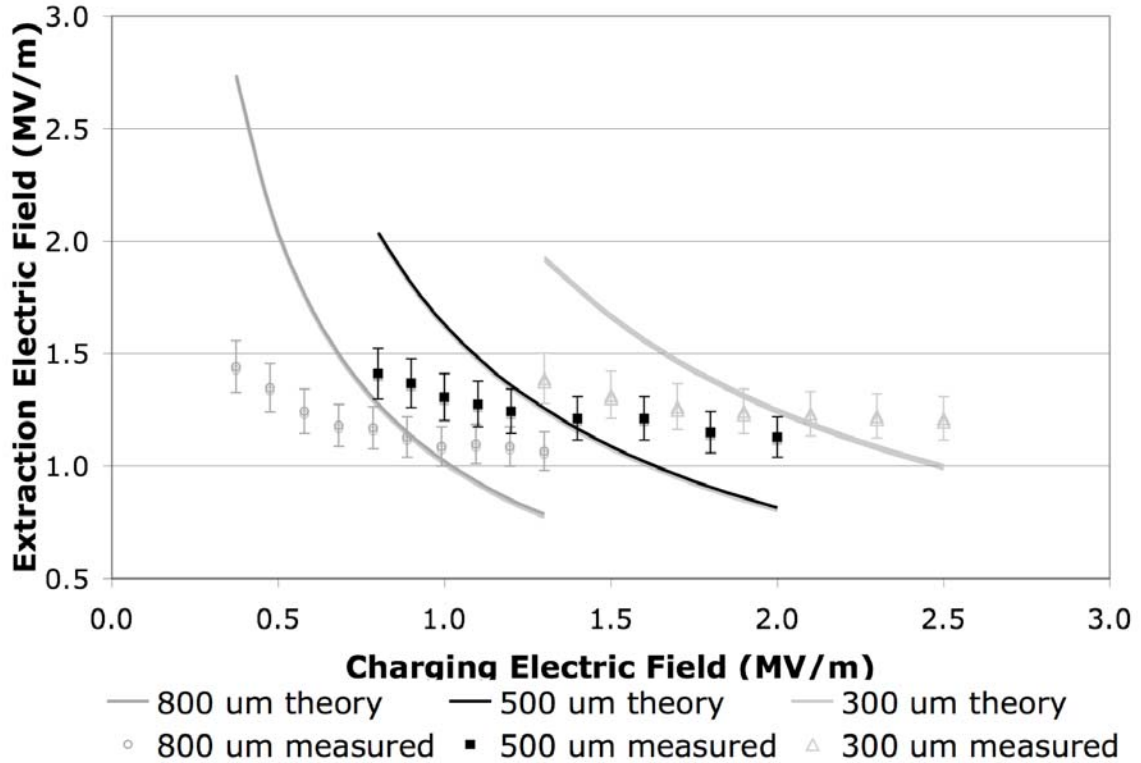


Figure 4.19: Measured electric fields required for spherical particle extraction as a function of the charging electric field for various particle sizes.

The experimental results plotted in Figure 4.19 suggest that the spherical particles were extracted on the order of the lower bound of the theoretical predictions. But, note that the theoretical predictions over estimate the required field strength when a relatively low charging field is used and underestimate the required field strength when a relatively high charging field is used.

Next, Table 4.7 lists the measured threshold extraction electric fields required to extract the cylindrical particles from silicone oil for a given charging electric field. Also

listed in the table are the lower ($\delta_l = 0$) and upper ($\delta_l = r$) bounds of the theoretical extraction electric fields from Equation (4.13).

Particle Shape	Material	Particle Dia. (μm)	Aspect Ratio	Charging Field (MV/m)	Measured Extraction Field (kV/m)	Lower Theoretical Extraction Field (kV/m)	Upper Theoretical Extraction Field (kV/m)
Cylinder	Al	330	6.67	1.5	470 ± 45	150	290
Cylinder	W	152	13	1.5	470 ± 45	150	240
Cylinder	W	102	13	1.5	550 ± 50	170	310
Cylinder	W	50.8	13	1.5	630 ± 60	290	570
Cylinder	W	25.4	60	1.5	160 ± 20	40	80

Table 4.7: Measured minimum required extraction electric fields for various spherical and cylindrical particles.

The experimental results listed in Table 4.7 suggest that the cylindrical particles required much greater extraction electric fields than predicted.

It is important to note that the frames from Figure 4.17 and Figure 4.18 show liquid strands clinging to the particles after they have been extracted, which is a result of the liquid draining slowly from the particle surface. Since the strands form after the particles have been extracted from the liquid, it is not expected that they will affect the strength of the electric field required to achieve extraction. In the laboratory environment, these strands eventually break off and form small droplets that drop back into the liquid. When using this system as an in-space thruster, these liquid strands and droplets could have severe implications, which include changing the propellant specific-charge and introducing free liquid droplets that could limit the thruster lifetime. Future work should focus on developing methods to prevent the liquid from wetting the particles so that these liquid strands do not occur.

Explanations for the deviation of the experimental results for both spherical and cylindrical particles from the predictions are the topics of the following section.

4.5. Discussion of Experimental Results

The deviations of the experimental results from the theoretical models are most likely a result of several errors in the models. First, the strength of the extraction electric field given by Equation (4.2) may not be completely accurate throughout the duration of the experiment. It is only valid when the liquid surface is completely charge free. Since the extraction electric field was applied before the charging electric field was turned on, it is very reasonable that some charge migrated through the liquid and accumulated on the liquid surface. For the liquid properties and the prototype dimensions presented in a previous section, it is possible that when the liquid surface is completely charged, the strength of the extraction electric field is increased by a factor of approximately 1.2.

Also, recall from Section 4.2.1 that the extraction models assume that the extraction electric field acting on the particles at the liquid surface is uniform. But, it is likely that as the particles begin to deform the liquid surface, the electric field may intensify on the perturbations when the surrounding liquid surface is slightly charged. This field intensification increases the local electric field used to extract the particle. The derivation of this field intensification is beyond the scope of this thesis, but it is expected to be a function of the liquid properties, the surface charge density of the liquid and the particle, and the shape of the perturbation. Based on the analysis of the field-focusing on a fully charged liquid surface perturbation from Figure 3.4, it is reasonable to expect that the

field intensification may increase the local extraction electric field by as much as another factor of 3.

Second, it is possible that incomplete particle charging is another error in the models. Recall that Chapter 2 investigated the time required to charge particles against a source electrode and suggested that an inadequate electrical contact between the source electrode and the particle limits the rate at which the particle can be charged, which, in certain situations, can lead to incomplete particle charging. Note that using a low conductivity particle material would also limit the rate of particle charging. Results suggest this problem is more significant when higher strength charging electric fields are applied, which may result in a particle being removed from the source electrode prior to achieving its final charge state. The experimental results from Chapter 2 suggest that some of the spherical particles were only charged to approximately 80% of the predicted charge when electric fields on the order of 650 kV/m were used. It is also expected that as the charging electric field is increased to the values used in the extraction experiment, the particles would acquire even a lower percentage of the predicted charge. This could explain why the spherical particles charged with a relatively high strength charging field required a greater extraction field than predicted. It could also explain why the measured data does not scale as predicted by the models. It is recommended that future experiments use materials that resist oxidation so that the particle charging times do not limit particle extraction.

Video recordings from the cylindrical particle extraction experiments confirm that the cylindrical particles are lifted from the source electrode prior to achieving a vertical orientation. The particles are initially placed on the source electrode in a horizontal

orientation and then rotated toward vertical when the charging electric field is generated. But, videos show that the particles considered are rotating to an average of 42° off vertical before leaving the electrode surface as shown in Figure 4.20. A non-vertical particle acquires less charge due to a decrease in field focusing at the particle tip, and leads to an increase in the required extraction electric field for cylindrical particles. Future models should include the angle of the particle when it leaves contact with the source electrode in the extraction models.

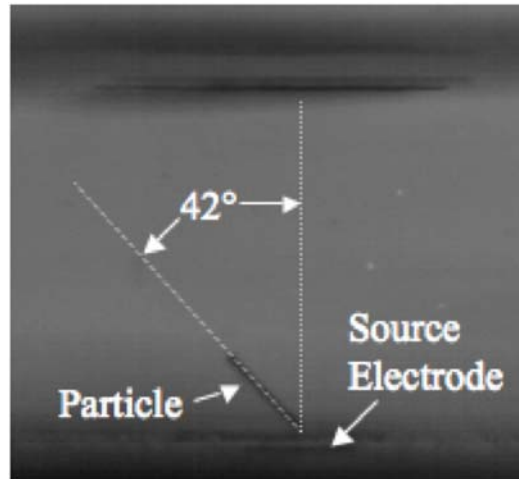


Figure 4.20: Photograph of a cylindrical particle at approximately 42° off vertical just before removal from the source electrode.

Another error in the extraction models may be the value used for the liquid surface tension. As mentioned in Chapter 3, the liquid surface tension is a function of its temperature. It is possible that any localized heating or cooling could have changed the liquid surface tension as shown in Figure 3.5, which changes the strength of the required extraction electric field. Assuming a maximum temperature range during testing of 18°C to 32°C , it is possible to predict the error in the measured extraction electric fields associated with surface tension. Using a temperature coefficient of surface tension, γ_T ,

for silicone oil of -0.072 mN/m-K from Figure 3.5, the surface tension may range from approximately 0.0204 N/m to 0.0214 N/m . This variability in surface tension can be shown to produce an error of approximately 2.5% in the required extraction electric fields. Therefore, it is not expected to be a significant error in the models.

The final possible error that will be addressed in this thesis is the thickness of the liquid shell coating the particle during extraction. Recall that the models assume the liquid shell to be of uniform thickness ranging from zero to the radius of the particle. According to the extraction models in Equations (4.7) and (4.15), the thickness of the liquid shell has the potential to produce as much as 100% error in the measured extraction electric fields and could be another significant factor leading to the deviations of the measured data from the predicted values.

4.6. Effects of Particle Extraction on Micro- and Nano-Particle Thrusters

The insulating liquid configuration used to supply charged particles as propellant for an electrostatic thruster may prove to be insufficient. To obtain sufficiently high specific impulses for use as an electric propulsion system, the particle size needs to be scaled down. The maximum expected specific impulse that can be obtained using the insulating liquid configuration is calculated from the minimum extractable particle diameters from Table 4.5 using the expression for the specific impulse from Equation (1.6).

To maximize the specific impulse, the smallest particle size from the range of extractable particles is used. The liquid medium is silicone oil. All particles considered have a density of $1,000 \text{ kg/m}^3$ and are accelerated through a potential drop of 40 kV. It is important to understand that using a lower density metal for the particles and a higher

accelerating potential will increase the specific impulse as dictated by Equation (1.6), but the parameters chosen here are adequate to give a first order approximation. Also recall that the charging electric field was chosen so the maximum electric field within the liquid region, which is focused at the tip of the particle, would be equal to the dielectric breakdown of the liquid.

Particle Shape	Aspect Ratio	Charging Electric Field (kV/m)	Minimum Extractable Particle Diameter	Maximum Isp (s)
Sphere	N/A	3,600	44 μm	2
Cylinder	10	770	2 μm	7
Cylinder	30	300	0.3 μm	15
Cylinder	80	120	0.06 μm	30

Table 4.8: Maximum obtainable specific impulses using the particles from Table 4.5.

The obtainable specific impulses listed in Table 4.8 are a couple orders of magnitude lower than current electric propulsion systems. To be useful, the insulating liquid configuration must be capable of extracting particles with much smaller diameters or much higher aspect ratio must be used.

Recall from Section 3.2.1 that the surface tension of a liquid scales inversely with its temperature. This suggests that when the temperature is reduced, the surface tension increases. The increased surface tension increases both the electric fields required to initiate the liquid instability and to extract particles. When the temperature is increased, the surface tension decreases. The decreased surface tension decreases both the electric fields required to initiate the liquid instability and to extract particles.

4.7. Conclusion

A method of extracting spherical and cylindrical conducting particles from an insulating liquid with an applied electric field was investigated for use with micro- and nano- particle thrusters. The theoretical models suggest particle extraction is possible, and the experimental results proved the feasibility. The required strength of the extraction electric field is dependent on particle size, particle charge, and the surface tension of the liquid. But, the strength of the extraction electric field is limited by the tendency of the liquid surface to become unstable, which in turn limits the size of extractable particles.

Current models suggest that the smallest extractable cylindrical particles are on the order of many tens of nanometers in diameter. When particles with a density of $1,000 \text{ kg/m}^3$ are accelerated with a potential drop of 40 kV, the maximum obtainable specific impulse is on the order of 40 seconds, which is much less than required for use with an electric propulsion system.

The ability to extract particles from an insulating liquid with an applied electric field may be a significant limiting factor for the insulating liquid configuration as a micro- and nano-particles thruster.

Chapter 5

Adhesion and Cohesion of Dry Micro- and Nano-Particles

5.1. Introduction

As a result of the insulating liquid configuration studies discussed in Chapter 4, a parallel design configuration is being pursued that eliminates the use of the liquid and the microfluidic channels, and instead transports, charges, and ejects dry micro- and nano-particles. The operational design of this system, which operates without a liquid, will be discussed in the next chapter. This thesis refers to this approach as the “no liquid design configuration.” Figure 5.1 is a preliminary illustration showing only the charging and acceleration stages of the “no liquid design configuration”, and not accounting for the particle delivery system. The spherical particles are charged in contact with the source electrode by the applied charging electric field, E_{ch} . Once charged, the particles are removed from the source electrode and are accelerated through the acceleration channels by the applied electric potential drops, V_{ch} and V_{ac} .

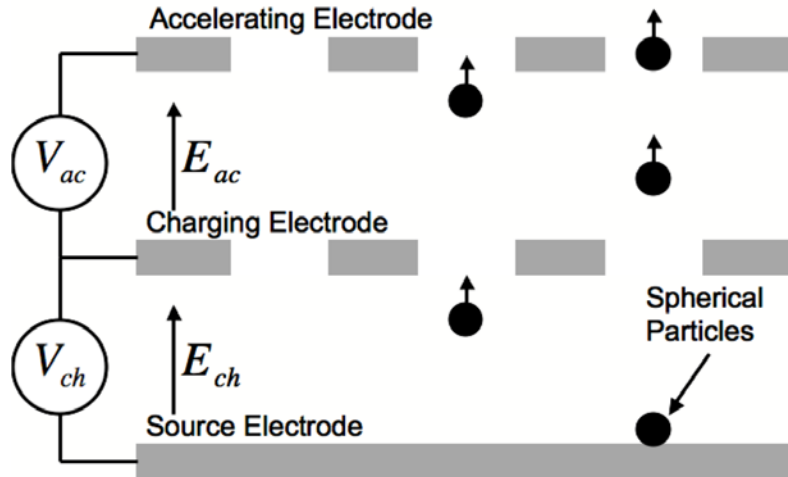


Figure 5.1: Illustration of the no liquid design configuration showing only the charging and accelerating processes. Not included is the particle delivery system.

Previous studies working with dry nanometer and micron-sized particles explain that particles on this size scale have a strong tendency to aggregate with each other and to stick other objects that they contact.⁷² This thesis refers to aggregation between particles as cohesion and particles sticking to other objects as adhesion. Therefore, an understanding of the adhesion and cohesion forces and how to overcome them is extremely important to the development of micro- and nano-particle thrusters. This chapter primarily focuses on the adhesion force between a single conducting spherical particle and the planar source electrode shown in Figure 5.1, but does briefly touch on the cohesion force. In addition, the electric force arising from the charging electric field acting on the charged particle is investigated, both theoretically and experimentally, as a method to overcome the adhesion force and achieve particle removal, specifically for the application of micro- and nano-particle thrusters.⁷³

5.2. Adhesion and Cohesion Forces

There are four primary forces generally credited for the adhesion and cohesion of small particles.^{72,74} The relative magnitude of these forces is dependent on the size of the particles, the materials involved, and the environmental conditions. The following subsections briefly present these forces and discuss their relevance to micro- and nano-particle thrusters.

5.2.1. Electrostatic Force from Excess Charge

The electrostatic force between two charged bodies is well known to be dependent on the charge of each body, q_1 and q_2 , and the distance between the charge centers, z_c , when the bodies are modeled as point sources.²⁷

$$F_e = \frac{q_1 q_2}{4\pi\epsilon z_c^2} \quad (5.1)$$

The electrostatic force is attractive when the bodies are charged with opposite polarity, and the force is repulsive when the bodies are charged with the same polarity. When considering the attractive force between two bodies in contact, this force is generally only important when one or both of the charged bodies are poor conductors, which does not provide an adequate electrical contact to allow the charge to pass between the bodies. When both charged bodies in contact are good conductors with a good electrical contact, as is the expected case for micro- and nano-particle thrusters, charge passes between the bodies until equilibrium is reached, ensuring that the two bodies in contact are charged

with the same polarity, which ensures that the electrostatic force is not attractive. Therefore, it is reasonable to ignore this force for the analysis presented in this chapter.

5.2.2. Electrical Double Layer Force

An electrical double layer force arises from a small electrical potential difference between the two bodies in contact that generally has a value up to 0.5 V.⁷⁴ The potential difference is a result of the differences in the local energy states and electron work functions of the two materials in contact, which leads to the transfer of electrons between the materials in contact. The electrical double layer force is directly proportional to the size of the particle and the square of the potential difference and inversely proportional to the distance between the bodies.

$$F_{edl} \propto \frac{rV_{edl}^2}{z} \quad (5.2)$$

According to Bowling,⁷⁴ the electrical double layer force is usually more than an order of magnitude less than the van der Waals force, which is discussed shortly. Therefore, it is reasonable for this analysis to neglect this force.

5.2.3. Liquid Surface Tension Force

It is possible for the two bodies in contact to be held together by a thin liquid film coating that may form if the bodies in contact are exposed to high humidity or directly subjected to a liquid. The force from the liquid film is due to the surface tension of the

liquid and is directly proportional to the size of the bodies in contact and the surface tension of the liquid.⁵⁰

$$F_{\ell} \propto r\gamma \quad (5.3)$$

According to Bowling,⁷⁴ the liquid surface tension force can be significant for particles in the nanometer and micron ranges. But, it is possible for the micro- and nano-particle thrusters to avoid the formation of the liquid film by controlling the operational environment. For example, the adhesion experiments presented later in this chapter were performed at pressures on the order of 10^{-8} Torr. Therefore, this chapter neglects the liquid surface tension force. Note that when a liquid film is present, it is expected that the surface tension force will be significant. This has been demonstrated where the liquid film was a result of humidity in the air.

5.2.4. Van der Waals Force

The van der Waals force has the potential to be a dominating force contributing to the cohesion and adhesion of particles smaller than several hundred microns in size,⁷⁴ and is the focus of the remainder of this chapter. The van der Waals force between molecules arises from the force between permanent, temporary, and/or induced dipoles. In the case of non-polar molecules, the movement of the electron cloud with respect to the nucleus may temporarily create a dipole. This temporary dipole creates an electric field, which induces dipoles in neighboring molecules. The resulting dipoles attract each other as the positive end of one molecule aligns with the negative end of another.⁷²

The van der Waals force between macroscopic bodies is calculated by taking the summation of the van der Waals forces between the molecules of the different bodies. The van der Waals force density of an infinite planar surface on an adjacent surface is calculated to be dependent on the Lifshitz-van der Waals constant, h , and the separation between the surfaces, z .⁷² Note that the temperature dependence on the van der Waals force between non-polar molecules has been shown to be negligible.⁷⁵

$$\frac{F_{vdw}}{A} \approx \frac{h}{8\pi^2 z^3} \quad (5.4)$$

The Lifshitz-van der Waals constant has units of energy and is a function of the material combination involved. The values for select materials are published, but are disputed by many authors, which is discussed in Section 5.7. It is accepted that typical values of the Lifshitz-van der Waals constant range from 0.6 to 9.0 eV.⁷⁴ According to Curran, a minimum separation distance between the surfaces of 4 Angstroms, z , is acceptable when evaluating the van der Waals force.⁷⁶

Using the van der Waals force density in Equation (5.4), the force between a spherical particle and a planar surface is calculated, which is referred to as adhesion in this thesis. Figure 5.2 depicts the adhesion of a spherical particle with radius, r , on an infinite planar surface.

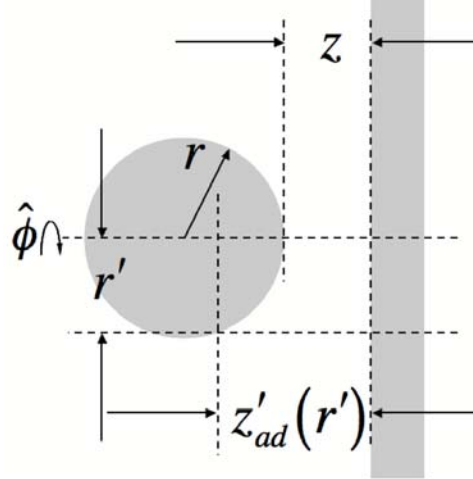


Figure 5.2: Illustration of a spherical particle in contact with a planar surface (Adhesion).

The separation distance between the spherical particle and the planar surface, $z'_{ad}(r')$, is a function of the particle radius and the minimum separation between the particle and the surface.

$$z'_{ad}(r') = z + r - \sqrt{r^2 - r'^2} \quad (5.5)$$

The total adhesion van der Waals force is calculated by substituting Equation (5.5) into the force density expression in Equation (5.4) and integrating over the surface of the particle exposed to the planar surface.

$$F_{vdw-ad} = \int_0^{2\pi} \int_0^r \frac{h}{8\pi^2 z'_{ad}(r')^3} r' dr' d\phi \quad (5.6)$$

The resulting adhesion van der Waals force is only dependent on the particle radius, the minimum separation distance, and the Lifshitz-van der Waals constant.

$$F_{vdw-ad} = \frac{hr^2}{8\pi z^2(r+z)} \quad (5.7)$$

This expression is reduced by assuming that the particle radius is much larger than the minimum separation distance.⁷²

$$F_{vdw-ad} \approx \frac{hr}{8\pi z^2} \quad (5.8)$$

The simple expression for the adhesion van der Waals force scales directly with the particle radius and inversely with the square of the minimum separation.

Using a similar derivation, the force between two identical spherical particles can be calculated, which is referred to as cohesion in this thesis. Figure 5.3 depicts the cohesion of two spherical particles with radii, r .

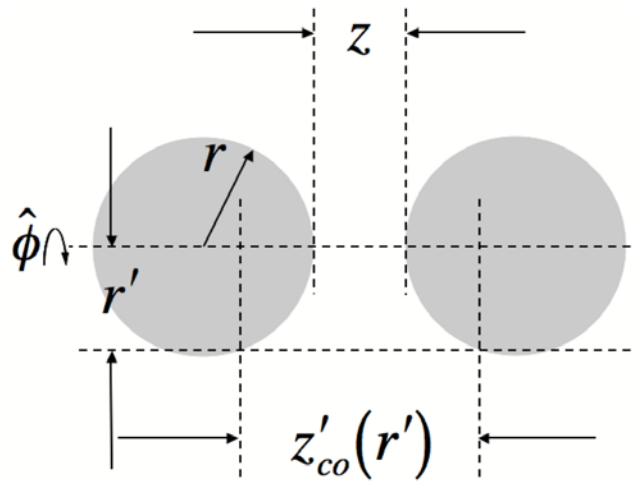


Figure 5.3: Illustration of two spherical particles in contact (cohesion).

Assuming that the particles radii are much larger than the minimum separation distance, the van der Waals force can be approximated.⁷²

$$F_{vdw-co} \approx \frac{hr}{16\pi\epsilon^2} \quad (5.9)$$

The simple expression for the cohesion van der Waals force scales directly with the particles radii and inversely with the square of the minimum separation.

A comparison of the van der Waals forces reveals that the adhesion and cohesion forces scale the same with the particle size, but the adhesion force is approximately twice the cohesion force when using particles of the same size. Figure 5.4 is a plot of the adhesion and cohesion forces as a function of particle diameter when using a Lifshitz-van der Waals constant of 9 eV, which is the maximum predicted value. For comparison purposes, the weight of the particle is included in the plot when the particle is made from aluminum.

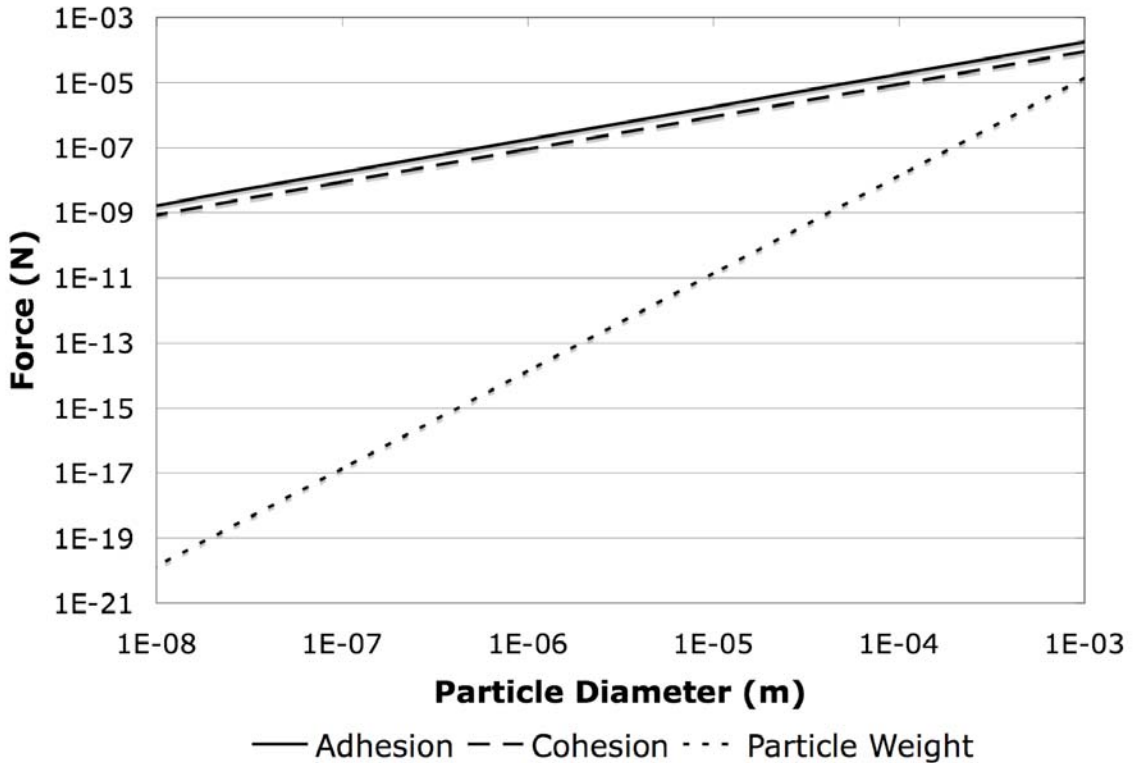


Figure 5.4: Plot of the adhesion and cohesion forces using a Lifshitz-van der Waals constant of 9 eV and the weight of an aluminum particle.

The plot in Figure 5.4 shows that as the particle size decreases, the adhesion and cohesion forces decrease. This is somewhat misleading because, by comparison to the gravitational force, both the adhesion and cohesion forces are greater than the gravitational force over the entire range of the plot (10 nm to 1 mm). In fact, the gravitational force decreases faster ($\sim r^3$) than the van der Waals forces ($\sim r$) as the particle size decreases, meaning that the van der Waals forces become more significant for smaller particles. Another method of understanding the adhesion and cohesion forces is through the potential energy in the bonds. The energy in the adhesion bond is approximated by integrating the adhesion force from Equation (5.8).

$$W_{vdw-ad} \approx \int_z^{\infty} \frac{hr}{8\pi z'^2} dz' \approx \frac{hr}{8\pi z} \quad (5.10)$$

Similarly, the energy in the cohesion bond is approximated by integrating the cohesion force from Equation (5.9).

$$W_{vdw-co} \approx \int_z^{\infty} \frac{hr}{16\pi z'^2} dz' \approx \frac{hr}{16\pi z} \quad (5.11)$$

Figure 5.5 is a plot of the energies in the adhesion and cohesion bonds as a function of particle diameter when using a Lifshitz-van der Waals constant of 9 eV.

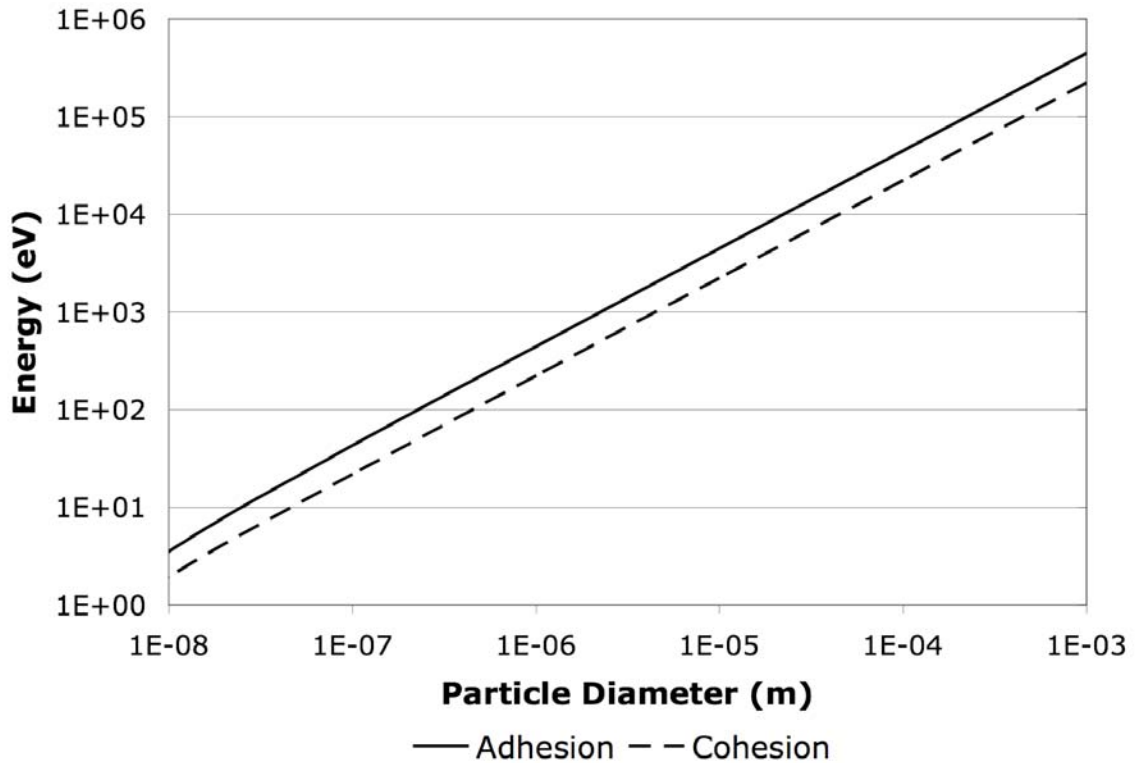


Figure 5.5: Plot of the energies in the adhesion and cohesion bonds using a Lifshitz-van der Waals constant of 9 eV.

Figure 5.5 shows that as the particle size decreases, the adhesion and cohesion forces decrease. Again, this is somewhat misleading. To help clarify, the required accelerations imparted onto the particles to overcome the adhesion and cohesion bonds are plotted in Figure 5.6. The accelerations are calculated by dividing the forces by the particle mass, when using a particle density of $2,700 \text{ kg/m}^3$, which is the density of aluminum.

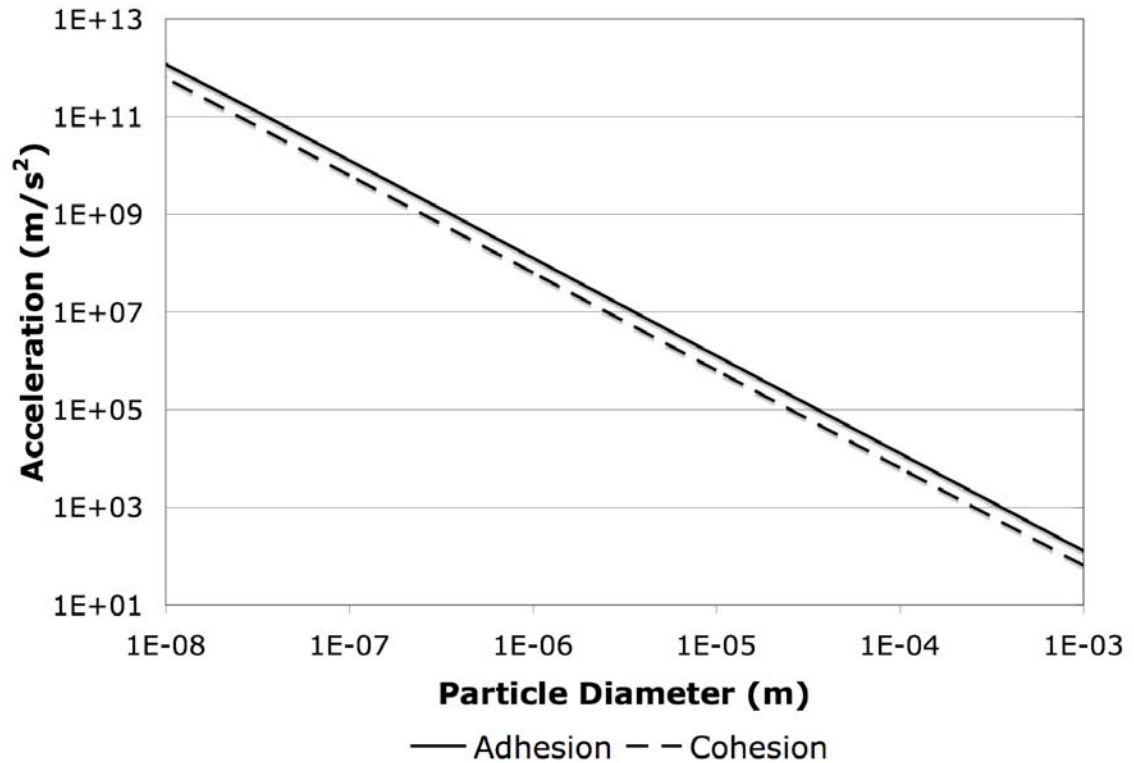


Figure 5.6: Plot of the required accelerations to overcome the adhesion and cohesion forces using a Lifshitz-van der Waals constant of 9 eV and a particle density of 2,700 kg/m³.

The required accelerations to overcome the adhesion and cohesion forces scale inversely with the square of the particle radius. Therefore, as the particle size decreases, the required acceleration increases, illustrating that, as the particle size decreases, the van der Waals forces dominate other forces such as gravity.

This section demonstrated that when considering the adhesion and cohesion of conducting micro- and nano-spherical particles, the dominant force is most likely the van-der Waals force given in Equations (5.8) and (5.9), respectively. The following sections investigate overcoming the adhesion force using high strength electric fields.

5.3. Overcoming the Adhesion Force Using High Strength Electric Fields

The removal of micro- and nano-particles from surfaces is important to many applications, particularly in the MEMS and pharmaceutical industries. A few techniques currently used for particle removal are ultrasonic vibration, mechanical vibration, and laser irradiation.^{72,77} These techniques work by accelerating the particles relative to the surface. This chapter investigates an alternative method of particle removal using high strength electric fields, which lends itself nicely to the design of micro- and nano-particle thrusters, which use high strength electric fields to charge the particles when they are in contact with the source electrode. This section presents the derivation of the electric force on a spherical conducting particle when in contact with an infinite planar electrode and applies this force to determine the required electric field to overcome the van der Waals adhesion force.

5.3.1. Electric Force on a Spherical Particle in Contact with a Planar Electrode

The model for spherical particle removal from an infinite planar electrode is identical to the model shown in Figure 2.1, which was used to determine the charge acquired by a spherical particle in contact with an infinite planar electrode. The model is reproduced in Figure 5.1 and consists of two infinite parallel electrodes with a conducting spherical particle in contact with the upper surface of the bottom electrode. An electric potential bias, V , is applied across the electrodes to generate an electric field within the gap.

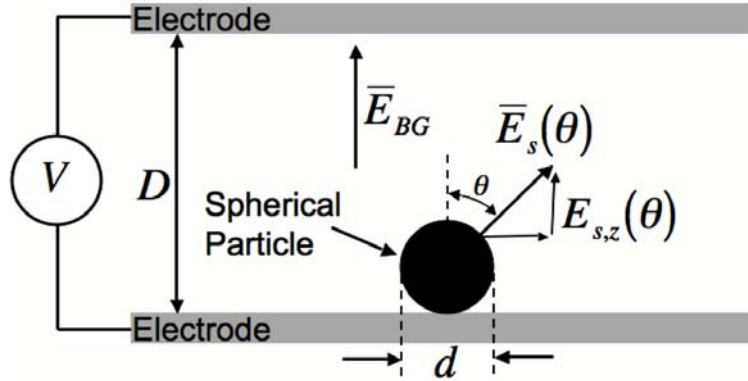


Figure 5.7: Model for the removal of a conducting spherical particle from a planar electrode using a high strength electric field.

The background electric field, E_{BG} , is defined as the electric field in the electrode gap without the presence of the particle and is only dependent on the applied voltage and the electrode separation.

$$E_{BG} = \frac{V}{D} \quad (5.12)$$

The presence of the particle in the electrode gap modifies the electric field, with the largest field modification occurring in the vicinity of the particle. The electric field at the surface of the conducting particle, E_s , is normal to the particle surface and is the key to understanding the electric force acting on the particle, just as it was the key to understanding the total charge acquired by the particle in Chapter 2. The following derivation of the electric force on the particle follows the derivation of the charge acquired by the particle closely with some important differences. Due to the similarity of the derivations, some material is repeated, but the author feels it is important to preserve the complete derivation.

The electric force acting on the particle is the product of the particle's surface charge density with the surface electric field and integrated over the particle's surface.⁷⁸

$$\bar{F}_{el} = \frac{1}{2} \oint \rho_s \bar{E} dA \quad (5.13)$$

Due to the symmetry about ϕ , the surface charge density and the electric field at the surface of the particle are functions of θ , where $\theta=0^\circ$ corresponds to the top of the particle and $\theta=180^\circ$ corresponds to the bottom of the particle. In addition, the net force on the particle is only in the vertical direction.

$$F_{el,z} = \frac{1}{2} \oint \rho_s(\theta) E_{s,z}(\theta) dA \quad (5.14)$$

The surface charge density is dependent on the electric field normal to the particle surface and the permittivity of the surrounding medium.

$$\rho_s(\theta) = \hat{r} \cdot \epsilon \bar{E}_s(\theta) = \epsilon E_s(\theta) \quad (5.15)$$

The vertical component of the electric field at the surface of the particle is easily calculated.

$$E_{s,z}(\theta) = E_s(\theta) \cos(\theta) \quad (5.16)$$

The electric field at the surface of the particle is a function of the background electric field, θ , and the ratio of the particle diameter to the electrode gap, ζ_{sph} , as is any symmetrical perturbation or particle.²⁸

$$E_s(\theta) = E_{BG} \alpha_{sph}(\theta, \zeta_{sph}) \quad (5.17)$$

$\alpha_{sph}(\theta, \zeta_{sph})$ can be thought of as the field-focusing factor at the surface of the particle. Equations (5.15), (5.16), and (5.17) are substituted into Equation (5.14) so that the only unknown in the electric force on the particle is $\alpha_{sph}(\theta, \zeta_{sph})$.

$$F_{el,z} = \frac{1}{2} \int_0^{2\pi} \int_0^\pi \epsilon E_{BG}^2 \alpha_{sph}(\theta, \zeta_{sph})^2 \cos(\theta) r^2 \sin(\theta) d\theta d\phi \quad (5.18)$$

Equation (5.18) is simplified leaving only the θ dependent functions inside the integral.

$$F_{el,z} = \pi r^2 \epsilon E_{BG}^2 \int_0^\pi \alpha_{sph}(\theta, \zeta_{sph})^2 \cos(\theta) \sin(\theta) d\theta = \pi r^2 \epsilon E_{BG}^2 A_f(\zeta_{sph}) \quad (5.19)$$

The solution to the integral in Equation (5.19), $A_f(\zeta_{sph})$, is a function of the ratio of the electrode gap to the particle diameter and can be thought of as the integrated field focusing factor for the electric force on the particle.

$$A_f(\zeta_{sph}) = \int_0^\pi \alpha_{sph}(\theta, \zeta_{sph})^2 \cos(\theta) \sin(\theta) d\theta \quad (5.20)$$

Finally, the electric force on the particle when in contact with the electrode is directly proportional to the square of the particle radius, the square of the background electric field, the permittivity of the surrounding medium, and a function of ζ_{sph} .

Before finding values for $A_f(\zeta_{\text{sph}})$, $\alpha_{\text{sph}}(\theta, \zeta_{\text{sph}})$ needs to be examined. $\alpha_{\text{sph}}(\theta, \zeta_{\text{sph}})$ was investigated for conducting spherical particles in the setup shown in Figure 5.7 by employing COMSOLTM in Section 2.2.1. Using the plot of $\alpha_{\text{sph}}(\theta, \zeta_{\text{sph}})$ in Figure 2.2 and Equation (5.19), $A_f(\zeta_{\text{sph}})$ is numerically calculated. Figure 5.8 is a plot of $A_f(\zeta_{\text{sph}})$ as ζ_{sph} ranges from 0.05 to 0.95.

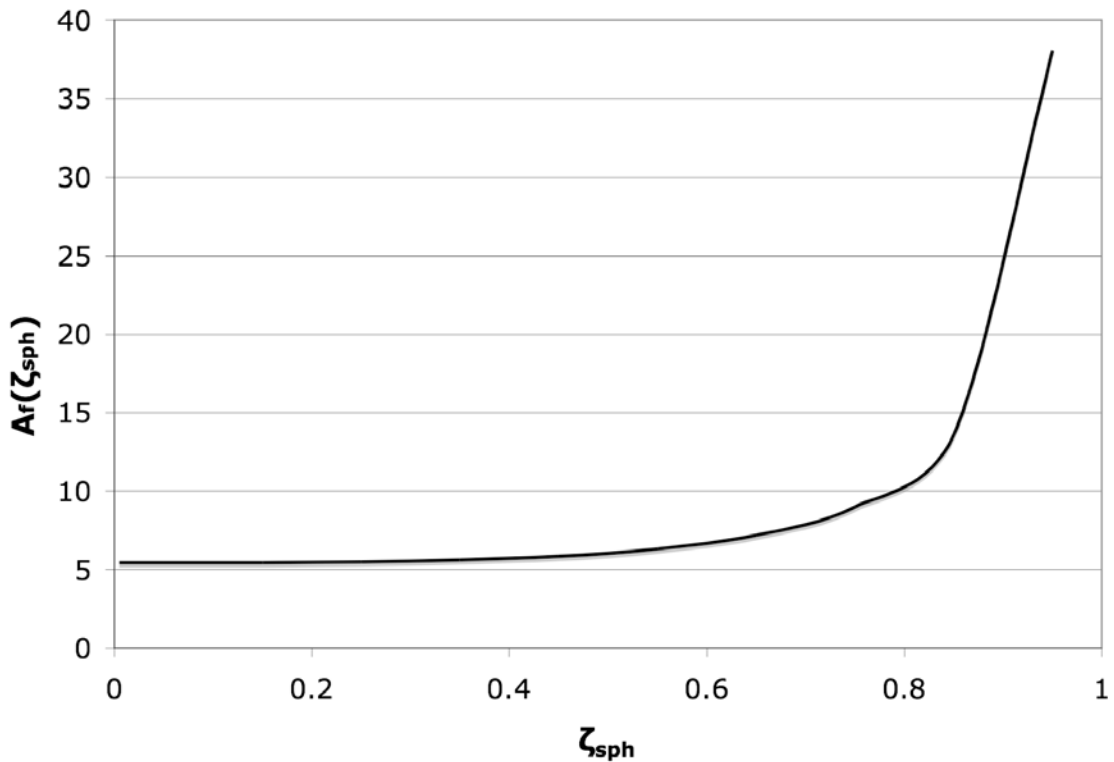


Figure 5.8: Plot of $A_f(\zeta_{\text{sph}})$ as a function of ζ_{sph} .

According to Figure 5.8, $A_f(\zeta_{\text{sph}})$ approaches approximately 5.43 as the ratio of the particle diameter to the electrode gap approaches 0 ($\zeta_{\text{sph}} \rightarrow 0$). This approximation appears to be valid to within less than 4% error when the particle diameter is less than

one-third of the electrode gap ($\zeta_{\text{sph}} < 0.33$). As the particle size increases relative to the electrode gap, $A_f(\zeta_{\text{sph}})$ increases. Figure 5.8 along with Equation (5.19) completes the derivation of the electric force on the particle when in contact with the source electrode, and suggests that as ζ_{sph} increases, the electric force on the particle increases when holding everything else constant. However, this result can be somewhat misleading. When removing spherical particles from a source electrode as shown in Figure 5.7, it is important to maintain the maximum electric field in the system, which is located at the top of the particle, below the electrical breakdown of the background medium. If this maximum electric field is held constant as ζ_{sph} varies, the background electric field does not remain constant.

The following analysis investigates the effects on the electric force as ζ_{sph} varies while holding the maximum electric field in the system constant. The maximum electric field at the top of the particle, E_{max} , is determined from Equation (2.8). The expression in Equation (2.8) is substituted into Equation (5.19) to find the electric force on the spherical particle when the maximum electric field is held constant. Note that when $\theta=0^\circ$, it will be omitted for the remainder of this analysis.

$$F_{el,z}(\zeta_{\text{sph}}) = \pi r^2 \epsilon \left(\frac{E_{\text{max}}}{\alpha_{\text{sph}}(\zeta_{\text{sph}})} \right)^2 A_f(\zeta_{\text{sph}}) \quad (5.21)$$

The ratio of the electric force on the particle when $\zeta_{\text{sph}}=\zeta_1$ to the force when $\zeta_{\text{sph}}=\zeta_2$ is only dependent on $\alpha_{\text{sph}}(\zeta_{\text{sph}})$ and $A_{\text{sph}}(\zeta_{\text{sph}})$.

$$\frac{F_{el,z}(\xi_1)}{F_{el,z}(\xi_2)} = \frac{A_f(\xi_1)}{A_f(\xi_2)} \left[\frac{\alpha_{sph}(\xi_2)}{\alpha_{sph}(\xi_1)} \right]^2 \quad (5.22)$$

Figure 5.9 is a plot of $F_{el,z}(\zeta_{sph}):F_{el,z}(\zeta_{sph}=0)$, and illustrates how the electric force on a spherical particle changes when the maximum electric field is held constant as the ratio of the particle diameter to the electrode gap varies. In other words, it is a plot of the electric force on the particle normalized to the case when the particle is much smaller than the electrode gap.

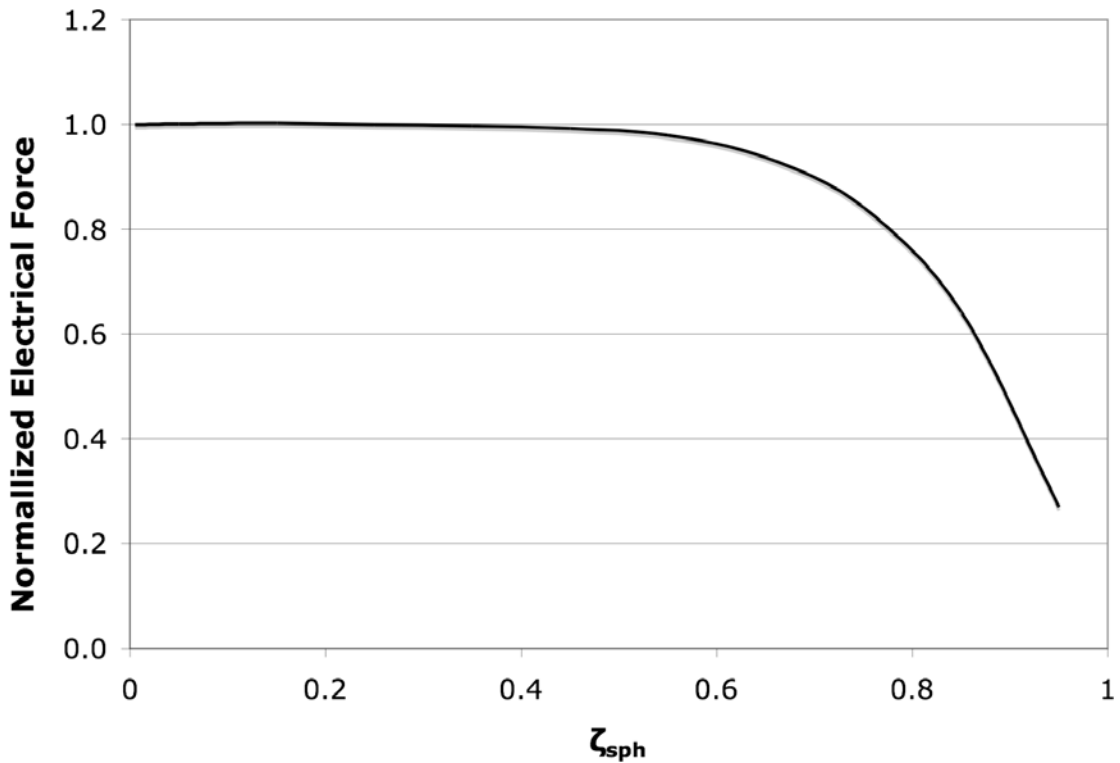


Figure 5.9: Plot of $F_{el,z}(\zeta_{sph}):F_{el,z}(\zeta_{sph}=0)$ as a function of ζ_{sph} .

Figure 5.9 indicates that when the maximum electric field is held constant, the electric force on the particle is greatest when the ratio of the particle diameter to the electrode gap is minimized. This occurs because minimizing the ratio of the particle

diameter to the electrode gap ensures that the charge density is distributed as evenly over the entire particle surface as possible when using this geometry.

Due to the results of this analysis, the remainder of this chapter focuses only on the case when the particle is small compared to the electrode gap, which is valid to within less than 1% error when the particle diameter is less than one-third of the electrode gap ($\zeta < 0.33$). It should be noted this result agrees with Felici's calculation.²⁹

$$F_{el,z}(\zeta_{sph} < 0.33) \approx \pi r^2 \epsilon E_{BG}^2 \quad 5.43 \quad (5.23)$$

The electric force on the particle can be expressed in terms of the particle charge and the applied background electric field by substituting Equation (2.11) into Equation (5.23).

$$F_{el,z}(\zeta < 0.33) \approx 0.83qE_{BG} \quad (5.24)$$

Note that the total force on the particle, when in contact with the source electrode, is less than the product of the particle charge and the applied background electric field, which may not be intuitive. This occurs because charge is not distributed evenly over the entire surface of the particle and the electric field is affected by the presence of the electrode. Note that as the particle leaves the source electrode, the electrostatic force approaches the product of the particle charge and the applied background electric field. When the particle reaches a distance from the source electrode equal to its diameter, the force is approximately 98% this product ($F_{el,z} \rightarrow 0.98qE_{BG}$).³⁰ At this point, it is reasonable to treat the particle as a point charge.

5.3.2. Overcoming the van der Waals Adhesion Force

Using the model for the electric force on a conducting particle in contact with the source electrode (Equation (5.23)) presented in the previous subsection and the van der Waals adhesion force from Equation (5.8), the threshold background electric field for particle removal can be calculated when the van der Waals force is dominant. It is important to include the gravitational force on the particle in this calculation to show where the adhesion force becomes more important than gravity.

$$F_g = \frac{4}{3} \pi r^3 \rho g \quad (5.25)$$

By combining Equations (5.8), (5.23), and (5.25), the threshold background electric field for overcoming the adhesion force is determined when the particle is much smaller than the electrode gap.

$$E_{thresh} \approx \sqrt{\frac{1}{r} \frac{h}{z^2 \epsilon} (0.0023) + r \frac{\rho g}{\epsilon} (0.24)} \quad (5.26)$$

It is important to note that the threshold electric field can both be broken down into two terms: the adhesion dominant term and the gravitational dominant term. The adhesion dominant term scales inversely with the square root of the particle size while the gravitational term scales directly with the square root of the particle size. Note that for zero-gravity applications, the threshold electric field is simplified by letting g go to zero.

Figure 5.10 is a plot of the predicted threshold electric field for overcoming the van der Waals adhesion force and the gravitational force for the two cases when the Lifshitz-van der Waals constant is 9 eV and 0.6 eV. The particle density is assumed to be 1,000 kg/m³ and the surrounding medium is vacuum. A 1,000 kg/m³ density can be either a hollow particle or a glass particle with a thin metallic coating.

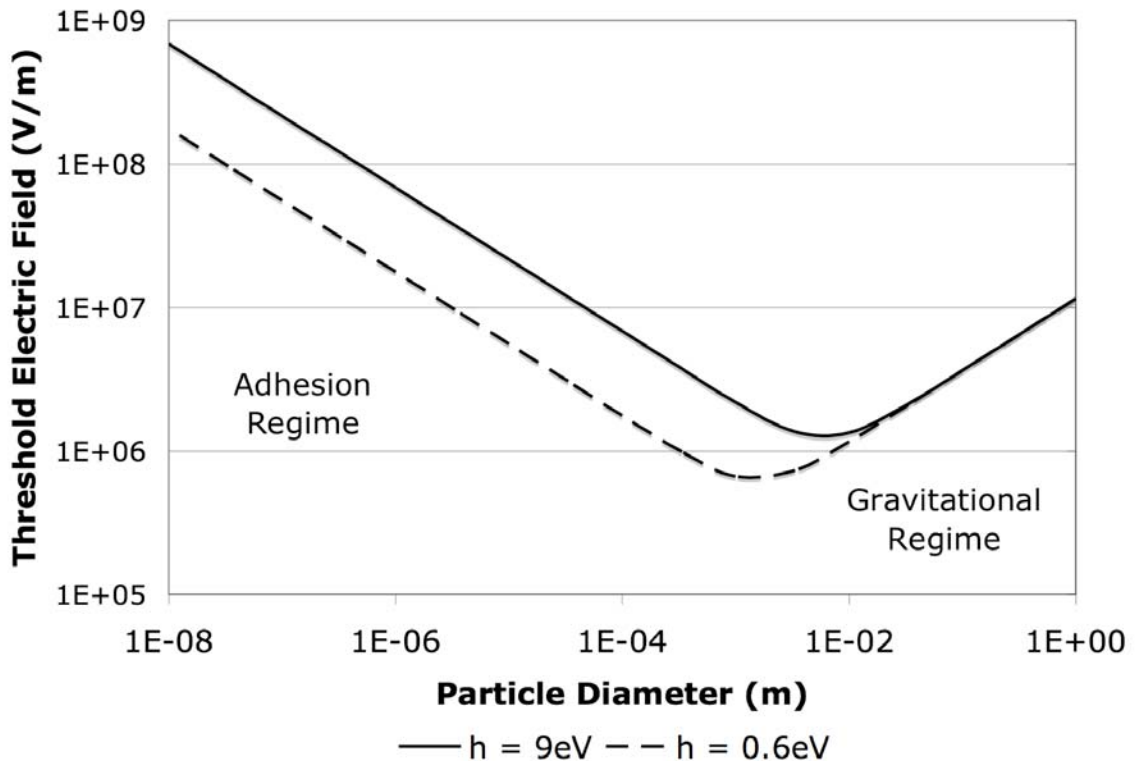


Figure 5.10: Plot of the threshold electric field to overcome the adhesion and gravitational forces holding a spherical particle in contact with the source electrode. The particle has a density of 1,000 kg/m³.

The plot of the threshold electric field clearly illustrates the two regimes. Particles much larger than the centimeter range lie within the gravitational regime and particles much smaller than millimeter range lie within the adhesion regime. Both forces affect particles between these two ranges significantly. When limiting the background electric field strength to a maximum value of 100 MV/m, Figure 5.10 suggests that the smallest

particles that can be removed have diameters of approximately 30 nm and 450 nm when using Lifshitz van-der Waals constants of 0.6 and 9.0 eV, respectively. The attainable specific impulse when using particles of this size is discussed in Section 5.8.

5.4. Experimental Setup

To experimentally investigate the van der Waals adhesion force and overcome this force by way of an electric force, the system depicted in Figure 5.11 was constructed, which is very similar to the model in Figure 5.7 with the addition of the thin strip of Kapton® tape over the surface of the upper electrode.

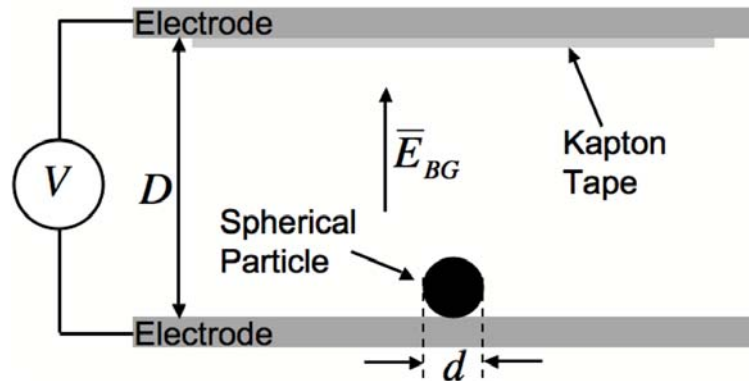


Figure 5.11: Depiction of the experimental setup used for investigating the adhesion force and using an electric force to overcome this adhesion force.

The goals of the experiment are to measure the threshold electric field required for removing conducting spherical particles from the surface of a conducting electrode for various particles in the adhesion dominant regime, investigate the effects of particle size on the adhesion force, and investigate the effects of the particle and electrode materials on the adhesion force.

The experiment is performed by depositing approximately 100 conducting spherical micro-particles on the surface of the bottom electrode. To prevent the particles from

clumping together through cohesion, the particles are passed through a micro-sieve to separate the clumps into individual particles prior to deposition onto the electrode surface. It is desirable to have the particles separated by a distance of at least ten times their diameter to ensure that neighboring particles do not affect the electric field profile at their surfaces as discussed in Section 2.2.5. Once the particles are deposited, the upper electrode is secured in place to provide the correct uniform electrode gap, which is regulated by a spacer, either 1.0 mm or 4.0 mm thick. Next, the voltage across the electrodes is increased incrementally to generate the strong electric field within the gap. At each voltage increment, a photograph of the particles remaining in contact with the bottom electrode is taken to provide visual evidence of the number of particles removed. The process is repeated until all of the particles have been removed. Finally, the number of particles removed from the electrode surface at each voltage increment is counted, providing an experimental measurement of the threshold electric field required for particle removal.

The particles removed from the source electrode during testing are accelerated across the electrode gap towards the upper electrode and onto the Kapton® tape, where they remain trapped. The Kapton® tape serves to collect the removed particles so that they do not oscillate between the electrodes and disrupt the particles still adhered to the bottom electrode. The thickness of the Kapton® tape was chosen to be as thin as possible relative to the electrode gap so that the electric field is affected as little as possible. But, of course, the electric field is modified slightly from Equation (5.12) and depends on the thickness and dielectric constant of the tape.

$$E_{BG} = \frac{V}{D - d_k \left(1 - \frac{\epsilon_o}{\epsilon_k} \right)} \quad (5.27)$$

The tape used for this experiment had a thickness of approximately 25 μm and Kapton® typically has a relative dielectric constant of approximately 2.7.⁷⁹

This experiment was performed with four different particle sizes in the tens to hundreds of microns range and with two different electrode materials to give a total of eight test cases. The following subsections present the particles and electrodes used.

Figure 5.12 is photograph of the 100 micron particles in contact with the bottom electrode before the electric fields were applied.

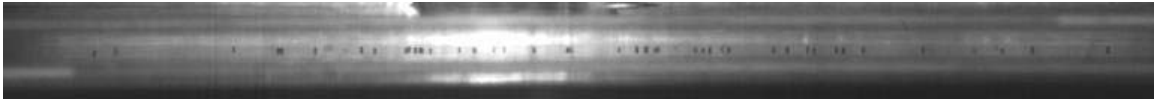


Figure 5.12: photograph of the 100 micron particles in contact with the bottom electrode before the electric fields were applied

5.4.1. Particles Used with Adhesion Experiment

The experiment was performed with four different spherical particle sizes, ranging in diameter from 53 microns to 305 microns, which are all in the adhesion dominant regime. Table 5.1 lists the mean diameters, tolerances, materials, densities, and manufacturers of the particles.

Mean Diameter (μm)	Tolerance (μm)	Material Composition	Density (kg/m^3)	Manufacturer
305	± 10	95%Sn / 5%Sb	7,250	Indium Corp
196	± 16	Soda-lime glass coated w/ Ag	2,500	Mo-Sci Corp
102	± 10	95%Sn / 5%Sb	7,250	Indium Corp
53	± 4	Soda-lime glass coated w/ Ag	2,500	Mo-Sci Corp

Table 5.1: Properties of the four particles used in the particle adhesion experiment.

Figure 5.13 is a set of close and more distant photos of the four particles. These photos were taken using a scanning electron microscope (SEM).

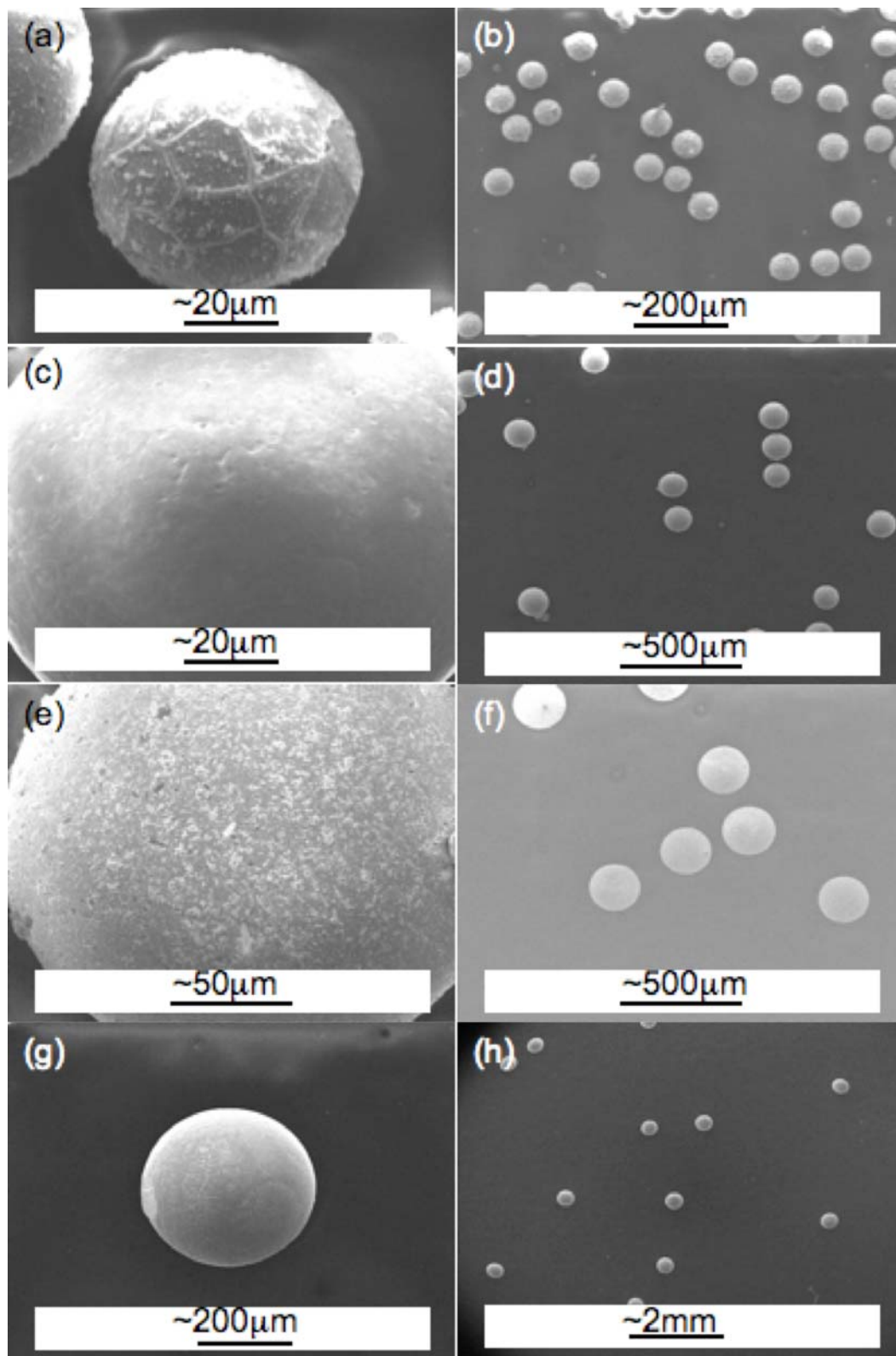


Figure 5.13: SEM photos of the silver 53 μm (a and b), tin 102 μm (c and d), silver 196 μm (e and f), and tin 305 μm (g and h) micron particles.

The photos in Figure 5.13 confirm the tolerances that were reported by the manufacturers and that the particles are very close to spherical. But, it should be noted that the surfaces of the particles are not perfectly smooth, which is assumed in the model. The silver coated glass particles appear to have much rougher surfaces than the 95Sn/5Sb particles, particularly the 53 μm particles. The effects of the rough particle surfaces are addressed in more detail in the Section 5.6.3.

5.4.2. Electrodes Used with Adhesion Experiment

The experiment was performed with two different electrode materials, gold and platinum. These materials were chosen because resist oxidation at room temperature when exposed to the atmosphere unlike most other metals. When manufacturing the electrodes, the two biggest concerns were controlling the surface flatness and the surface roughness. Controlling surface flatness is important for reducing the error in the applied electric field since a warped surface can lead to varying electric field strengths at the electrode surface. The surface roughness is important because the model for the van der Waals adhesion force assumes that the surface of the electrode is perfectly smooth.

To minimize the surface roughness and control the flatness, the electrodes were fabricated using plasma vapor deposition of the metals onto glass wafers. The wafers had a total thickness variation (TTV) less than 10 μm and a surface roughness less than 1.5 nm.⁸⁰ All depositions were performed using the EnerJet Evaporator at the Lurie Nanofabrication Facility (LNF) located at the University of Michigan. The gold electrodes were fabricated by depositing 300 nm of gold on top of a 30 nm adhesion layer of chromium, and the platinum electrodes were fabricated by depositing 100 nm of

platinum on top of a 10 nm adhesion layer of titanium. Figure 5.14 is a picture of one of the gold electrodes.



Figure 5.14: Picture of a gold electrode deposited on a glass wafer.

The electrodes are circular with 50 mm diameters and were deposited onto 100 mm glass wafers. A thin tail of metal stretches from the electrode and wraps around the wafer to provide an electrical connection on the reverse side.

An atomic force microscope (AFM) was used to measure the surface roughness of both the gold and platinum electrodes. Figure 5.15 shows the surface profile measured for each material.

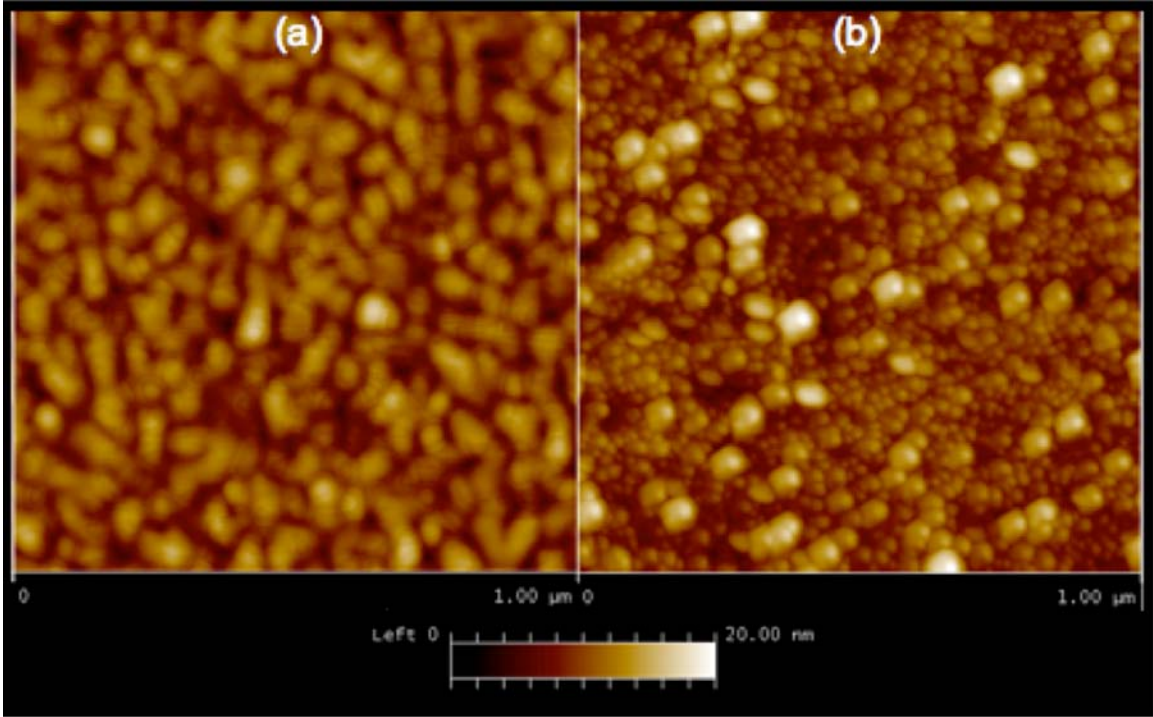


Figure 5.15: AFM surface profile of the gold (a) and platinum (b) electrodes.

According to the AFM images in Figure 5.15, both the gold and platinum electrodes have a surface roughness on the order of 20 nm. The effects of the electrode surface roughness are presented in the discussion section.

5.4.3. Vacuum Chamber

The experiment was performed in the Ultra High Vacuum (UHV) chamber at the Space Electrodynamics and Tether Systems (SETS) laboratory at the University of Michigan, which is pumped by a mechanical roughing pump and a turbo pump and has an ultimate pressure on the order of 10^{-9} Torr. Each experiment was performed at a pressure less 40 nTorr to prevent arcing within the electrode gap. In addition, operating at a low pressure helped to evaporate liquid films coating the particles, which allows the

surface tension force from Section 5.2.3 to be neglected. Figure 5.16 is a picture of the chamber.



Figure 5.16: Picture the UHV chamber at the Space Electrodynamics and Tether Systems Laboratory at the University of Michigan.

5.5. Experimental Results

Before presenting the experimental results, it is important to remind the reader that the Lifshitz-van der Waals constant from Equation (5.8) is not well known for most material combinations. Further, in the cases of reported values, many authors are not in agreement.⁸¹ Therefore, this chapter does not assume any values for the Lifshitz-van der Waals constant when analyzing the results. Instead, values for the Lifshitz-van der Waals constant that best fit the experimental results are evaluated and used for comparison between the test cases. The threshold electric field for particle removal is defined as the field strength at which 50% of the particles in contact with the source electrode are removed.

Figure 5.17 and Figure 5.18 are plots showing the measured electric fields required for particle removal for all eight cases tested. Each plot shows the results for all four

particles tested against one of the two electrode materials. The solid black dots represent the electric field strength at which 50% of the particles tested were removed. The upper and lower dashes represent the electric field strengths at which 33% and 67% of the particles were removed, respectively. Each test case measured the threshold electric field of several hundred particles over several experimental runs, with the exception of the 305 μm particles, which used less than ten particles per experimental run due to the tendency of the particles to roll off of the electrode during setup. There is an estimated total error of approximately 5% in the measurements, which was determined with the sum of squares method. The error in the electric fields is due mostly to two error terms in the experimental setup. These error terms are as follows: the electrode gap separation (4.7%), and the applied voltage (0.1%).

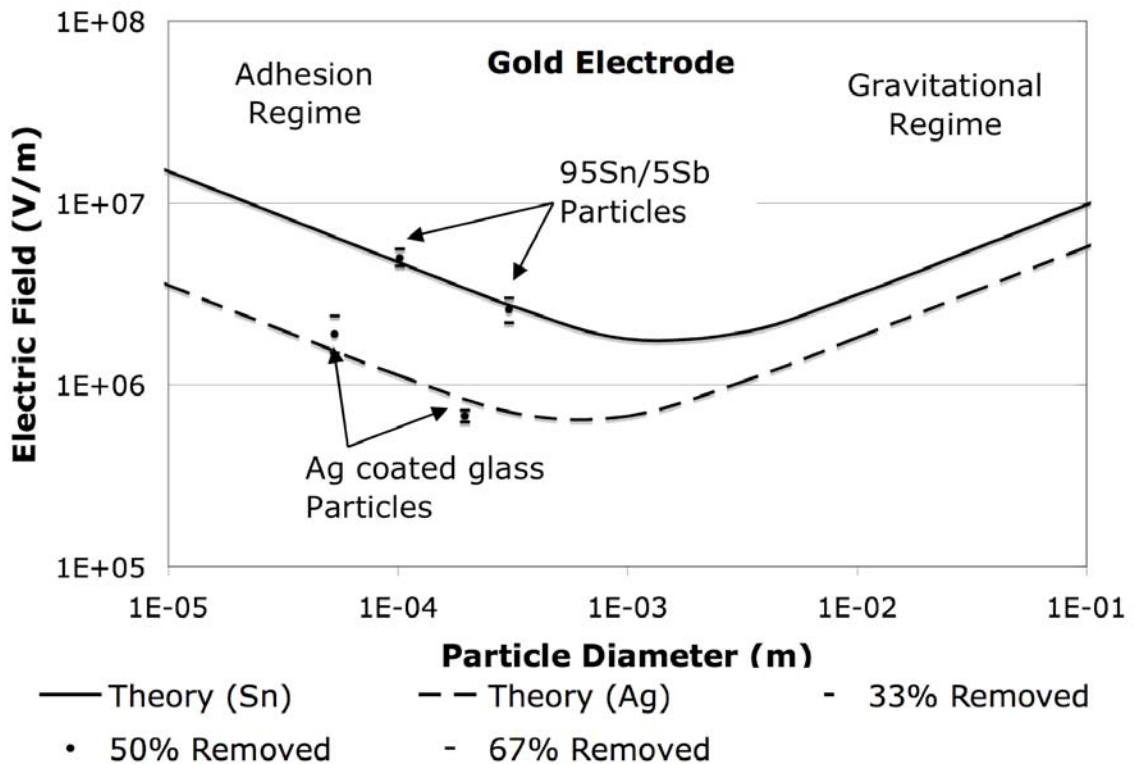


Figure 5.17: Measured threshold electric fields for removal of spherical particles from a gold planar electrode when in the adhesion dominant regime.

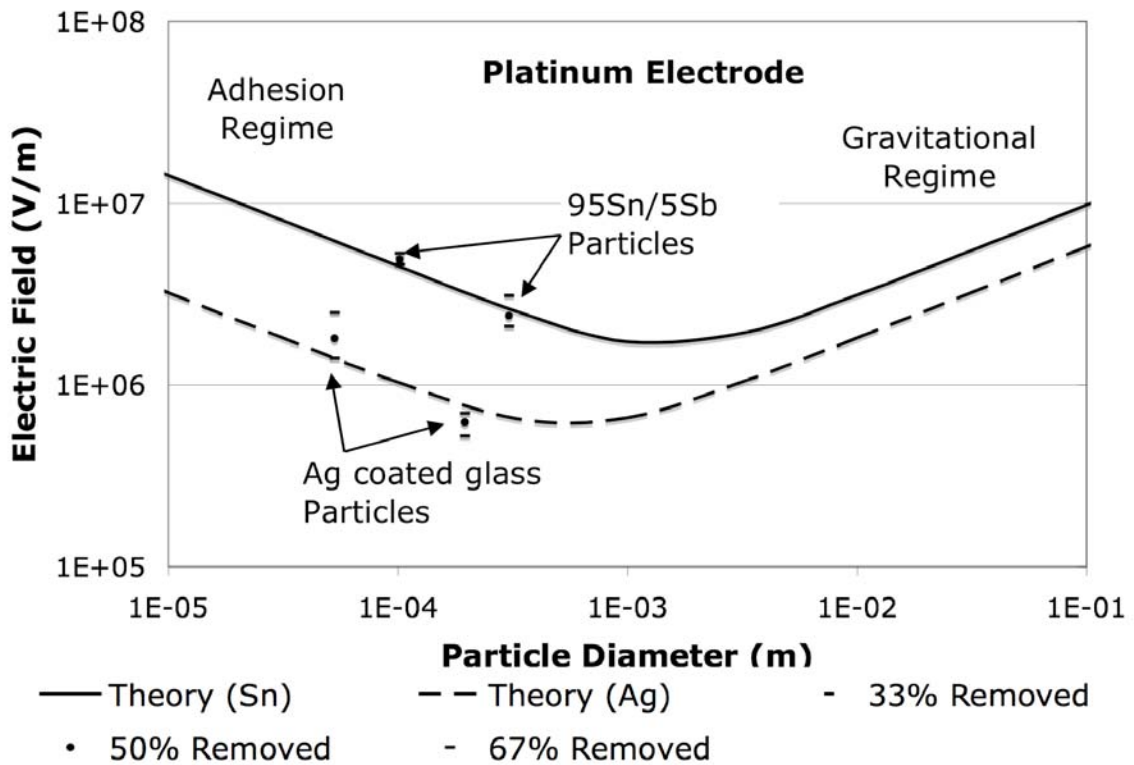


Figure 5.18: Measured threshold electric fields for removal of spherical particles from a platinum planar electrode when in the adhesion dominant regime.

The experimental data is plotted against the theoretical threshold electric fields when using the Lifshitz-van der Waals constants evaluated to provide the best fit. Table 5.2 lists the evaluated Lifshitz-van der Waals constants for the four material combinations used in Figure 5.17 and Figure 5.18. As predicted by the model, the threshold electric fields required for particle removal increase as the particle size decreases for each material combination. The evaluated Lifshitz-van der Waals constants for the tin particles lie within the expected range of 0.6 to 9 eV, but the evaluated values for the silver particles are slightly less than typical range. However, this may be a result of a difference between the actual Lifshitz-van der Waals constants, surface roughness, and/or particle deformation, which are presented in the upcoming sections. Also, note that

changing the electrode material from gold to platinum has very little effect on particle adhesion.

Material Combination	Lifshitz Constant (eV)
95Sn/5Sb – Au	4.3
95Sn/5Sb – Pt	3.9
Ag coated glass – Au	0.24
Ag coated glass – Pt	0.20

Table 5.2: Lifshitz-van der Waals constants evaluated to match experimental data for all material combinations tested.

The spread of the threshold electric field required for particle removal is larger than expected. Figure 5.19 shows the percentage of particles removed as a function of the applied electric field for all eight test cases.

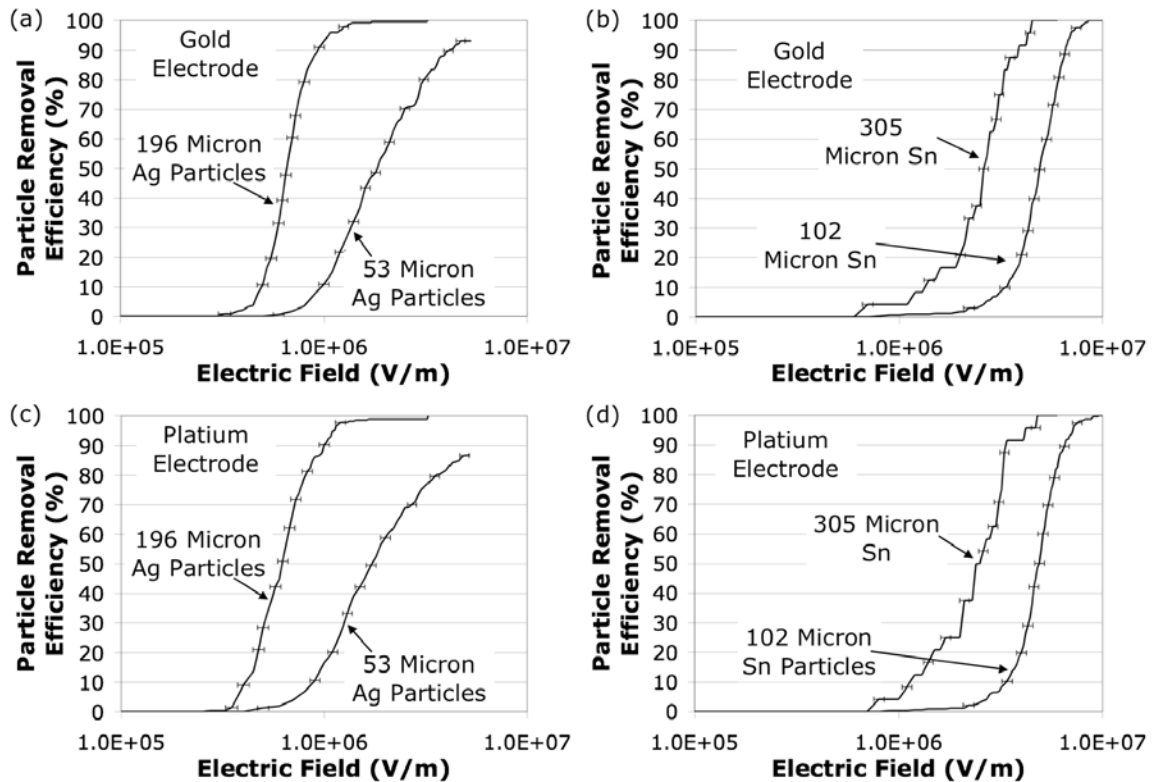


Figure 5.19: Plots of the particle removal efficiency as a function of applied electric field for all eight test cases.

To complement Figure 5.19, Table 5.3 lists the median threshold electric field strength for particle removal along with the electric field strengths required to remove 15%, 33%, 67%, and 85% of the particles.

Particle Size and Materials	Required Electric Field to Remove Stated Percentage of Particles				
	15% (MV/m)	33% (MV/m)	50% (MV/m)	67% (MV/m)	85% (MV/m)
305 μm Sn on Au	1.6	2.2	2.6	3.0	3.5
305 μm Sn on Pt	1.4	2.1	2.4	3.1	3.3
196 μm Ag on Au	0.53	0.63	0.68	0.73	0.85
196 μm Ag on Pt	0.48	0.53	0.63	0.70	0.88
102 μm Sn on Au	3.7	4.5	5.0	5.6	6.3
102 μm Sn on Pt	3.7	4.6	4.9	5.3	6.1
53 μm Ag on Au	1.1	1.5	1.9	2.4	3.6
53 μm Ag on Pt	1.0	1.4	1.8	2.5	4.5

Table 5.3: Threshold electric fields required to remove 15%, 33%, 50%, 67%, and 85% of the particles.

Potential reasons for the spread in the electric field required for particle removal, such as spread in particle size, particle and electrode surface roughness, and surface deformation are presented in the upcoming sections.

5.6. Variables of the Experiment

While the measured threshold electric fields trend as predicted by the model for each material combination, the evaluated Lifshitz-van der Waals constants for the two particle materials are quite different. The evaluated Lifshitz-van der Waals constants may be reasonable measurements of the actual values, but the difference may also be a result of uncontrolled variables in the experiment. In addition, the spread of the electric fields required for the removal of all the particles is quite large, which may also result from uncontrolled variables in the experiment. This section examines three variables in the

experiment and the following section is a discussion of how the Lifshitz-van der Waals constant is calculated.

5.6.1. Spread In Particle Size

The first experimental variable to consider is the spread in particle size, which may contribute to the spread in the electric fields required for particle removal. Using the tolerances on the particle diameters given in Table 5.1 and the predicted threshold electric field from Equation (5.26), the expected electric field spread can be calculated.

$$E_{spread,part} = E_{thresh}(r_{up}) - E_{thresh}(r_{lo}) \quad (5.28)$$

Using this expression, Table 5.4 lists the approximate expected electric field spread resulting from the particle size spread along with the measured spread to remove 15%-85% and 33%-67% of the particles.

Particle Diameter (μm)	Electrode Material	Theoretical Spread (MV/m)	33%-67% Measured Spread (MV/m)	15%-85% Measured Spread (MV/m)
305	Au	0.09	0.80	1.9
305	Pt		1.0	1.9
196	Au	0.07	0.10	0.33
196	Pt		0.18	0.40
102	Au	0.48	1.1	2.6
102	Pt		0.70	2.4
53	Au	0.13	0.90	2.5
53	Pt		1.1	3.5

Table 5.4: The estimated spread in the threshold electric field due to the spread in particle size and the measured threshold electric field spread.

The calculations in Table 5.4 suggest that the spread in particle size can lead to a spread in the electric field, but not enough to account for the entire spread in the experimental data.

5.6.2. Particle and Electrode Deformation

The second experimental variable is possible deformation of the particle and/or the source electrode by compression. The model presented in Equation (5.8) assumes that the particle is a perfect sphere and that the electrode is a perfect plane, but, due to defects in the particle and/or the electrode, this is most likely not the case. The compression of either the particle or the electrode leads to a contact area between the two greater than just the point contact that is assumed. An increase in the contact area leads to an increase in the adhesion force. Figure 5.20 illustrates how a deformation of the particle and/or the electrode leads to a greater contact area.

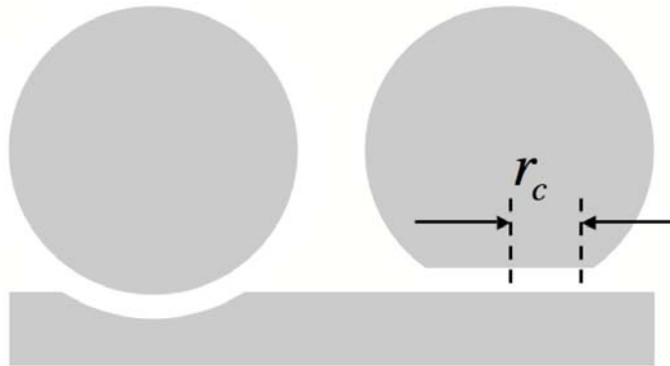


Figure 5.20: Illustration showing deformation of electrode (left) and particle (right).

Approximating the change in the adhesion force due to the deformation of the particle and/or the electrode is not straightforward because the exact geometry after deformation has occurred is unknown and can be quite complex. To approximate the change in the

adhesion force resulting from deformation, all of the deformation is assumed to be at the bottom of the particle as shown in the right illustration of Figure 5.20. Using Equation (5.4), the additional adhesion force is calculated to be a function of the contact area radius, r_c .⁷⁴

$$F_{vdw,def} = \frac{hr_c^2}{8\pi z^3} \quad (5.29)$$

The total van der Waals adhesion force for a deformed particle is approximated as the sum of Equations (5.8) and (5.29).

$$F_{vdw,tot} \approx \frac{h}{8\pi z^2} \left(r + \frac{r_c^2}{z} \right) \quad (5.30)$$

Assuming that the electric force on the particle does not change significantly if the particle experiences a small deformation, which is appropriate as long as the deformation occurs at the bottom of the particle, the new threshold electric field is calculated by modifying Equation (5.26) and assuming that the particle is in the adhesion dominant regime.

$$E_{thresh,tot} \approx \sqrt{\left(\frac{1}{r} + \frac{r_c^2}{r^2 z} \right) \frac{h}{z^2 \epsilon}} (0.0023) \quad (5.31)$$

The deformation of the particle may lead to an error in the evaluated values of the Lifshitz-van der Waals constant from the experimental results. If the threshold electric

field is known, an expression for the Lifshitz-van der Waals constant can be obtained from Equation (5.31).

$$h \approx \frac{\epsilon z^3 r^2 E_{thresh,tot}^2}{(0.0023)(rz + r_c^2)} \quad (5.32)$$

Using Equation (5.32), the percent error in the evaluated Lifshitz-van der Waals constants from the experimental results can be approximated, which is dependent only on the particle radius, the contact radius, and the minimum separation distance.

$$Error \approx \frac{h(r_c = 0) - h(r_c)}{h(r_c)} \approx \frac{r_c^2}{rz} \quad (5.33)$$

Figure 5.21 is a plot of the percent error in the evaluated Lifshitz-van der Waals constants as a function of percent deformation of the particle for all four particles tested. The deformation of the particle is defined as the ratio of the contact area radius to the particle radius, $r_c:r$.

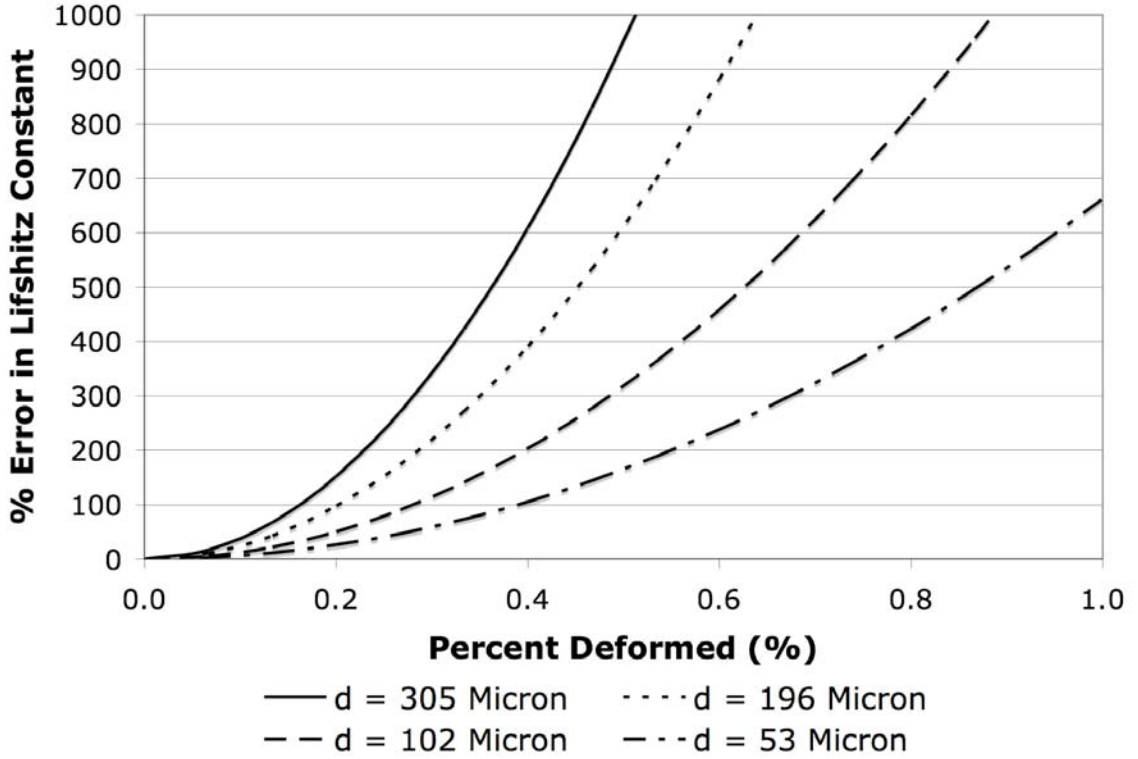


Figure 5.21: The estimated percent error of the evaluated Lifshitz-van der Waals constants due to deformation of the particle.

Figure 5.21 shows that just a slight deformation of the particle can lead to a very large error in the evaluated Lifshitz-van der Waals constant, which could be a large error in the evaluated values listed in Table 5.2.

In addition to increasing the error in the evaluated values for the Lifshitz-van der Waals constant, the particle deformation may also be a source of the spread in the electric field required to remove all the particles. This spread is calculated by finding the difference between Equations (5.26) and (5.31).

$$E_{spread,def} = E_{thresh}(r) - E_{thresh,tot}(r, r_c) \quad (5.34)$$

Using Equation (5.34), Figure 5.22 plots the approximate expected threshold electric field spread resulting from particle deformation for all 4 particles tested. The figure assumes Lifshitz-van der Waals constants of 4.0 and 0.2 eV for the 95Sn/5Sb and Ag particles, respectively.

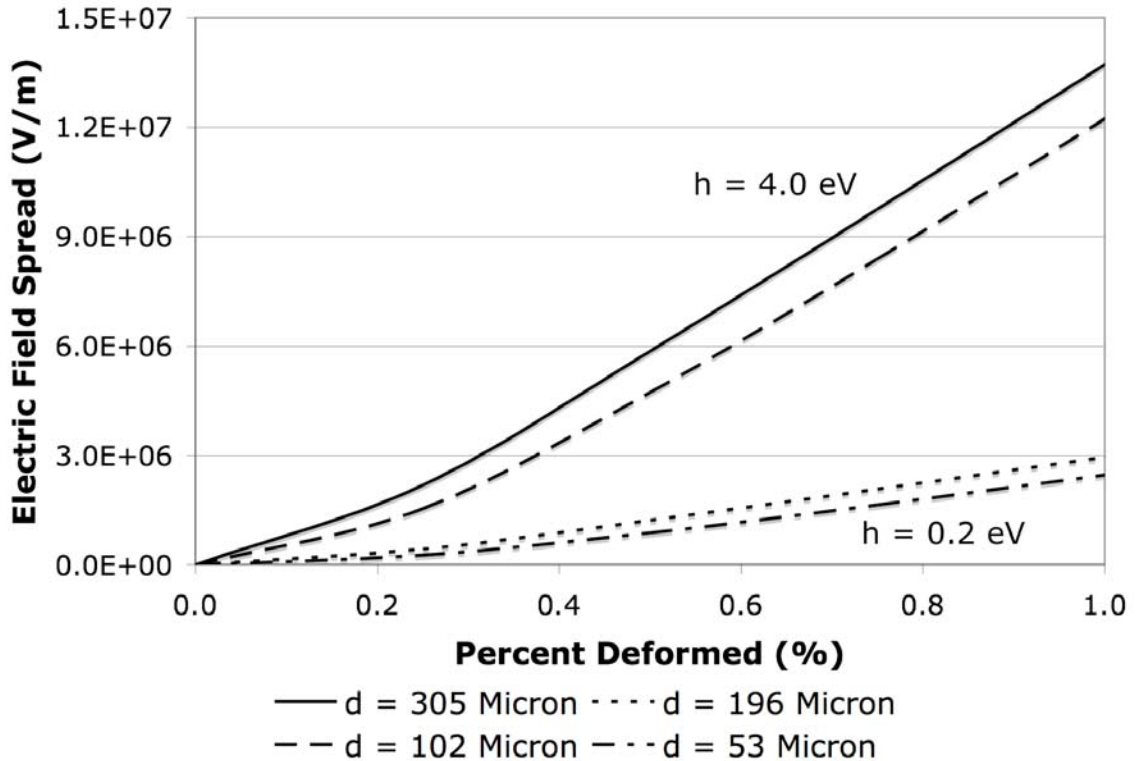


Figure 5.22: The estimated spread in the threshold electric field due to deformation of the particle.

Comparing the theoretical spread in the electric field with the measured spread from Table 5.3, it is very possible that a small deformation could make significant contributions.

To make a first order approximation of the particle deformation, the Hertzian theory of elastic deformation can be used. This theory predicts the contact radius, r_c , to be a

function of the adhesion force, the particle radius, the Young's modulus (E_1 and E_2) and, the Poisson's ratio (ν_1 and ν_2) of the two materials in contact.⁸²

$$r_c \approx \left(\frac{3F_{vdw}r}{4E^*} \right)^{1/3}, \quad E^* = \left[\frac{(1-\nu_1^2)}{E_1} + \frac{(1-\nu_2^2)}{E_2} \right]^{-1} \quad (5.35)$$

The predicted contact radius is further simplified by substituting the van der Waals force from Equation (5.8) into Equation (5.35).

$$r_c \approx \left(\frac{3hr^2}{32\pi\zeta^2 E^*} \right)^{1/3}, \quad E^* = \left[\frac{(1-\nu_1^2)}{E_1} + \frac{(1-\nu_2^2)}{E_2} \right]^{-1} \quad (5.36)$$

Table 5.5 lists the Young's Modulus and Poisson's ratio of the particle and electrode materials used in the experiments.

Material	Young's Modulus	Poisson's Ratio
Silver	83 GPa	0.37
Tin	50 GPa	0.36
Gold	78 GPa	0.44
Platinum	168 GPa	0.38

Table 5.5: Reported values of the Young's Modulus and Poisson's ratio of the materials used in the experimental section.⁶⁶

Finally, the first order predictions of the contact radii between the particles and electrode surfaces of all eight test cases are calculated and listed in Table 5.6 using the measured values of the Lifshitz-van der Waals constants from Table 5.2.

Particle Diameter (μm)	Material Combination	Contact Radius (μm)	% Deformation	Contact Area (μm^2)
305	95Sn/5Sb – Au	0.4	0.3	0.6
196	Ag – Au	0.1	0.1	0.04
102	95Sn/5Sb – Au	0.2	0.4	0.1
53	Ag – Au	0.05	0.2	0.01
305	95Sn/5Sb – Pt	0.4	0.3	0.5
196	Ag – Pt	0.1	0.1	0.03
102	95Sn/5Sb – Pt	0.2	0.4	0.1
53	Ag – Pt	0.04	0.2	0.01

Table 5.6: First order predicted contact radii between particles and electrodes.

The predicted contact radii suggest that the particles will deform on the order of a few tenth of a percent, which, according to Figure 5.21, can produce significant changes in the required electric fields to overcome adhesion.

5.6.3. Particle and Electrode Surface Roughness

The final possible cause for the electric field spread that is discussed in this chapter is the surface roughness of both the particle and the electrode surface. The surface roughness of the materials in contact can lead to an increase or decrease in the adhesion van der Waals force depending on their relative roughness and alignment.⁸³ Due to the complexity and large number of variations of surface roughness and alignments, it is not possible to provide a general relationship between the adhesion force and the materials surface roughness. Only in the case when the exact geometry of the two surfaces is known, can Equation (5.4) be integrated to find the adhesion force.

Figure 5.23 illustrates four possible surface orientations between the electrode surface and the particle. Note that the examples discussed here are not all inclusive and there exists many other possible surface orientations that may lead to a change in the adhesion force.

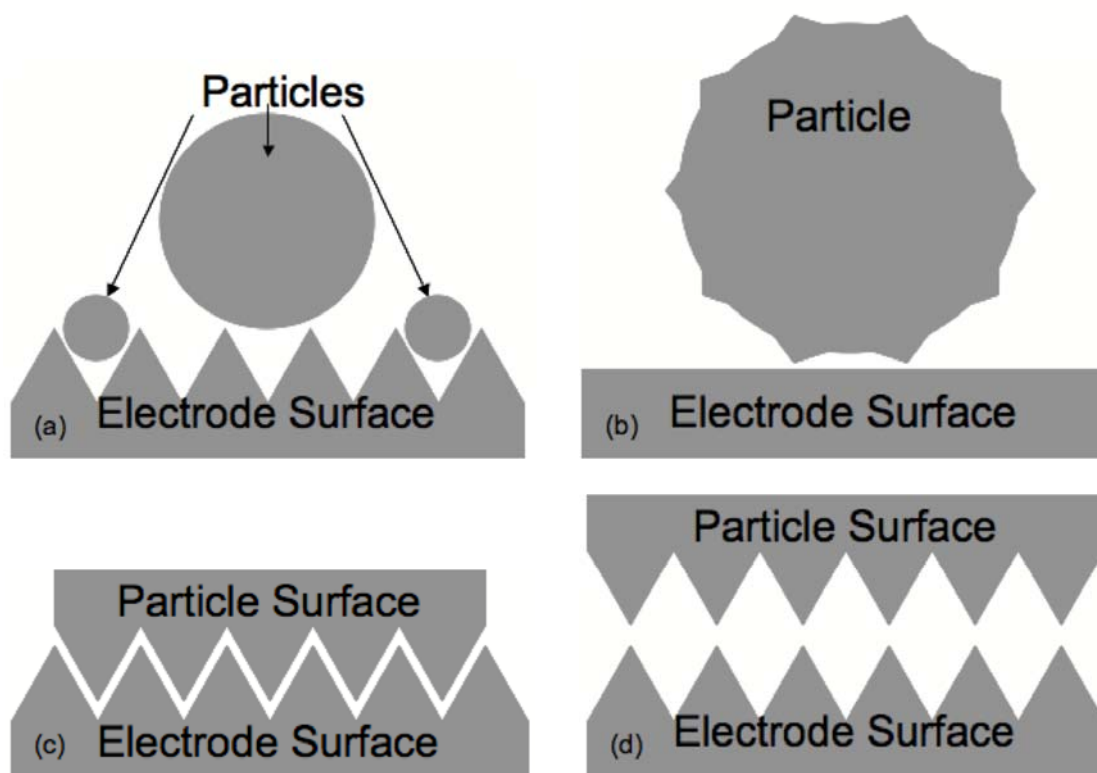


Figure 5.23: Possible electrode and particle surface orientations.

Sketch (a) from Figure 5.23 illustrates two possible situations. First, it is possible that the particles are much smaller than the surface roughness of the source electrode. In this case, the particles may fit between the peaks and valleys of the electrode, which increases the contact area and increases the adhesion force. Second, it is possible that the particles are much larger than the surface roughness and sit on the peaks of the electrode, which decreases the contact area and decreases the adhesion force. Picture (b) illustrates a case when the surface roughness of the electrode is much less than the particle size and the surface roughness of the particle is significant. This decreases the contact area and the adhesion force. Picture (c) illustrates a case when the surface roughness of the particle and the electrode are approximately the same and are aligned so that the peaks of the

particle fit into the valleys of the electrode. Again, this increases the contact area and the adhesion force. Picture (d) illustrates a case when the surface roughness of the particle and the electrode are approximately the same and are aligned so that the peaks of the particle and electrode are touching. This decreases the contact area and the adhesion force.

As stated earlier, there exist many other possible orientations between the particle and electrode surfaces, and their effects on the adhesion force can be determined by understanding how the contact area changes. Since the surface roughness affects the adhesion force by changing the contact area, it is reasonable to expect that the error in the evaluated values for the Lifshitz-van der Waals constants and the resulting spread of the electric field required for particle removal could be quite large. Based on the SEM images of the particles' surfaces from Figure 5.13 and the AFM surface profiles of the electrodes from Figure 5.15, it is reasonable to assume that the experimental cases matched case (b) from Figure 5.23 the best where the electrode surface roughness is much less than the particle size, but the particle surface roughness is significant.

Figure 5.13 is a set of SEM photographs of the particles used for this chapter and Figure 5.15 is an AFM surface profile of the source electrodes. The particles all have surface defects on the order of what appears to be microns, but note that the defects on the silver coated glass spheres are much larger than on the 95Sn/5Sb particles. Both electrode surfaces have a surface roughness on the order of 20 nm.

When the particle surface is much rougher than the electrode surface, the result may increase the total separation between the particle and the electrode surface, z . This is a result of the surface roughness acting as standoffs. To understand how the separation

between the surfaces influences the adhesion force, Figure 5.24 plots the van der Waals adhesion force from Equation (5.8) as a function of the separation for all of the tested particles. Recall that the model typically uses a separation of 4 Angstroms when the surfaces are smooth.

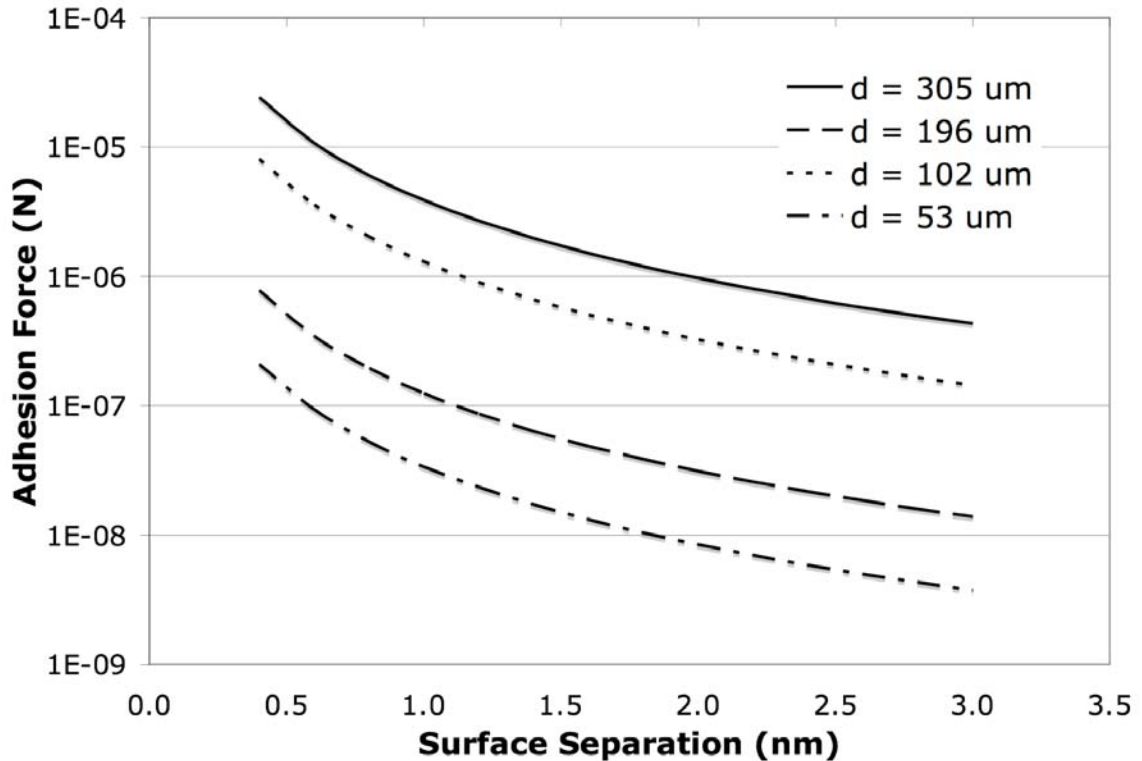


Figure 5.24: Van der Waals adhesion force as a function of the separation. The four curves are for the four particles tested.

Figure 5.24 suggests that as the separation between the surfaces increases, which could be a result of a large surface roughness, the adhesion force decreases. For example, increasing the separation from 4 Angstroms to 4 nm decreases the adhesion force by a factor of 100.

Based on the analysis presented in this subsection, it is possible that the evaluated values for the Lifshitz-van der Waals constants deviate from the actual values due to the

deformation of the particles and/or the electrode and the surface roughness of particles and the electrode. The large spread in the electric field required for particle removal is most likely contributed to significantly by the same two experimental variables, and to a lesser extent, the spread in particle size.

5.7. Lifshitz-van der Waals Constant

As discussed in a previous section, the Lifshitz-van der Waals constant is used to calculate the van der Waals force between two macroscopic materials and is a measure of the energy of the van der Waals interaction.⁷² For materials in atmosphere or vacuum, its value generally ranges from 0.6 to 9.0 eV and is obtained using dielectric spectroscopy.^{84,85} According to Visser,⁸¹ the Lifshitz-van der Waals constant between materials a and b when in medium c is dependent on the dielectric constant, $\varepsilon(i\xi)$, along the imaginary frequency axis, $i\xi$, of each material.

$$h_{acb} = \hbar \int_0^{\infty} \left[\frac{\varepsilon_a(i\xi) - \varepsilon_c(i\xi)}{\varepsilon_a(i\xi) + \varepsilon_c(i\xi)} \right] \left[\frac{\varepsilon_b(i\xi) - \varepsilon_c(i\xi)}{\varepsilon_b(i\xi) + \varepsilon_c(i\xi)} \right] d(i\xi) \quad (5.37)$$

$\varepsilon(i\xi)$ is a function of the complex component of the material's dielectric constant, $\varepsilon''(\omega)$.⁸⁶

$$\varepsilon(i\xi) = 1.0 + \frac{2}{\pi} \int_0^{\infty} \frac{\omega \varepsilon''(\omega)}{\omega^2 + \xi^2} d\omega \quad (5.38)$$

When in vacuum, $\varepsilon_c(i\xi)$ goes to 1.

Calculating the Lifshitz-van der Waals constant is beyond the scope of this chapter, but is known to be difficult due to the lack of accurate optical data.⁸¹ Values for individual materials, h_{aca} , have been approximated for many materials using various methods to simplify the calculation of Equations (5.37) and (5.38). If the Lifshitz-van der Waals constant is known for two individual materials, its value between them, h_{acb} , can be approximated.⁸¹

$$h_{acb} = \sqrt{h_{aca}h_{bcb}} \quad (5.39)$$

Table 5.7 lists the ranges of published values of the Lifshitz-van der Waals constants, h_{aca} , for several materials when in vacuum as calculated by several different authors and reported by Visser⁸¹ and Bowling⁷⁴.

Material	Lifshitz –van der Waals Constant (eV)	Reference
Ag	4.3-10.5	[87], [88], [84]
Au	7.7-11.9	[88], [87]
Cu	7.4-8.5	[84]
Fe	5.5	[88]
Ge	6.4-7.8	[89], [84]
Hg	11.3	[88]
Pb	5.6	[88]
Se	2.0-5.1	[90], [87]
Si	5.8-7.2	[87], [91], [84]
Sn	5.7	[88]
Te	3.7	[91]

Table 5.7: List of ranges of published values of the Lifshitz-van der Waals constant for many materials.

Note that the large ranges of reported Lifshitz-van der Waals constants are a result of lack of optical data and the limits of the simplifying approximations used.

Using Equation (5.39) and the values from Table 5.7, the expected ranges of the Lifshitz-van der Waals constants for a couple of the experimental material combinations

are calculated and listed in Table 5.8. For comparison, the evaluated values of the Lifshitz-van der Waals constants from the experimental results are included in the table.

Materials	Predicted Lifshitz-van der Waals Constant (eV)	Evaluated Lifshitz-van der Waals constant (eV)
Au-95Sn/5Sb	6.6-8.2	4.3
Au-Ag	5.8-10.3	0.20

Table 5.8: List of ranges of the expected values of the Lifshitz-van der Waals constant for select test cases compared with the evaluated values.

Note that the evaluated Lifshitz-van der Waals constants lay outside the range of predicted values for the given material properties. The evaluated values for the tin particles are on the same order of magnitude as predicted, but the evaluated values for the silver particles an order of magnitude less than predicted. The discrepancy with the silver particles is likely a result of the particles' rough surfaces. There is also possible uncertainty in the evaluated values as discussed in the previous subsection. But, according to Visser:

“Comparison of the theoretically calculated Lifshitz-van der Waals/Hamaker constants with those derived from experiments show that in a large number of cases the values from colloid [particles] chemistry and surface tension measurements deviate substantially from the theoretically calculated ones. This finding is a clear indication that the interpretations used for their calculation are based on incomplete theories.”

5.8. Effects of the van der Waals Adhesion Force on Micro- and Nano-Particle Thrusters

The experimental results show that spherical particles down to at least 50 microns in diameter can be removed from a source electrode by way of a high strength applied electric field. In addition, theory predicts that when restricting the background electric field to approximately 100 MV/m, which is approximately one order of magnitude less

than the threshold for electron emission,⁹² the minimum removable particle diameters are on the order of hundreds and tens of nanometers when assuming Lifshitz-van der Waals constants of 9 eV and 0.6 eV, respectively. Of course, future experiments need to confirm the possibility of removing particles of this size scale as it is unclear at which point the particles can no longer be modeled as macroscopic and need to be treated at the molecular level.

Assuming, for now, that the model is reasonably reliable for particles at tens and hundreds of nanometers, it is possible to predict the maximum specific impulse attainable by micro- and nano-particle thrusters using the no liquid configuration, which depends on the particle charge-to-mass ratio and the accelerating voltage.⁸

Table 5.9 lists the maximum expected specific impulses (Equation (2.28)) attainable when using the minimum removable particle diameters from Section 5.3.2. The background electric field is 100 MV/m, the accelerating voltage is 40 kV, and the particle density is 1,000 kg/m³.

Particle Diameter (nm)	Lifshitz van-der Waals Constant (eV)	Specific Impulse (s)
450	9.0	130
30	0.6	500

Table 5.9: The predicted specific impulse when using the smallest removable particles from the source electrode by electric force only.

The specific impulse values listed in Table 5.9 are the upper theoretical limits when using only an electric force to overcome the van der Waals adhesion force with a planar source electrode and assuming Lifshitz constants of 9 eV and 0.6 eV. Current and future work involves lowering the required electric field for particle removal by way of a vibrational source. This should allow the removal of smaller particles and make it

possible to reach higher specific impulses. This is beyond the scope of this thesis, but is currently being investigated by Liu.⁶²

5.9. Conclusion

A method of removing spherical conducting particles from a planar source electrode by way of applied electric fields was investigated for use with micro- and nano-particle thrusters. For conducting particles in a dry environment, the dominant adhesion force between the particles and the source electrode is the van der Waals force, which scales directly with the particle size. The electric force responsible for particle removal scales directly with the square of the particle size, suggesting that as the particle size decreases, the required electric field for removal increases. The models developed predict that particles with diameters down to tens or hundreds of nanometers can be removed from a planar electrode, which may be capable of providing specific impulses upwards of 500 seconds. Note that there may exist other methods of reducing the particle size or improving the particle charge-to-mass ratio to allow for higher specific impulses

To investigate the particle removal model, eight test cases, involving 4 particle sizes and 2 electrode materials, were studied. The tests agreed reasonably well with the model when using values of the Lifshitz-van der Waals constants close to the expected ranges for all materials. But, most of the values evaluated from the experimental data disagree with published values for the specific material combinations. Note that many authors are not in agreement on the published values. In addition, the spread in the electric fields required to remove particles was large. The possible error in the Lifshitz-van der Waals constants and the spread of the electric fields may be attributed primarily to the surface

roughness and deformation of both the particles and the electrode. Due to the wide range of variability, it will be essential to measure the lift-off electric field when new particles and electrode materials are used.

Using high strength electric fields to remove conducting particles from a source electrode by overcoming the van der Waals adhesion force for use with micro- and nano-particle thrusters appears promising.

Chapter 6

Dry Particle Transport

6.1. Introduction

As a result of the insulating liquid configuration studies discussed in Chapter 4, which presented the challenges of extracting micro- and nano-particles through a liquid surface, and the no liquid configuration studies discussed in Chapter 5, which presented the promise of removing micro- and nano-particles from electrode surfaces, the no liquid configuration became the central research focus. Therefore, methods of transporting dry particles while preventing the particles from clumping together are important topics for the no liquid configuration. This chapter investigates two possible methods of transportation. The first method utilizes the electric force on uncharged particles that arises from the gradient in the electric field, and the second method uses a simple method of expelling the particles through micro- and nano-sieves. In addition to theoretical discussions, this chapter presents simple proof-of-concept experiments for each method.

6.2. Particle Transport Using the Gradient in an Applied Electric Field

This section investigates the possibility of transporting individually uncharged spherical particles from a storage area to the charging and accelerating zones by way of the electric force that arises from the gradient in an applied electric field, and begins by presenting a derivation of the gradient force on uncharged conducting and insulating

spherical particles.⁹³ Next, it is shown that this method of particle transport may provide a technique of maintaining a separation between particles.⁹⁴ Two methods of generating the required electric field gradients are investigated, and one is demonstrated using a simple proof-of-concept experiment.

6.2.1. Gradient Force on Individual Uncharged Spherical Particles

It is important to note that the gradient force on spherical particles has previously been derived and is a highly researched area in the field of optical tweezers and particle manipulation.^{95,96} Previous research has shown that an uncharged particle subjected to a gradient in an electric field, experiences a force pulling the particle to the location of the maximum intensity of the electric field as depicted in Figure 6.1. In the Rayleigh regime, where the electric field gradient is approximately uniform over the particle dimension,⁹⁷ the force arises from polarization or separation of charge within the particle, which acts as a point electric dipole moment. The electric force from the applied electric field acting on the separated charge is not uniform and is stronger in the region where the external electric field is strongest, resulting in a net force towards higher intensity electric fields.

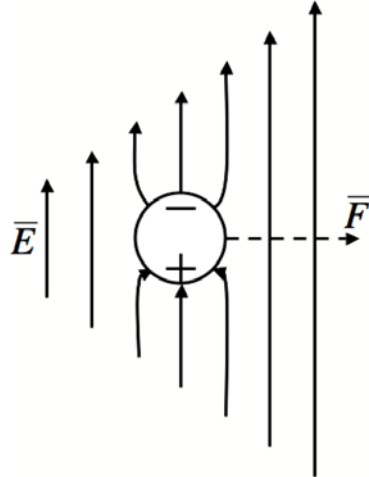


Figure 6.1: An uncharged spherical particle subjected to a gradient in the electric field experiences a force pulling it to the region of maximum intensity.

Before beginning the derivation, several assumptions, which are listed below, are imposed for simplification purposes and to help clarify the problem.

- There is no applied magnetic field:

Most derivations use an applied magnetic field in addition to the electric field, but this derivation assumes that there is no applied magnetic field.

- The particle is uncharged:

The particle has a net charge of zero, but does become polarized in the presence of an electric field

- The particle is in the Rayleigh regime and can be approximated as a point electric dipole moment in a uniform electric field.^{98,99}

The particle size is small compared to the electric field gradient so that the external electric field can be approximated as constant over the dimension of the particle when determining the electric dipole moment.

The derivation begins with the Lorentz force, with the magnetic field set equal to zero.¹⁰⁰

$$\bar{F} = q\bar{E} \quad (6.1)$$

Because the particle is uncharged and polarized, the Lorentz force is rewritten in terms of the electric dipole moment of the particle, p . Figure 6.2 illustrates an arbitrary electric dipole with charges of $\pm q'$ separated by a distance d' and subjected to a non-uniform electric field.

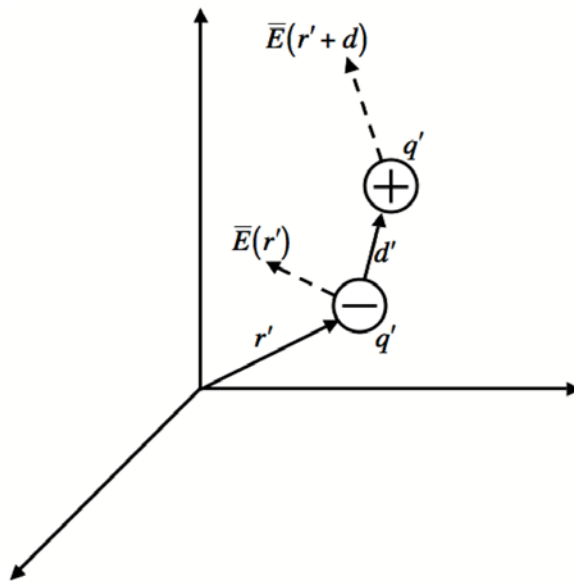


Figure 6.2: Electric dipole with charges $\pm q'$ separated by a distance d' and subjected to a non-uniform electric field.

The net force acting on the dipole is calculated by summing the forces acting on each charge.

$$\bar{F} = q' \left[\bar{E}(\bar{r}' + \bar{d}') - \bar{E}(\bar{r}') \right] \quad (6.2)$$

Equation (6.2) is approximated in terms of the gradient of the electric field magnitude and the electric dipole moment of the particle.¹⁰¹

$$\bar{F} = q' \left[\bar{E}(\bar{r}') + \bar{d}' \cdot \nabla E - \bar{E}(\bar{r}') \right] = q' \bar{d}' \cdot \nabla E = \bar{p} \cdot \nabla E \quad (6.3)$$

The gradient force acting on an uncharged particle is finalized by substituting in the electric dipole moment of the particle. In the case of an insulating sphere, the dipole moment has been shown to be dependent on the particle size, the dielectric constant of the particle, ϵ_p , and the surrounding medium, ϵ , and the strength of the electric field in the surrounding medium.^{102,99}

$$\bar{P}_{ins,sph} = 4\pi r^3 \epsilon \left(\frac{\epsilon_p - \epsilon}{\epsilon_p + 2\epsilon} \right) \bar{E} \quad (6.4)$$

Combining Equations (6.3) and (6.4), and using a vector identity, the net gradient force on an uncharged insulating spherical particle is determined.^{102,99}

$$\bar{F}_{grad,ins,sph} = 2\pi r^3 \epsilon \left(\frac{\epsilon_p - \epsilon}{\epsilon_p + 2\epsilon} \right) \nabla E^2 \quad (6.5)$$

The gradient force on a conducting sphere follows the derivation for the force on an insulating sphere with the only difference being the electric dipole moment. The electric dipole moment is defined as a function of the charges and the separation between them.³⁸

$$\vec{p} = q\vec{d} \quad (6.6)$$

When a conducting sphere is subjected to an external electric field, free charges within the particle distribute over the surface of the sphere in order to cancel out all internal electric fields. The magnitude of the charge separation and the distance that the charge separates can be integrated over the surface of the sphere to calculate the particle's electric dipole moment. Figure 6.3 shows a conducting sphere subjected to a uniform external electric field.

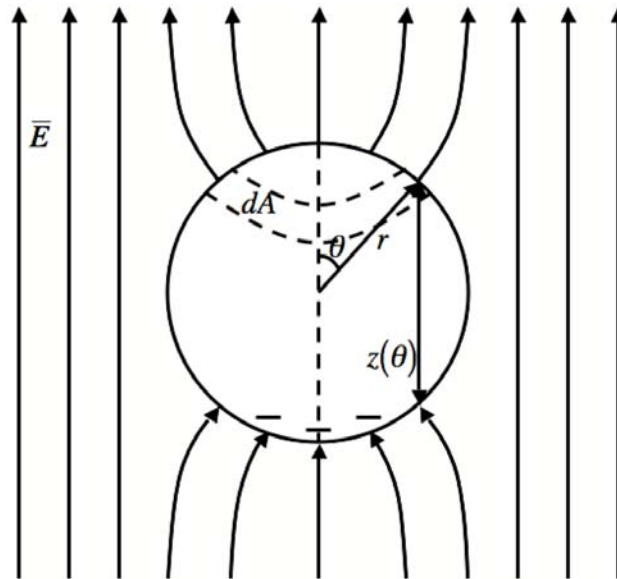


Figure 6.3: Conducting sphere subjected to a uniform external electric field.

The differential dipole moment element, dp , at θ is dependent on the surface charge density, $\rho_s(\theta)$, the differential area element, dA , and the charge separation, $z(\theta)$.

$$d\bar{p} = \rho_s(\theta)\bar{z}(\theta)dA \quad (6.7)$$

The surface charge density is dependent on the magnitude of the electric field at the surface of the particle and the dielectric constant of the surrounding medium.¹⁰³ Recall from Chapter 2 that the surface electric field is normal to the particle surface.

$$\rho_s(\theta) = \hat{r}' \cdot \epsilon\bar{E}_s(\theta) = \epsilon E_s(\theta) \quad (6.8)$$

The magnitude of the electric field at the surface of the particle is dependent on the magnitude of the external electric field and a field-focusing factor, which is a function of θ and similar to the field-focusing factors examined for particle charging in Chapter 2 and the electric force on a particle in Chapter 5.

$$E_s(\theta) = \alpha_p(\theta)|\bar{E}| = \alpha_p(\theta)E \quad (6.9)$$

The charge separation within the particle is dependent on the particle size, θ , and is in the direction of the external electric field.

$$\bar{z}(\theta) = \frac{\bar{E}}{|\bar{E}|} 2r \cos(\theta) \quad (6.10)$$

Equation (6.7) is simplified by substituting in Equations (6.8), (6.9), and (6.10).

$$d\bar{p} = 2\epsilon r \bar{E} \alpha_p(\theta) \cos(\theta) dA \quad (6.11)$$

Equation (6.11) is integrated over the surface of the particle to calculate its effective electric dipole moment.

$$\bar{p} = \int_0^{2\pi} \int_0^{\pi/2} 2\epsilon r \bar{E} \alpha_p(\theta) \cos(\theta) r^2 \sin(\theta) d\theta d\phi \quad (6.12)$$

Equation (6.12) is simplified by pulling all θ independent function out of the integral.

$$\bar{p} = 4\pi r^3 \epsilon \bar{E} \int_0^{\pi/2} \alpha_p(\theta) \cos(\theta) \sin(\theta) d\theta \quad (6.13)$$

Before the integral in Equation (6.13) can be evaluated, the field-focusing factor must be investigated. The parameter $\alpha_p(\theta)$ was investigated for conducting spherical particles in the setup shown in Figure 6.3 by employing COMSOL™, a multi-physics simulation environment. The simulation was created in a 2-dimensional environment with axial symmetry and used parallel electrodes to generate the uniform background electric field with the particle located at the midpoint between the electrodes. The electrode gap was chosen to be much larger than the particle diameter to ensure that the electrode gap did not influence the electric fields at the particle surface. The width of the simulation environment was set to 10 times the electrode gap to minimize field screening due to edge effects,²⁸ and the simulation cell size was chosen through trial and error to ensure that the simulation solution was not a function of cell size, but truly represents the

expected results. Note that this simulation is an extension to the simulations presented in Chapters 2 and 3.

It is expected that the absolute value of $\alpha_p(\theta)$ is maximum at the top ($\theta=0^\circ$) and bottom ($\theta=180^\circ$) of the particle where the external electric field is normal to the particle surface, and is minimum at the sides ($\theta=90^\circ$) of the particle where the external electric field is perpendicular to the particle surface. Figure 6.4 is a plot of $\alpha_p(\theta)$ as a function of θ .

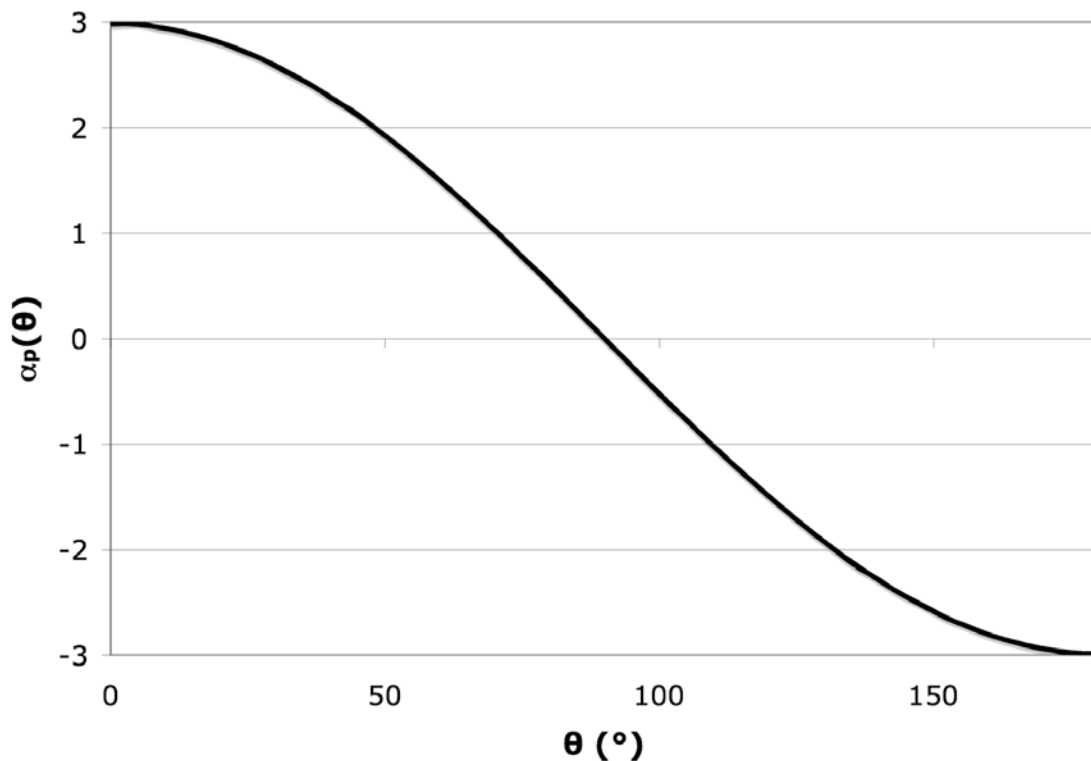


Figure 6.4: Field-focusing factor on a conducting spherical particle in a uniform background electric field.

The plot suggests that the magnitude of the field-focusing factor ranges from 0 at $\theta = 90^\circ$ to 3 at $\theta = 0^\circ$ and $\theta = 180^\circ$. As expected, the average field-focusing factor is 0, which is

a result of the particle having zero net charge. The integral from Equation (6.13) is approximated numerically using the data from Figure 6.4.

$$\int_0^{\pi/2} \alpha_p(\theta) \cos(\theta) \sin(\theta) d\theta \approx \sum_{\theta=0}^{\pi/2} \alpha_p(\theta) \cos(\theta) \sin(\theta) \Delta\theta \approx 1 \quad (6.14)$$

The electric dipole moment of a conducting particle in a uniform background electric field is determined by substituting Equation (6.14) into Equation (6.13).

$$\bar{p} \approx 4\pi r^3 \epsilon \bar{E} \quad (6.15)$$

Finally, the gradient force on a conducting sphere is determined by substituting Equation (6.15) into Equation (6.3) and using a vector identity.¹⁰⁴

$$\bar{F}_{grad,cond,sph} = 2\pi r^3 \epsilon \nabla E^2 \quad (6.16)$$

Note that the result from Equation (6.16) is consistent with Equation (6.5) when the dielectric constant of the particle is allowed to go to infinity. The electric field can be either time dependent or time independent, which will be discussed in further detail in the upcoming sections.

6.2.2. Maintaining Separation Between Uncharged Particles

It is important to maintain a separation between the uncharged particles once they reach the charging zones to ensure that all particles achieve the same charge-to-mass ratio

and final exhaust velocity, which was presented in Chapter 2. The use of the gradient force as a method of particle transport may lend itself nicely to maintaining particle separation. Previous research has shown, both theoretically and experimentally, that uncharged spherical particles subjected to either uniform or gradient electric fields experience either an attractive or repulsive force depending on the particles' orientation relative to the direction of the applied field, as depicted by Figure 6.5.¹⁰⁴ The relative force between two conducting spherical particles is determined by examining the effects of the electric field generated by one particle on a second particle.

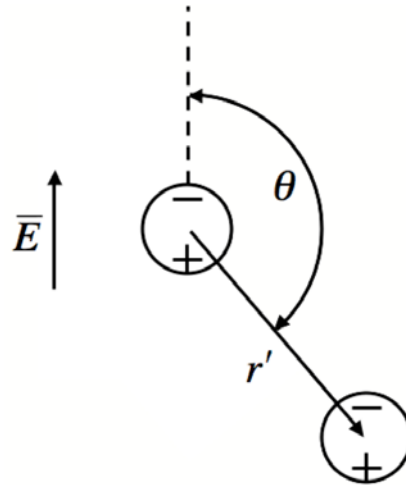


Figure 6.5: Two conducting spherical particles modeled as electric dipoles induced by an applied electric field.

The electric field generated by a spherical conducting particle modeled as an electric dipole is dependent on the particle's dipole moment and the distance from the particle.¹⁰⁰

$$\vec{E}_{dipole} = \frac{1}{4\pi\epsilon r'^3} [3(\vec{p} \cdot \hat{r}')\hat{r}' - \vec{p}] \quad (6.17)$$

Recall that the dipole moment of the conducting spherical particle is given by Equation (6.15), which simplifies Equation (6.17) to a function of the background electric field.

$$\bar{E}_{dipole} = E \frac{r^3}{r'^3} \left[\hat{r}' 3 \cos \theta - \frac{\bar{E}}{E} \right] \quad (6.18)$$

The potential energy of the second particle due to the electric field generated by the first particle is a function of the particles' dipole moments.¹⁰⁰

$$U_{dipole} = -\bar{p} \cdot \bar{E}_{dipole} \quad (6.19)$$

Equation (6.19) is simplified by substituting in Equations (6.15) and (6.18).

$$U_{dipole} = \frac{4\pi\epsilon r^6}{r'^3} E^2 (1 - 3 \cos^2 \theta) \quad (6.20)$$

Finally, the force between two conducting spherical particles modeled as electric dipoles subjected to an applied electric field is calculated from Equation (6.20).¹⁰⁴

$$F_{dipole} = \frac{12\pi\epsilon r^6}{r'^4} E^2 \left[\hat{r}' (1 - 3 \cos^2 \theta) - \hat{\theta} (2 \cos \theta \sin \theta) \right] \quad (6.21)$$

Figure 6.6 is a plot of the radial and tangential components of the force between the spherical particles normalized to the maximum force. A positive value represents a repulsive force and a negative value represents an attractive force.

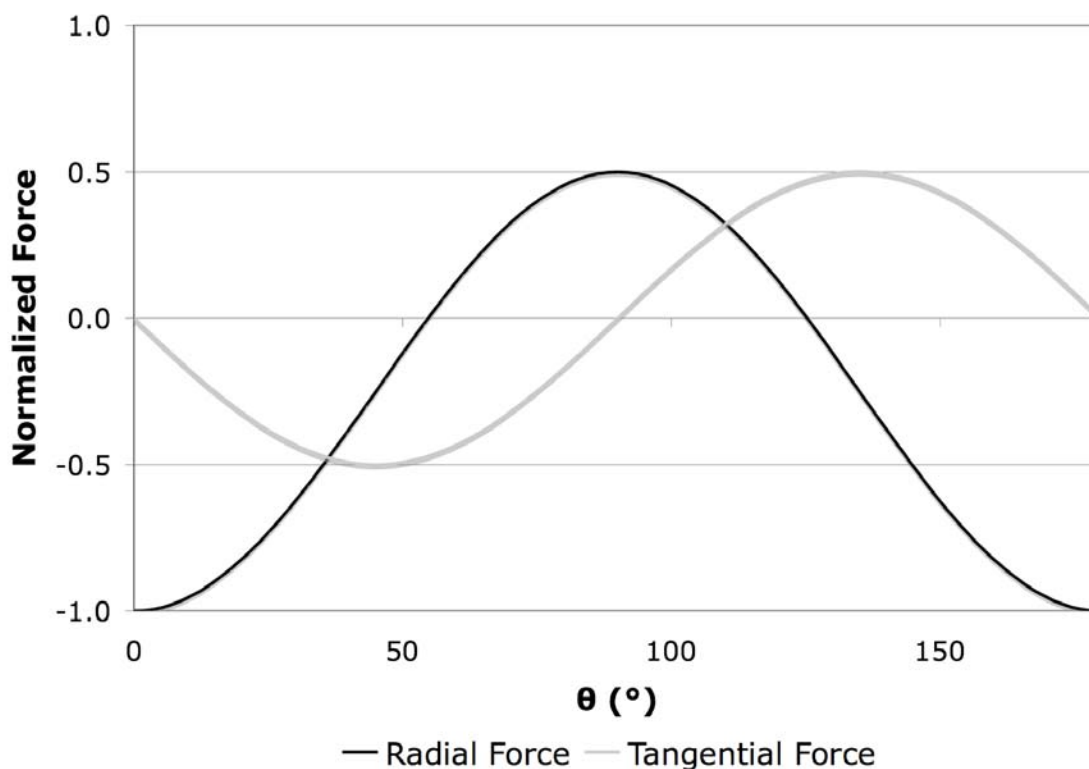


Figure 6.6: Normalized radial and tangential components of the force between two conducting spherical particles.

Figure 6.6 suggests that the radial force is attractive between the particles when θ is less than approximately 54.7° or greater than approximately 125.3° , and repulsive when θ ranges from 54.7° to 125.3° .¹⁰⁰ In addition, the tangential force works to align the particles with the external electric field. This analysis suggests that it may be possible to maintain separation between uncharged spherical particles during transport as long as the particles are maintained in the same plane ($\theta = 90^\circ$), which is normal to the applied electric field.

One method of maintaining the particles in the same plane is to transport the particles in contact with a planar surface. The exact design of a transport system is beyond the scope of this thesis, but it is possible to imagine a system that uses the adhesion force,

which was discussed in Chapter 5, to hold the particles in contact with a planar surface and uses an applied electric field, which is normal to the surface, to transport the particles via the gradient force and to help maintain proper particle separation. The particles may roll or drag along the planar surface depending on the coefficients of friction. Note that the theoretical analysis presented here assumes that the planar surface is a perfect insulator with a low dielectric constant and is taken to be infinitely thin. In addition, no charge accumulates on the interface between the mediums. These assumptions allow the analysis to neglect the affects of the dielectric surface on the shape and strength of the electric field. Of course in a real work application, these affects would need to be taken into account, but they are neglected for the sake of this analysis.

6.2.3. Methods of Particle Transport Utilizing the Gradient Force

This subsection investigates two methods of generating the non-uniform electric fields required to transport particles with the gradient force along a planar surface. Recall from Section 6.2.2 that the radial force repels the particles when they are maintained in the same plane that is normal to the applied electric field. Figure 6.7 is a one-dimensional model depicting the infinitely thin dielectric planar surface, which coincides with the x-y plane, the particles that are adhered to the surface, and the applied electric field in the z-direction. Note that the electric field is normal to the surface and is only a function of x.

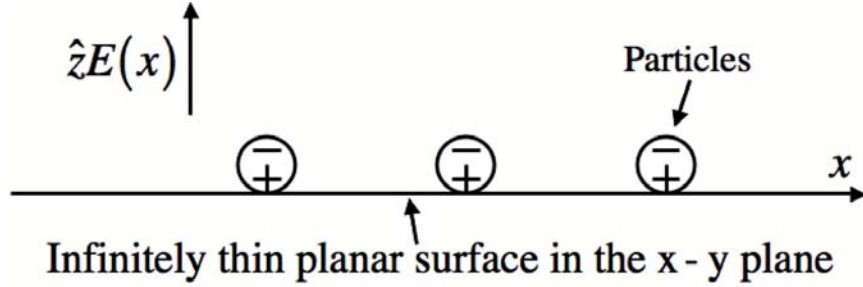


Figure 6.7: Particles are maintained in contact with a planar surface, which is normal to the applied electric field, during transport.

Assuming that the dielectric planer surface is infinitely thin and does not affect the shape or strength of the applied electric field, the gradient force on the conducting spherical particles is reduced to one-dimension from Equation (6.16).

$$\bar{F}_{grad,cond,sph} = \hat{x}2\pi r^3 \epsilon \frac{d}{dx} E^2 \quad (6.22)$$

When the particles are in contact with the planar surface, the force resisting movement parallel to the surface is the frictional force, which is dependent on the normal force and the coefficient of friction.

$$F_f = \mu_f F_N \quad (6.23)$$

The normal force is the force holding the particle and surface together, which is the sum of the adhesion and gravitational forces, presented in Chapter 5. Recall that for most micro- and nano-particles that the adhesion force is much greater than the gravitational force.

$$F_N \approx \frac{hr}{8\pi z^2} + \frac{4}{3}\pi r^3 \rho g \quad (6.24)$$

The coefficient of friction between micro- and nano-particles and the surface is difficult to determine because it is highly dependent on many parameters that are difficult to control, such as the particle and surface materials and roughness. In addition, the coefficient of friction depends on whether the particle slides or rolls along the surface. One source reported the coefficient of friction of pitch carbon microspheres with average diameters of 200 microns against steel 4130 to range from 0.12 to 0.38 depending on the particle velocity.¹⁰⁵ The analysis presented in this section assumes a coefficient of friction equal to 1 to provide a conservative approximation.

There exist many methods of generating gradients in an electric field that can be used to create a gradient force on micro- and nano-particles. Perhaps the most used method is through a laser system, which is a highly researched area for use with optical tweezers, which control and trap individual particles.¹⁰⁶ But, a laser system may not be an ideal method for use with micro- and nano-particle thrusters due to the large number of particles requiring transport. The following subsection investigates creating the non-uniform electric fields by generating standing waves or applying potential differences across non-uniform geometries. Note that the applied electric field can be time independent or dependent. For the case of a time dependent field, the force on the particles does change over time, but a time-average value can be calculated to determine the average force on the particles.

6.2.3.1. Gradient Forces from Standing Waves

Another previously researched area of moving particles with the gradient force is by creating a standing wave,⁹⁴ which can be created with a simple antenna and a cavity resonator. The basic equation of a standing wave in one-dimension is dependent on time, the wave number, frequency, and the position.

$$\bar{E}_{sw}(x, t) = \bar{E}_o \cos(\omega t) \sin(kx) \quad (6.25)$$

The gradient force from a standing wave is determined by substituting Equation (6.25) into Equation (6.22).

$$\bar{F}_{sw}(x, t) = \hat{x} 2\pi r^3 \epsilon_o E_o^2 k \cos^2(\omega t) \sin(2kx) \quad (6.26)$$

The time average gradient force on a conducting spherical particle is determined from Equation (6.26).⁹⁴

$$\langle \bar{F}_{sw}(x) \rangle = \hat{x} \pi r^3 \epsilon_o E_o^2 k \sin(2kx) \quad (6.27)$$

Equation (6.27) indicates that to increase the gradient force, the amplitude of the wave should be increased and the wavelength should be decreased. The wavelength is constrained with regards to the particle size. Recall from Section 6.2.1 that the electric field gradient is assumed to be small compared to the particle size in the Rayleigh regime, which requires the wavelength to be much greater than the diameter of the particles. Typically, the wavelength is at least ten times larger than the particle diameter. Figure

6.8 is a plot of the standing wave and the resulting gradient force both normalized to their respective maximum values over one and one-half wavelengths.

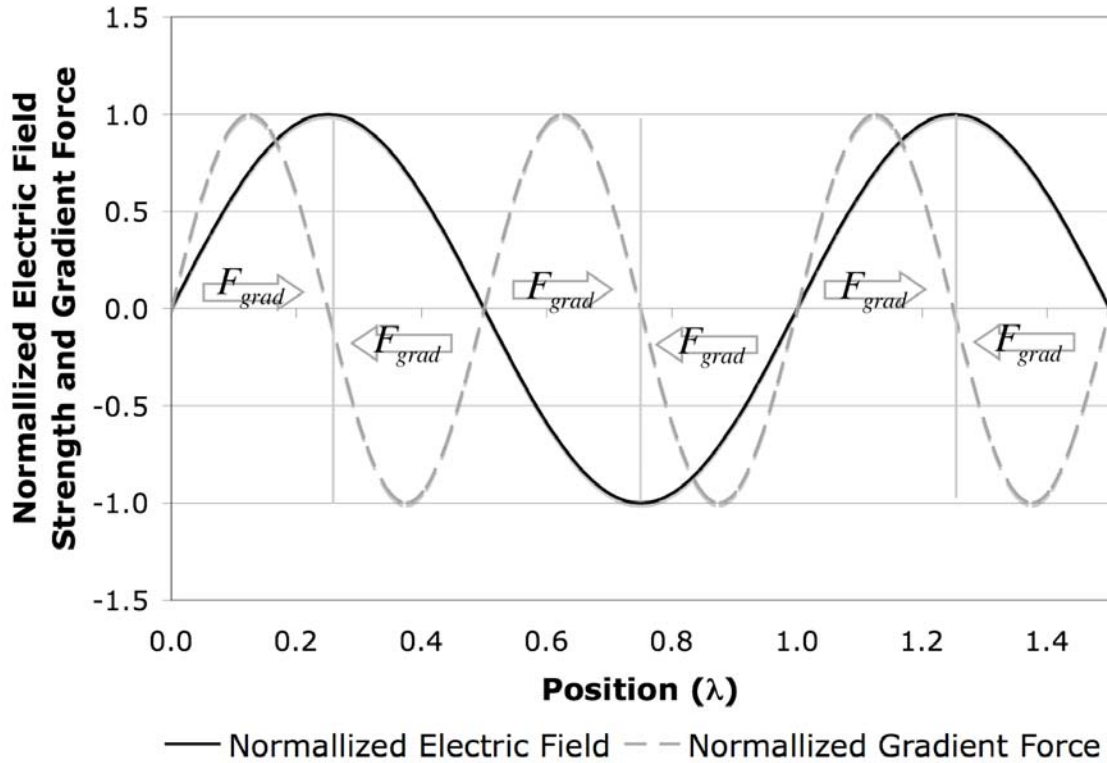


Figure 6.8: 1D standing wave and the gradient force.

As expected, the gradient force pulls the particles to the maximum field strength locations. Note that the force on the particles is zero at the maximum strength locations as well as the nodes. The gradient force is strongest at the midpoints between the peaks and nodes.

Assuming that the particles are adhered to an infinitely thin dielectric planar surface that is normal to the applied electric field (Figure 6.7), the required electric field amplitude to slide or roll a spherical particle across the planar surface is approximated with the normal force given by Equation (6.24) with a coefficient of friction of 1 and the gradient force given by Equation (6.27).

$$E_{thresh} \approx \sqrt{\frac{h\lambda}{16\pi^3 \epsilon_0 r^2 z^2} + \frac{2\rho g \lambda}{3\pi \epsilon_0}} \quad (6.28)$$

Similar to the particle extraction through a liquid surface from Chapter 4, and the removal of a particle from a dry surface from Chapter 5, the required amplitude of the standing wave can be separated into two components, the adhesion term and the gravitational term. In this case, the adhesion term scales inversely with the particle size and the gravitational term is independent of the particle size. Figure 6.9 is a plot of the calculated electric field threshold to transport conducting spheres as a function of particle diameter in the adhesion dominant regime. The four curves represent wavelengths of 10 μm , 100 μm , 1 mm, and 10 mm. The Lifshitz constant is taken as 9 eV, and the distance between the particle and the planar surface is 4 Angstroms.

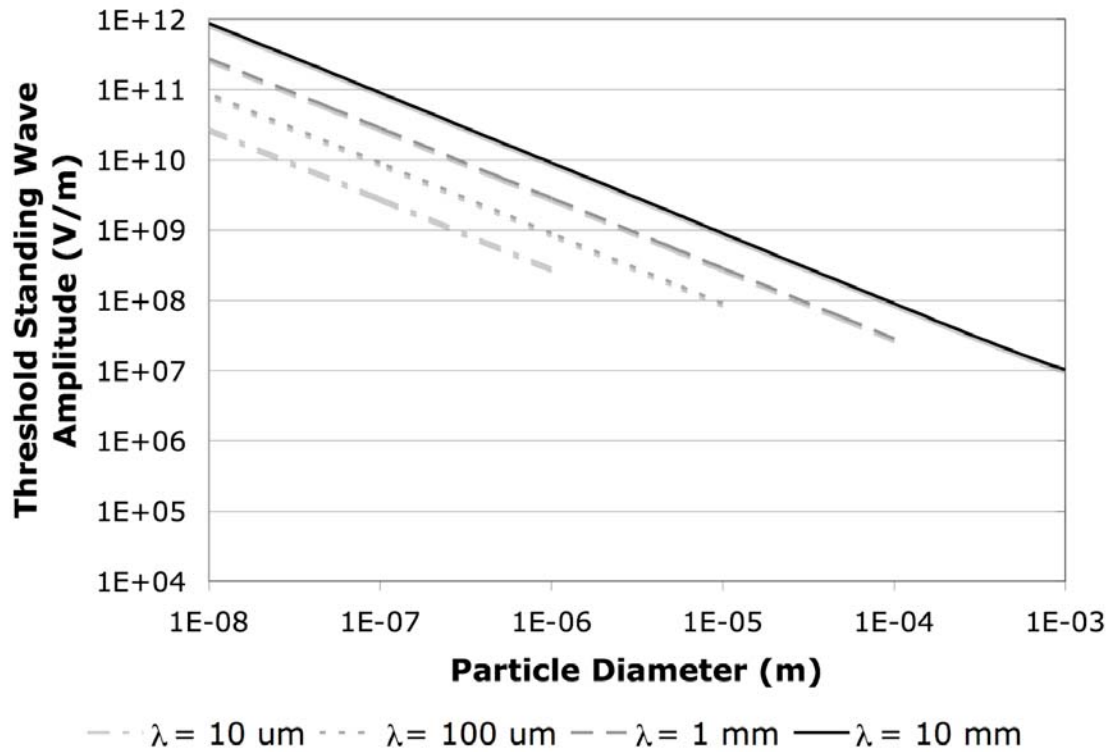


Figure 6.9: Threshold amplitude of a standing wave required to move a particle across a planar surface.

Figure 6.9 suggests that particles at the micron scale and below require electric field amplitudes on the order of hundreds of megavolts per meter and greater to achieve transport across the planar surface, which may be very difficult to produce without inducing an electrical breakdown.

The analysis presented in this subsection indicates that using sinusoidal standing waves alone to transport micro- and nano-particles across a planar surface may not be feasible, but it is possible that the addition of a mechanical vibration source may reduce the required field strengths.⁶²

6.2.3.2. Gradient Forces from High Aspect Ratio Posts

Another method of generating strong gradients in an electric field is by using high aspect ratio posts. The electric field intensification is greatest at the post tip and decreases quickly with the distance from the post tip. Figure 6.10 is one possible setup that utilizes an array of opposed high aspect ratio posts biased oppositely to produce strong electric fields. This model is two-dimensional extending infinitely in the y -direction.

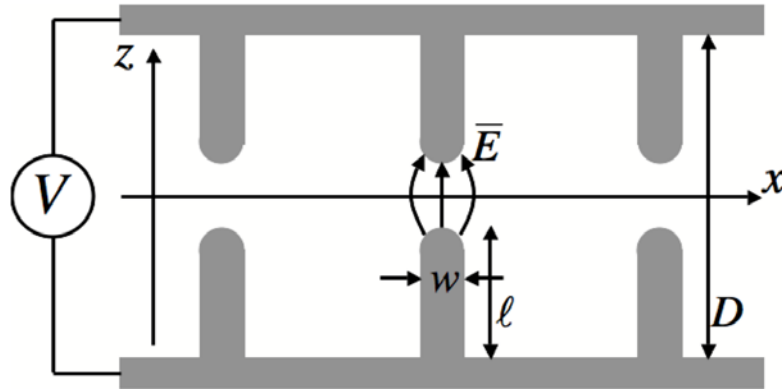


Figure 6.10: Possible setup using high aspect ratio posts to generate strong gradients in the electric field. An infinitely thin dielectric planar surface coincides with the x - y plane

The particles are confined to the infinitely thin dielectric planar surface that coincides with the x - y plane, and the gradient forces pull the particle to the regions of highest electric field strength, which are the points directly between and centered on the posts. If the pairs of opposed posts can be biased independently, it may be possible to transport particles along the x -axis by stepping the voltage along the post pairs in the desired direction of travel. To examine this possibility, the force on a particle as a function of x in the x - y plane resulting from a single biased post pair is investigated.

To determine if the geometry shown in Figure 6.10 can provide sufficient force to transport particles, a simulation pushing what state-of-the-art MEMS fabrication can achieve when creating narrow high aspect ratio posts is tested.^{107,108,109,110} The simulation was performed using a two-dimensional geometry with COMSOL. The total electrode gap, D , is $210\ \mu\text{m}$, the posts have a length of $100\ \mu\text{m}$ and a width of $1\ \mu\text{m}$. The tops of the posts are hemispheres to ensure that the maximum electric field strength is located between the posts. A potential bias of approximately $3.44\ \text{kV}$ was applied between the posts, which generates a maximum electric field strength of $1\ \text{GV/m}$ on the tips of the posts, which is near the threshold for electron emission.¹¹¹ The width of the simulation environment was set to 10 times the electrode gap to eliminate field screening due to edge effects,²⁸ and the simulation cell size was chosen through trial and error to ensure that the simulation solution was not a function of cell size, but truly represents the expected results.

The simulation provided the strength of the electric field as a function of x and the gradient force was calculated numerically using Equation (6.22). Figure 6.11 is a plot of the normalized electric field strength in the x - z plane as a function of the displacement divided by the width of the post. The origin represents the point directly between the posts. Also included in the plot is the normalized magnitude of the force on a conducting spherical particle confined to the x - z plane. Note that the force always acts towards the origin.

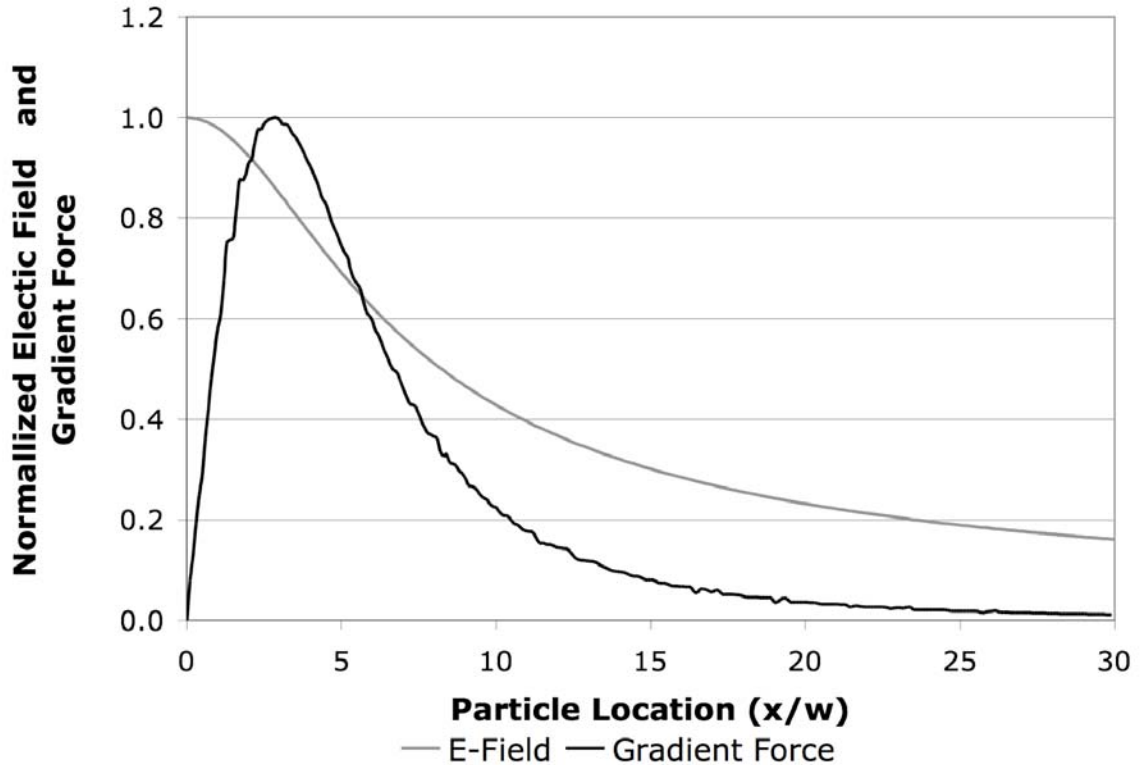


Figure 6.11: Normalized electric field strength and gradient force on conducting spheres in the x-y plane.

As expected, the electric field is maximum directly between the posts and falls off quickly in the x-direction. Note that the electric field strength falls to approximately 20% of its maximum value in the x-z plane at a displacement of only 20 times the width of the post ($x \approx 20w \approx 0.2\ell$). The gradient force is maximized at a displacement of approximately 2.9 times the width of the post and falls to 20% of its maximum value at about 10 times the width of the post ($x \approx 10w \approx 0.1\ell$). This implies that the gradient force from a high aspect ratio post may have a very limited range. Using the optimistic dimensions of the simulation, Table 6.1 lists the resulting maximum gradient forces on various sized spherical particles along with the required force to overcome the frictional force when a coefficient of friction of 1 is used. The Lifshitz constant is 9 eV.

Particle Dia. (m)	10^{-4}	10^{-5}	10^{-6}	10^{-7}	10^{-8}
Friction Force (N)	$2*10^{-5}$	$2*10^{-6}$	$2*10^{-7}$	$2*10^{-8}$	$2*10^{-9}$
Gradient Force (N)	$6*10^{-2}$	$6*10^{-5}$	$6*10^{-8}$	$6*10^{-11}$	$6*10^{-14}$

Table 6.1: Required force to overcome the frictional force and the maximum gradient force on various sized conducting spherical particles.

The table indicates that the gradient force should be capable of moving particles on the order of tens of microns and larger, but will not be capable of moving particles on the order of microns and smaller. This analysis, along with the limited range of the gradient force, suggests the use of high aspect ratio posts alone to generate a gradient force to transport particles along a planar surface may not be sufficient. But, it is possible that this method could be combined with another method, such as mechanical or acoustic vibration. The following subsection presents a brief proof-of-concept experiment for the post method discussed here.

6.2.3.3. Experimental Setup

To experimentally investigate the method of transporting dry spherical particles along a planar surface by way of the gradient force generated by high aspect ratio posts, the system depicted in Figure 6.12 was constructed with 10 cm aluminum electrodes. The aluminum post extending from the bottom electrode has a length of 8.5 mm and a diameter of 1.0 mm. Surrounding the post is a highly resistive material, LexanTM polycarbonate, which provides the planar surface for the particles to be transported across. Since the LexanTM material is not infinitely thin as was assumed in the analysis, it does affect the shape and strength of the electric field and, therefore, the gradient force. But, this experiment is only used as demonstration of transporting particles with the gradient force and is not intended to provide any accurate measurements.

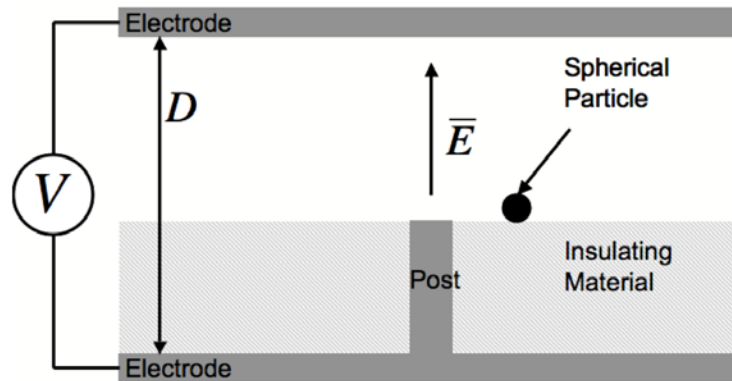


Figure 6.12: Experimental setup to prove the feasibility of transporting spherical particle by way of the gradient force generated by a high aspect ratio post.

The goal of the experiment is simply to demonstrate the transport of both conducting and insulating spherical particles across an insulating planar surface by way of the gradient force generated by a high aspect ratio post. It is performed by placing the particle in contact with the LexanTM surface next to, but not in contact with, the aluminum post as shown in Figure 6.12. Next, the upper electrode is secured in place to provide the correct uniform electrode gap, which is regulated by an insulating spacer to range from approximately 11 mm to 23 mm. The electric potential between the electrodes is applied to generate the strong non-uniform electric field, which imposes the gradient force on the particle and pulls the particle to the area of highest field strength, which exists at the tip of the post. The movement of the particle is monitored and recorded using a high-speed camera. The experiment was performed using various sized aluminum and nylon particles with diameters ranging from approximately 800 μm to 2.9 mm.

6.2.3.4. Experimental Results

Figure 6.13 is a series of frames from the high-speed camera showing the process of transporting a 1.6 mm aluminum particle across the planar surface by way of the gradient force, which was generated by the non-uniform electric field resulting from the high aspect ratio post. Note that all of the proof-of-concept experiments performed with various particle sizes and materials had similar outcomes, but no direct measurements of the gradient forces were made. The dimensions of the post are given in Section 6.2.3.3, the electrode gap is approximately 26 mm, and the applied electric potential is approximately 19 kV. The gap dimension and applied voltage were chosen so that the maximum electric field at the post tip is slightly less than the breakdown of the air, which was determined experimentally. Using the maximum allowable field strength provides the greatest force on the particle given by Equation (6.22). Frame (a) shows the particle at rest on the LexanTM and slightly to the right of the post before the electric field was applied. The particle begins to roll across the LexanTM surface towards the post due to the gradient force as shown in frame (b). The particle continues to roll across the surface until it finally contacts the post in frame (c). Recall from Chapter 2 that when a conducting particle contacts a source electrode in the presence of an electric field, it becomes charged in order to cancel out all internal electric fields. Once the particle is charged, the electrostatic force on the particle is much greater than the gradient force, and the particle is accelerated along the electric field lines as shown in frame (d).

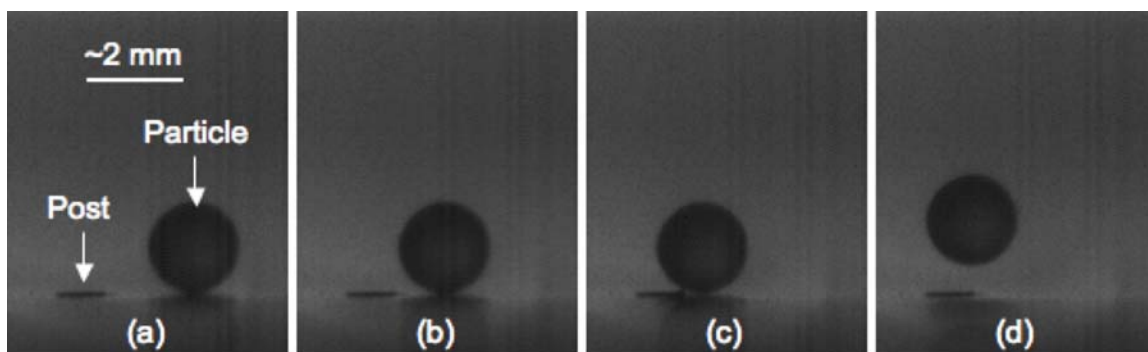


Figure 6.13: Series of frames showing the transport of an aluminum spherical particle by the gradient force, which is generated by a high aspect ratio post.

The series of frames shown in Figure 6.13 confirms the feasibility of transporting particles by way of the gradient force when generated by a high aspect ratio post. But, note that the particle is transported over a distance of only a couple times the diameter of the post. Moving the particle over a greater distance is not possible using this setup due to the limited range of the gradient force presented in Figure 6.11. All of the particles tested were successfully transported, but no measurements of the gradient force were made. The largest noticeable difference between the transport of the aluminum and the nylon particles was in the ability to charge the particles once they contacted the post. While the aluminum particles were charged and lifted in the vertical direction as shown by frame (d) of Figure 6.13, the nylon particles did not charge fast enough to be lifted.

The experimental results presented in this subsection along with the theoretical predictions from Section 6.2.3.3 indicate that using high aspect ratio posts to create strong gradient forces to transport micro- and nano-particles across a planar surface is possible, but may not be reasonable due to the required electric field strengths and the limited range of the gradient force around the post.

6.3. Particle Transport Through Micro- and Nano-Sieves

This section investigates the feasibility of a simple method of transporting the dry particle propellant as a dense clumped powder and then forcing the powder through an ultra-fine sieve to separate it into individually isolated particles prior to charging and acceleration. Figure 6.14 is a simplified model of the sieving configuration for use with dry particles and consists of a particle storage reservoir directly against the ultra-fine sieve. Beneath the storage reservoir is a control piston that supplies pressure to help force the particles through the sieve, which is aided by a vibrational source and a lateral translational puck (not shown). The sieve size is matched to the particle size with the hope that only one particle is capable of passing through each sieve orifice at a time, which breaks the clumped powder into individually isolated particles. Above the sieve are the stacked charging and acceleration grids. Electric potentials are applied across the conducting sieve and the stacked grids to generate the charging and accelerating electric fields used to charge and accelerate the individual particles that pass through the sieve.

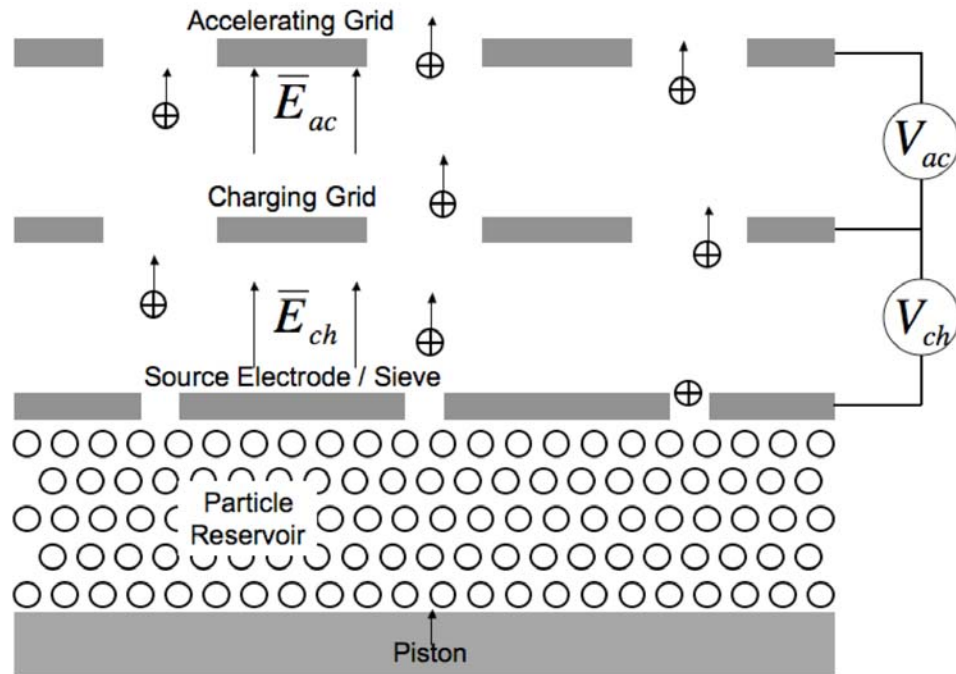


Figure 6.14: Simplified model of sieving delivery system for dry particles.

This section presents a proof-of-concept experiment with the goal of demonstrating the feasibility of this delivery system, which will provide direction for future research and development. The main goals of the proof-of concept experiment are to demonstrate the functionality of the prototype by demonstrating continuous operation and confirming that particles are charged, accelerated and ejected individually.

6.3.1. Experimental Setup

To experimentally investigate the method of delivering individual dry spherical particles through an ultra-fine sieve prior to charging and accelerating, the prototype depicted in Figure 6.15 was constructed. Picture (a) is a schematic of the system and picture (b) is the actual prototype. The sieve was made from a stainless steel cloth with orifice diameters of approximately 20 μm and was tested with hollow aluminum

spherical particles with diameters ranging from 5 μm to 20 μm . A 1 ml syringe that has an inner diameter of approximately 4.7 mm is mounted beneath the sieve and acts as the particle reservoir. The syringe's plunger is driven by a linear actuator to help feed the particles through the sieve. A measurement of the force applied by the linear actuator with a piezoelectric force sensor and the displacement of the actuator are used along with a LabVIEW control program to regulate the applied pressure and displacement. Applied pressures ranged from approximately 0.3 to 0.6 N/mm^2 . A mechanical vibrational source is mounted to vibrate the entire system on the order of tenths of a g to aid with particle delivery. In addition, a lateral translational puck, as shown in Figure 6.15, is placed between the particle reservoir and sieve. The translational puck is made from polyvinyl chloride (PVC) into a cylindrical shape with a circular orifice the same size as the syringe orifice through its center. The particles pass through the puck's orifice as they are fed from the syringe to the sieve. The translational puck is driven laterally with a solenoid at a displacement of approximately 2 mm, which provides lateral movement of the particles against the sieve surface to help prevent the particles from jamming. Note that future prototype designs will most likely implement piezoelectric devices to replace both the vibrational source and the translational puck. Mounted on the topside of the sieve is the charging grid, which is approximately 15 mm from the sieve surface, and has a single 5 mm orifice to allow the passage of particles. Above the charging grid is the collection anode used to collect all ejected particles. The entire system is mounted on a tripod fabricated from 80/20.

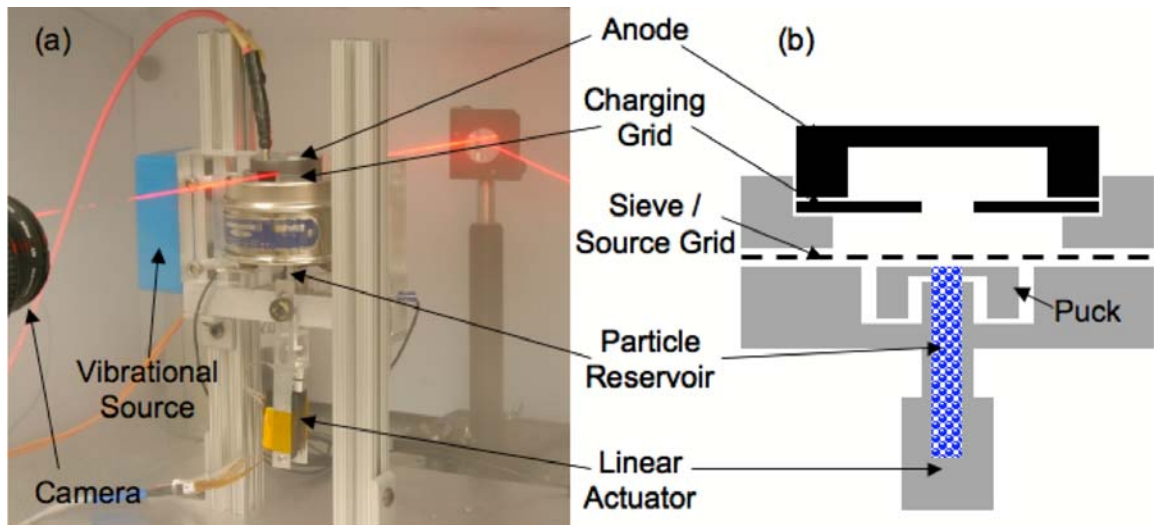


Figure 6.15: (a) Schematic and (b) photograph of the sieving delivery system prototype.

The sieve is electrically connected to ground while the charging grid and the collection anode are biased positively using a high voltage power supply to generate the charging electric field. Note that this prototype does not include any additional accelerating grids, but stacking additional grids above the charging grid is possible. To confirm particle emission, a high-speed camera images the ejected particles as they transit the gap between the charging grid and the collection anode. A 15 mW, 632 nm, Helium-Neon laser is used to illuminate the particles. An additional verification technique collects the emitted particles on a copper slide placed just above the orifice in the charging grid and images the collected particles using a scanning electron microscope (SEM).

6.3.2. Experimental Results

Figure 6.16 is a photograph from the high-speed camera showing what appear to be individually emitted particles as they transit the gap between the charging grid and the collection anode, which confirms the operation of the prototype.

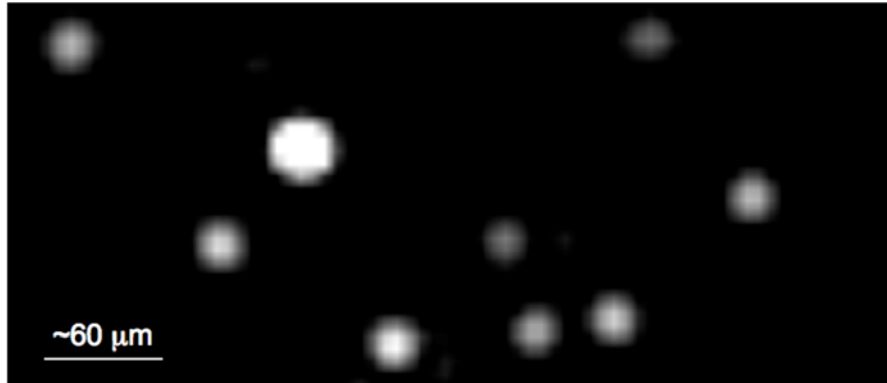


Figure 6.16: Photograph showing individual micron particles as they transit the gap between the charging grid and the collection anode.

Figure 6.17 is an SEM image of the glass slide after bombardment of the aluminum particles for a short impulse.

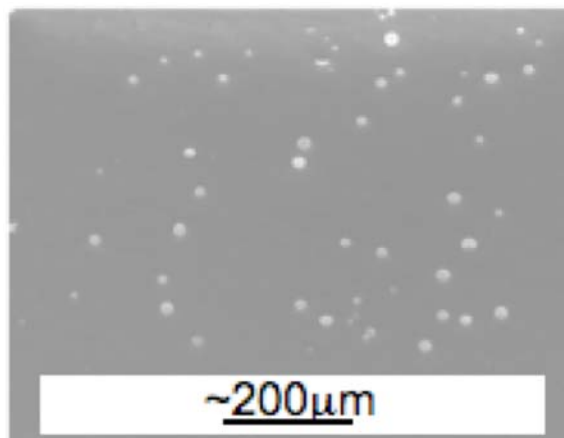


Figure 6.17: Images showing individual aluminum particles collected on a glass slide after bombardment.

Figure 6.17 supports the idea that the particles are ejected individually as all the particles collected by the glass slide are individually isolated. In addition, the prototype successfully demonstrated continuous emission of approximately 1 gram of particles over a period of approximately 3 minutes.

The application of the vibrational source did not appear to affect the operation of the prototype, but the translational puck was essential. Without the translational puck, the particles became jammed and continuous emission was not possible. But, with the translational puck operating, particle jamming was significantly reduced, and the rate of emission appeared to correlate with the oscillation rate of the puck. The proof-of-concept experiment presented in this subsection suggests that the sieving delivery method is capable of continuously ejecting individually isolated particles. It is recommended that future work continue improving this prototype and characterize its performance to gain additional insight.

6.4. Conclusion

Two possible methods of transporting dry micro- and nano-particles were investigated for use with micro- and nano-particle thrusters. The first method takes advantage of the gradient force on uncharged spherical conducting particles when subjected to non-uniform electric fields. In addition to transporting the particles, it was shown that the gradient force might be capable of maintaining particle separation during transport as long as the particles are kept in the same plane that is perpendicular to the applied electric field. Two approaches of generating the gradient electric fields were presented and discussed. The first approach generated high amplitude standing waves

and the second approach used high aspect ratio posts to focus and shape the electric fields. Both approaches appear to be feasible for particles larger than approximately 10 μm , but may not be effective on their own for particles much smaller. A simple proof-of-concept experiment validated the use of high aspect ratio posts to generate the non-uniform electric fields required to induce the gradient force and transport spherical particles in the millimeter range.

The second method of transportation forces the particles in a clumped powder through an ultra-fine sieve to break the powder into individually isolated particles before charging, accelerating, and ejecting the propellant. A simple proof-of-concept experiment with the first sieving prototype indicates that this is a viable method for transport and is capable of continuously emitting single particles at the micron scale.

The discussions and results presented in this chapter give promise to the feasibility of the no liquid configuration, especially through the use of the sieving design. Although, many more experiments are required to validate additional aspects of the method, it is the recommendation of the author to continue research and development to fully understand the sieving design and to reduce the particle size.

Chapter 7

Conclusions and Recommendations for Future Research

In this dissertation, a concept of utilizing charged, conducting micro- and nano-particles accelerated to high energies and velocities for the purpose of in-space electric propulsion has been investigated. Several potential critical obstacles were identified and thoroughly studied. In some instances, the potential obstacles proved to be realistic constraints that required modification of the overall system design. In other situations, the potential obstacles were overcome using alternate approaches. One area that is expected to help advance this concept is the ability to fabricate complex three-dimensional structures using MEMS/NEMS technologies. It should also be noted that high energy and velocity particles might be beneficial to other terrestrial applications such as materials processing, nano-printing, and biomedical engineering.

7.1. Summary and Conclusions of Research

The nano-particle field extraction thruster (nanoFET) research team at the University of Michigan was the first to study the concept of a micro- and nano-particle thruster in depth. The research presented in this thesis developed an understanding of the physics pertaining to the advanced thruster concept through theoretical and experimental work.

7.1.1. Particle Charging

A method of charging both spherical and vertically oriented cylindrical conducting particles when in contact with an electrode surface and subjected to an applied electric field were investigated for use with micro- and nano-particle thrusters. The models developed in this thesis suggest that the attainable charge-to-mass ratios of both spherical and cylindrical particles are increased when the particle diameters are decreased. Further, the charge-to-mass ratio of a spherical particle is shown to be greater than the charge-to-mass ratio of a cylindrical particle with the same diameter if the maximum electric field strength focused at the particle tip is maintained (although it is easier to achieve the maximum electric field with cylindrical particles with high aspect ratios due to their large field-focusing factors). In addition, simulation results suggest that it may be possible to increase the charge on a spherical particle by nearly a factor of two by charging it on a high aspect ratio charging posts.

To investigate the particle charging models, various particle shapes, sizes, and materials were studied. The tests agreed reasonably well with the models when the particles remained in contact with the source electrode much longer than the particle charging time constants. But, the charge acquired by the some particles was less than predicted when the particles were removed from the source electrode sooner than required by the particle charging time model. It is possible that the these particles were not charged as predicted due to a higher electrical contact resistance, which may result from an oxide layer on coating the surfaces and the small contact area between the particle and the electrode. Nonetheless, the results suggest that using micro- and nano-

particles charged electrostatically by high strength electric fields is feasible from the charging standpoint assuming charging time is properly managed.

7.1.2. Liquid Instability

The initiation of an instability on a liquid surface by way of an applied high strength electric field was investigated in both earth-gravity and zero-gravity environments. The required threshold electric field was shown to be a function of the liquid's properties and the allowable size of the liquid perturbation. Controlling the size of the liquid perturbation was suggested as a method to suppress and control the liquid instability. The liquid's conductivity does not have an effect on the threshold electric field required to initiate the instability, but it does affect the time required for the instability to occur. Experimental results of inducing a liquid surface instability on both insulating and conducting liquid surfaces in an earth-gravity environment agreed with the theoretical predictions.

7.1.3. Particle Extraction

Extracting spherical and cylindrical conducting particles from an insulating liquid with an applied electric field was investigated, theoretically and experimentally, for use with micro- and nano-particle thrusters. The theoretical models suggest particle extraction is possible, and the experimental results confirmed the prediction and proved the feasibility. The required strength of the extraction electric field was shown to be dependent on particle size, particle charge, and the surface tension of the liquid. But, the

strength of the extraction electric field is limited by the tendency of the liquid surface to become unstable, which in turn restricts the size of extractable particles.

Current models suggest that the smallest extractable cylindrical particles from silicone oil are on the order of several tens of nanometers in diameter, when keeping the cylindrical particle aspect ratio less than 80. When these particles with a density of 1,000 kg/m³ are accelerated with a potential drop of 40 kV, the maximum obtainable specific impulse is on the order of 40 seconds, which is much less than required for use with an electric propulsion system.

The limited ability to extract particles from an insulating liquid with an applied electric field was shown to be a significant limiting factor for the insulating liquid configuration as a micro- and nano-particles thruster.

7.1.4. Particle Adhesion and Cohesion

The adhesion and cohesion forces affecting micro- and nano-particles were presented and their effects on the operation of micro- and nano-particle thrusters were investigated. For conducting particles in a dry environment, the dominant adhesion and cohesion force is the van der Waals force, which scales directly with the particle size. A method of overcoming the adhesion between a spherical particle and the source electrode with the application of a high strength electric field was presented. The resulting electric force responsible for particle removal scales directly with the square of the particle size, suggesting that as the particle size decreases, the required electric field for removal increases. The developed models predict that particles with diameters down to tens or

hundreds of nanometers can be removed from a planar electrode depending on the effective Lifshitz constant.

To investigate the particle removal model, eight test cases, involving 4 particle sizes and 2 electrode materials, were studied. The tests agreed reasonably well with the model when using values of the Lifshitz-van der Waals constants within the expected ranges for all materials. But, the values evaluated from the experimental data disagree with published values for the specific material combinations. But, recall that many authors are not in agreement on the published values. In addition, the spread in the electric fields required to remove particles was very large. The error in the Lifshitz-van der Waals constants and the large spread of the electric fields may be attributed primarily to the surface roughness and deformation of both the particles and the electrode.

7.1.5. Dry Particle Transport

Two potential methods of transporting dry micro- and nano-particles across a planar surface were investigated for use with micro- and nano-particle thrusters. The first method takes advantage of the gradient force on uncharged spherical conducting particles when subjected to non-uniform electric fields. In addition to transporting the particles, it was shown that the gradient force might be capable of maintaining particle separation during transport as long as the particles are kept in the same plane that is perpendicular to the applied electric field. Two approaches of generating the gradient electric fields were presented and discussed. The first approach generated high amplitude standing waves and the second approach used high aspect ratio posts to focus and shape the electric fields. Simulation results suggest that both approaches appear to be feasible for particles

larger than approximately 10 μm , but may not be reasonable on their own for particles much smaller. A simple proof-of-concept experiment validated the use of high aspect ratio posts to generate the non-uniform electric fields required to induce the gradient force and transport spherical particles in the millimeter range.

The second method of transportation forces the particles in a clumped powder through an ultra-fine sieve to break the powder into individually isolated particles before charging, accelerating, and ejecting the propellant. A simple proof-of-concept experiment with a prototype indicates that this is a viable method for the transport of particles with diameters around 10 microns and is capable of emitting single particles.

7.1.6. Thruster Performance

The results and conclusions from this thesis help to estimate the possible performance of a nano-particle thruster. For example, when using a background electric field of 100 MV/m to charge a spherical particle with a density of $1,000 \text{ kg/m}^3$ on a planar electrode, and using an accelerating voltage of 40 kV, it may be possible to provide specific impulses upwards of 500 seconds. Note that there may exist methods of increasing the obtainable specific impulse to the 1,000 to 2,000 second range. Some methods include decreasing the particle size, decreasing the particle density, and charging the particles on high aspect ratio posts.

In addition, this thesis helped to identify several advantages of micro- and nano-particle thrusters over current electrostatic propulsion technologies. Unlike traditional electric propulsion systems, which ionize atoms, this concept electrostatically charges the particles, which allows the charge-to-mass ratio of the propellant to be adjusted.

Adjusting the charge-to-mass ratio provides the capability of tuning various operational parameters. In addition, this concept appears to offer a way to eliminate life-limiting physical characteristics of present state-of-the-art ion propulsion systems by eliminating the need for a discharge chamber and reducing or eliminating charge-exchange (CEX) collision effects in the ion optics region. Further, the use of MEMS technologies may provide an approach to achieve scalability and system simplification by creating scalable “flat panel” thrusters.

7.2. Recommendations for Future Work

The overall development of the micro- and nano-particle propulsion system discussed in this thesis has the goal of finalizing the system design and fabricating a flight ready thruster. To accomplish this goal, many aspects of the system require additional research and development. The following subsections briefly discuss the next areas of interest recommended by the author.

7.2.1. Scale Particle Size Down into the Nanometer Range

To date, all experiments have been performed with particles at or above the micron level. It is important to continue scaling down the particle size into the nanometer regime to determine if the models presented in this thesis are still applicable. It is suspected that at some particle size, the particles will stop behaving as macroscopic bodies and effects at the molecular level will need to be addressed. For example, the particle charging model presented in Chapter 2 predicts that particles with diameters on the order of a few

nanometers will become charged with a value less than the elementary charge, which is, of course, not possible.

7.2.2. Further Research and Development of the Sieving Delivery System

It is the author's belief that the no-liquid configuration, which utilizes an ultra-fine sieve to break the particle propellant into individual isolated particles prior to charging, accelerating, and ejecting, to be the most promising configuration. It offers a simple and elegant solution compared to both of the liquid design configurations. But, there are still potential roadblocks that may limit the feasibility of this system. As stated in the previous subsection, it is critical to continue scaling down the particle size to determine if this sieving method will continue to work with smaller and smaller particles. In addition, present off-the-shelf particle sieves have been found to go down to only the single micron level. It is important to the development of the sieving method to fabricate much smaller particle sieves, which will most likely require MEMS expertise.

7.2.3. Use of a Vibrational Source

Current research lead by Liu,^{62,112} a member of the nanoFET team at the University of Michigan is investigating the use of a piezoelectric device as a vibrational source to help overcome the adhesion and cohesion of micro-particles. The incorporation of a vibrational source may significantly ease the removal of particles from the source electrode and ease the passage of the particles through the sieve. It is expected that the application of a vibrational source will become more important as the particle size scales down and the adhesion and cohesion forces become even more significant.

7.2.4. Develop Better Understanding of the Adhesion and Cohesion Forces

The models and experimental results from Chapter 5 suggest that the adhesion and cohesion forces become more dominant as the particle size is reduced, which will complicate the design of a micro- and nano-particle thruster. But, it was suggested that in addition to the particle size, the adhesion and cohesion forces have strong dependencies on the materials and/or the surface characteristics of the bodies in contact. Therefore, it is possible that choosing a proper material combination or modifying the surface characteristics may reduce the adhesion and cohesion forces.

7.2.5. Keep Building Prototypes

The significant advances in the development of the micro- and nano-particle thruster have come by way of experimental results. In addition, these results have provided direction for the development process. It is the author's recommendation to continue building simple prototypes to test the potential roadblocks and to help guide and redirect research efforts.

Appendices

Appendix A

Matlab Code

The computer code utilized in Chapter 2 to calculate the charge of both spherical and cylindrical particles was written in Matlab™ version 7.4.0 and is presented here. The program uses the output voltage from the current measuring circuit discussed in Section 2.3 along with values of the feedback resistor, the feedback capacitor, and the offset voltage to calculate the current. The current is integrated to calculate the total charge acquired by the particle.

$$q_m = \int i(t)dt \quad (\text{A.1})$$

A second method calculates the charge of the particle using the average particle current, velocity, and the electrode gap separation for confirmation.

$$q_m = \frac{i_{avg}\Delta s}{u_{avg}} \quad (\text{A.2})$$

```

function [Q1 Q2 Tcharging] = ChargeMeasurement_Final()

% Clear current variables and close all figures
clear
clc
close all

% The user is prompted to enter experimental parameters
R_feedback = input('Enter the value of the feedback resistor (Ohms) (positive value): ');
clc
V_offset = input('Enter the voltage offset (Volts): ');
clc
C_feedback = input('Enter the value of the feedback capacitor (F): ');
clc
Gap_Width = input('Enter the width of the electrode gap (m): ');
clc

% Load the measured voltage (V) as a function of time (s)
load TimeAll.mat TimeAll
load VoltageAll.mat VoltageAll

% Compute the time step between measurements
delta_t = TimeAll(2)-TimeAll(1);

% Compute the total current through the feedback resistor
Current_R = -(VoltageAll+V_offset)/R_feedback;

% Compute the total current through the feedback capacitor
for(n = 1:length(VoltageAll))
    if(n < 2 | n > length(VoltageAll)-1)
        dV(n) = 0;
    else
        dV(n) = VoltageAll(n+1) - VoltageAll(n-1);
    end
end
dV(1) = dV(2);
dV(length(VoltageAll))=dV(length(VoltageAll)-1);
dVdt = dV./(2*delta_t);
Current_C = -C_feedback*dVdt;
Current_C = transpose(Current_C);

% Compute total current from both feedback resistor and capacitor
CurrentAll = Current_R+Current_C;

% Plot output voltage as a function of time
figure(1)
plot(TimeAll, VoltageAll)
title('Output Voltage')
xlabel('Time(s)')
ylabel('Voltage (V)')

% Plot total current as a function of time
figure(2)
plot(TimeAll, CurrentAll)
title('Current Through Experimental Cell')

```

```

xlabel('Time(s)')
ylabel('Current (A)')

% Plot current through resistor as a function of time
figure(3)
plot(TimeAll, Current_R)
title('Resistor Current')
xlabel('Time(s)')
ylabel('Current (A)')

% Plot current through capacitor as a function of time
figure(4)
plot(TimeAll, Current_C)
title('Capacitor Current')
xlabel('Time(s)')
ylabel('Current (A)')

% Using inputs from user, determine stages of current
kk = 0;
k = 1;
while(kk == 0)
    Point1(k) = input('Enter start time (s) for particle charging: ');
    clc
    Point2(k) = input('Enter the time (s) when the particle leaves the 1st electrode: ');
    clc
    Point3(k) = input('Enter the time (s) when the particle arrives at the 2nd electrode: ');
    clc
    if(Point2(k) == Point3(k))
        kk = 99;
    end
    k = k+1;
end

% Isolate desired oscillation
for(p = 1:1:k-2)
    TimeStart = Point1(p);
    Coord_Start = find(TimeAll == TimeStart);
    clc
    TimeEnd = Point3(p);
    Coord_End = find(TimeAll == TimeEnd);
    clc
    TimeSection = TimeAll(Coord_Start:1:Coord_End)
    CurrentSection = CurrentAll(Coord_Start:1:Coord_End)

% Determine base current level (will be subtracted out of total current)
TimeStart_Base = Point1(p);
Coord_Start_Base = find(TimeAll == TimeStart_Base);
clc
TimeEnd_Base = Point2(p);
Coord_End_Base = find(TimeAll == TimeEnd_Base);
clc
CurrentBase =
sum(CurrentAll(Coord_Start_Base:1:Coord_End_Base))/length(CurrentAll(Coord_Start_Base:1:Coord_End_Base));

```

```

% Determine particle current during chosen oscillation
ParticleCurrent = CurrentSection - CurrentBase;
AvgParticleCurrent = sum(ParticleCurrent)/length(ParticleCurrent);

% Plot the particle current as function of time for single oscillation
figure(p+4)
plot(TimeSection, ParticleCurrent)
title('Particle Current During Particle Transport')
xlabel('Time(s)')
ylabel('Current (A)')

% Determine average particle velocity during chosen oscillation
AvgVel = Gap_Width/(TimeEnd - TimeStart);

% Calculate particle charge by integrating
Q1(p) = AvgParticleCurrent*Gap_Width/AvgVel;

% Calculate particle charge using average values
Q2(p) = trapz(ParticleCurrent)*delta_t;

% Calculate charging time of particle
% Total time in contact with electrode
Tcharging(p) = Point2(p)-Point1(p);

end

return

```

Appendix B

COMSOL MultiPhysics

COMSOL Multiphysics® was used in Chapters 2, 3, and 5 as a tool to analyze the magnitude and direction of electric fields in the vicinity of complex structures. In this thesis, the complex structures of interest were spherical and cylindrical particles as well as spherical liquid perturbations. An understanding of the electric fields around these structures provided methods of calculating the surface charge densities, the total charge, and the net force acting on the structures. This appendix presents a brief overview of COMSOL Multiphysics® and how it was implemented to calculate the required electric fields.

COMSOL Multiphysics® is a finite element simulation package designed for many different physics and engineering applications, which include electromagnetics, acoustics, chemical, heat transfer, materials, and many more. The user can build structures in a CAD-like environment or import actual CAD files into the COMSOL software. After completing the structures, the user specifies physical boundary and initial conditions. Then, the software breaks the structure down into finite elements (mesh), which can be regulated by the user. Next, the software solves the systems over the specified mesh using predefined or user entered partial differential equations (PDEs)

along with the boundary and initial conditions. Finally, COMSOL offers many methods to display the results through a variety of plots.

Here an example of a COMSOL structure used in Chapter 2 to determine the total charge acquired by spherical particles in contact with a planar electrode and subjected to an applied electric field is presented. Recall that the model for charging spherical particles (Figure 2.1) assumes two parallel electrodes with a single conducting spherical particle in contact with the upper surface of the bottom electrode. An electric potential bias, V , is applied across the electrodes to generate the electric field within the gap. The geometry from Figure 2.1 was created in COMSOL in a 2-dimensional environment with axial symmetry and meshed as shown in Figure B.1.

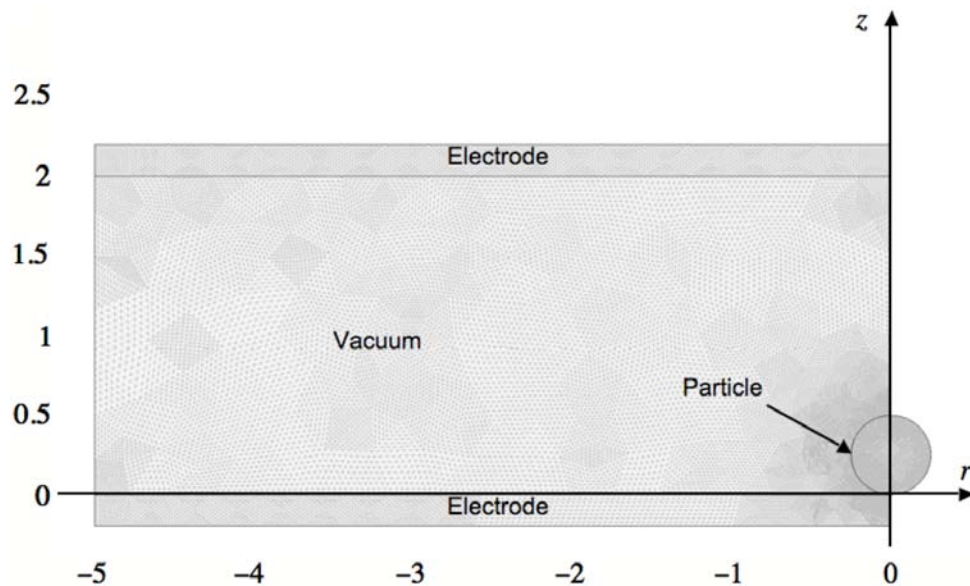


Figure B.1: Meshed COMSOL structure used to determine the electric field at the surface of a spherical particle when charged in contact with a planar electrode and subjected to an applied electric field.

The structure in Figure B.1 shows the particle just above the origin in a cylindrical coordinate system, where the entire 3-dimensional structure is realized by rotating the image around the z -axis. The boundary conditions maintain the conducting bottom

electrode and particle at ground potential, and the top electrode at potential V . The boundary at $z = 0$ is chosen as “axial symmetry,” and the boundary at $z = 5$ is chosen as “zero charge/symmetry.” The background medium within the electrode gap is chosen as vacuum.

The dimensions on the r - and z -axes are normalized, and the dimensions of the structures are only dependent on their relative size to each other. When building the structure, it was recommended by Smith et al²⁸ that the width of the electrodes should be on the order of ten times the electrode gap to eliminate edge effects. Note the structure in Figure B.1 has an electrode width of only five times larger than the electrode gap, which was done here to improve the readability of the image, but Smith’s recommendation was followed for the simulations used in the thesis.

After creating the structure, it was divided into approximately 50,000 finite elements. COMSOL initially chooses the number and size of the elements. Generally, smaller elements are used around complex structures, such as the particle. The user then has the option to decrease the size of the elements, which increases the number of elements. The element size was chosen through an experimental process that solved the system many times using a different number of elements. This process was used to assure that the solution was completely independent of the element size. For the simulations used in this thesis, it was determined that using elements as much as 100 times smaller than the particle diameter at the surface of particle was sufficient. Figure B.2 is a close-up image of the particle showing the finite elements around the particle surface.

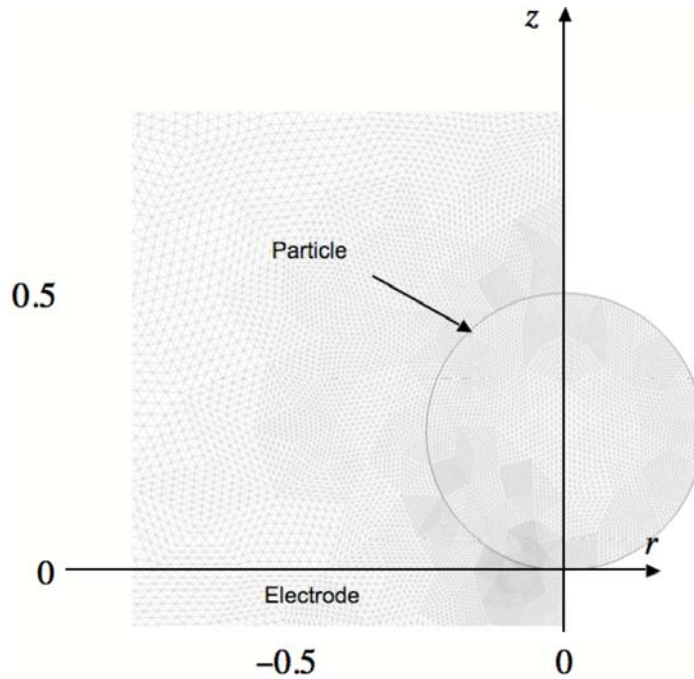


Figure B.2: Close-up image of the particle when charging against a planar electrode.

After dividing the structure into an appropriate mesh, the system is solved using predefined PDEs that are part of COMSOL's electrostatic module. Once solved, the relative magnitude of the electric field everywhere in the system is displayed in the surface plot shown in Figure B.3.

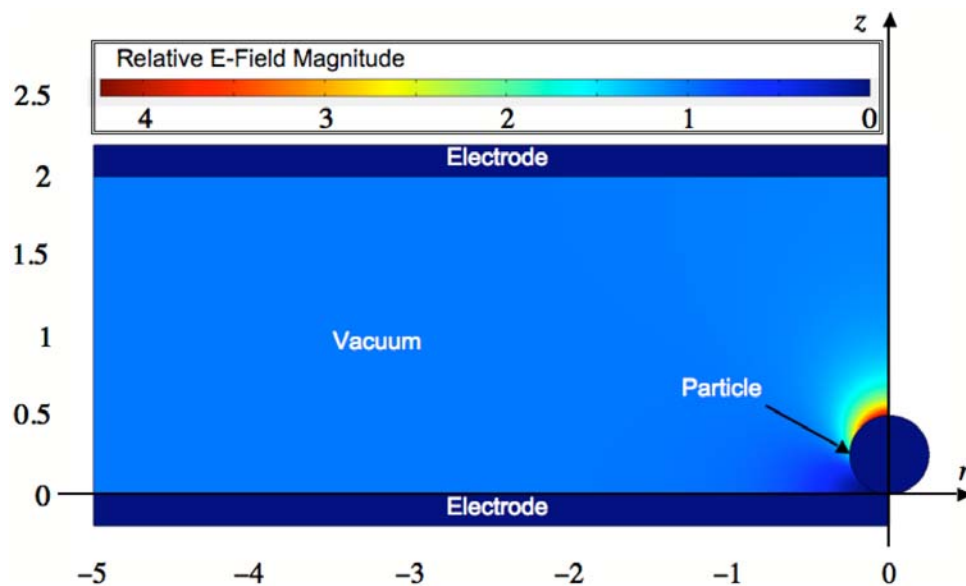


Figure B.3: Relative magnitude of the electrical field everywhere in the system.

The electric field magnitude shown Figure B.3 has been normalized to the strength of the background electric field within the electrode gap. As expected, the electric fields within the conducting electrodes and particle are zero. The majority of the fields within the electrode gap are not affected by the presence of the particle. But, the fields in the vicinity of the particle surface are significantly affected. It is shown that the field strength at the top surface of the particle is approximately 4.2 times stronger than the background field. Moving from the top of the particle to the bottom of the particle, the electric field at the surface decreases to zero. Plots of the normalized electric field at the particle surface are included in Chapter 2, which were used to determine the total particle charge.

COMSOL Multiphysics® proved to be an easy to use software tool essential to this thesis.

Bibliography

Bibliography

- [1] Musinski, L., Liu, T., Gilchrist, B., Gallimore, A., and Keidar, M., “Scalable Flat-Panel Nano-Particle MEMS/NEMS Thruster,” International Electric Propulsion Conference, Princeton, NJ, October 31 – November 4, 2005.
- [2] Musinski, L., Liu, T., Gilchrist, B., Gallimore, A., and Keidar, M., “Nanoparticle Electric Propulsion: Experimental Results,” AIAA-2006-4803, 42nd AIAA/ASME/SAE/ASEE Joint Propulsion Conference, Sacramento, CA, July 9-12, 2006.
- [3] Liu, T., Keidar, M., Musinski, L., Gallimore, A., and Gilchrist, B., “Theoretical Aspects of Nanoparticle Electric Propulsion,” AIAA-2006-4335, 42nd AIAA/ASME/SAE/ASEE Joint Propulsion Conference, Sacramento, CA, July 9-12, 2006.
- [4] Liu, T., Musinski, L., Patel, P., Gallimore, A., Gilchrist, B., and Keidar, M., “Nanoparticle Electric Propulsion for Space Exploration,” Space Technology and Applications International Forum, Albuquerque, NM, February 11-15, 2007.
- [5] Turner, M., “Rocket and Spacecraft Propulsion, Principles, Practice, and New Developments (Second Edition),” *Springer*, 2005.
- [6] Wertz, J. and Larson, W., “Space Mission Analysis and Design (Third Edition),” *Microcosm Press*, 1999.
- [7] Hale, F., “Introduction to Space Flight,” *Prentice Hall*, 1994.
- [8] Jahn, R., “Physics of Electric Propulsion,” *Dover Publications*, 2006.
- [9] Rayman, M., Varghese, P., Lehman, D., and Livesay, L., “Results from the Deep Space 1 Technology Validation Mission,” *Acta Astronautica*, Vol. 47, 2000, pp. 475-487.
- [10] Humble, R., Henry, G., and Larson, W., “Space Propulsion Analysis and Design,” *McGraw-Hill*, 1995.
- [11] Huang, W., Wang, K., and Chen, Q., “Effects of the Rocket Engine on the Single-Stage-to-Orbit Vehicle,” *Journal of Spacecraft and Rockets*, Vol. 35, 1998, pp. 113-114.
- [12] Glenn Research Center, <http://www.nasa.gov/centers/glenn/about/fs08grc.html>.

- [13] The University of Michigan's Plasmadynamics and Electric Propulsion Laboratory (PEPL), <http://aerospace.engin.umich.edu/spacelab>.
- [14] Wilbur, P., Rawlin, V., Beattie, J., "Ion Thruster Development Trends and Status in the United States," *Journal of Propulsion and Power*, Vol. 14, No. 5, 1998, pp. 708-715.
- [15] Sovey, J., et al. "Development of an Ion Thruster and Power Processor for New Millennium's Deep Space 1 Mission," National Aeronautics and Space Administration, 1997.
- [16] Staack, D., http://en.wikipedia.org/wiki/Ion_thruster.
- [17] Keidar, M. and Boyd, I., "Effect of a Magnetic Field on the Plasma Plume From Hall Thrusters," *Journal of Applied Physics*, Vol. 86, 1999.
- [18] Haas, J., et al, "Performance Characteristics of a 5 kW Laboratory Hall Thruster," AIAA-98-3656, 34th AIAA/ASME/SAE/ASEE Joint Propulsion Conference and Exhibit, Cleveland, OH, July 12-15, 1998.
- [19] Tajmar, M., Scharlemann, C., Genovese, A., and Buldrini, N., "Indium FEEP Micropropulsion Subsystem for LISA Pathfinder," 42nd AIAA/ASME/SAE/ASEE Joint Propulsion Conference and Exhibit, Sacramento, CA, 2006.
- [20] Marcuccio, S., Genovese, A., and Andrenucci, M., "FEEP Microthruster Technology Status and Potential Applications," *International Astronautical Federation*, 1997.
- [21] Marcuccio, S., Giannelli, S., and Andrenucci, M., "Attitude and Orbit Control of Small Satellite and Constellations with FEEP Thrusters," *Electric Rocket Propulsion Society*, 1997.
- [22] Marcuccio, S., Paita, L., Saviozzi, M., and Andrenucci, M., "Flight Demonstration of FEEP on Get Away Special," AIAA-98-3332, 33rd AIAA/ASME/SAE/ASEE Joint Propulsion Conference and Exhibit, Cleveland, OH, 1998.
- [23] Paine, M. and Gabriel, S., "A Micro-Fabricated Colloidal Thruster Array." AIAA-2001-3329, 37th AIAA/ASME/SAE/ASEE Joint Propulsion Conference and Exhibit, Salt Lake City, UT, July 8-11, 2001.
- [24] Stark, J., Stevens, B., Kent, B., Standford, M., and Alexander, M., "Micro-Fabricated and Operational Nano Emitters Suitable for a Colloid Thruster Array," *Journal of Spacecraft and Rockets*, Vol. 42, 2005, pp. 628-639.
- [25] Bailey, A., "Investigation of a Single Spraying Site of a Colloid Thruster," *Journal of Applied Physics*, Vol. 6, 1973, pp. 276-288.

- [26] Mukhija, D., Solomon, M., Burns, M., Personal Communication, October 2007.
- [27] Ulaby, F. "Fundamentals of Applied Electromagnetics," *Pearson Prentice Hall*, 2004.
- [28] Smith, R., Carey, J., Forrest, R., and Silva, S., "Effect of Aspect Ratio and Anode Location on the Field Emission Properties of a Single Tip Based Emitter," *American Vacuum Society*, Vol. 23, 2005, pp. 632 – 635.
- [29] Felici, N. "Forces et Charges de Petits Objets en Contact Avec une Electrode Affectee d'um Champ Electrique," *Revue Generale d'Electricite*, Vol. 75, 1966, pp. 1145-1160.
- [30] Tobazeon, R., "Electrohydrodynamic Behavior of Single Spherical or Cylindrical Conducting Particles in an Insulating Liquid Subjected to a Uniform DC Field," *Journal of Physics D: Applied Physics*, Vol. 29, 1996, pp. 2595 – 2608.
- [31] Tobazeon, R., "Charges and Discharges of Conducting Particles in a Plane Oil Gap Subjected to a DC Voltage," 12th International Conference on Conduction and Breakdown in Dielectric Liquids, Rome, Italy, July 15-19, 1996.
- [32] Tobazeon, R., "Behavior of Spherical and Cylindrical Particles in an Insulating Liquid Subjected to a DC Uniform Field," *Laboratoire d'Electrostatique et de Materiaux Dielectriques*, 1993, pp. 415-419.
- [33] Clearco Products Co., Inc., "Product Information," www.clearcoproducts.com.
- [34] Wu, C. and Conrad, H., "The Temperature Dependence of the Conductivity of Silicone Oil and Related Electrorheology of Suspensions Containing Zeolite Particles," *Journal of Physics D: Applied Physics*, Vol. 31, 1998, pp. 3403-3409.
- [35] Analog Devices. "Low-Bias-Current, High-Stability JFET Operational Amplifier. OP-41," US Patent Number: 4,538,115.
- [36] Pozar, D., "Microwave Engineering (Third Edition)," *John Wiley & Sons, Inc.*, 2004.
- [37] Barnes, J. "Electronic System Design: Interference and Noise Control Techniques," *Prentice-Hall*, 1987.
- [38] Cheng, D., "Field and Wave Electromagnetics," *Addison-Wesley Publishing Company, Inc.*, 1992
- [39] Matweb, "Material Property Data," <http://www.matweb.com>.
- [40] Tamura, K., Kimura, Y., Suzuki, H., Kido, O., Sato, T., and Tanigaki, T., "Structure and Thickness of Natural Oxide Layer Ultrafine Particles," *Journal of Applied Physics*, Vol. 42, 2003, pp. 7489-7492.

- [41] Oberg, E., Jones, F., Horton, H., and Ryffel, H., "Machinery's Handbook 25," *Industrial Press Inc.*, 1995.
- [42] AZoM.com. "The A to Z of Materials and AZojomo," *The AZo Journal of Materials Online*, 2008.
- [43] Cho, S., Idrobo, J., Olamit, J., Liu, K., Browning, N., and Kauzlarich, S., "Growth Mechanisms and Oxidation-Resistance of Gold-Coated Iron Nanoparticles," *Chem. Mater.*, Vol. 17, No. 12, 2005, pp. 3181-3186.
- [44] Joo, D., Park, S., Jung, Y., Lee, J., Ye, C., and Lee, K., "Effect of Platinum Pre-Coating on isothermal Oxidation Behavior of MCrAlY Coating by Plasma Spray Process," *Materials Science Forum*, Vol. 544-545, 2007, pp. 721-724.
- [45] Wilm, M. and Mann, M. "Electrospray and Taylor-Cone Theory, Dole's Beam of Macromolecules at Last?," *International Journal of Mass Spectrometry and Ion Processes*, Vol. 136, 1994, pp. 167-180.
- [46] Yarin, A., Koombhongse, S., and Reneker, D. "Taylor Cone and Jetting from Liquid Droplets in Electrospinning of Nanofibers," *Journal of Applied Physics*, Vol. 90, 2001, pp. 4836-4846.
- [47] Meesters, G., Vercoulen, P., Marijnissen, J., and Scarlett, B. "Generation of Micron-Sized Droplets from the Taylor Cone." *Journal of Aerosol Science*, Vol. 23. 1992, pp. 37-49.
- [48] Gamero-Casta, M. and Hruby, V., "Electrospray as a Source of Nanoparticles for Efficient Colloid Thrusters," *Journal of Propulsion and Power*. Vol. 17, No. 5, 2001, pp. 977-987.
- [49] Shtyrlin, A. "State of the Art and Future Prospects of Colloidal Electric Thrusters," 24th International Electric Propulsion Conference, Moscow, Russia, 1995.
- [50] Tonks, L., "A Theory of Liquid Surface Rupture by a Uniform Electric Field," *Physical Review*, Vol. 48, 1935, pp. 562-568.
- [51] Wilkes, J., "Fluid Mechanics for Chemical Engineers." *Prentice Hall, Inc.*, 1999
- [52] Jasper, J., *Journal of Physical Chemistry*, 1972.
- [53] Walker, R., "Specific Gravity of Liquids," *SiMetric.co.uk*, 2007.
- [54] McMurry, J. and Fay, R. "Chemistry, Third Edition." *Prentice Hall, Inc.*, 2001.

- [55] Perry, R. and Green, D. "Perry's Chemical Engineers' Handbook (Sixth Edition)," *McGraw-Hill*, 1987.
- [56] Kamineni, V., Lvov, Y., and Dobbins, T. "Layer-by-Layer Nanoassembly of Polyelectrolytes Using Formamide as the Working Medium." *American Chemical Society*, Vol. 23, No. 14, 2007, pp. 7423-7427.
- [57] Hui, Y., "Encyclopedia of Food Science and Technology (Volume 4)," *John Wiley and Sons*, 1992.
- [58] Hodgman, C., and Lange, A., "Handbook of Chemistry and Physics," *Chemical Rubber Publishing Company*, 1954.
- [59] Basu, A., "Microthermal Devices for Fluidic Actuation by Modulation of Surface Tension." Ph.D. Dissertation, University of Michigan, 2008.
- [60] Ohta, A., Arash, J., Valley, J., Hsu, H., Wu, M., "Optically Actuated Thermocapillary Movement of Gas Bubbles on an Absorbing Substrate." *Applied Physics Letters*, 2007.
- [61] Man, P., Mastrangelo, C., Burns, M., and Burke, D. "Microfabricated Capillarity-Driven Stop Valve and Sample Injector," *Micro Electro mechanical Systems*, 1998.
- [62] Liu, T., Drenkow, B., Musinski, L., Gallimore, A., Gilchrist, B., Millunchick, J., Morris, D., Doan, A., Munski, J., and Muldoon, A., "Developmental Progress of the Nanoparticle Field Extraction Thruster." AIAA-2008-5096, 44th AIAA/ASME/SAE/ASEE Joint Propulsion Conference and Exhibit, Hartford, CT, July 21-23, 2008.
- [63] Liu, T., Musinski, L., Keidar, M., Gallimore, A., and Gilchrist, B., "Physical Models and Performance Implications for the Nanoparticle Field Extraction Thruster," International Electric Propulsion Conference, Florence, Italy, September 17-20, 2007.
- [64] Light, T., Litch, S., Bevilacqua, A., and Morashc, K., "The Fundamental Conductivity and Resistivity of Water," *Electrochemical and Solid-State Letters*, Vol. 8, No. 1, 2005. Pp. 16-19.
- [65] Drake, F., Pierce, G., and Dow, M., "Measurement of the Dielectric Constant and Index of Refraction of Water and Aqueous Solutions of KCl at High Frequencies," *Physical Review*, Vol. 35, pp. 613-622.
- [66] Winter, M., "WebElements: The Periodic Table on the WWW." *The University of Sheffield and WebElements Ltd*, 1993-2008.

- [67] Musinski, L., Liu, T., Gilchrist, B., Gallimore, A., and Keidar, M., "Experimental Results and Modeling Advances in the Study of Nanoparticle Field Extraction Thruster," AIAA-2007-5254, 43rd AIAA/ASME/SAE/ASEE Joint Propulsion Conference, Cincinnati, OH, July 8-11, 2007.
- [68] Musinski, L., Liu, T., Gilchrist, B., Gallimore, A., and Keidar, M., "Nanoparticle Field Extraction Thruster (nanoFET): Design and Results of the Microparticle Emitter Prototype," International Electric Propulsion Conference, Florence, Italy, September 17-20, 2007.
- [69] Liu, T., Morris, D., Cionca, C., Gallimore, A., Gilchrist, B., and Clarke, R., "MEMS Gate Structures for Electric Propulsion Applications," AIAA-2006-5011, 42nd AIAA/ASME/SAE/ASEE Joint Propulsion Conference and Exhibit, Sacramento, CA, July 9-12, 2006.
- [70] Crowe, C., "Multiphase Flow Handbook," *Taylor & Francis*. 2005.
- [71] Elert, G., "The Physics Hypertextbook," <http://hypertextbook.com/physics/>, 1998-2007.
- [72] Podczek, F., "Particle-Particle Adhesion in Pharmaceutical Powder Handling," *Imperial College Press*, 1998.
- [73] Musinski, L., Liu, T., Eu, I., Gilchrist, B., Gallimore, A., Mirecki-Millunchick, J., and Morris, D. "Nanoparticle Field Extraction Thruster (nanoFET): Introduction to, Analysis of, and Experimental Results from the 'No Liquid Design Configuration'," AIAA-2008-5097, 44th AIAA/ASME/SAE/ASEE Joint Propulsion Conference, Hartford, CT, July 21-23, 2008.
- [74] Bowling, R. "An Analysis of Particle Adhesion on Semiconductor Surfaces," *Journal of the Electrochemical Society*, Vol. 132, 1985, pp. 2208-2214.
- [75] Dzyaloshinski, I., Lifshitz, E., Pitaevski, P. "General Theory of Van Der Waals' Forces." *Soviet Physics Uspekhi*, Vol. 73, 1961, pp. 153-176.
- [76] Curran, C., Watkins, K., and Lee, J. "Shock Pressure Measurements for the Removal of Particles of Submicron Dimensions from Silicone Wafers," 21st International Congress on Applications of Lasers and Electro-Optics, Scottsdale, October 14-17, 2002.
- [77] Leider, P., Olapinski, M., Mosbacher, M., and Boneberg, J. "Nanoparticle Adhesion and Removal Studied by Pulsed Laser Irradiation," *High-Power Laser Ablation*, Vol. 6261, 2006.
- [78] Anis, H. and Srivastava, K., "Free Conducting Particles in Compressed Gas Insulation," *IEEE Transactions on Electrical Insulation*, Vol. EI-16, 1981, pp. 327-338.

- [79] Dupont Technical Information “Dupont™, Kapton® Insulation Substrate,” Dupont High Performance Materials, 2001.
- [80] Lurie Nanofabrication, Personal Communication, University of Michigan, 2008.
- [81] Visser, J., “On Hamaker Constants: A Comparison Between Hamaker Constants and Lifshitz-Van Der Waals Constants,” *Advances in Colloid and Interface Science*, 1972, pp. 331-363.
- [82] Johnson, K. L., “Contact Mechanics,” Cambridge University Press, Cambridge, 1985.
- [83] Rabinovich, Y., Adler, J., Ata, A., Singh, R., and Moudgil, B. “Adhesion Between Nanoscale Rough Surfaces,” *Journal of Colloid and Interface Science*, Vol. 232, 2000, pp. 17-24.
- [84] Krupp, H., “Particle Adhesion Theory and Experiment,” *Advances in Colloid Interface Sciences*, Vol. 1, 1967, pp. 111-239.
- [85] Anandarajah, A. and Chen, J. “Single Correction Function for Computing Retarded Van der Waals Attraction” *Journal of Colloid and Interface Science*, Vol. 176, 1995, pp. 293-300.
- [86] Lee-Desautels, R., “Theory of van der Waals Forces as Applied to Particulate Materials.” *Educational Resources for Particle Technology*, 2005.
- [87] Bohm, G., Krupp, H, and Schnabel, W., “Molecular Processes at Solid Surfaces,” *McGraw Hill*, 1969.
- [88] Fowkes, F. “Surfaces and Interfaces.” *Syracuse University Press*, Vol. 1, 1967, p. 199.
- [89] Ebert, K., Wittman, F., *Phys. Let.* 1970.
- [90] Watillon, A., Joseph-Petit, *Discuss. Faraday Soc.* 42 1969.
- [91] Buttner, H., Gerlach, E. *Chem. Phys. Lett.*, 1970.
- [92] Deline, C., Goldberg, H., Morris, D., and Ramos, R. “Field Emission Cathodes Used in the FEGI Get Away Special Shutter Mission,” AIAA-2004-3498, 40th AIAA/ASME/SAE/ASEE Joint Propulsion Conference and Exhibit, Fort Lauderdale, FL, July 11-14, 2004.
- [93] Maia, P. and Nussenzevig, H., “Theory of Optical Tweezers,” *Europhysics Letter*, Vol. 50, 2000, pp. 702-708.

- [94] Wanis, S., Rangedera, T., and Komerath, N., "Particle-Particle Interaction in Electromagnetic Fields for Force-Field Tayloring," Space Technology and Applications International Forum, Albuquerque, NM, February 11-15, 2007.
- [95] Ashkin, A., "Optical Trapping and Manipulation of Neutral Particles Using Lasers," *The National Academy of Science of the USA*, Vol. 94, 1997, pp. 4853-4860.
- [96] Wanis, S., Komerath, N., "Force-Field Tayloring: First Principles Derivation of Wall Formation Physics." 57th International Astronautical Federation Congress, Valencia, Spain, October 2006.
- [97] Ashkin, A. and Gordon, J., "Stability of Radiation-Pressure Particle Traps: An Optical Earnshaw Theorem," *Optical Letters*, Vol. 8, No. 10, 1983, pp. 511-513.
- [98] Ashkin, A., Dziedzic, J., Bjorkholm, E., and Chu, S. "Observation of a Single Beam Gradient Force Optical Trap for Dielectric Particles," *Optics Letters*, Vol. 11, No. 5, 1996, pp. 288-290.
- [99] Wang, L. and Zhao, C., "Dynamic Radiation Force of a Pulsed Gaussian Beam Acting on a Rayleigh Dielectric Sphere," *Optical Society of America*, Vol. 15, No. 17, 2007.
- [100] Cheng, D., "Field and Wave Electromagnetics (2nd Edition)," *Addison-Wesley Series in Electrical Engineering*, 1989.
- [101] Margulies, S. "Force on a Dielectric Slab Inserted into a Parallel-Plate Capacitor," *American Journal of Physics*, Vol. 56, 1984, pp. 515-518.
- [102] Rohrbach, A. and Stelzer, E., "Optical Trapping of Dielectric Particles in Arbitrary Fields," *Journal of the Optical Society of America*, Vol. 18, 2001, pp. 839-853.
- [103] Ulaby, F., "Fundamentals of Applied Electromagnetics (5th Edition)." *Prentice Hall*, 2006.
- [104] Wanis, S. "Tailored Force Fields for Flexible Fabrication." Ph.D. Thesis, Georgia Institute of Technology, 2006.
- [105] Price, H. and Nelson, J., "Properties and Applications of a Pitch Carbon Microsphere Composite," *Polymer Engineering and Science*, Vol. 17, 2004, pp. 341-348.
- [106] Brown, B. and Brown, P., "Optical Tweezers: Theory and Current Applications," *American Laboratory*, 2001.

- [107] Abdolvand, R., and Ayazi, F., “An Advanced Reactive Ion Etching Process for Very High Aspect-Ratio Sub-Micron Wide Trenches in Silicon,” *Sensors and Actuators*, Vol. 144, 2008, pp. 109-116.
- [108] Vanderelzen, B. “The Bosch Process,” The University of Michigan Nanofabrication Laboratory Internal Presentation.
- [109] Bauer, T. “High Density Through Wafer Via Technology,” Nano Science and Technology Institute, Vol 3, 2007.
- [110] Gomez, P. “State-of-the-Art of MEMS Technology for Design and Fabrication of Micro-Mirrors,” Florida International University, Advanced Electronic Systems I, 2003.
- [111] Goldberg, H. P. Encarnación, D. Morris, B. Gilchrist, and R. Clarke, “Cold-Cathode Electron Field Emission of Boron Nitride Thin Film with a MEMS-based Gate for Space Applications,” 40th AIAA/ASME/SAE/ASEE Joint Propulsion Conference & Exhibit, AIAA-2004-3499 Ft. Lauderdale, July 11-14, 2004.
- [112] Liu, T., Personal Communication, 2008.